MICROCOPY RESOLUTION TEST CHART

NATIONAL BUREAU OF STANDARDS-1963-A

(12)

DTNSRDC/SME-CR-24-86
DTNSRDC Code 2814
Contractor Report

AD-A180 200

DTIC
SELECTED
MAY 1 4 1987
D

A PHYSICAL METALLURGICAL BASIS FOR HEAT-AFFECTED ZONE AND

BASE-PLATE PROPERTIES OF A MICROALLOYED HSLA STEEL

by
Roger A. Nichting
Elliot L. Brown

87   5   13   160

REPORT DOCUMENTATION PAGE

1a. REPORT SECURITY CLASSIFICATION		1b. RESTRICTIVE MARKINGS *A180 200*
Unclassified		

2a. SECURITY CLASSIFICATION AUTHORITY	3. DISTRIBUTION/AVAILABILITY OF REPORT
	Approved for public release; distribution unlimited.
2b. DECLASSIFICATION/DOWNGRADING SCHEDULE	

4. PERFORMING ORGANIZATION REPORT NUMBER(S)	5. MONITORING ORGANIZATION REPORT NUMBER(S)
T-3136	DTNSRDC/SME-CR-24-86

6a. NAME OF PERFORMING ORGANIZATION	6b. OFFICE SYMBOL (If applicable)	7a. NAME OF MONITORING ORGANIZATION
Colorado School of Mines Metallurgical Engineering Dept.		David Taylor Naval Ship Research and Development Center

6c. ADDRESS (City, State, and ZIP Code)	7b. ADDRESS (City, State, and ZIP Code)
Golden CO 80401	Bethesda, MD 20084-5000

8a. NAME OF FUNDING/SPONSORING ORGANIZATION	8b. OFFICE SYMBOL (If applicable)	9. PROCUREMENT INSTRUMENT IDENTIFICATION NUMBER
DTNSRDC	Code 012.5	N00167-83-Re-00159

8c. ADDRESS (City, State, and ZIP Code)	10. SOURCE OF FUNDING NUMBERS			
Bethesda, MD 20084-5000	PROGRAM ELEMENT NO	PROJECT NO	TASK NO RS	WORK UNIT ACCESSION NO
	62234N	RS 34S50	34550-001	DN 778013

11. TITLE (Include Security Classification)

A PHYSICAL METALLURGICAL BASIS FOR HEAT-AFFECTED ZONE AND BASE-PLATE PROPERTIES OF A MICROALLOYED HSLA STEEL

12. PERSONAL AUTHOR(S)
Roger A. Nichting and Elliot L. Brown

13a. TYPE OF REPORT	13b. TIME COVERED	14. DATE OF REPORT (Year, Month, Day)	15. PAGE COUNT
Final	FROM 1984 TO 1986	December 1986	

16. SUPPLEMENTARY NOTATION

17. COSATI CODES			18. SUBJECT TERMS (Continue on reverse if necessary and identify by block number)
FIELD	GROUP	SUB-GROUP	Welding
			HSLA steels
			Impact toughness

19. ABSTRACT (Continue on reverse if necessary and identify by block number)

The overall objective of this study was to elucidate the processing structure-property relationship associated with the heat-affected zone (HAZ) produced in an HSLA microalloyed steel during arc welding.

Single pass submerged arc welds on a Nb-V microalloyed steel were made with variable heat input. The thermal cycle as a function of heat input and position in the HAZ was determined experimentally in the course of welding. In addition, weld simulations were produced for selected heat inputs and HAZ locations.

The evolution of austenite and transformation product microstructure as well as the state of microalloy precipitation was monitored as a function of heat input and HAZ location primarily via light and electron microscopy on specimens from actual welds and simulation specimens. These observations were utilized to support efforts to model austenite microstructure evolution and continuous cooling transformation behavior in the HAZ.
(Continued)

20. DISTRIBUTION/AVAILABILITY OF ABSTRACT	21. ABSTRACT SECURITY CLASSIFICATION
☐ UNCLASSIFIED/UNLIMITED ☒ SAME AS RPT ☐ DTIC USERS	Unclassified

22a. NAME OF RESPONSIBLE INDIVIDUAL	22b. TELEPHONE (Include Area Code)	22c. OFFICE SYMBOL
G.E. Sutton and M.G. Vassilaros	(301) 267-3755	DTNSRDC Code 2814

DD FORM 1473, 84 MAR
83 APR edition may be used until exhausted
All other editions are obsolete

Block 19 Continued

Charpy impact toughness testing was performed on actual weld HAZ specimens and specimens of selected simulation specimens. Impact transition curves were determined and the microstructure through which fracture propagated was correlated with impact transition energies and fracture surface morphology determined via scanning electron microscopy (SEM).

Variations of the Rosenthal equations were found to be inadequate in predicting thermal transient curves under various weld and material parameters for this submerged arc welding investigation. However, the Rosenthal equations did predict the general slope of the thermal curve and was utilized in the formation of an empirical thermal model via a least squares fit.

Austenite grain growth kinetics for athermal weld heat treatments were found to be quite different than those of isothermal furnace heat treatments. In general, grain growth for rapid heating rates in excess of 100 degrees C. per second was found to be greater than that of slow furnace heat treatment conditions. In addition, austenite grain coarsening behavior during welding is characterized by abrupt grain coarsening at 1100 degrees C and is controlled by precipitate dissolution of V(C,N).

The grain coarsened region in the near fusion zone for all heat inputs was characterized by a maximum in hardness that decreased to a shallow minimum in the grain refined region as the unaffected base-plate was approached. Hardness was the greatest for low heat input (1.97 KJ/mm) and was attributed to martensitic transformation product microstructure. A second hardness maximum in the high heat input (4.92 KJ/mm) occured in the fine polygonal ferrite/pearlite microstructural region and was due to an iron carbide precipitate dispersion.

Toughness was found to be a function of heat input and position. Low toughness occured in the austenite grain coarsened region for all heat inputs. The transformation product microstructure associated with the low toughness was upper bainite and auto-tempered martensite. Crack nucleation in the bainite was due to large interlath carbides while slightly higher toughness in martensite was due to finer intralath carbides. The grain refined region was generally very high in toughness, moreso than the base-plate and was attributed to the ductility of the fine ferritic grain structure.

Finally, in comparison of simulation to experimental data, Gleeble simulation heat treated samples did adequately simulate local HAZ microstructures and mechanical properties associated with a particular location and heat input.

ABSTRACT

The overall objective of this study was to elucidate the processing structure-property relationship associated with the heat-affected zone (HAZ) produced in an HSLA microalloyed steel during arc welding.

Single pass submerged arc welds on a Nb-V microalloyed steel were made with variable heat input. The thermal cycle as a function of heat input and position in the HAZ was determined experimentally in the course of welding. In addition, weld simulations were produced for selected heat inputs and HAZ locations.

The evolution of austenite and transformation product microstructure as well as the state of microalloy precipitation was monitored as a function of heat input and HAZ location primarily via light and electron microscopy on specimens from actual welds and simulation specimens. These observations were utilized to support efforts to model austenite microstructure evolution and continuous cooling transformation behavior in the HAZ.

Charpy impact toughness testing was performed on actual weld HAZ specimens and specimens of selected simulation specimens. Impact transition curves were determined and

iii

the microstructure through which fracture propagated was correlated with impact transition energies and fracture surface morphology determined via scanning electron microscopy (SEM).

Variations of the Rosenthal equations were found to be inadequate in predicting thermal transient curves under various weld and material parameters for this submerged arc welding investigation. However, the Rosenthal equations did predict the general slope of the thermal curve and was utilized in the formation of an empirical thermal model via a least squares fit.

Austenite grain growth kinetics for athermal weld heat treatments were found to be quite different than those of isothermal furnace heat treatments. In general, grain growth for rapid heating rates in excess of 100 degrees C. per second was found to be greater than that of slow furnace heat treatment conditions. In addition, austenite grain coarsening behavior during welding is characterized by abrupt grain coarsening at 1100 degrees C. and is controlled by precipitate dissolution of V(C,N).

The grain coarsened region in the near fusion zone for all heat inputs was characterized by a maximum in hardness that decreased to a shallow minimum in the grain refined region as the unaffected base-plate was approached.

Hardness was the greatest for low heat input (1.97 KJ/mm) and was attributed to martensitic transformation product microstructure. A second hardness maximum in the high heat input (4.92 KJ/mm) occured in the fine polygonal ferrite/pearlite microstructural region and was due to an iron carbide precipitate dispersion.

Toughness was found to be a function of heat input and position. Low toughness occured in the austenite grain coarsened region for all heat inputs. The transformation product microstructure associated with the low thoughness was upper bainite and auto-tempered martensite. Crack nucleation in the bainite was due to large interlath carbides while slightly higher toughness in martensite was due to finer intralath carbides. The grain refined region was generally very high in toughness, moreso than the base-plate and was attributed to the ductility of the fine ferritic grain structure.

Finally, in comparison of simulation to experimental data, Gleeble simulation heat treated samples did adequately simulate local HAZ microstructures and mechanical properties associated with a particular location and heat input.

T-3136

TABLE OF CONTENTS

T-3136

LIST OF FIGURES

x

T-3136

T-3136

xxiii

FIGURE   PAGE

T-3136

T-3136

LIST OF TABLES

ACKNOWLEDGEMENTS

1. INTRODUCTION AND BACKGROUND

Welded construction is an economical means for joining components of varying chemical composition, section size, geometry and material condition. According to the American Welding Society, [1] a weld is a "localized coalesence of metals produced by heating the materials to suitable temperatures with or without the use of filler metal". Since the majority of welded components are steel the processes developed for welding steel are commercially important.

Electric arc welding employs the arc to melt base-plate and melt and transfer filler metal during joining. A variety of arc welding procedures have been developed that are distinguished by the means for producing the arc, introducing filler metal and protecting molten metal from oxidation. [2]

Submerged arc welding utilizes a molten fluxing agent to protect the molten filler wire metal during transfer to and in the molten pool during metal deposition. The flux also participates in the chemical reactions associated with steel refinement.

The welded joint made by the electric arc welding

process has generally been considered to be compromised of
two major zones:

(a)   The fusion zone, where temperatures have exceeded the
melting temperature and material is liquified.

(b)   The heat-affected zone, extending outward from the
fusion zone in which the microstructure of the base-plate
has been altered by the heat of the welding process,
Figure 1.

The molten metal in the fusion zone cools primarily by
conduction of heat away from the fusion zone by the members
being welded.   It is primarily this conduction of heat that
produces the heat-affected zone.

The heat of welding induces many changes in the
microstructure and properties of the HAZ of a steel
weldment.   Furthermore, due to the variation of thermal
cycle with position in the HAZ a microstructural and
property gradient exists so that the HAZ justifiably
represents a microcomposite material.

Portions of the HAZ are fully austenitized and can
transform to ferrite products in association with a range
of cooling rates, dependent upon the welding parameters
employed.   Other regions of the HAZ may represent
base-plate microstructure altered by intercritical and
subcritical heat treatments.
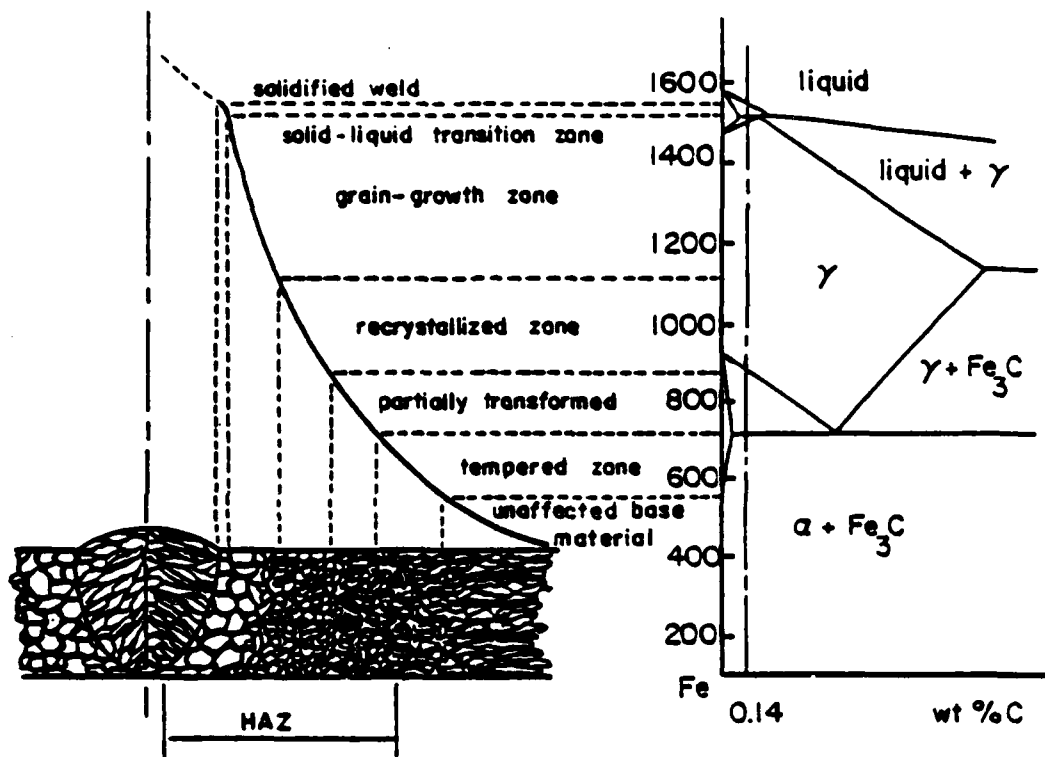
Figure 1.   Transformation schematic of the heat affected
             zone for HSLA steel (0.14 wt% C).

The need for high deposition rate/high productivity welding has necessitated the usage of high heat input/minimum number of pass welding procedures. Increased heat input can produce thermal cycles that result in deleterious HAZ microstructures.

The advent of microalloyed, high strength low alloy (HSLA) steel technology has resulted in additional problems related to high heat input welding. Low carbon microalloyed HSLA steel base-plate relies on a fine grained ferrite, precipitation strengthened microstructure for high strength and high toughness. Therefore, this base-plate microstructure/property package is extremely sensitive to the thermal treatment of the HAZ, especially that associated with high heat-input. Without proper care the excellent properties developed in the base-plate may be destroyed during welding.

In the past, a costly empirical approach has been made to establish the inter-relationship of welding parameters and weldment properties. High strength-high toughness weldments of metallurgically complex microalloyed steels requires a more fundamental approach to the economical development of welding procedures.

The interrelationship of processing (weld parameters), structure and properties is the basis for this approach.

In this regard, a number of models must be formulated and
experimentally supported in order to construct a general
model. A thermal model is needed to specify the thermal
cycle as a function of welding parameters and position in
the HAZ. A microstructural model is necessary to predict
austenite and transformation product microstructural
evolution in the context of the thermal model. Finally,
the relationship between structure and mechanical
properties must be established.

2. LITERATURE REVIEW

2.1. Microalloyed HSLA Technology

The development of high-strength, low-alloy (HSLA)
steels, is based on the control of microstructure via
thermomechanical treatment to produce a unique combination
of high strength, high toughness, good formability, good
notch fatigue resistance, good weldability at relatively
low cost. Microalloyed HSLA steel is typically a low
carbon - manganese steel with small amounts of strong
carbide and nitride formers added such as Nb, V, and Ti.
Microalloy precipitation of transition metal carbonitrides
in austenite results in microstructural refinement during
thermomechanical treatment. Austenite microstructural
refinement via controlled rolling [3] results in ferrite
transformation product and increases in ferrite nucleation
via alloying and controlled cooling refinement.
Precipitation in ferrite provides precipitation
strengthening. Multiple transition metal additions have
been made to control microstructure over a wide range of
temperatures as well as well as precipitation
strengthening. Thus microalloyed steels derive their high

strength from grain and subgrain refinement and
precipitation strengthening. In addition to increasing the
strength, fine ferrite grain size enhances toughness by
lowering the impact transition temperature.

It is the simultaneous enhancement of strength and
toughness by grain refinement that offsets the appreciable
decrease in toughness via precipitation strengthening.

The optimization of alloying and thermomechanical
treatment has been the subject of extensive review.[4]

2.2. Heat Flow During Welding

In order to model microstructural evolution in the HAZ
during submerged arc welding a thermal model for the
welding process must first be established. This model
allows for the specification of temperature as a function
of position in the HAZ, time, and heat input. Ideally it
should also account for variations in weld geometry and
preparation. An accurate thermal model can then be
utilized to integrate kinetic equations for pertinent
thermally activated processes over the weld thermal cycle
i.e. precipitate coarsening, dissolution and grain growth.

Theoretical treatments of heat flow during welding have
been accomplished and could be utilized for modeling

purposes. However, a dearth of experimental data exists in support of specific models for the various welding processes.

It is pertinent to inquire as to the adequacy of current theoretical models in predicting the observed thermal response.

A review of the literature in this area reveals two basic mathematical approaches to the heat flow problem. One approach is analytical and involves the solution of a pertinent differential equation in closed form. This approach necessarily requires a number of simplifying assumptions regarding thermal parameters, heat source geometry, weld preparation geometry, plate thickness, boundary conditions, and welding procedures in order to obtain a solution in closed form. These assumptions can introduce significant deviations between measured and predicted thermal response dependent upon the particular set of welding conditions under consideration.

Meyers and others [5,6] have reviewed this subject in depth. Closed form solutions suffer from several weaknesses. The geometry is highly idealized into forms such as infinite plates or bars. The thermal properties and boundary conditions are usually set equal to a constant value. Convection and radiation are usually ignored. The

point, line and plane sources idealize a heat source which
in reality is distributed.   These solutions are most
accurate far from the heat source.   At the source, the
error in temperature is large--usually infinite.   Near the
heat source, the accuracy can be improved by matching the
theoretical solution to experimental data.   This is usually
done by choosing a fictitous thermal conductivity value.

The second approach is a solution of the heat flow
transient problem by means of numerical methods.   Finite
difference and finite element solutions are invariably
accomplished by means of high speed digital computation and
require sophisticated computer codes.   However, they
obviate the need for certain of the abovementioned
simplifying assumptions in order to obtain a tractable
solution.

2.2.1. Analytical Models

The earliest analytical approach specific to welding is
due to Rosenthal [7] Other developments in this area have
essentially been modifications of this approach. [8,13,23]
Developments since that time include the Adams [9,10] and
Graville [11] modifications a   the alternative formulation
of Tanaka. [12,13,14] These analytical models

have been summarized and reviewed. [6,15,16]

In the Rosenthal approach the effects of a moving heat source on the temperature distribution in a body are considered with certain simplifying assumptions. [15,16] The thermal parameters such as conductivity and specific heat are assumed constant and heat transfer to the surroundings is insignificant with respect to conduction within the body. The former assumption is generally regarded as a significant draw back to analytical solutions since thermal parameters can vary significantly with temperature, Figure 2, and composition. [15,17] The assumption of constant thermal parameters is required to produce a tractable linear differential equation. The assumption regarding heat transfer to surroundings may be a problem with regard to thin sheet specimens.

Rosenthal type analytical solutions are associated with the attainment of a so-called quasi-stationary state. This state is associated with the heat saturation of a volume of material surrounding the moving source. In this state there is no time variation of temperature for points in the body if a coordinate system referenced to the moving heat source is employed. This assumption simplifies the differential equation to be solved but implies that welding has been going on for a period of time. Various
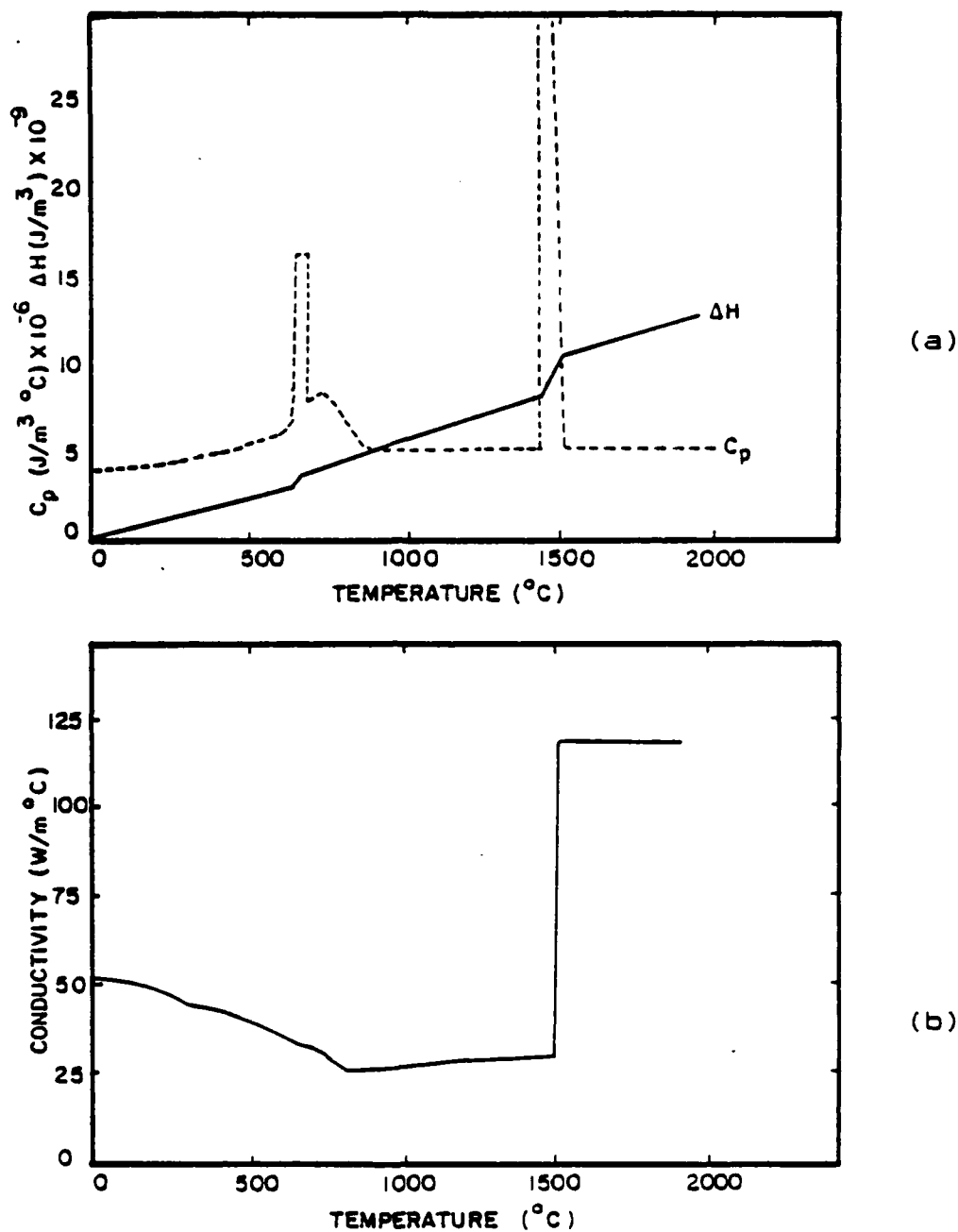
Figure 2. Thermal parameters used in modeling equations.
            (a) Volumetric heat capacity and latent heats
                of fusion as a function of temperature.
            (b) Thermal conductivity as a function of
                temperature.

investigators have termed this a limit state [15] and a
pseudo-steady state. [16]

The solutions for various idealized circumstances can
be classified with regard to models for the heated body
(semi-infinite, plate, sheet), the heat source (point,
linear), duration of heat source (instantaneous,
continuous) and motion of heat source (moving, quickly
moving). [15]

For a point source acting on a semi-infinite plate the
solution is:

(2.1) $$T - T_o = \frac{q}{(2\pi\lambda R)} \cdot \exp\left(\frac{-v}{(2a)\cdot(R + \varepsilon)}\right)$$
where,

T, T_o = temperature and initial temperature

q = heat input

v = speed of travel for source

$R = (\varepsilon^2 + Y^2 + Z^2)^{0.5}$ = magnitude of the

position vector

λ = thermal conductivity

$\varepsilon = x - vt$

a = thermal diffusivity = $\lambda/\rho c$

ρ = density

c = specific heat

The spatial parameters are defined in Figure 3. This
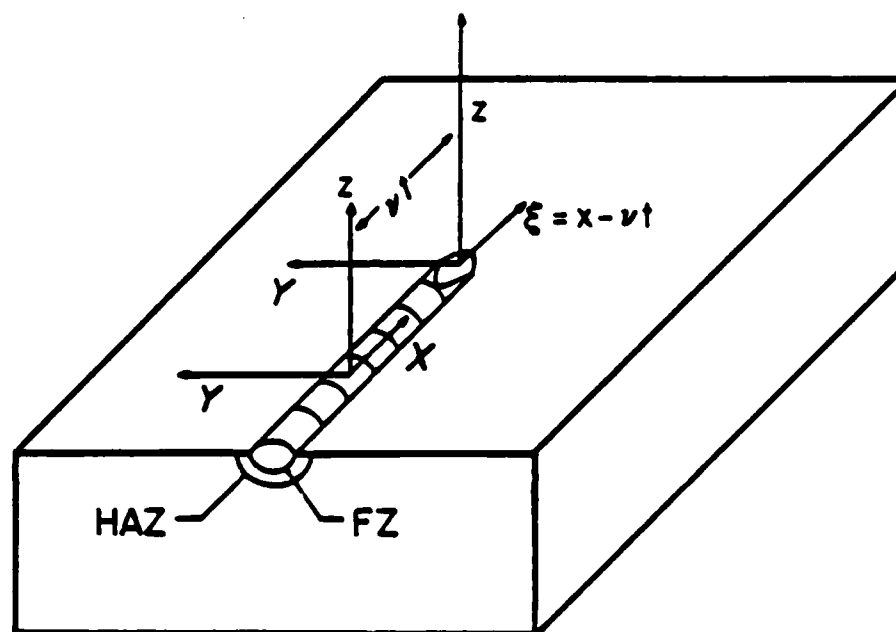
Figure 3.   Schematic representation of a weld bead on plate
            weld with various spatial parameters and
            coordinate system for theoretical modeling of
            heat flow in welded plate.

equation is only approximately valid after short periods of welding and large values of R, the position vector and a, thermal diffusivity. Finite thickness may be accounted for by adding a convergent infinite series correction factor to the above solution. The temperature distributions for point sources are generally indicative of three dimensional heat flow and might be expected to adequately model a bead-on-plate weld.

For a linear heat source in a relatively thin sheet the solution is [16] :

$$(2.2) \qquad T - T_O = \frac{q/\delta}{(2\pi\lambda)} \cdot K_O(R \frac{v^2}{(4a)^2} + \frac{b}{a^2})0.5$$

δ = thickness of plate - length of line source

b = 2h/δec

h = surface heat transfer coefficient

K_O = zero order Bessel function of second kind

For thicker sheet the surface heat transfer may be neglected to yield [7] :

$$(2.3) \qquad T - T_O = \frac{q/\delta}{(2\pi\lambda)} \cdot \exp(\frac{-v\epsilon}{2a}) \cdot K_O(\frac{Rv}{2a})$$

The temperature distribution described for linear sources are in general, characteristic of two dimensional heat flow and may more accurately describe the heat flow associated with arc butt welding.

Further simplification in the solutions may be made if high power (high q), rapidly moving (high ν) sources are considered. For a point source [15,16] :

$$(2.4) \qquad T - T_o = \frac{q/\nu}{(2\pi\lambda t)} \cdot \exp(\frac{-R^2}{4at})$$

For a high power, rapidly moving linear source [15,16]:

$$(2.5) \qquad T - T_o = (\frac{(q/\nu\delta)}{\rho c(4\pi at)^{0.5}} \cdot \exp(\frac{-y^2}{4at})$$

Implicit in the assumption of high power, rapidly moving sources is the restriction of heat flow to direction(s) perpendicular to the axis of travel. This approximation applies near the axis of travel. [15]

In considering medium thickness plates the description of the zone close to the fusion line may be adequately approximated by thick plate solutions whereas that zone far from the fusion line may be approximated by thin sheet solutions. The intermediate region requires finite dimension corrections described above. [16]

The parameter q in these solutions is the heat input
from the heat source. In the case of arc welding this is
the product of the welding voltage, current and an arc
efficiency, η:

(2.6) $q = V \cdot I \cdot \eta$

In submerged arc welding the arc efficiency resides between
0.8 and 0.95. [15,16]

Compendiums of solutions have been published. [5,16]
In addition, refinements to the basic Rosenthal formalism
have been made to account for the effects of phase changes
and circulation in the molten pool. [18,19]

Distribution functions can be criticized as "fit"
factors, but enable accurate temperature fields to be
computed. Chosen wisely, varying any parameter changes the
computed temperature field. It can be argued that they are
needed to model the many complex effects that are
quantitatively known, such as electrode angle, arc length,
joint design and shielding gas composition. Since they
allow the analyst to accurately compute the temperature
field in weldments, they are to be prefered until better
models are developed. [6]

2.2.2. Numerical Models

Numerical methods have been employed to eliminate the problems inherent in analytical approaches to modeling heat flow in welding. The non-linearity introduced by the temperature dependence of thermal parameters may be accounted for as well as complex boundary conditions, phase changes and distributed heat sources. [20,21]

Some of the earlier models assumed constant power density, uniformly distributed in the fusion zone. [22] Later, the heat source was modeled as a circular disc energy profile with a Gaussian flux distribution. [23,24]

Models in which the temperature of the molten pool has been set equal to the melting temperature, the fusion zone/HAZ interface temperature has been set equal to the melting temperature, or a maximum temperature is assumed at the center of the fusion zone and decayed to the melting temperature at the fusion zone/HAZ interface. The latter boundary condition in the temperature field is the most realistic and is due to Goldak,et al. [6] A double elliptical disc with a Gaussian distribution of flux for the surface of the weld is used in conjunction with a double ellipsoid function with a Gaussian distribution for power density. The latter models the plasma impingement.

In addition, another double ellipsoid Gaussian distribution has been employed to model the energy distribution in the stirring liquid metal. [25]

2.2.3. Athermal Processes and the Rule of Additivity

Frequently kinetic information is available for isothermal processes in the form of kinetic equation of state. However, many processes of concern are athermal in nature and it is of interest to explore formalisms for converting the isothermal kinetic data to athermal kinetic data. The nature and validity of this conversion is extremely important with respect to integrating the effects of thermally activated processes over a weld thermal cycle, an athermal process.

It seems that if abnormal grain growth is associated with the grain coarsened region of a weld HAZ then the applicability of the cited kinetic equations (for normal growth) do not apply. However, at least the regimes of unpinning in the HAZ can be specified.

2.3. Austenite Microstructural Evolution

The formation of a microstructural model for the HAZ

requires a model for austenite microstructural evolution.
The prior austenite microstructure is an important factor
in determining the nature of ferrite transformation
products.

Towards this end, the literature on formation and
isothermal growth of austenite will be reviewed. Then
attempts to model the athermal growth of austenite will be
assessed.

Nippes and Nelson [26] showed that in welding, where rapid
heating occurs, the degree of homogenization of austenite
as well as the raising of the upper critical temperature
influences the continuous-cooling transformation behavior
of steels. The rapid heating and the short times at peak
temperature experienced by the HAZ, in general would
produce an inhomogeneous austenite.

2.3.1. Austenite Formation

The formation of austenite has been studied in much
less detail than the decomposition of austenite, primarily
because of the importance of hardenability in determining
the mechanical properties of steel. However, it has been
recognized that factors such as austenite grain size are of
considerable importance for mechanical behavior and

hardenability. The structure from which austenite forms is an important factor in determining the kinetics of austenite nucleation and subsequent grain growth.

The growth of austenite has been investigated [27,28] The majority of recent studies have been associated with austenite formation during intercritical annealing. However, it is apparent that the transformation is very rapid with heating above the A_{c3}. [29] Rapid heating raises the transformation temperature. [30]

Nucleation is extremely rapid and occurs at carbides located at ferrite-ferrite grain boundaries in spheroidite microstructures. [28,31] In banded ferrite-pearlite microstructures austenite forms preferentially in the banded pearlite regions. [31] Austenite formation in an Fe-V-C alloy with no pearlite was found to require dissolution of interphase VC precipitates and then reprecipitation in the growing austenite.

The rate of austenitization in a binary FeC system was found by Roosz [32] to be controlled by diffusion of carbon along the carbide-austenite interface rather than volume diffusion. For growth of the austenite to occur, carbon atoms must diffuse to ferrite-austenite boundaries from austenite cementite boundaries through the austenite and from ferrite-cementite boundaries through the ferrite. The

ferrite lattice must also transform to the austenite
lattice.

There is little data concerning austenitization and
growth, available for short term austenitization. Speich
and others [33] showed that the austenization was complete
within about 8 seconds at 910 deg.C for 1.5 Mn-0.12 C
steels via dilatometry.

Other data from Mehl and Hagel [34] show that the time
for pearlite to transform completely varies from about 1000
seconds for a few degrees above the austenite start
temperature to a few seconds at 100 deg.C above austenite
start temperature.

According to Datta and Gokhale [35] attainment of the
equilibrium level of austenite takes several minutes and
procedes relatively slowly at first, compared with the
results of Speich. [33]

2.3.2. Grain Growth - General Theory

Grain growth is a thermally activated process that may
occur via a normal or abnormal mode. Normal grain growth
occurs in association with a gradual increase in the mean
size of a unimodal distribution. Abnormal growth or
secondary recrystallization occurs in association with the

catastrophic growth of a few large grains at the expense of a relatively fine grained matrix. Theoretical aspects have been considered by various investigators. [36-39]

Grain growth can be described by a kinetic equation of the following form:

(2.7) $D_\gamma = (Kt)^n$

where,

D_γ = grain diameter

K = constant that contains temperature dependence

n = time exponent, ideally equal to 0.5

The process and associated kinetic equation must be considered with reference to solute atoms [40] and second phase particles [36-38] that can retard grain growth.

Second phase particles act to retard grain growth by introducing a pinning force on boundaries.

Zener [41] developed a simple expression for the pinning force. The particles in his treatment are of uniform radius, r_p and posses a total volume fraction, f:

(2.8) $F_p = 3f\gamma/4r_p$

Zener calculated a limiting grain size from the pinning force:

(2.9) $D_L = 2r_p/3f$

Note that when $D = D_L$, $dD/dt = 0$ and growth ceases. Normal grain growth then occurs up to a limiting grain size.

When normal grain growth ceases at the limiting grain size, further modifications in grain size must be accompanied by modifications in the particle dispersion. Precipitate growth and/or dissolution is required. The manner in which this is accomplished determines whether normal or abnormal grain growth prevails.

The theoretical study of Hillert [36] suggests that there are two average grain size limits. Normal grain growth will not occur above the lower one (D_L) and no grain growth at all will occur above the upper one. Abnormal grain growth can take place between the two limits if normal grain growth is prevented by second phase particles, the average grain size is below the upper limit and there is at least one grain much larger than the average. Abnormal grain growth is more likely as the limits increase due to particle coarsening or dissolution.

Hillert cites dissolution as the likely controlling process.

Gladman [37] has also treated grain growth in the presence of second phase particles and has calculated a critical particle size r_{crit} for the unpinning of a grain:

(2.10) $$r_{crit} = \frac{(6R_0 f)}{\pi} \cdot \frac{1}{1.5 - 2/Z}$$

where,

R_0 = matrix grain size

f = volume fraction of particles

$Z = R/R_0$

R = size of grain whose boundaries are being unpinned

This theory actually describes a critical particle dispersion necessary to pin grains of a certain size but does not necessarily imply a criterion for abnormal grain growth. However, if most grains are pinned eventually the largest grain is unpinned and its rate of growth increases. Gladman emphasizes that this could occur via particle coarsening to greater than r_{crit}, as well as particle dissolution. Abnormal grain growth is rationalized as occuring when just a relatively few grain

boundaries become unpinned. At higher temperatures the
volume fraction of particles decreases and particles
coarsen more readily so that more of the boundaries become
unpinned and normal grain growth once again ensues. Other
investigators [40,42,43] have, in fact, observed transition
from normal to abnormal back to normal grain growth with
increases in temperature. Novikov [39] has simulated
grain growth by means of computer methods and cites the
rate of decrease in a time dependent pinning force as the
factor that determines whether normal or abnormal growth
will take place. His findings are consistent with
Gladman's proposal in that rapid decreases in the pinning
force result in normal growth whereas a slower decrease
results in abnormal growth. He further states that only
particle dissolution is capable of providing the proper
time dependence of the pinning force for abnormal growth to
occur. Novikov has also shown that larger average initial
grain sizes and wider initial distributions delay the onset
of abnormal grain growth.

     To summarize, it would appear that the kinetic
equations governing normal grain growth in the absence and
presence of second phase particles are well established.
The initiation and rate of abnormal grain growth is not so
well established but general boundary unpinning criteria

have been established. Whether normal or abnormal growth

occurs on unpinning appears to depend upon the number of

grains that become unpinned and the rate at which they do

so. The conditions for abnormal growth are enhanced by

narrow initial grain size distributions and cessation of

normal growth. Particle growth and dissolution facilitate

the boundary unpinning process.

2.3.3. Athermal Processes/ Austenite Evolution in HAZ During Welding

Austenite grain growth at a given location in a weld

HAZ represents an athermal grain growth process due to the

athermal nature of the HAZ thermal cycle as a function of

position. Austenite grain growth in a weld HAZ and during

athermal heat treatment in general has not been as

extensively studied as isothermal grain growth.

Models for HAZ microstructural evolution have been

proposed in the past.[44-50]

The Japanese workers [44-47] in this area have mainly

investigated the eficacy of employing isothermal grain

growth kinetics and various weld thermal cycles to predict

HAZ grain growth during welding in single phase metal

matrices. Alberry and Jones [48,49] and Ashby and

Easterling [50] employ similar approaches for microalloyed

steels in which grain growth is inhibited by microalloy precipitates. For grain growth to occur in this case the precipitate dispersion must be modified to result in boundary unpinning. In describing models for microalloyed steel behavior each of these groups assumes essentially different criteria for boundary unpinning; precipitate coarsening [48,49] and precipitate dissolution. [50]

Actually, both fundamental processes may, in part control grain growth behavior in a weld HAZ. In addition, it has not yet been established whether isothermal kinetic equations can be utilized to accurately predict athermal kinetic response during welding. Finally, the implicit non-equilibrium set of conditions extended during welding precludes the assumption of equilibrium volume fractions of precipitates during welding whether particles are coarsening or dissolving. This must be considered in any comprehensive model of HAZ austenite microstructural evolution.

All attempts to model athermal grain growth appear to involve the integration of isothermal kinetic equations over a thermal cycle by assuming a so-called rule of additivity. The rule of additivity requires adherence to a set of assumptions but allows the thermal cycle to be divided into incremental isothermal sections within which

isothermal kinetics may be applied.

The work of Avrami [51] provides the fundamental basis for all conversion formalisms. These formalisms, in essence, state that all thermally activated processes (nucleation, growth, diffusion) that represent a series of unit events can be described by dividing the athermal process into a series of short isothermal steps and summing them. Hence, Avrami's work implies a "rule of additivity".

More recently Cahn and Kirkaldy [52,53] have considered the rule of additivity from a more fundamental view. The fundamental equation is a path-independent line integral:

$$(2.11) \qquad \int f(X,T)dt = X_0$$

where,

   X_0 = fixed fraction of reaction

   $f(X,T) = dX/dT$ = kinetic equation of state

An isothermal process con be chosen as a particular path such that:

$$(2.12) \qquad f' = f(X,T) = X_0/\tau(T)$$

where,

   $\tau(T)$ = time for X_0 of reaction isothermally

Substitution of Equation (2.12) into Equation (2.11) yields
the following identity:

(2.13) $\int dt/\tau(T) = 1$

The integral identity of Equation (2.13) is the
condition for additivity. The kinetic equation of state
must satisfy this identity for additivity to apply.

Cahn [52] generalizes the constraints on the kinetic
equation of state by showing that it must only be a
function of X, the fixed fraction of the reaction and T,
the temperature. Furthermore a reaction involving more
than one time-temperature parameter need not be additive.

It is necessary to examine the eficacy of employing the
rule of additivity in modeling the thermally activated
processes that occur during a weld thermal cycle.

Alberry and co-workers [48,49] assume particle growth,
via Ostwald ripening, to control unpinning and austenite
grain growth in their model of HAZ microstructural
evolution. However, they do not cite the mode of grain
growth, normal or abnormal, that produces the grain
coarsened region. Ashby and Easterling [50] indicate that
particle dissolution is the controlling factor in unpinning
and grain growth. Furthermore, they impose a very

restrictive criterion in that complete dissolution of
precipitates (pinning force = 0) is required for unpinning
of boundaries and grain growth. However, they do not
specify the model(s) of grain growth after unpinning
either.

2.4. Toughness

In body-centered-cubic alloys toughness and ductility
increase with increasing temperature, and fracture mode
changes from brittle at low temperatures to ductile at high
temperature. This transition, is a consequence of the
temperature dependence of flow stress, the temperature
independence of the cleavage fracture stress, and the
associated notch sensitivity [54]

The transition temperature of alloys is traditionally
determined by Charpy V-notch (CVN) impact testing at
different temperatures. Typical CVN energy versus
temperature behavior of various materials are shown in
Figure 4. Numerous criteria for determining the transition
temperature from CVN testing results have been used. [55]
These criteria are based either on the macroscopic
observation of fracture surfaces (fibrous versus brittle)
or on an energy criterion, i.e. an average or arbitrary
impact energy.
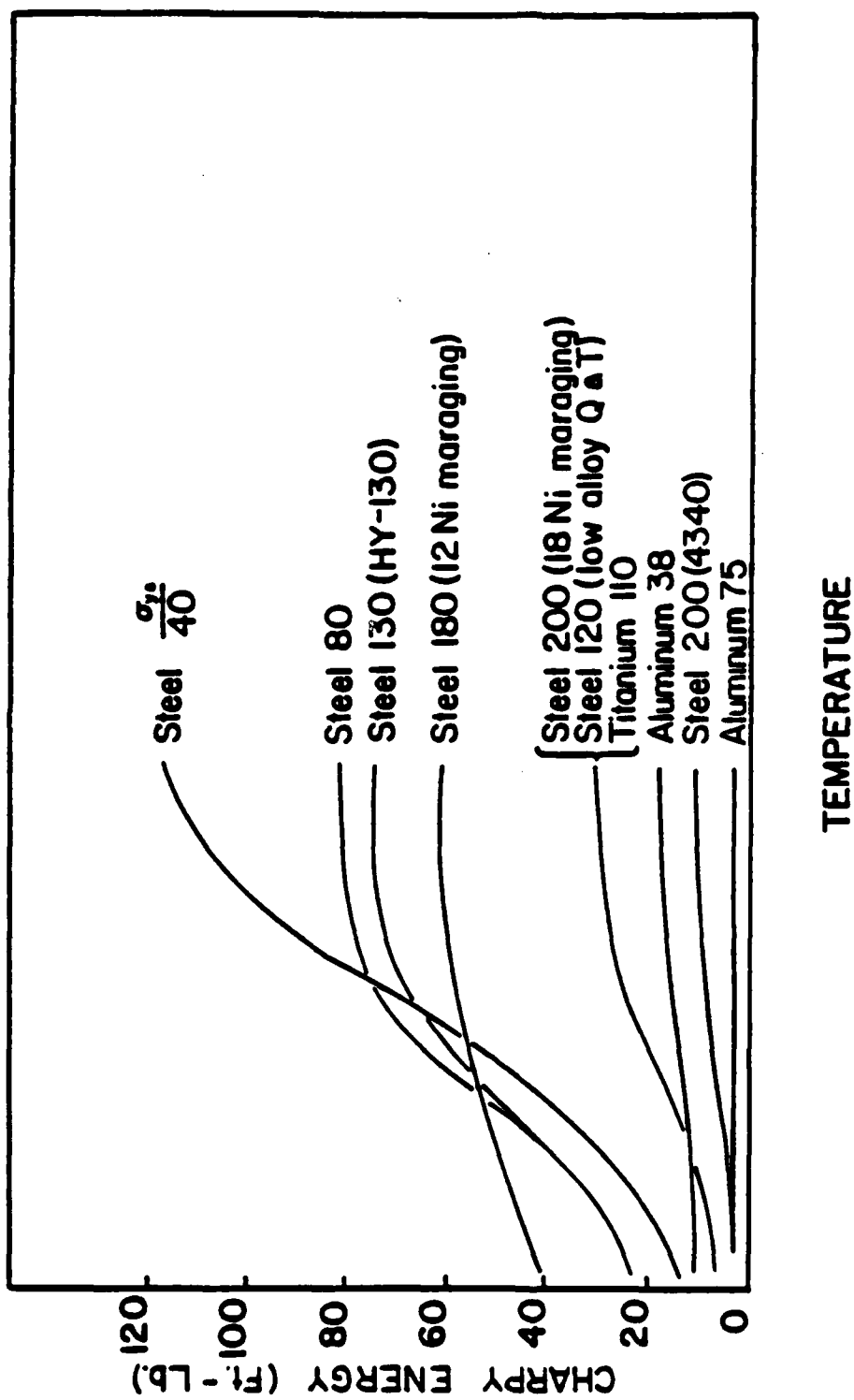
Figure 4.   Charpy impact curves as a function of
temperature for various materials.[75]

2.4.1 General Properties

There are many factors that contribute to the toughness of steels. These have been extensively reviewed. [56-69] Steel composition and microstructure affect strength and ductility. Therefore, mechanisms such as solid solution, grain size deformation and precipitation/dispersion strengthening attribute to toughness by modifying deformation and fracture modes.

As the yield stress is increased, the upper shelf energy decreases drastically. Since high yield stresses are frequently obtained by formation of hard second phase particles, the ductility is reduced significantly and high-strength materials fail by low energy mechanisms at the upper-shelf.

Lowering the carbon level increases the upper shelf energy and to some extent lowers the transition temperature. The lowering of carbon decreases the amount of carbides in the material such as in pearlite, which are normally detrimental to impact energy. [70,71]

Recent work by Lindley [72] who suggested that crack nucleation in carbides after several percent plastic strain is best explained by a fibre-loading model and not by slip or twin bands impinging on carbides. This highlights the

probable importance of carbide shape and carbide plates
would be expected to fracture more readily than spheroidal
carbides. Thus bainitic carbides could nucleate
microcracks at lower applied strains than carbides in
martensite.

The toughness of martensite tends to exceed that of
bainite. Effects on deterioration of toughness results has
led to the suggestion that an increase in the proportion of
bainite in the martensite microstructures was a major
factor accounting for the fall in toughness. [73-76]

2.4.2. Toughness in Weld HAZ

The deleterious effects of weld thermal cycles on the
microstructure and toughness of ferritic steels have been
the subject of many investigations [77-79]   Attention has
concentrated on the coarse-grained austenitic region of the
HAZ of single pass welds in the as-welded condition. This
region transforms to coarse bainitic/martensitic
microstituents that are characterized by lowest toughness
and corresponds to the final pass in a multipass weld.

Studies of toughness elsewhere have tended to emphasize
Charpy testing [80-83] which has a number of experimental

advantages, particularly for HAZ work. The major factors affecting HAZ toughness, however measured, have been found to be the composition and the arc energy.

The changes in HAZ microstructure produced by a weld in a low carbon, microalloyed steel may be summarized as follows. In withdrawing heat from the fusion zone, the material immediately adjacent to the fusion zone is heated high into the austenitic temperature range. Cementite and microalloy precipitates coarsen and/or dissolve and therefore rapid grain growth can produce coarse austenite grains. The peak temperature attained, and therefore the scale of the austenite microstructure decrease with increasing distance from the fusion zone. Lower peak temperatures produce finer austenite microstructures. Positions further from the fusion zone result in peak temperatures that produce intercritical microstructures and those furthest from the fusion zone are associated with subcritical peak temperatures. One must, however, be aware that the time for phase transformations to occur is short, on the order of of seconds, and therefore the temperatures required to produce the observed microstructural changes are always considerably higher than the temperatures which govern equilibrium reactions.

Reaustenitization and subcritical heating can have a

profound effect on subsequent structures and properties of
the HAZ. Coarse austenite grain size in the near fusion
region of the HAZ can suppress high temperature
transformation products in favor of martensite or bainite,
Widmanstatten ferrite transformation products on cooling.
[84]

The cooling rates through the transformation also vary
from point to point in the HAZ. The rate of cooling
increased with increasing peak temperature and decreases
with increasing heat input. Thus cooling rate can further
influence the resultant transformation product
microstructure. [62,85]

2.5 Purpose of the Investigation

The purpose of this investigation was to develop a
detailed physical metallurgical understanding of the
structure-property-processing relationships in Bethstar-80
HSLA steel. Several major areas of research have been
studied to evaluate and develop from experimental welds a
thermal model to be used in reproducing weld heat
treatments at selected positions in the HAZ, that could be
subsequently used in mechanical testing and metallographic
evaluation. In addition, formulation of a model for HAZ

microstructural evolution as a function of welding parameters that utilizes the state of microalloy precipitation derived from those present in the base plate and that utilizes prior austenite grain size could be invaluable in predicting and assessing the toughness based on transformation product microstructure. Finally, to examine the validity of simulation specimens by comparison of experimental data and simulated data for both mechanical and microstructural properties.

3. MATERIALS AND EXPERIMENTAL PROCEDURE

3.1 Base-Plate Composition and Primary Fabrication

The base-plate employed in this study is a Nb-V microalloyed steel. The steel composition is described in Table 1. with the ASTM A656 specification for this class of steel. The steel was control rolled to a thickness of 16.0-mm (0.625-in.) and was air cooled to room temperature subsequent to rolling.

3.2. Weld Plate Preparation

Several types of weld preparation configurations were considered for this investigation. The criteria in choosing a particular configuration are related to the extent and orientation of the HAZ produced.

A vertical butt weld generally yields a straight, vertically oriented HAZ that allows for ease in obtaining the various test specimens to be employed in this study. However, this type of configuration possesses draw backs in fabricating thermocouple installations for measurement of thermal cycles. These installations are small diameter,

Table 1

Chemical Analysis of Nb-V Base-Plate (w/o)

Elements	Weight Percent	ASTM A656 Type 7
C	0.1419	0.18 max
S	---	0.035
P	0.0228	0.025
Al	0.0366	0.020
N	0.016	0.005-0.03
O	0.0029	---
Cr	0.0475	---
Cu	0.0099	---
Mn	1.5448	1.65
Ni	0.0176	---
Si	0.2163	0.60
Mo	0.0045	---
Nb	0.0375	0.005-0.10
V	0.0897	0.05 -0.15
Ti	0.0029	---
W	0.0010	---
Ta	0.0253	---
As	0.0087	---
Mg	0.0003	---

blind holes drilled into the plate interior with fine
thermocouples welded to the bottom of the holes.
Therefore, a weld preparation configuration is required
that will minimize the lengths of holes to be drilled and
facilitate their location in the plate. A 45 degree bevel
represents the optimum configuration for thermal cycle
measurement.

An adequate compromise for the overall weld
configuration is therefore the so-called "half-V"
preparation in which one side of the weld groove is
vertical and the other beveled at a 45 degree angle. This
groove configuration allows test specimens to be removed
from the vertical side and thermocouple installation holes
to be easily drilled from the bottom of the plate
perpendicular to the beveled face, Figure 5. Plates with
dimensions 381.0 mm × 205.0 mm × 159.0 mm were cut from the
control rolled plates.   The length and width of the plates
were established on the basis of other work [86,87] and are
deemed sufficiently large to ensure the absence of edge
effects in the vicinity of temperature measurement.

The grooves were prepared parallel to the rolling
direction via saw cutting in lieu of flame cutting. The
latter produces a HAZ prior to any experimental welding.

A 100mm weld tab was added so as to conserve base-plate
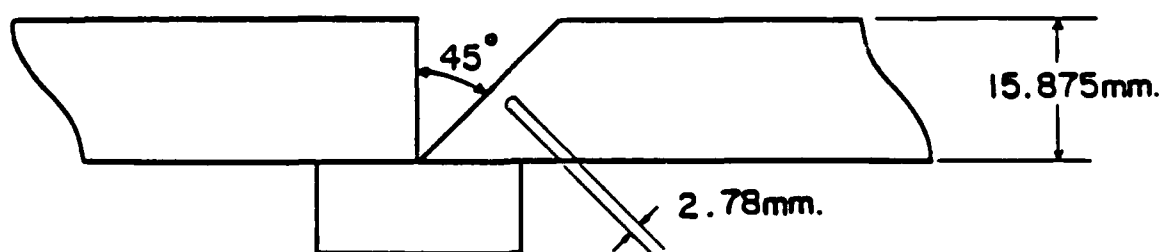
Figure 5.   Weld preparation configuration and thermocouple
            installation.

while the welding arc, power input, travel speed and wire

feed stabilized. A 50.0 mm wide back-up plate was

tack-welded to the underside of the joint to prevent

runout.

These weld plates provided the specimens employed in

all studies of actual welds in this program.

3.2.1. Thermocouple Installation and Design

The lag time must be minimized. It is convenient to

consider two sources of lag time; lag time associated with

the thermocouple hot junction and lag time associated with

the indicating or recording system. The lag time at the

thermocouple hot junction will be considered first in an

effort to specify the maximum volume of the hot junction,

i.e. the installation, consistent with accurate temporal

resolution of a typical thermal transient in the HAZ. A

design calculation, such as this, is necessary in order to

choose the proper gage thermocouple wire and properly

design the installation. Of course, the size of the

installation could have significant implications with

regard to spatial resolution in a steep temperature

gradient.

It is convenient to express the rate of approach to

equilibrium for any system that has been perturbed, by a
lag or response time, τ. This is a measure of the time
for approach to equilibrium. The degree of approximation
to equilibrium may be arbitrarily defined, thus τ usually
measures the time for the system to come within $1/e$ of an
equilibrium value, that is to say within $1-1/e = 0.632$ of
the equilibrium value ($e = 2.718$, base of natural
logarithm). Obviously, under a given set cf conditions
longer times are necessary for a closer approach to an
equilibrium value, i.e. 2.3τ for 0.9 of the equilibrium
value or 6.9τ for 0.999 of the equilibrium value.

   Now consider that the system that has been perturbed
from an equilbrium is the hot junction of a thermocouple in
contact with a medium. In setting a criteria for the
design of the installation a choice of a desired proximity
to equilbrium represents a compromise between the desired
accuracy and the rapidity with which the thermocouple
responds. The latter is embodied in τ. The time to
attain a given fraction of full response (attaining a given
accuracy) must be consistent with any time dependent
changes in temperature.

   In the case of the HAZ measurements the time to attain
a given accuracy must be significantly less than the
characteristic time over which temperature transients

occur.   Therefore, we must first calculate τ for a given
thermocouple installation for comparison with the
characteristic transient time.   The latter may be
determined from a survey of empirical studies made in the
literature or calculated by solution of the heat transfer
problem appropriate to arc welding.

   The derivation of τ for thermocouple installations
has been performed.[88]   The derivation is briefly
summarized below.   The attainment of hot junction-medium
equilibrium is considered.

(3.1) $q = V \cdot c \cdot (dT/dt)$

 where,

   q = heat flow into hot junction from medium.

   V = volume of hot junction

   c = mean volumetric heat capacity

   T = temperature

   t = time

Equation (3.1) is Fourier's Law of Heat Conduction.

   Another relationship exists for q in terms of the
temperature difference between hot junction and medium and
a thermal resistance to heat flow between the medium and
hot junction:

(3.2) $q = (T' - T)/ R$

  where,

    $T' =$ mean temperature of medium

    $T =$ mean temperature of hot junction

    $R =$ thermal resistance

    Equation (3.2) is Newton's Heat Transfer Law.
Equations (3.1) and (3.2) are equated:

(3.3) $T' - T = V \cdot c \cdot R \cdot (dT/dt)$

Assume a linear increase in temperature of the medium with
respect to time.

(3.4) $T' = T_O' + mt$

where,

    $T_O' =$ initial medium temperature

    $m =$ constant rate of temperature increase

    Substitution of Equation (3.4) into Equation (3.3) and
solution of the differential equation yields:

(3.5) $T' - T = m \cdot \tau + (T_O' - T_O - m \cdot \tau) \cdot e^{-t/\tau}$

where,

   T_O = initial hot junction temperature

   $\tau = V \cdot c \cdot R$

After $t >> \tau$ the second term on the right hand side of Equation (3.5) is negligible and $T' - T = m \cdot \tau$. Therefore, the hot junction temperature lags the medium temperature by an amount $m \cdot \tau$, for the case of a linear change in medium temperature. This simple offset in temperature does not obtain for more complex variations in medium temperature. However, $\tau = V \cdot c \cdot R$ is still an adequate indication of the time lag.

In considering the factors that affect response time, heat capacity, cannot be varied widely but response time can be minimized by minimizing volume of hot junction and thermal resistance. A design calculation has been performed, assuming 0.254mm (0.010in) diameter thermocouple wires, to determine response time. This calculation yielded $\tau = 0.0026$ sec. which must be compared to the characteristic time for the thermal transient.

A preliminary assessment of the expected thermal transients was made, employing a heat transfer model described in the literature. [15]

The heat diffusion process in a semi-infinite body at a

point a relatively small distance, r_x, from the axis of
electrode travel is approximated by the following
equations:

(3.6) $T = (A/t) \cdot \exp(-B/t)$

(3.7) $A = q/(2\pi\lambda\upsilon)$

(3.8) $B = r_x^2/4a$

where,

   T = temperature (deg.K)

   t = time after arc has passed point (sec)

   q = heat input (amperage · voltage ·efficiency)
      (cal/sec)

   υ= speed of electrode travel along axis (cm/sec)

   γ = specific heat (cal/g-deg.C)

   c = density (g/cm^3)

   λ = thermal conductivity (cal/cm-sec-deg.C)

   $a = \lambda/(c \cdot \gamma)$

   $r_x = \sqrt{Y^2 + Z^2}$

      =magnitude of vector describing the position of a
      point in the y-z plane, perpendicular to the axis
      of travel (cm).

A schematic diagram, illustrating the pertinent spatial
parameters, is shown in Figure 6.
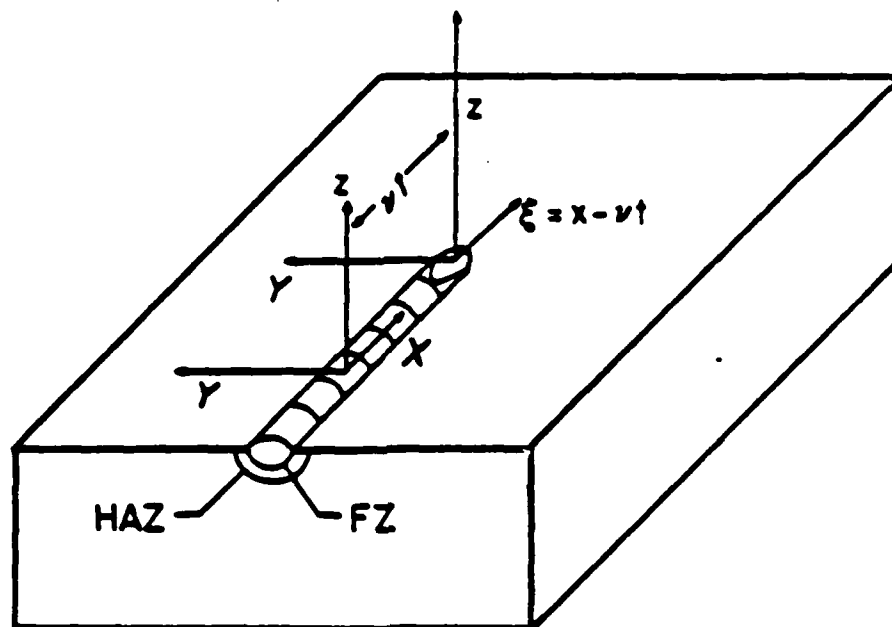
Figure 6. Schematic diagram of pertinent spatial
           parameters.

For the purposes of this design calculation it is
necessary to calculate the maximum rate of temperature
variation that could occur within the region of HAZ during
welding in order to specify a characteristic time for the
thermal transient. The rate of change of temperature with
respect to time results from differentiation of
Equation (3.6):

(3.9) $$\frac{dT}{dt} = \frac{A}{t^2} \cdot \left(\frac{B}{t} - 1 \right) \cdot \exp\left(\frac{-B}{t} \right)$$

The maximum or minimum in the rate of change is
determined by differentiating once again and setting the
result equal to zero:

(3.10) $$\frac{d^2T}{dt^2} = \frac{d}{dt} \cdot \frac{dT}{dt} = \frac{2A}{t^3} - \frac{4AB}{t^4} + \frac{AB^2}{t^5} \cdot \exp\left(\frac{-B}{t}\right)$$

(3.11) $$\frac{d^2T}{dt^2} = 0$$

(3.12) $$2t^2 - 4Bt + B^2 = 0$$

Equation (3.12) is quadratic in t and may be solved for two
roots:

(3.13) $$t = B \cdot (1 \pm \sqrt{2}/2)$$

(3.14) $$t_1 = 0.29B$$

$$t_2 = 1.71B$$

The solutions for t may be substituted into Equation (3.9):

(3.15) $(dT/dt)_1 = (0.931) \cdot A/B^2$

(3.16) $(dT/dt)_2 = -(0.079) \cdot A/B^2$

The difference in signs for the rates calculated via t_1 and t_2 indicates that t_1 refers to heating and t_2 refers to cooling. Therefore the magnitude of the maximum in rate of temperature change is greater during heating than during cooling at a given location. Evaluation of the parameter A/B^2 yields:

(3.17) $(A/B^2) = (8/\pi) \cdot (q/(vr_x^4)) \cdot (\lambda/(c\gamma))^2$

The parameter is inversely proportional to $(r_x)^4$ and the maximum heating and cooling rates should occur near the fusion zone/HAZ interface. Therefore, to evaluate a worst case situation, represented by a maximum rate of temperature change, the heating rate at the fusion zone/HAZ interface must be determined. This requires specification of the location of that interface, (r_x).

A calculation can be made to define the locus of points of maximum temperature with respect to time by noting that

Equation (3.9) will vanish if the quantity

$((r_x)^2/4at)- 1)$ vanishes:

(3.18) $t = (r_x)^2/4a$

Equation (3.18) specifies the time at which a given

location undergoes a maximum in temperature after the arc

passes.   Substitution of Equation (3.18) into Equation

(3.6) yields:

(3.19) $T_{max} = (2q/(\pi\gamma vce(r_x)^2)$

(3.20) e = base of natural logarithm

     At the fusion zone/HAZ interface $T_{max} = T_{mp}$ where

the latter is the melting point.   Therefore, substitution

of Equation (3.19) into Equation (3.17) yields for the

melting point isotherm:

(3.21) $\dfrac{A}{B^2} = \dfrac{(2\pi\lambda ve^2(T_{mp})^2)}{q}$

Equation (3.19) specifies the position of the fusion

zone/HAZ interface and Equation (3.21) specifies the A/B^2

term associated with that location.   For the heating rate

at this interface:

(3.22) $\left(\dfrac{dT}{dt}\right)_{Heating} = (0.931) \cdot \dfrac{(2\pi\lambda v e^2 (t_{mp})^2)}{q}$

3.23) $q = E \cdot A \cdot \eta$

where,

   E = voltage

   A = amperage

   η = arc efficiency

Substitution of the following typical values into Equation (3.22) yields a value for $(dT/dt)_{Heating}$:

   E = 35 volts

   A = 350 amps

   η = 0.8

   T_{mp} = 1465 deg.C

   v = .364 cm/sec

   λ = 0.097 cal/sec-cm-deg.C

(3.24) $(dT/dt)_{Heating} = 335$ deg.C/sec

Equation (3.24) describes the maximum rate of temperature variation that might be expected anywhere in the HAZ.

Now, a comparison with respect to temperature measurement may
be made by calculating the temperature change that the body
undergoes at that location during the lag time, τ :

(3.25) $(dT/dt)_{Heating} = \Delta T / \tau$

(3.26) $\Delta T = (dT/dt)_{Heating} \cdot \tau$

                $\Delta T = (0.0026) \cdot (335) = 1.0$ deg.C

Therefore, ΔT represents the maximum error in temperature
measurement introduced by the lag time. This error is judged
acceptable as a worst case so that the volume chosen for
thermocouple installation design may be adequate.

3.2.2. Measurement of HAZ Transient

From a practical standpoint, the attainment of a response time
of temperature measurement with a thermocouple depends upon the
nature of thermocouple installation. The thermocouple must be
placed in intimate contact with the steel plate at a specific
subsurface location. A small diameter blind-hole is generally
employed as a well for the installation. The thermocouple hot
junction is then welded to the bottom of the well.

The lag time associated with the measurement system depends
upon its' nature.   Successful measurement of

temperature by a thermocouple represents the solution of several separate problems. First, it is necessary to choose the correct thermocouple type for the magnitude of temperature to be measured. Of course, the thermocouple elements must be homogeneous and properly calibrated. The thermocouple must then be properly installed in the medium whose temperature is to be measured.

Ideally, the result of thermocouple installation is to have the temperature that is sensed and recorded be a spatially and temporally accurate determination of the temperature of the medium. This requires that the hot junction of the thermocouple be specifically located and be of small enough volume to rapidly attain the temperature of the medium. That is, the thermocouple installation must not unduly perturb the attainment of the actual temperature of the medium or its measurement.

The response time of thermocouple measurements are associated with a lag time. The measured temperature lags the actual temperature temporarily. Obviously the lag time must be made significantly less than the time over which the transient occurs for the proper measurement of the transient. The lag time is a function of various aspects of the design of the thermocouple installation, namely the size of the sensing volume and the heat transfer

characteristics of the medium and sensing volume, i.e.
thermal conductivity and heat capacity. Under a given set
of experimental conditions the heat transfer
characteristics are generally not a variable so that design
of the installation centers about producing a sufficiently
small sensing volume in adequate thermal contact with the
medium.

The literature associated with thermocouple temperature
measurement has been reviewed with a view toward applying
it to the measurement of thermal transients in the steep
temperature gradients associated with HAZ's of arc welds
of steels.

Additional problems obtain in the acquisition of data
from thermocouples. Output from a thermocouple is an
analog siginal, a voltage in the micro- to millivolt
range. This output must be differentiated and isolated
from noise generated from within and without the
measurement system. It may also have to be amplified to
facilitate data acquisition, as in the case of
analog-to-digital conversion prior to data acquisition with
a computer. All of these intervening operations could
induce distortion of the primary analog signal generated at
the thermocouple hot junction and will have to be
considered with respect to the overall accuracy and

precision in measurement that is required.

3.2.3. Thermocouple Installation

Temperature measurement in the HAZ with thermocouple were discussed previously and a design calculation performed. For each plate to be welded, two 2.8-mm (0.11-in.) diameter holes were drilled 100.0 cm (4.0-in.) from each end of the plate into the back-side of the bevel for insertion of the thermocouple, Figure 7.

These holes were drilled to depths of less than 12.5 mm (0.50-in) and approximately located in the anticipated HAZ. The orientation of an installation perpendicular to the groove face is critical in measuring the correct temperature at a particular location. This is primarily due to the potentially perturbing effects of the installation of the advancing thermal front that is approximately parallel to the groove face. The nature of the HAZ configuration and the approximate depths of thermocouple installation were determined during preliminary welding experiments. The exact location of the HAZ and therefore, of each thermocouple installation could not be predicted a priori due to variations in heat input and weld alignment during welding. Therefore, the exact
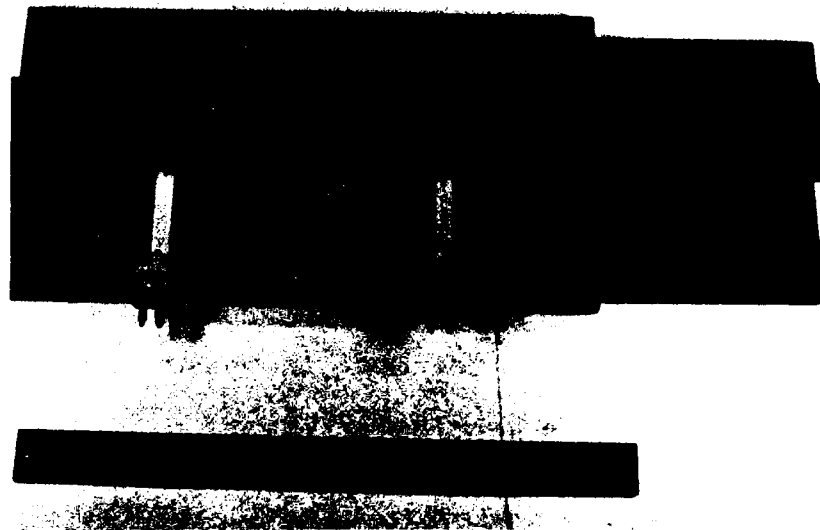
Figure 7.   Configuration of weld plate and thermocouple
            installation.

installation position had to be determined via
metallographic evaluation after welding, Figure 8.

Two nominally 0.125mm (0.005-in.) diameter
chromel-alumel thermocouple wires were inserted in pyrex
tubing 2.6-mm (0.10-in.) in diameter before being welded to
the bottom of the drilled hole. For this purpose, a
capacitive discharge welding apparatus has been
constructed, Figure 9. The welding is critical to
obtaining a highly responsive measurement of rapid thermal
transients. When properly performed, the weldment is of
extremely small volume and quite durable, Figure 10.

Thermosetting fiberglass tape was used to secure the
thermocouple wires emanating from the installation and also
provided electrical insulation from the plate. The tape
protected the wires from damage. Connections were made via
standard connectors in order to facilitate electrical
access between instrumentation and the welded plate and to
minimize electrical noise, Figure 11.

3.2.4. Data Acquisition and Processing

A problem related to data acquisition is isolation of
the entire temperature measurement system from the welding
process and other noise sources. This was accomplished via
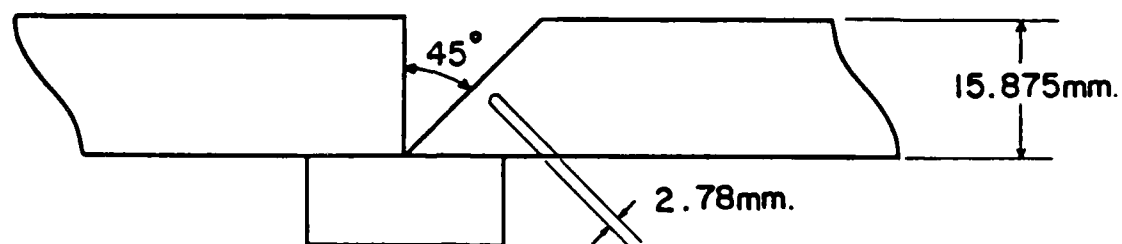
Figure 8.   Weld profile preparation configuration and
            thermocouple installation.
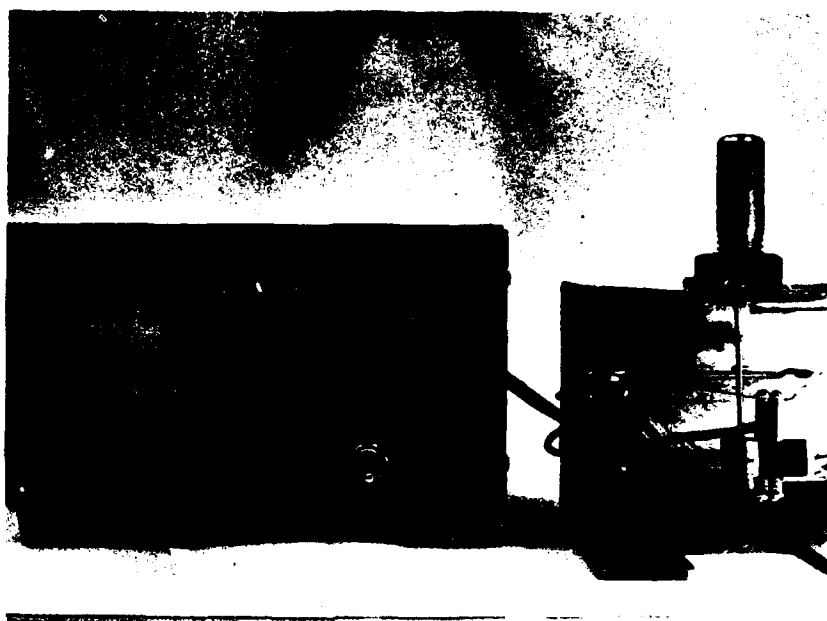
Figure 9.   Capacitor discharge welder used in thermocouple
weldment to weld plate.
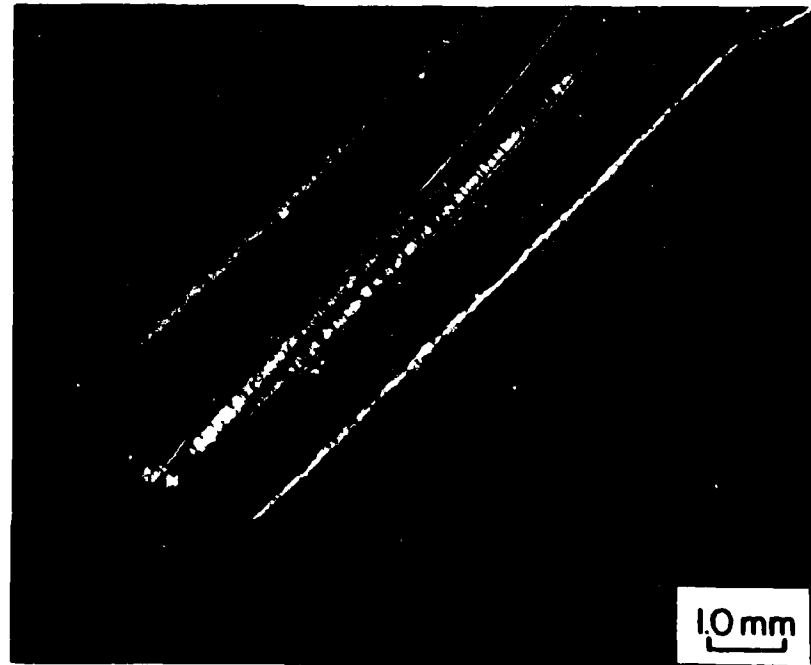
Figure 10.   Thermocouple weldment profile at the bottom of
             a thermocouple well.
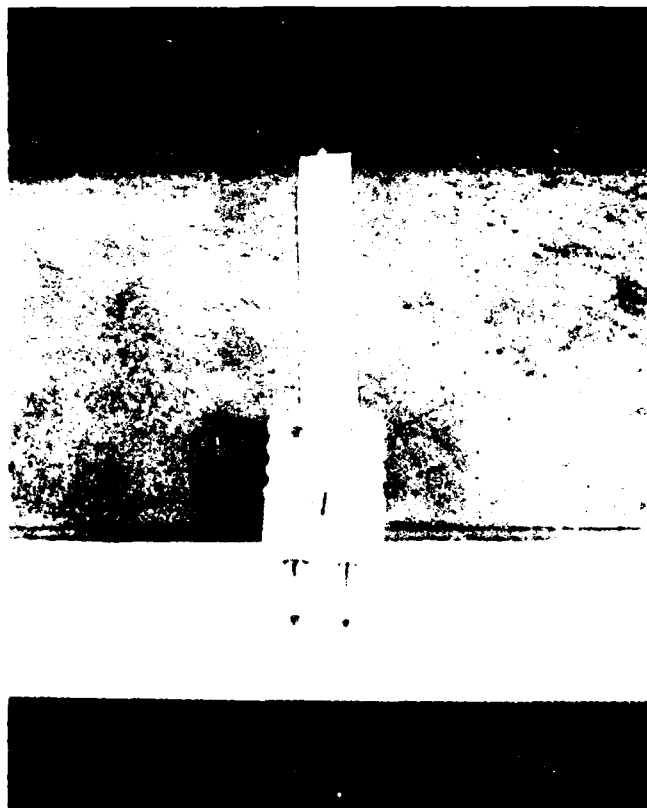
Figure 11.   Thermocouple connector assembly on back side of
weld plate.

a four channel, isolated thermocouple conditioner,
manufactured by Analog Devices, Inc. In addition to
isolating the thermocouple from noise sources, this device
amplifies the analog signal into the range of 0-5 volts.
This output range is convenient for analog-to-digital
conversion. An automatic cold junction compensation
device, also manufactured by Analog Devices, Inc., was
included in the signal conditioning portion of the system.

The collection of the thermocouple output of the two
installations in each plate were multiplexed by an
electronic switching device to allow information from both
thermocouples to be observed at time intervals of 100
milliseconds. Digital data acquisition was desired,
therefore analog-to-digital (A/D) conversion was required.
Initial efforts centered around application of a
microcomputer. However, the A/D conversion was too slow.
A Nicolet 1094 digital storage oscilliscope was eventually
employed for data acquisition. The compromise between
speed of data collection and precision determined from the
number of channels simultaneously monitored. The amplified
voltage signals sent to the Nicolet, were displayed as a
wave-form and then stored on floppy disks.

Once thermal cycle data was stored, the digitized
information was sent via a RS-232 asynchronous serial

interface line to a DEC 10 mainframe computer system where
it was stored onto magnetic tape.   This data transfer to a
mainframe computer was deemed important due to the data
points (15,872 pts.) per weld plate and the more efficient
data manipulation on a larger computer.   A schematic
diagram and picture of the data acquisition system is
depicted in Figure 12.

The entire system was checked and calibrated using a
Cohn model 321 DC voltage standard for the 10 volt range
having a 10 micro-volt step width and accuracy of .01%.

3.3. Welding Parameters and Equipment

3.3.1. Equipment

Welds were made with automatic Hobart Submerged Arc
Welding Equipment.   A Hobart RC500, DC Power Supply
provided the power required to produce various heat
inputs.   A single pass was accomplished for several plates
at each heat input.   Welding was accomplished without
preheat and the welds cooled in still air to room
temperature.   A Hobart 25P wire and Linde Flux 585 were
employed in welding.   The chemical composition of wire and
flux is described in Table 2.
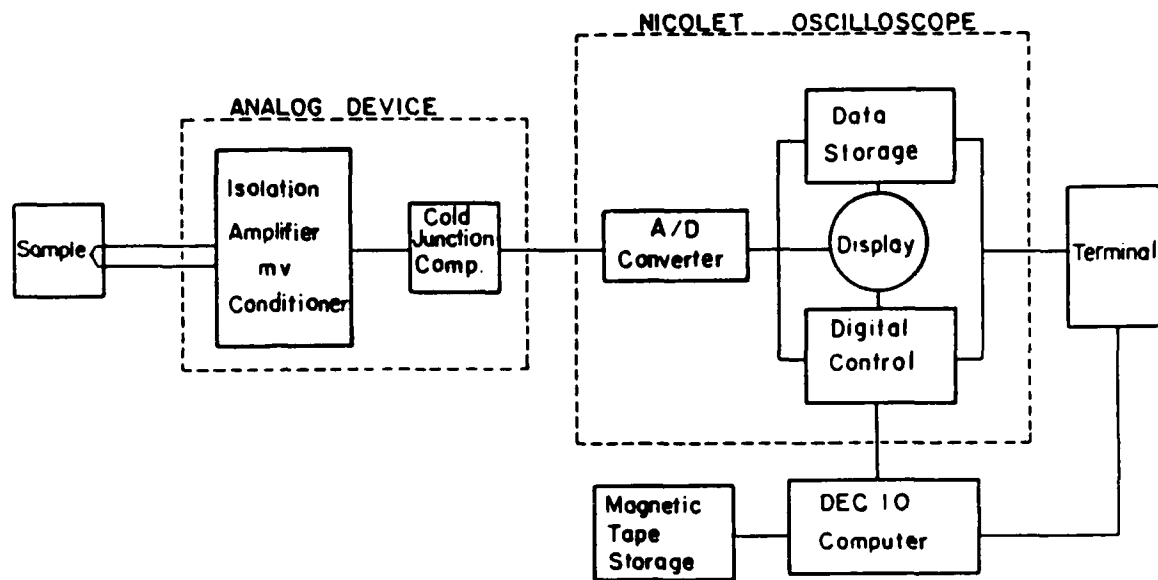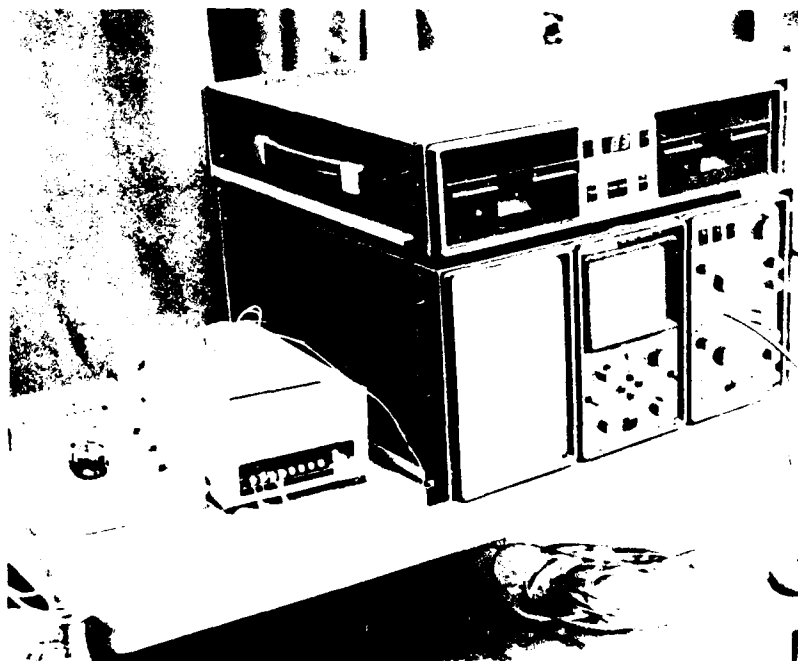
Figure 12.   Temperature measurement data acquisition
              system.
                   (a) Schematic diagram
                   (b) Equipment

Table 2

*Wire Composition and Mechanical Properties

C	–	0.110	TS	–	73,325 psi
Mn	–	1.120	YS	–	45,750 psi
Si	–	0.500	%E	–	26.5%
P	–	0.020	R.A.	–	66.0%
S	–	0.019	CVN.	–	30 ft·lb at 0.0 deg. C

**Flux Composition (wt%)

SiO2	–	40.0
MnO	–	20.0
CaO	–	15.0
TiO2	–	12.5
Al2O3	–	5.0
CaF	–	5.0
Misc.	–	2.5

*Hobart 25P solid wire, 3/32 inch diameter (AWS EM13K-EW)

**Linde Flux 585 – fused flux (non-hygroscopic)

3.3.2 Welding Parameters

Nominal welding parameters are listed in Table 3 . The target heat inputs for the investigation were 1.97, 3.35, 4.92 KJ/mm (50, 85, 125 KJ/in.) and were attained by varying the welding speed at a constant product of voltage and current. These heat inputs were assumed to be constant for particular dial settings, but the actual power output was monitored on a dual pen Hewlett Packard strip chart recorder. The power output varied due to power and transformer fluctuation in the power supply and a 6.5 volt, voltage drop was noted along the welding cable. Recorded local heat inputs are listed in Table 4.

3.4. Weld Simulations

Thermal cycle simulations of selected HAZ microstructures were performed with a Duffers' Gleeble 1500, programmed thermal cycle test apparatus. Thermal cycles for input were obtained from the direct measurements described in section 3.2.4.

Two types of specimens for HAZ simulation were prepared from base-plate material 6.35-mm (0.250-in.) diameter by

Table 3

Welding Parameters and Equipment

Power Supply: Hobart RC-500 with Hobart Beam
                                Carriage Model 1044

Rating: Hot Start with 0-800 Amps D.C.,
                                0-100 volts D.C.

Power Setting for
  Investigation: 350 Amps D.C., 35 Volts D.C.

Travel Speed
 (Independent Variable
  Setting):   2.45, 3.64, 6.14 mm/sec (5.8,
                                  8.6, 14.5 in/min)

Heat Input
 (Travel Speed
  Dependent Variable
  Setting):   1.97, 3.35, 4.92 KJ/mm (50.0, 85.0,
                                  125.0 KJ/in)
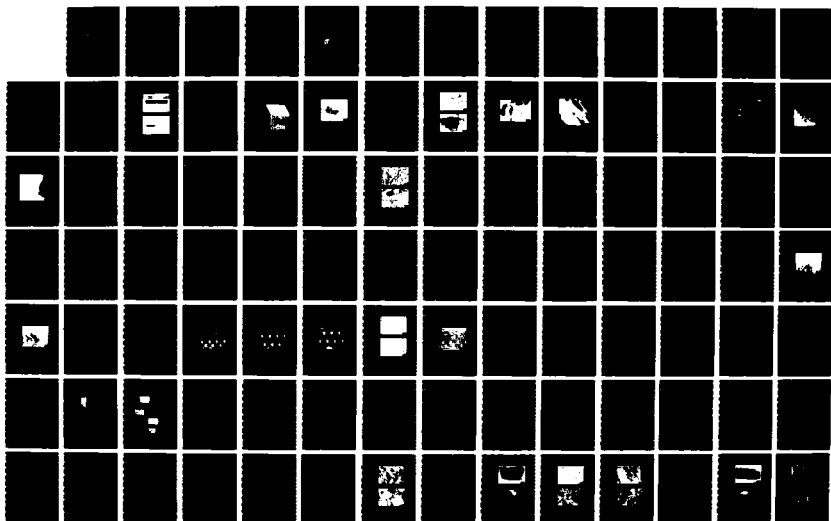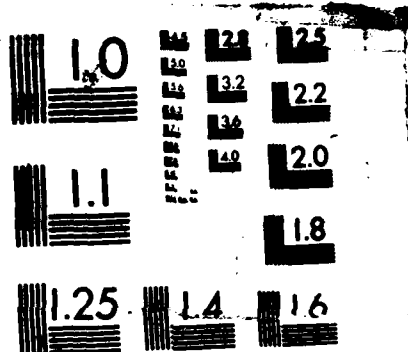
MICROCOPY RESOLUTION TEST CHART
NATIONAL BUREAU OF STANDARDS-1963-A

Table 4

Welding Parameters for Experimental Weld Plates

	Measured Voltage (V)	Measured Amperage (Amps)	Travel Speed (mm/sec)	Heat Input (@ 100% eff.) (KJ/mm)
High Heat Input (4.92 KJ/mm)				
Plate 1				
TC 1	31.5	380.0	2.45	4.87
TC 2	32.3	328.0	2.45	4.31
Plate 2				
TC 1	29.7	416.0	2.45	5.03
TC 2	31.7	400.0	2.45	5.16
Plate 4				
TC 1	30.1	416.0	2.45	5.10
TC 2	30.7	396.8	2.45	4.96
Plate 7				
TC 1	31.3	345.6	2.45	4.40
TC 2	32.5	339.0	2.45	4.48
Medium Heat Input (3.35 KJ/mm)				
Plate 10				
TC 1	31.1	364.8	3.64	3.11
TC 2	31.1	352.0	3.64	3.00
Plate 11				
TC 1	30.9	320.0	3.64	2.71
TC 2	31.7	352.0	3.64	3.06
Plate 12				
TC 1	32.1	352.0	3.64	3.10
TC 2	32.1	339.0	3.64	2.98
Plate 13				
TC 1	28.7	352.0	3.64	2.77
TC 2	28.1	374.0	3.64	2.88
Plate 14				
TC 1	26.5	342.0	3.64	2.49
TC 2	27.7	384.0	3.64	2.92

<u>Table 4 con't</u>

	Measured Voltage (V)	Measured Amperage (Amps)	Travel Speed (mm/sec)	Heat Input (@ 100% eff.) (KJ/mm)
		<u>Low Heat Input (1.97 KJ/mm)</u>		
Plate 5				
TC 1	32.7	336.0	6.14	1.79
TC 2	30.9	406.4	6.14	2.04
Plate 6				
TC 1	31.9	377.6	6.14	1.96
TC 2	31.3	406.4	6.14	2.07
Plate 8				
TC 1	30.5	355.0	6.14	1.76
TC 2	31.5	323.0	6.14	1.65
Plate 9				
TC 1	31.3	352.0	6.14	1.76
TC 2	30.9	348.8	6.14	1.75

approximately 152.4-mm (6.0-in.) long rods and 5.0 mm ×
10.0 mm × 100.0 mm (0.20-in. × .4400-in. × 4.00-in.) bars.
The former were for microstructure and dilatometry and the
latter for Charpy impact toughness testing. Details of
specimen preparation are shown in Figure 13. The specimen
axis was parallel to the transverse direction of the plate,
i.e. perpendicular to the welding direction.

A fine chromel-alumel or platinum-platinum/rhodium
thermocouple was welded to the center of each specimen.
The specimen was gripped in water cooled copper jaws. A
smoothed and digitized version of an experimentally
determined thermal cycle was then programmed into the
Gleeble and the HAZ simulation accomplished.

The diametral strain of the specimen (rods only) in the
region corresponding to the programmed thermal cycle was
measured and continuously monitored via a cross-wise strain
extensometer. The diametral strain measurement provided
the dilatometry information on the austenite-ferrite phase
transformation during welding. Sufficient axial and
transverse microstructural homogeneity was found to exist
in simulation specimens, indicating a sufficiently large
volume of simulated material.

6.35mm Dia.

Rolling Direction

10.0mm

5.0mm

Uniformly
Heat-Treated Zone

Thermocouple 0.254mm Dia.
Removed When Specimen is Notched
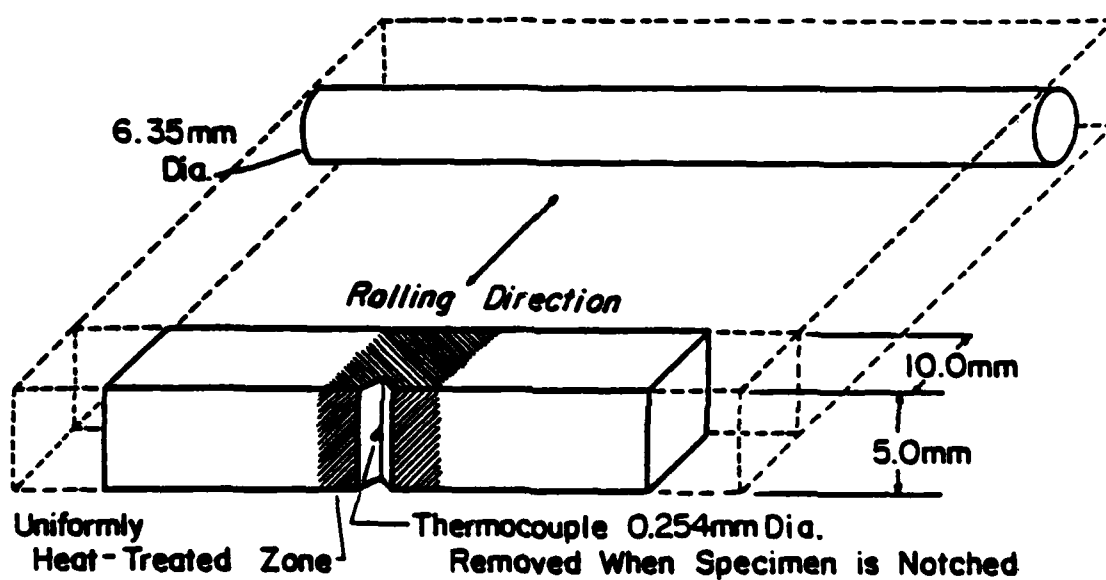
Figure 13.   Details of subsize charpy specimen and
             Gleeble HAZ microstructural simulation
             specimen.

3.5 Austenite Grain Coarsening Heat Treatments

Heat treatments were performed on base-plate material to determine kinetic equations that describe austenite grain growth as a function of temperature and time.

Two types of isothermal heat treatment were performed. Approximately 14.00-mm x 2.54-mm x 2.54-mm (0.56-in. x 1.00-in. x 1.00-in.) specimens were heated in a Lindberg 1500 Glow Bar Box Furnace with an argon atmosphere at temperatures between 900 deg.C and 1300 deg.C for times between 300 seconds and 6000 seconds. Specimens were water quenched subsequent to treatment.

An additional set of rod specimens 6.35-mm (0.25-in) in diameter were subjected to short term treatments between 5 and 300 seconds at the same temperatures. These treatments were performed on the Gleeble 1500 and were characterized by a very rapid heating rate (200 deg.C/sec.)

3.6   Microscopy

3.6.1 Light Microscopy

All specimens for light microscopy were prepared by standard grinding procedures with 240-600 grit silicon

carbide papers and polishing with 6μm diamond to 0.05μm
alumimia.   Light microscopic observations were made on a
Leco Neophot metallograph.

3.6.1.1. Water Quenched or Rapidly Cooled Specimens

These specimens were etched for observation of prior
austenite microstructure in a solution of 100-ml saturated
picric acid (aqueous), 1-2 grams sodium-tridecyl-
benzene-sulfonate and 4-ml hydrogen peroxide held at 80
deg.C.

3.6.1.2. HAZ Specimens

These specimens were etched in a 2% Nital solution for
observation of transformation product microstructures.

3.6.1.3. Quantitative Light Microscopy

The pearlite content was determined by a systematic
manual point count procedure and the ferrite grain size by
a linear intercept procedure outlined in ASTM E562 and ASTM
E112 respectfully.   Both determinations were made with 95%
confidence in the mean value.

Prior austenite grain size was determined by mean
linear intercept method outlined in ASTM E112. Tests were
made on a minimum of 5 widely separated, randomly selected
fields. Quantitative metallographic relationships
developed by Underwood [89] and given in ASTM E562 and E112
were used to quantitize the various amounts of constituents
present.

3.6.2. Transmission Electron Microscope

Precipitation and substructure of selected material
conditions were examined in a Phillips EM 400 transmission
electron microscope operated at 120 kV accelerating
potential. Two types of specimens were prepared: direct
carbon extraction replicas, and thin foils.

3.6.2.1 Carbon Extraction Replicas

Direct carbon extraction replication was employed for
the bulk of microstructural and microalloy precipitate
analysis. A 100-200Å thick, carbon coating was vacuum
deposited in a Denton DV-502 High Vacuum Evaporator, onto a
polished and very lightly etched specimen surface. After
removal from the evaporator, the carbon film on the

specimen surface was scribed into 2-mm squares which were
lifted off by etching in a 5 percent nital solution. The
replicas were then washed in methanol and water solutions
prior to placement on copper support grids for
observation.

3.6.2.2   Thin foils

Direct observations of fine structure required thin
foil specimens. Bulk thinning was done by cutting 0.254-mm
(0.010-in) thick wafers from test samples with a low speed
diamond cut off wheel. These slices were prethinned to a
thickness of approximately 0.076-mm (0.003-in.) by
alternate mechanical and chemical polishing. Chemical
polishing was accomplished with a solution of 80-ml
H_2O_2, 15-ml H_2O (distilled), and 5-ml HF. Final
thinning was performed with a Fischione automatic
electrolytic jet polisher using a solution of 5 percent
perchloric and 95 percent acetic acid at 24 volts/ 20
millamps.

3.6.2.3 Particle Size Analysis

Particle size distributions were determined from carbon

extraction replicas measurements made on enlarged
micrographs.   The raw data was analyzed via the procedure
described by Ashby and Ebeling. [90]

3.6.3. Scanning Electron Microscopy

Scanning electron microscopy of deep etched
metallographic specimens and fracture surfaces was
performed with a JEOL 840I SEM that is interfaced with a
Tracor Northern TN5500/5600 X-ray and image analysis
system.   The latter includes energy dispersive X-ray
spectrometry (EDS) and wave length dispersive X-ray
spectrometry (WDS) for microanalysis.   Specimens were gold
or carbon coated prior to observation.

3.7. Quantitative Macro-Metallography

3.7.1. Measurement of Weld Bead and HAZ Width

Measurements of weld bead width, visual heat affected
zone width and thermocouple position from the fusion line
were determined via low magnification light microscopy of
etched specimens.   Magnifications between 10X and 200X were
employed.   A stage micrometer was used to ensure maximum

precision.

Weld bead width was measured from one side of the fusion zone to the other side parallel to the plate surface at a location level with the top of the bead. The top surface of all weld beads were usually located below or level with the top surface of the plate.

Heat affected zone measurement was obtained by measuring from the fusion line to the outer fringe of a dark etching region. The measurement was made at the half thickness of the weld bead height.

Thermocouple position measurement was specified by the shortest distance between the thermocouple junction and the fusion zone line. This distance was usually perpendicular to the weld fusion zone line.

3.7.2. Fractography Preparation

Fractured CVN-bars were sectioned perpendicular to the notch by means of diamond wafering saws. Surfaces were then nickel-plated with a solution composed of 450 gm. $NiSO_4$, 66 gm. $NiCl_2$, 48 gm. H_3BO_3, 1.3 lit. H_2O and a current density of 0.5amps/cm^2 for 1-2 hours. [91] and then a standard polish for micrographs was performed to illustrate fracture profiles.

3.8. Microalloy Precipitation Bulk Analyses

3.8.1 Bulk Extraction Procedure

Bulk extractions procedure of microalloy precipitation were performed on specimens from base-plate and specimens heat-treated in the austenite grain coarsening study. This procedure involved dissolving degreased and rinsed drillings of the specimen in a solution of 10-50 v/o HCl in distilled water. The dissolution was performed at approximatly 40 deg.C under argon gas atmosphere. The dissolution tipically took 8 hours to perform. A residue of microalloy precipitates for subsequent analysis by X-ray diffraction was collected by vacuum filtering with a 0.025 micron millipore apparatus. Residues were rinsed in $HCl-H_2O$ and methanol solutions prior to drying under argon.

3.8.2. X-ray Analysis of Residues

X-ray analysis was accomplished via Debye-Schere powder camera measurements and X-ray diffractometry. The carbonitride phases present were qualitatively identified as a function of temperature and time and estimates made of

the respective lattice parameters.

3.9 Mechanical Properties

3.9.1 Hardness Measurements

Transverse sections of welds made at thermal couple installations for the three nominal heat inputs were metallographically prepared by standard grinding and polishing procedures and etched in a 2% Nital solution. Microhardness traverses were made from the fusion line through the HAZ into the base-plate for each of the three sections. A 650 gram load was employed to obtain diamond pyramid hardness (DPH) measurements. Spacing of the DPH impressions were sufficient to avoid overlap and work hardening effects as suggested by the procedure in ASTM E-92.

Overall Hardness measurements were made on the longitudinal section of the base-plate. Rockwell hardness data was obtained for the overall microstructure at a 100 kg load and diamond pyramid (DPH) microhardness measurements of the ferrite regions were made at a 20g load.

3.9.2. Tensile Testing of Base-plate

Sub-size tensile specimens of base-plate were prepared as described in ASTM E-8 with specimen dimensions 8.75mm × 105 mm (0.35-in. × 4.13-in.). The specimens were tested at room temperature on an Instron Tensile Machine, Model TT-D. Tensile specimens were strained at a constant displacement rate of 2×10^{-2} mm/sec. (.0051-in/sec.) which corresponded to an initial strain rate of 1.1×10^{-4} s^{-1}. Load measurements were continuously recorded with a time driven chart recorder.

3.9.3. Charpy V-Notch Toughness Tests

Sub-size charpy V-notch impact specimens were prepared as described in ASTM E-23 with dimensions 5.0 mm × 10.0 mm × 55.0 mm (0.20-in. ×0.40-in. × 2.17-in.). A Tinius Olsen Universal Impact Tester built to ASTM specifications was used in testing. Specimens were held at temperature in a bath of methanol for at least 10 minutes to ensure bar temperature to be that of the liquid. In transfer of the bars from the constant temperature bath to the test fixture, a time limit of 5 seconds was not exceeded, as required by the ASTM E-23 specification. A minimum of three CVN bars were used at

each temperature for statistical significance in producing CVN curves.

3.9.3.1 Notch Location in HAZ From Actual Welds

Notch tip location was found by etching the weld sample in 10% nital solution. The actual location in the weld HAZ was positioned in the coarse grain region HAZ, next to the fusion zone line. A representative view of the sample is seen in Figure 14.

3.9.3.2 Notch Location in Simulation HAZ

Notch location in simulated HAZ, was positioned where a thermocouple had been attached for temperature monitoring in the Gleeble, thermomechanical testing machine.

(a)

(b)

Figure 14.   Macrograph profile of subsize charpy specimen
              illustrating notch location.
              (a) Specimen width
              (b) Specimen thickness

4. RESULTS

4.1. Base-Plate Microstructure

The steel can be classified as a ferrite-pearlite steel with a mean pearlite content of 17 v/o and a mean ferrite grain size of 5.5μm. The pearlite is banded, Figure 15.

A wide distribution of ferrite grain sizes is apparent, and in addition, the overall ferrite microstructure is finer in the region of the plate surface. The latter observation is associated with more intense deformation and lower temperatures in this region during rolling. The mean ferrite grain size noted above was measured at the center thickness location.

The inclusions in the base-plate are spherical and inclusion content is fairly typical of a shape-controlled microalloyed steel, Figure 16.

With the exception of the plate surface region, the microstructures described above were determined to be homogeneously distributed through the entire volume of material received.

The fine structure of the base-plate was characterized via scanning electron microscopy of bulk specimens and transmission electron microscopy of carbon extraction

Longitudinal
Surface Section

Longitudinal
Section

Transverse
Section

50 μm
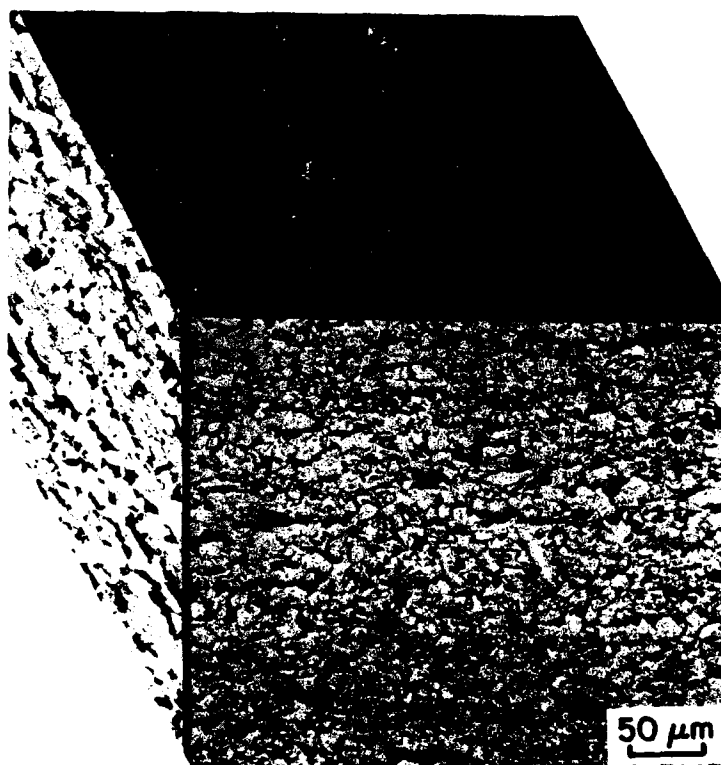
Figure 15.   Light micrograph of microalloyed Nb-V
base-plate microstructure.
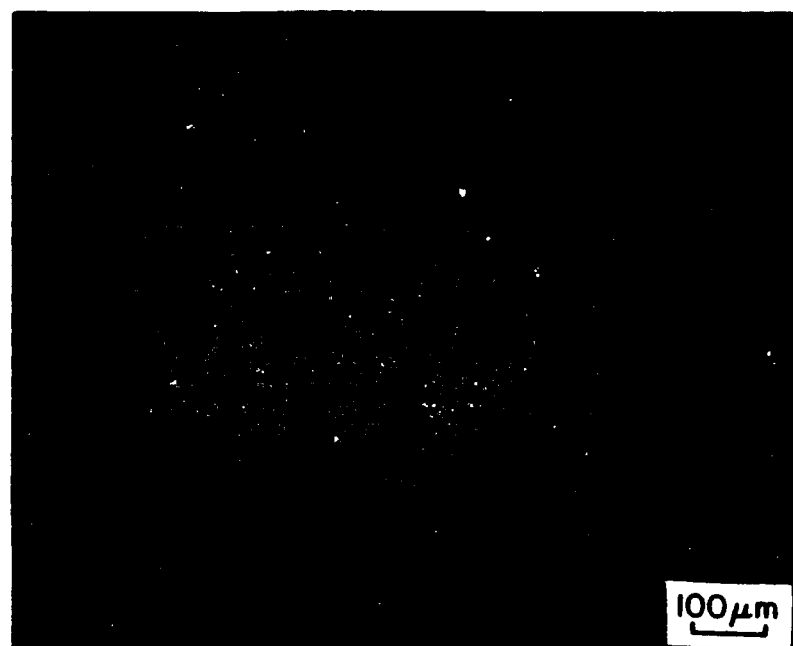
Figure 16.   Inclusion distribution in Nb-V base-plate.

replicas, and thin foil specimens.   X-ray diffraction of extracted precipitate residue was employed to support microscopy results.

Scanning electron microscopy was performed on a longitudinal section that was deeply etched in a 5% Nital solution.   The heterogeniety in polygonal ferrite grain size is again noted,   Figure 17(a).   High magnification observations of numerous regions corresponding to dark etching regions in light micrographs confirm the areas to be pearlitic with an extremely fine interlamellar spacing, Figure 17(b).

Transmission electron micrographs of thin foils revealed a dislocated matrix as well as some extremely fine ferrite grains, Figure 18.   Observations of fine pearlite as the dark-etching microconstituent of light microscopy was confirmed by TEM, Figure 19.

The transmission microscopy of carbon extraction replicas and thin foils revealed a fairly uniform dispersion of fine precipitates less than 200 angstroms in diameter. The precipitate size distribution was determined from carbon extraction replicas and the result is depicted in Figure 20. quantitatively.

The mean precipitate size was determined to be 184.0Å in diameter with a distribution mode value of 170.0Å.   A

(a)

(b)

Figure 17.   Scanning electron micrographs of deeply etched
             longitudinal section of base-plate.
             (a) Low magnification of pearlitic
                 microstructure.
             (b) High magnification of pearlite colony.

Figure 18. Transmission electron micrograph of a thin foil from the base-plate illustrating a dislocated substructure within extremely fine ferritic grains.

Figure 19. Transmission electron micrograph of thin foil from the base-plate containing a fine pearlitic structure and precipitate dispersion.
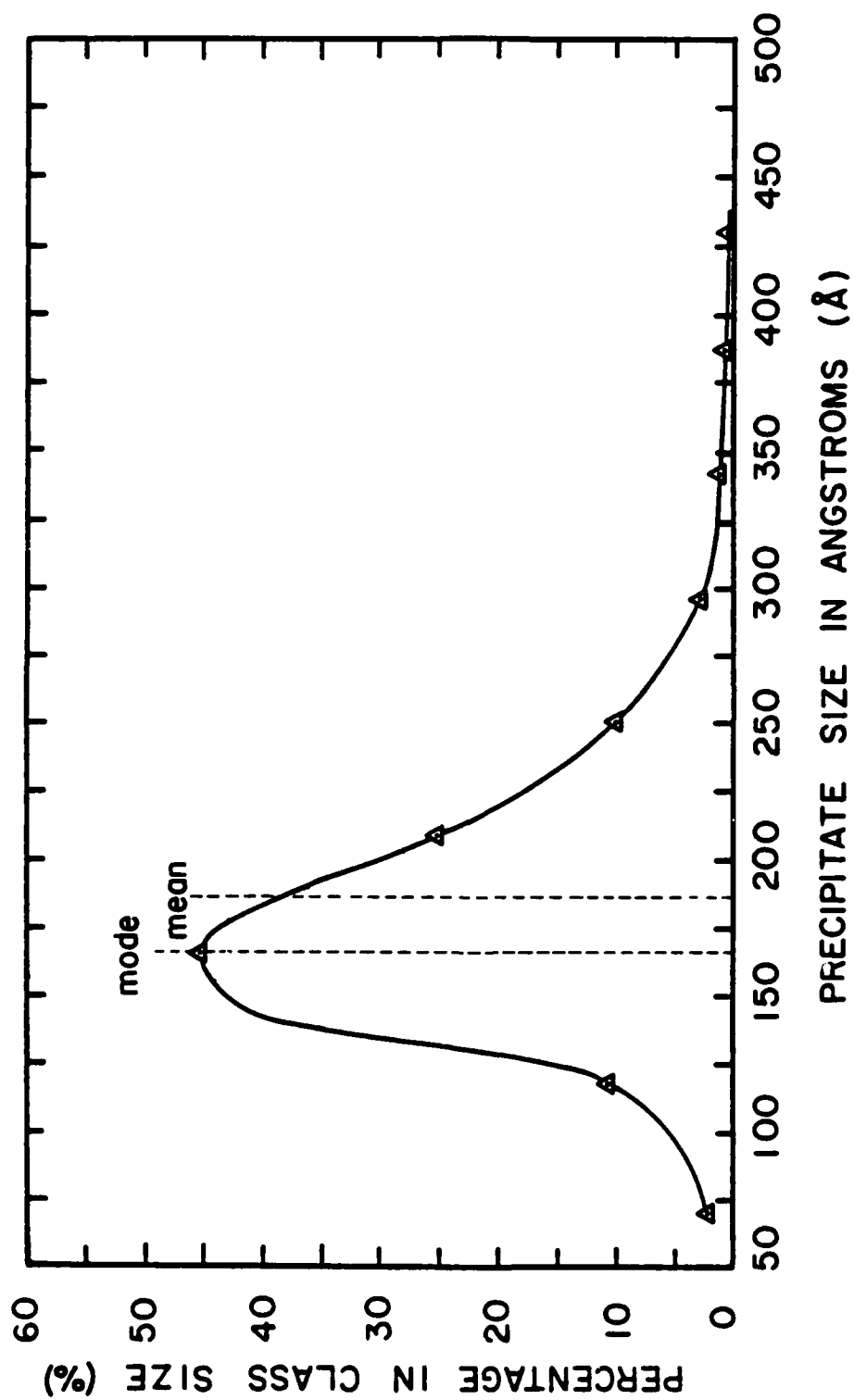
Figure 20.   Base-plate precipitate size distribution.

typical carbon extraction replica observation is shown in Figure 21. This size distribution represents all the particles observable at this level of resolution. Selected area electron diffraction (SAD) in a thin foil specimen indicated that most of the fine precipitates are vanadium carbonitrides (V(C,N)), Figure 22, and the large precipitates are Niobium carbonitrides, Nb(C,N), Figure 23.

X-ray diffraction of the residue collected via bulk extraction indicated the presence of two separate precipitate dispersions, each with a B1 crystal structure. One is V-based carbonitride and the other a Nb-based carbonitride. The measured lattice parameters were 4.1149Å and 4.424Å for the V-based and Nb-based precipitates,respectively. The accuracy of these measurements is somewhat diminished by the use of front-reflection lines. However, the intensity of back-reflection lines was insufficient to obtain useable data.

4.2 Mechanical Properties

All of the stereological parameters measured are tabulated in Table 5.

The results of tensile tests and hardness tests on

0.08 μm
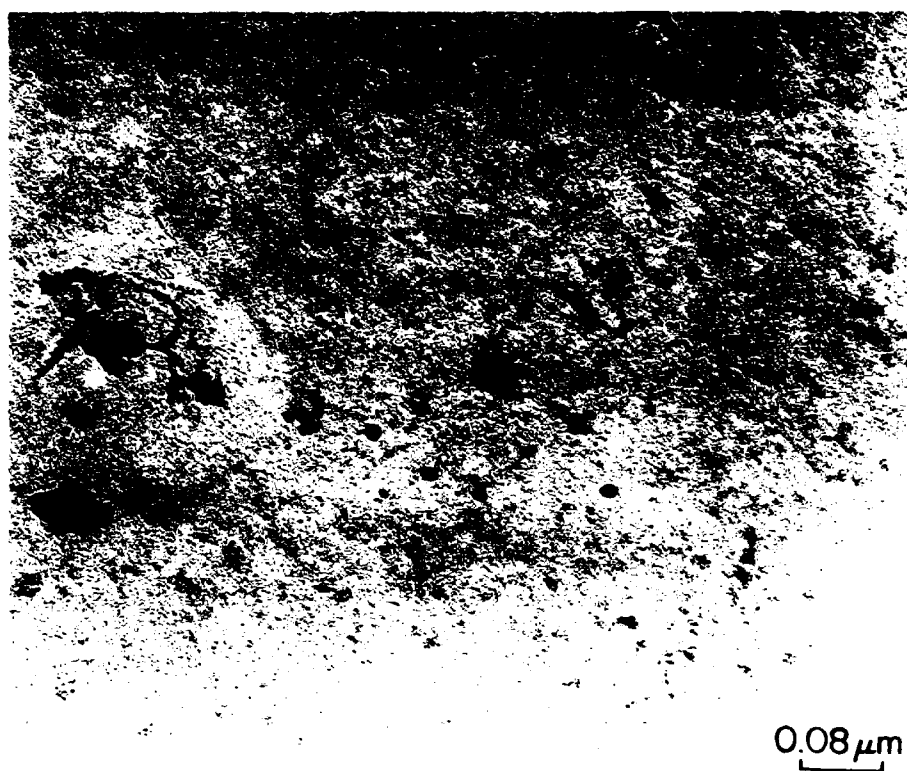
Figure 21.   Transmission electron micrograph of a carbon
             replica from the base-plate.   (A) indicates
             Nb-based precipitate, (B) indicates V-based
             precipitate.

0.08μm
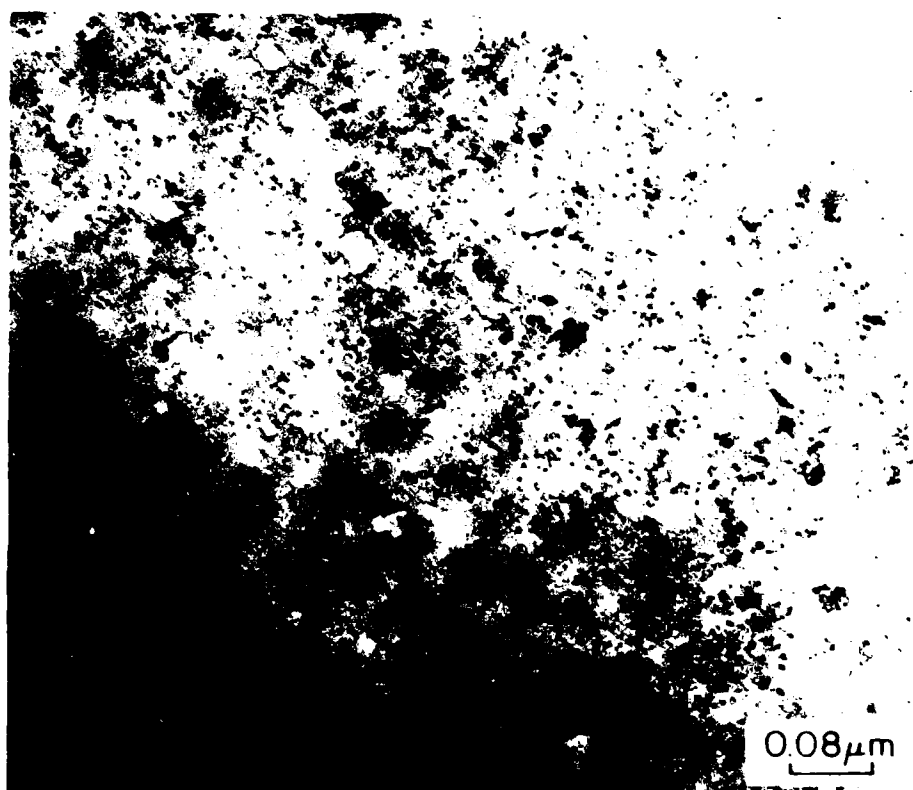
Figure 22.   Transmission electron micrograph of a thin foil
              from the base-plate containing a dispersion of
              fine V(C,N) precipitates.

0.16 μm
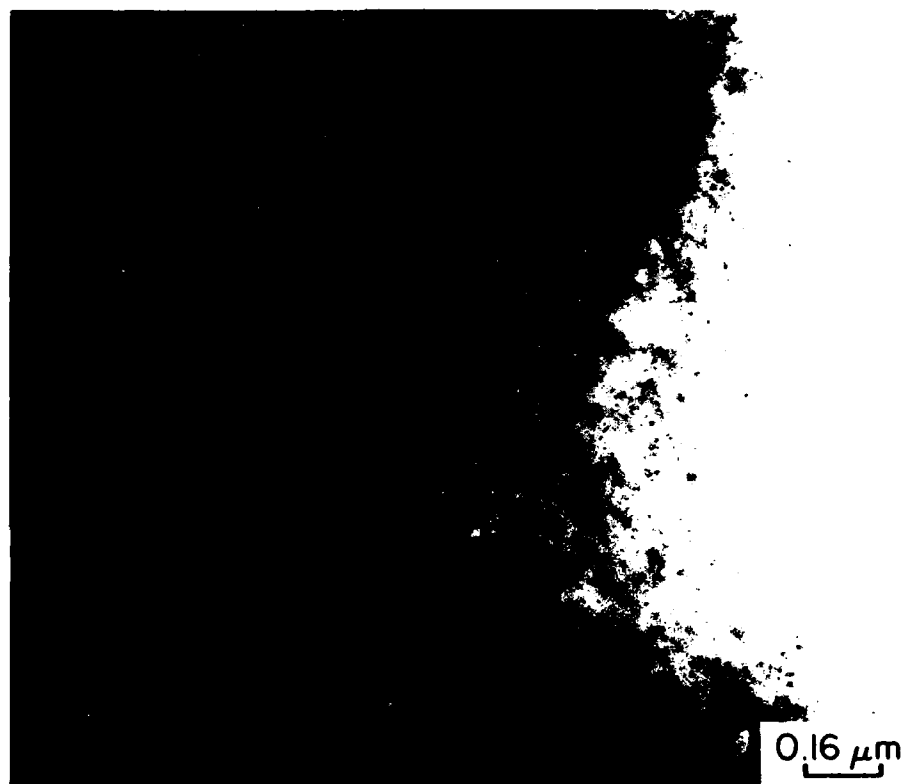
Figure 23.   Transmission electron micrograph of a thin foil
             from the base-plate containing large Nb(C,N)
             precipitates.

Table 5

Microstructural Characterization of Base-Plate

Average ferrite grain size calculated by the intercept method	5.5μm
Pearlite content for long. sect. at 500X-by grid point count, with a 95% confidence level interval	17%
Inclusion content for long. sect. at 100X-by J.K. chart ASTM E45	Globular type D
Mean precipitate size, fine V (C,N)	184Å
Precipitate distribution mode V (C,N)	170Å

base-plate specimens are summarized in Table 6.

Charpy V-notch (CVN) tests were performed to ascertain the ductile-to-brittle transition temperature and the upper shelf energy. Half-size specimens in the transverse orientation (longitudinal crack) were employed since it was anticipated that half-size specimens would be utilized in assessing the toughness of HAZ microstructures in actual weldments and Gleeble simulated specimens. The Charpy data is depicted in Figure 24 along with full size specimen data for this heat of base-plate. [92]

The transition temperature was determined on an energy basis due to difficulties in measuring consistant lateral contraction and also in determining a percentage of fracture surface area in fibrous appearance. Therefore, the transition temperature at 50% maximum impact energy at the highest temperature (25 deg.C) was chosen. This procedure is described in ASTM E-23-60 .

The transition temperature for the half size specimens is slightly lower than for the full-size specimens. Both transition temperatures were approximately -50 deg.C. There is however, a large difference in the upper shelf energies for the two specimen types. The full size specimen tests yield a higher upper shelf energy(~100 ft.-lb. vs ~50 ft.-lb.).

Table 6

Mechanical Properties

Tensile Testing Data

Mean Bar Diameter	8.84 mm (0.348 in)
Mean Cross Section Area	61.3 mm^2 (0.095 in^2)
Mean Maximum Load	3932 kg (8662 lb)
Mean Ultimate Tensile Strength	63.97 kg/mm^2 (90,913 psi)
Mean Yield Strength Upper Point	54.83 kg/mm^2 (77,926 psi)
Mean Yield Strength Lower Point	52.37 kg/mm^2 (74,421 psi)
Mean 0.2% Offset Yield Strength	53.08 kg/mm^2 (75,440) psi)
Mean Uniform Elongation	12.0%
Mean Percent Area Reduction	72.0%

Hardness Testing Data

Diamond pyramid hardness of ferrite grains- 20 g load	209.1
Rockwell B hardness average 100 kg load	93.3
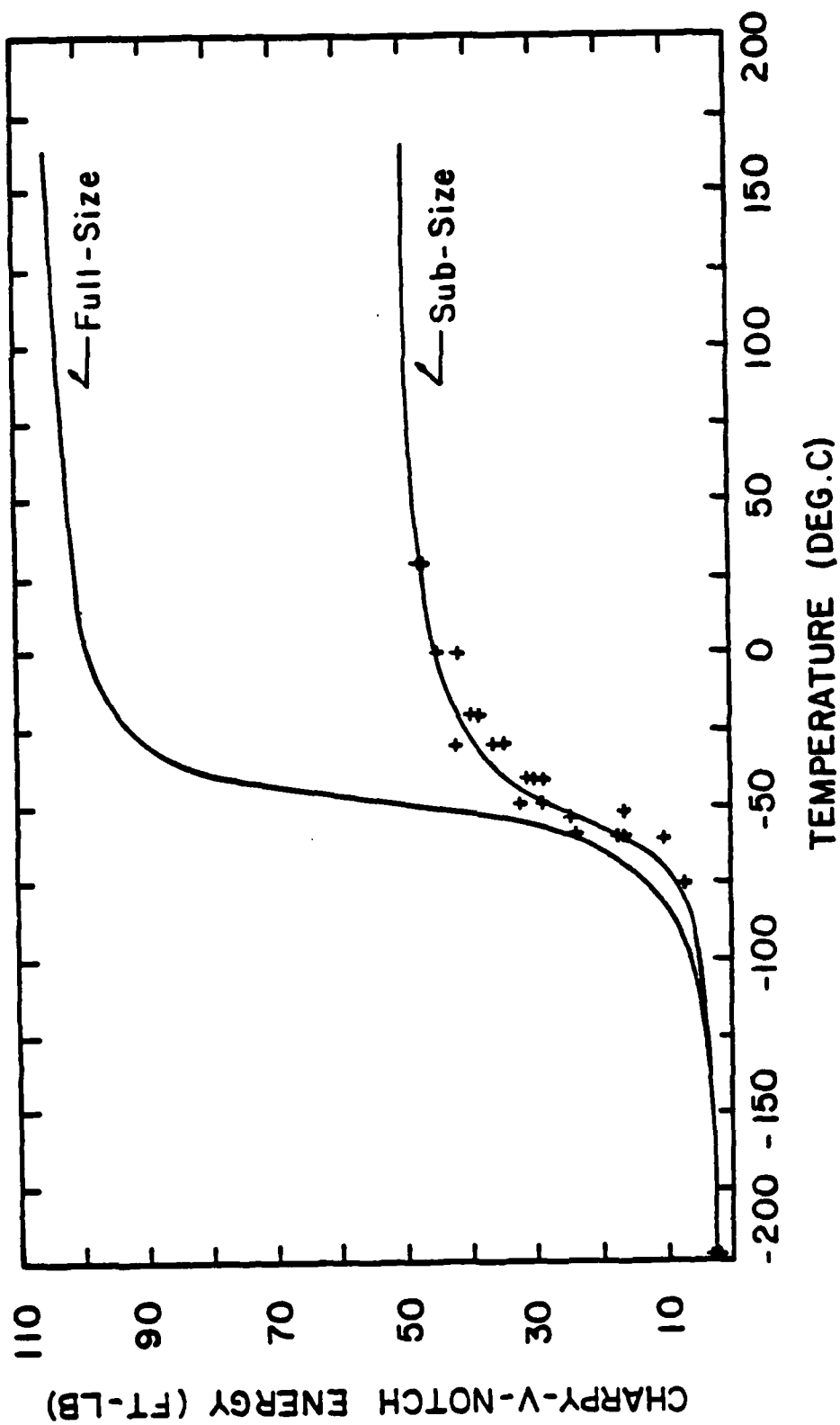
Figure 24.   Charpy V-notch energy as a function of
temperature for base-plate material.

It is apparent that sufficient restraint exists at the root of the notch in the half-size specimen to produce a transition temperature similar to that observed with full-size specimens. This is surprising since one might expect that narrower specimens, implying less restraint at the notch, would exhibit lower transition temperatures.

If the measured upper shelf energies are normalized with respect to the specimen cross-sectional area at the notch [93] the shelf energy for both specimens is approximately 1.25 ft.-lb./mm. Thus, on a normalized energy basis the two specimens produce similar upper shelf energies and in fact, it may be possible to correlate future Charpy results of half-size specimens with full-size specimen data.

Scanning electron microscopy (SEM) was performed to evaluate the fracture surface morphology of Charpy specimens, Figure 25. The fracture surfaces of specimens associated with the upper shelf were characterized by a dimpled morphology indicative of microvoid coalescence, Figure 25(a). The fracture surfaces of specimens associated with the lower shelf were characterized by cleavage facets, Figure 25(b). These fracture surface morphologies are consistent with the Charpy data.
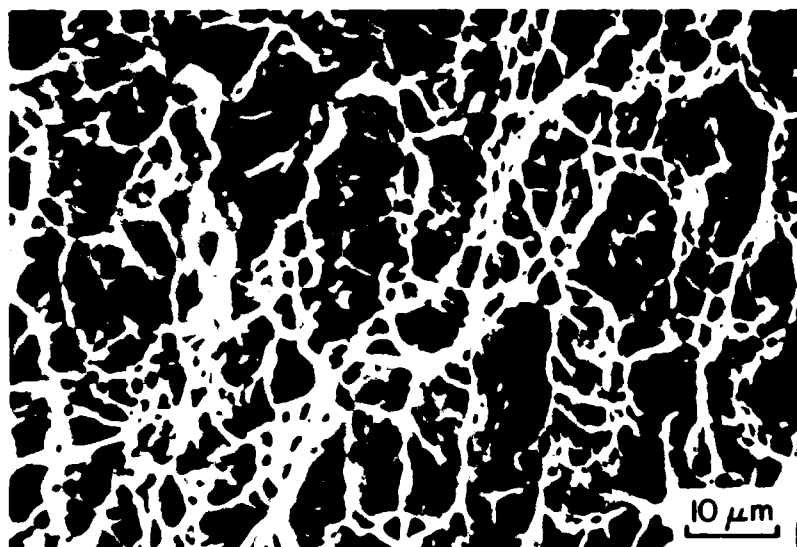
(a)
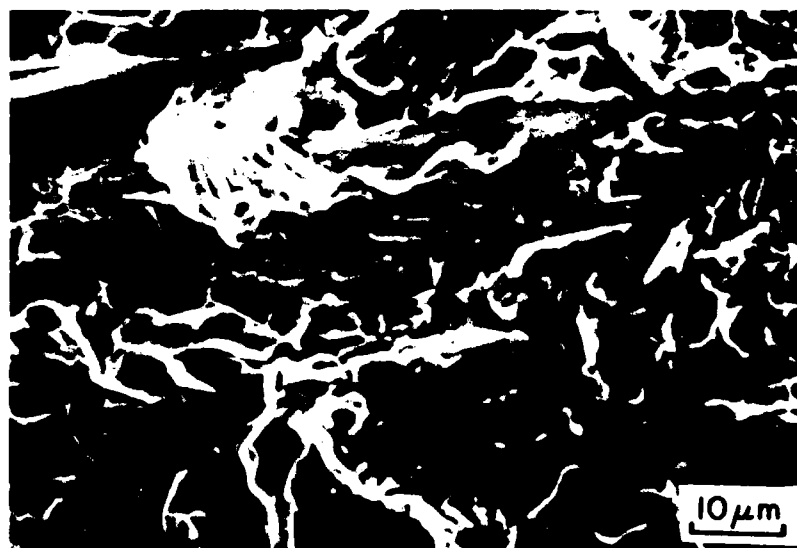
(b)

Figure 25.   Scanning electron micrographs of Charpy V-notch
             (CVN) fracture surface morphologies of
             base-plate specimens.
             (a) Upper shelf; , CVN energy = 48 ft-lb.
                 T = +25 deg.C
             (b) Lower shelf; , CVN energy = 0 ft-lb.
                 T = -200 deg.C

4.3 Austenite Microstructural Evolution

4.3.1 Austenite Grain Growth During Furnace Heat Treatment

The data from furnace, heat treated specimens is displayed in Figure 26. The austenite grain size at any time increases slowly with temperature up to approximately 1000 deg.C whereupon a fairly rapid increase in grain size occurs with further increase in temperature. This grain coarsening temperature is approximately independent of time although at higher temperatures grain size does increase with time. If a grain growth law of the following form is assumed:

(4.1) $D = (kt)^n$

then,

(4.2) $\log D = n \log k + n \log t$

Plots of log D vs. log t, Figure 27 then yield straight lines of slope equal to n. From these plots a mean value of n = 0.125 was calculated over the entire temperature range. Table 7 contains the individual values for k and n.

If the temperature dependence of grain growth is assumed to follow an Ahrenius relation and reside in k, then:
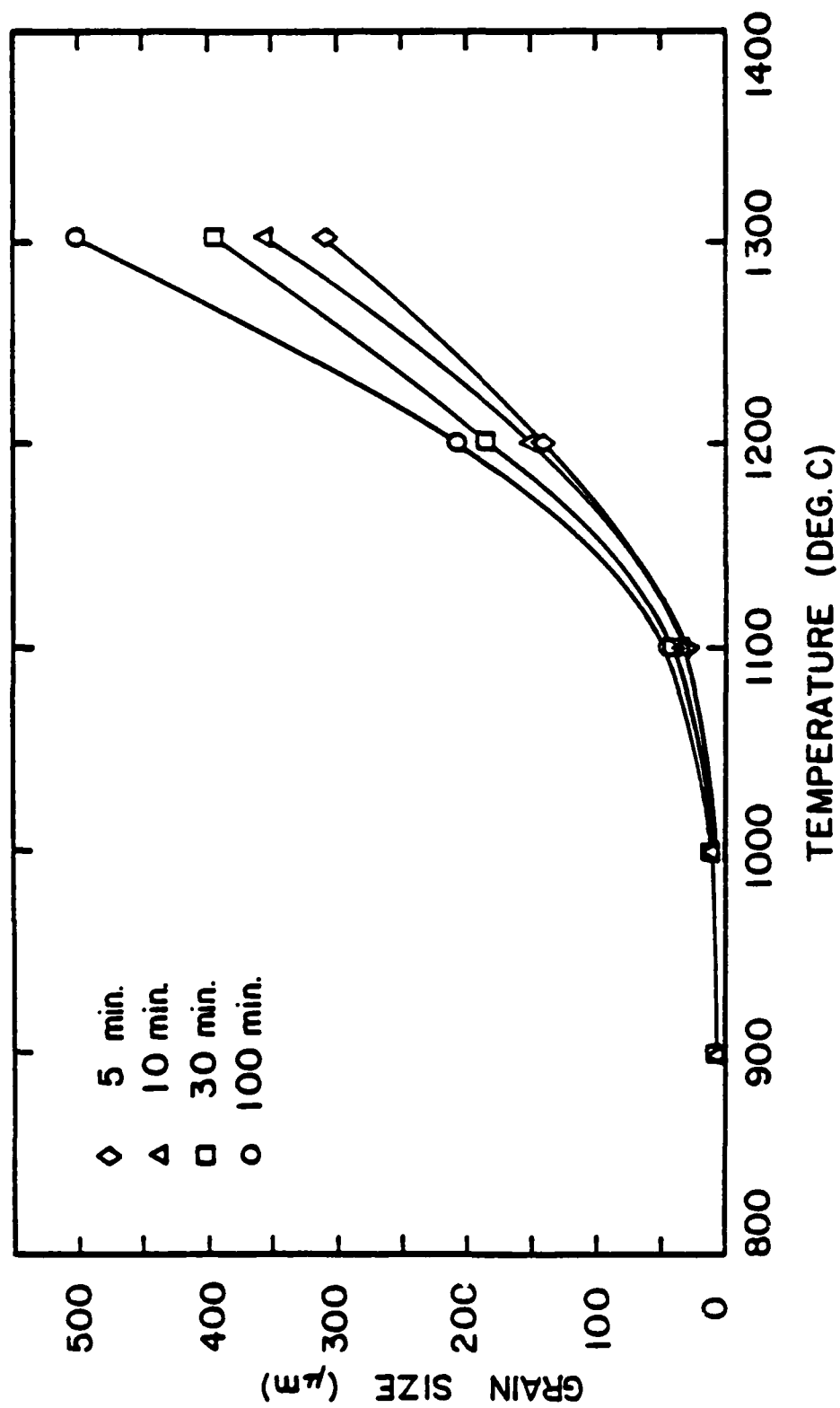
Figure 26. Austenite grain size as a function of
temperature for various isothermal hold times
during furnace heat treatments.
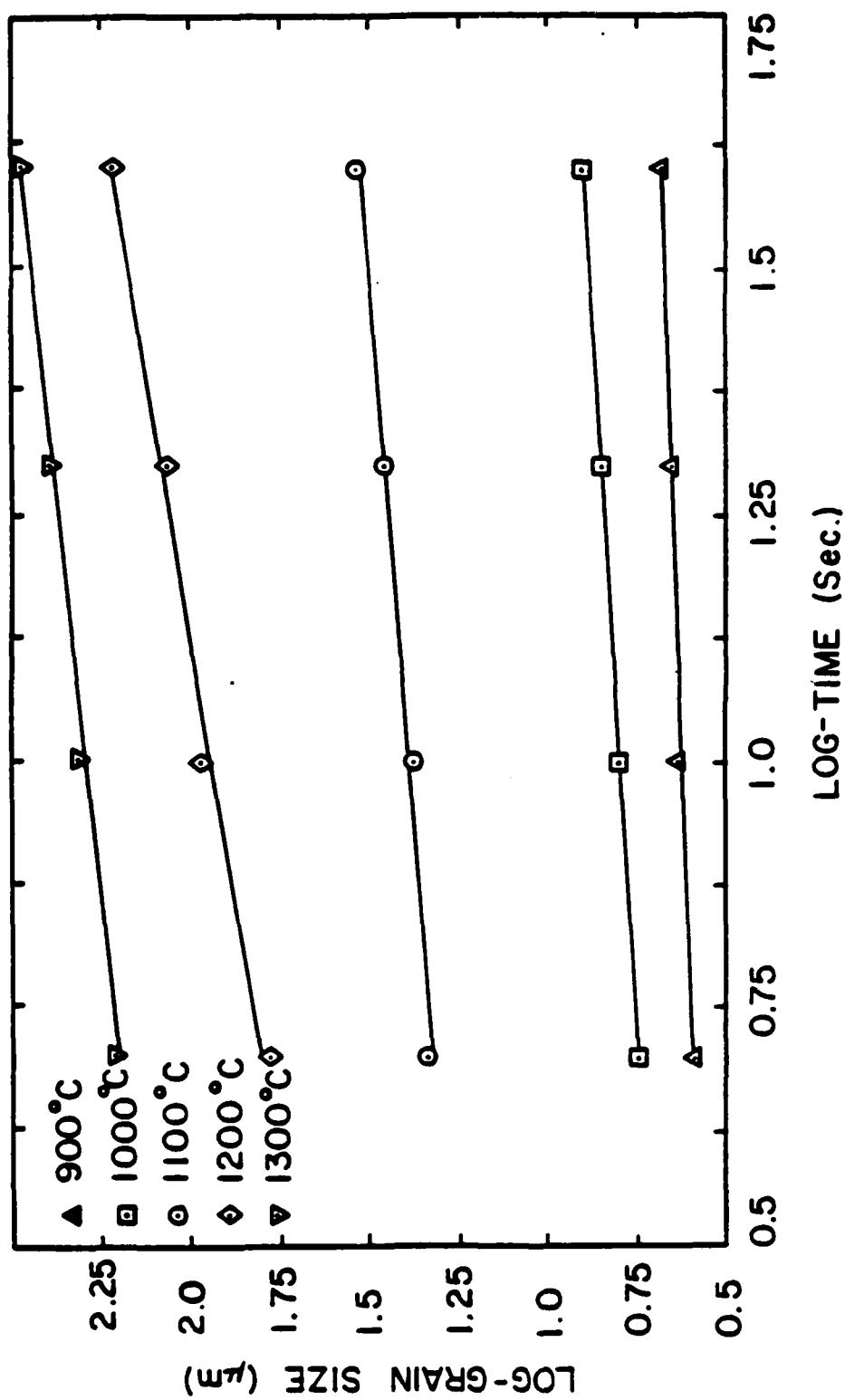
FIGURE 27.   Austenite grain size as a function of time for
various isothermal furnace heat treatments

Table 7

Grain Growth Parameters From Furnace Heat Treatments

Temperature (deg.C)	n (slope)	K (Y-intercept)
900	0.1240	4.00
1000	0.1160	6.84
1100	0.0990	27.16
1200	0.1310	112.98
1300	0.1550	242.10

(4.3) $D = (k't)^n$

where,

               $(k')^n = k$

(4.4) $k' = k_0 \cdot exp(-Q/RT)$

(4.5) $\log D = n \log k_0 \cdot (-nQ/2.303RT) + n \log t$

An Arrhenius plot of log D vs. 1/T at a given time should then yield a straight line with a slope equal to $-nQ/2.303R$ or $-(0.027)Q$, employing the mean value of n previously calculated. A single straight line would be obtained for a single, thermally activated controlling process. Such a plot is depicted in Fig.28. Examination of the plot reveals clustering of the isochronal plots and what appears to be three temperatures regimes of behavior; I, II, and III. The transition from regime I to II correlates with the previously described grain coarsening temperature. The transition from regime II to III does not appear to correlate with any significant physical process. The activation energies and pre-exponential terms were calculated for these regimes and are tabulated in Table 8. The apparent activation energies, have not as yet been associated with any fundamental processes.
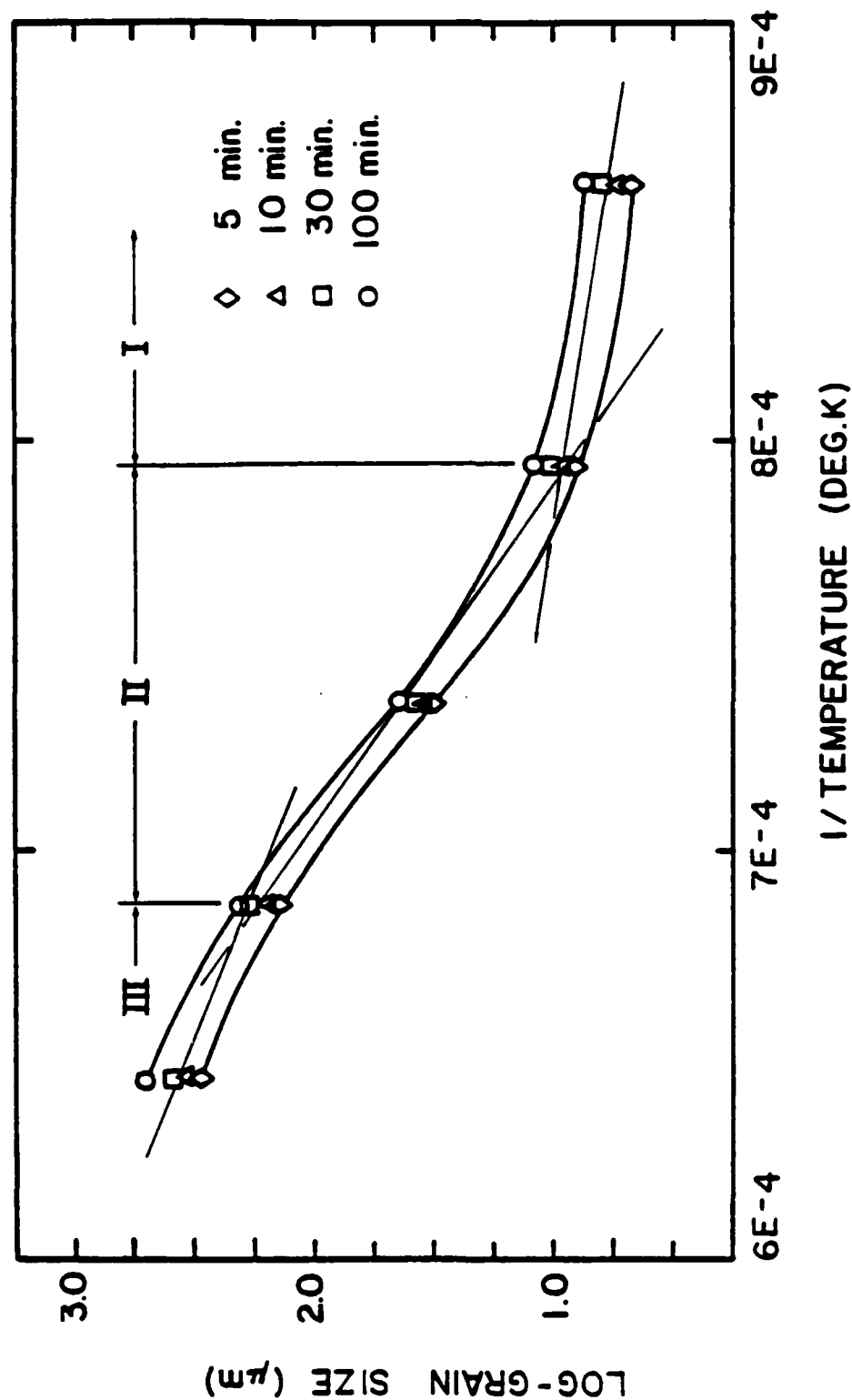
Figure 28. Arrhenius plot, Log-grain size versus inverse
temperature indicating three regimes of
behavior for austenite grain growth during a
furnace heat treatment.

Table 8

Grain Growth Kinetic Parameters for Furnace Heat Treatments

Regime	Q (Kcal/mole)	*$K_O \dfrac{(\mu m)^8}{min.}$
I	86.4	8.49×10^{20}
II	407.4	6.03×10^{77}
III	254.09	2.04×10^{54}

*An average time of 50 minutes was employed.

A similar analysis by Santella [43] on low carbon steel indicated that regimes I and III were assiciated with normal grain growth and regime II with abnormal grain growth.

4.3.2 Austenite Grain Growth During Welding

The thermal cycle chosen for this experiment was at an intermediate heat input and high peak temperature (Plate 12 TC 2; 3.35 KJ/mm, D_{FZL} = 0.39mm, T_p = 1380 deg.C). The evolution of austenite microstructure was studied between 800 deg.C on heating and 800 deg.C on cooling and austenite grain size is plotted as a function of time in the thermal cycle in Figure 29. The major increment of grain growth occurs in the vicinity of the peak temperature and the grain size saturates at a relatively high temperature in the cooling portion of the cycle (1100 deg.C). This is probably due to the high temperature sensitivity of thermally activated exponential processes such as grain growth. At least for the case of this thermal cycle, it would then seem justified to associate the degree of austenite grain growth with peak temperature.
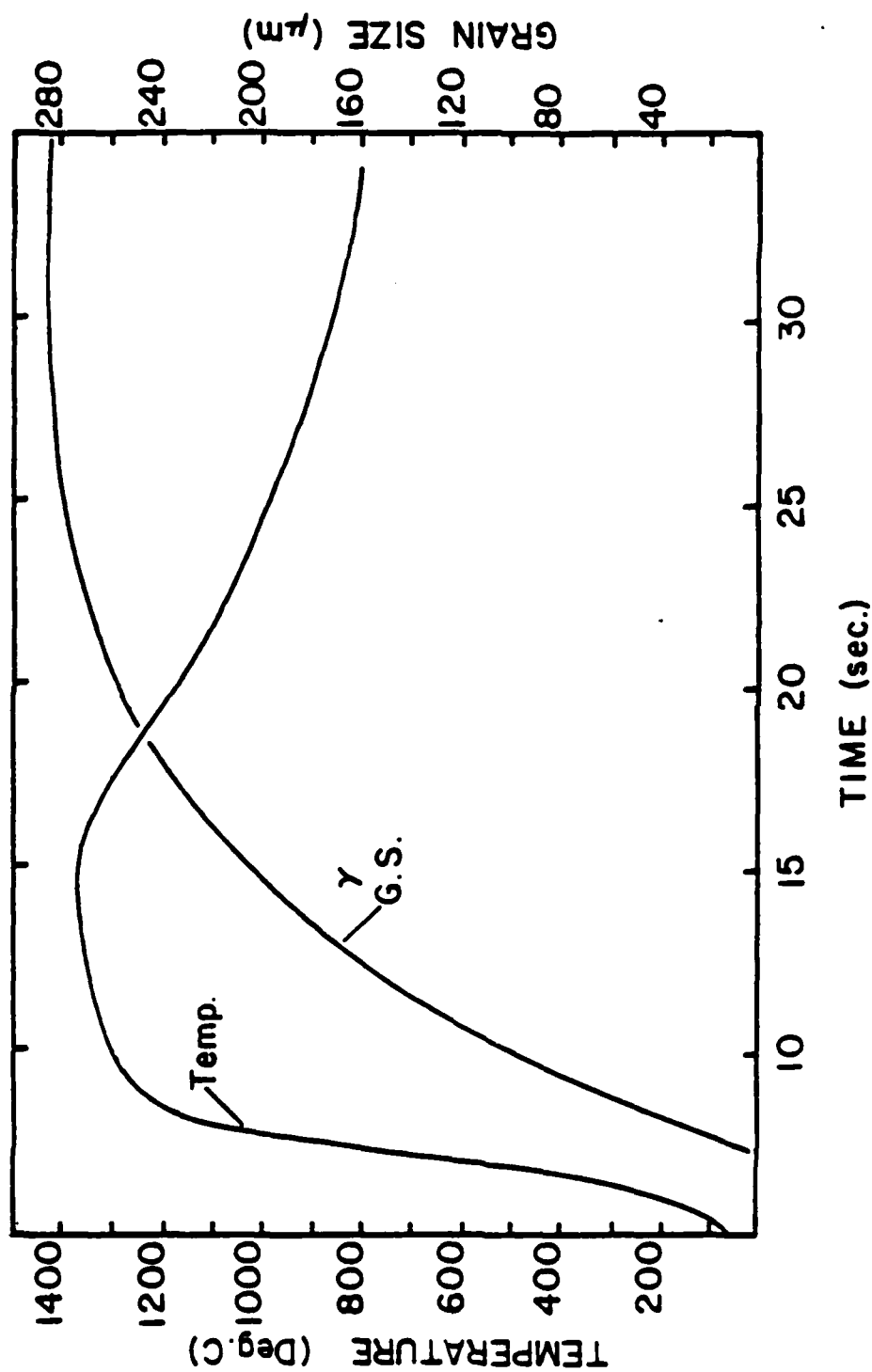
Figure 29. Austenite grain size growth data as a function of time during an athermal heat treatment. Austenite grain growth data produced from Plate 12. TC2 thermal cycle simulation, nominal heat input of 3.35 KJ/mm.

4.4. Microalloy Precipitation In Furnace Heat Treated Specimens

The heat treatment matrix to provide specimens for the austenite grain coarsening study as well as the precipitate coarsening results have been described previously.

The state of microalloy precipitation was assessed in selected conditions by two methods. Carbon extraction replicas were observed via transmission electron microscopy (TEM). X-ray diffraction was performed on bulk extractions. The use of water quenched specimens precludes microalloy precipitation in ferrite during or after the austenite-ferrite transformation.

Transmission electron microscopy work on carbon extraction replicas showed that most of the precipitate dispersion had dissolved with treatment temperatures in excess of 1000 deg.C. This is consistent with the observation of an austenite grain coarsening temperature in this range of temperature. The majority of precipitates observed and analyzed by selected area electron diffraction (SAD) were vanadium carbonitrides V(C,N). In fact, no Niobium carbonitride Nb(C,N) were specifically analyzed by electron diffraction. In addition, significant precipitate coarsening prior to dissolution was not observed.

X-ray diffraction of residues of extracted precipitates

revealed the presence of V(C,N) and Nb(C,N) precipitates,
as was observed previously for the base plate. A summary
of the results of X-ray diffraction work are contained in
Table 9. These results indicate significant levels of a
V(C,N) precipitate in addition to a Nb(C,N) precipitate at
900 Deg.C but only Nb(C,N) precipitates at higher
temperatures. This is generally consistent with TEM
observations. The Nb(C,N) precipitation is apparently too
sparsely distributed to be observed via TEM and this is
also consistent with the correlation of austenite grain
coarsening with V(C,N) dissolution.

4.5. HAZ Studies of Nb-V Base-Plate

Information of thermal history was obtained empirically
through temperature measurement in the HAZ as a function of
position. The experimental data for thermal cycles in
nominally 1.97 KJ/mm, 3.35 KJ/mm, 4.92 KJ/mm (50 KJ/in., 85
KJ/in., 125 KJ/in.) welds are depicted in Appendix 1.

The measured peak temperature is plotted against
distance from the fusion line for the various nominal heat
inputs in Figure 30. The scatter in data for each heat
input is probably due to the scatter about the nominal heat
input. However, the trends are consistent in that peak

Table 9

X-Ray Diffraction of Extracted Microalloy Precipitates

Temperature (deg.C)	Precipitates Present	
	5 min.	100 min.
900	V(C,N)+Nb(C,N)	V(C,N)+Nb(C,N)
1000	Nb(C,N)	Nb(C,N)
1100	Nb(C,N)	Nb(C,N)
1200	Nb(C,N)	Nb(C,N)
1300	Nb(C,N)	Nb(C,N)
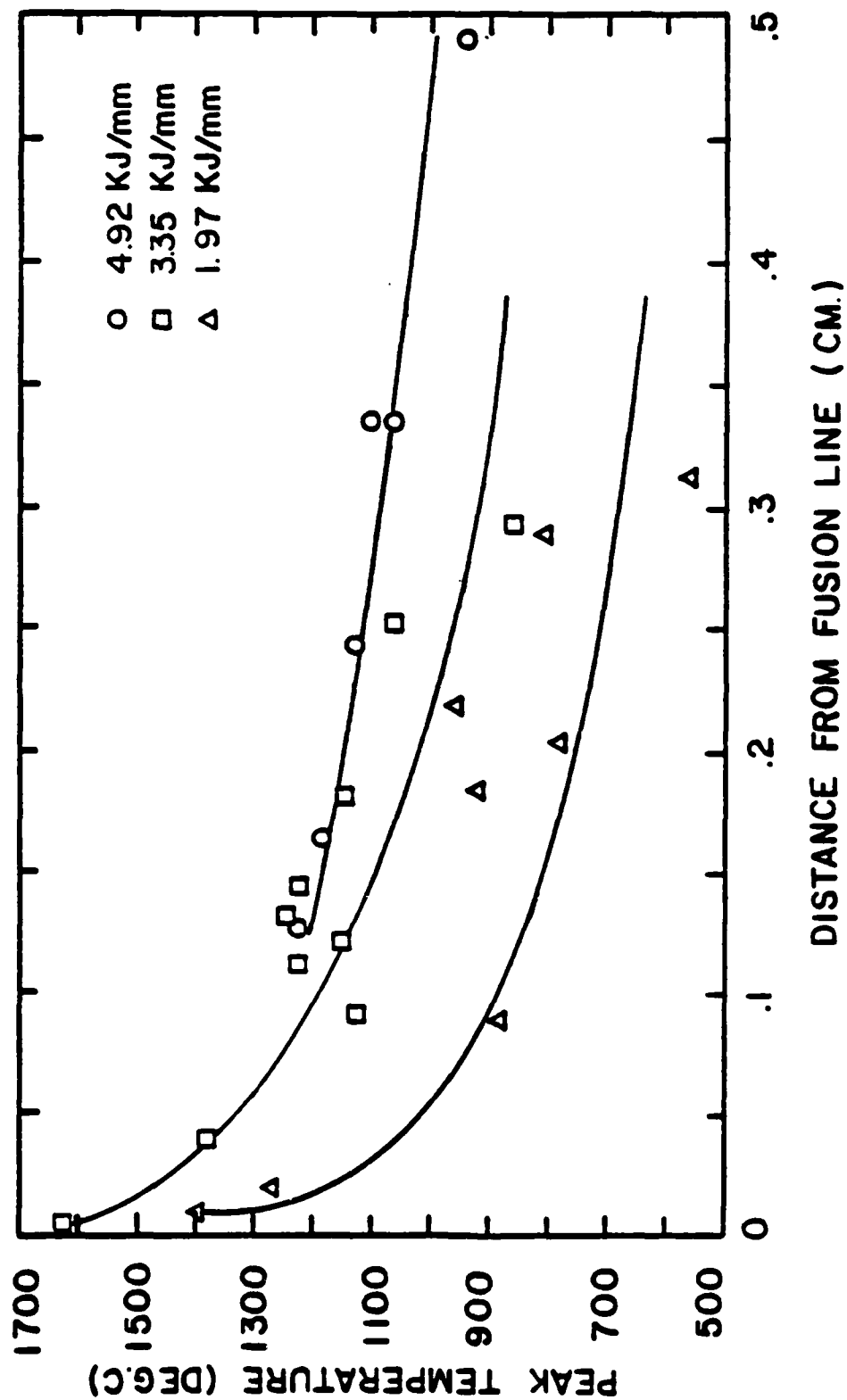
Figure 30.   Summary of experimental peak temperatures as a function of distance from the fusion zone.

temperature decreases with distance from the fusion line at
a given heat input and increases with heat input at a given
distance from the fusion line.

4.5.1. Weld Macrostructure

Weld bead and HAZ widths were measured from macro-
etching effects. The etched boundaries can be seen in
Figure 8 and the measured values are tabulated in Table 10.

The weld bead and HAZ widths generally increased with
heat input, Figures 31, 32. There appeared to be some
scatter in bead and HAZ width for particular heat inputs.
A least-squares analysis of the data indicates the
following equations:

Weld bead width:

(4.6) $Y = 6.18 + 0.129 * (Heat Input KJ/mm)$

Coeficient of Determination: 0.887

HAZ width:

(4.7) $Y = 23.4 + 0.49 * (Heat Input KJ/mm)$

Coeficient of Determination: 0.958

TABLE 10

WELD BEAD AND HEAT AFFECTED ZONE MEASUREMENTS

	Heat input @ 100% eff. (KJ/mm)	HAZ Peak Temp. (Deg.C)	Distance from FZL (mm)	Weld Bead Width (mm)	HAZ Width From FZL(mm)
High Heat Input					
Plate 1					
TC 1	4.87	1234	1.27	24.5	7.40
TC 2	4.31	1125	2.43	22.2	5.95
Plate 2					
TC 1	5.03	----	1.52	26.3	7.30
TC 2	5.16	1098	3.35	26.8	6.60
Plate 4					
TC 1	5.10	1063	3.35	27.1	7.00
TC 2	4.96	931	4.92	28.6	7.40
Plate 7					
TC 1	4.40	1180	1.64	25.2	5.85
TC 2	4.48	----	----	25.0	6.3
Medium Heat Input					
Plate 10					
TC 1	3.11	1224	1.11	17.5	3.90
TC 2	3.00	1245	1.31	17.2	5.30
Plate 11					
TC 1	2.71	1149	1.21	17.2	3.90
TC 2	3.06	856	2.73	19.3	4.60
Plate 12					
TC 1	3.10	1623	melt	18.0	4.30
TC 2	2.98	1380	0.39	15.1	4.68

TABLE 10 (Cont.)

WELD BEAD AND HEAT AFFECTED ZONE MEASUREMENTS

	Heat input @ 100% eff. (KJ/mm)	HAZ Peak Temp. (Deg.C)	Distance from FZL (mm)	Weld Bead Width (mm)	HAZ Width From FZL (mm)
Medium Heat Input (cont.)					
Plate 13					
TC 1	2.77	1223	1.44	17.5	4.68
TC 2	2.88	1058	2.89	17.8	5.17
Plate 14					
TC 1	2.49	1123	0.91	17.2	5.07
TC 2	2.92	1143	1.81	17.3	4.58
Low Heat Input					
Plate 5					
TC 1	1.79	558	3.12	11.5	2.40
TC 2	2.04	803	2.88	11.5	2.50
Plate 6					
TC 1	1.96	1398	0.09	10.8	2.30
TC 2	2.07	9.16	1.83	11.0	3.40
Plate 8					
TC 1	1.76	954	2.18	10.0	3.70
TC 2	1.65	785	2.04	10.5	2.40
Plate 9					
TC 1	1.79	1272	0.19	10.0	2.40
TC 2	1.75	881	0.88	11.1	3.20
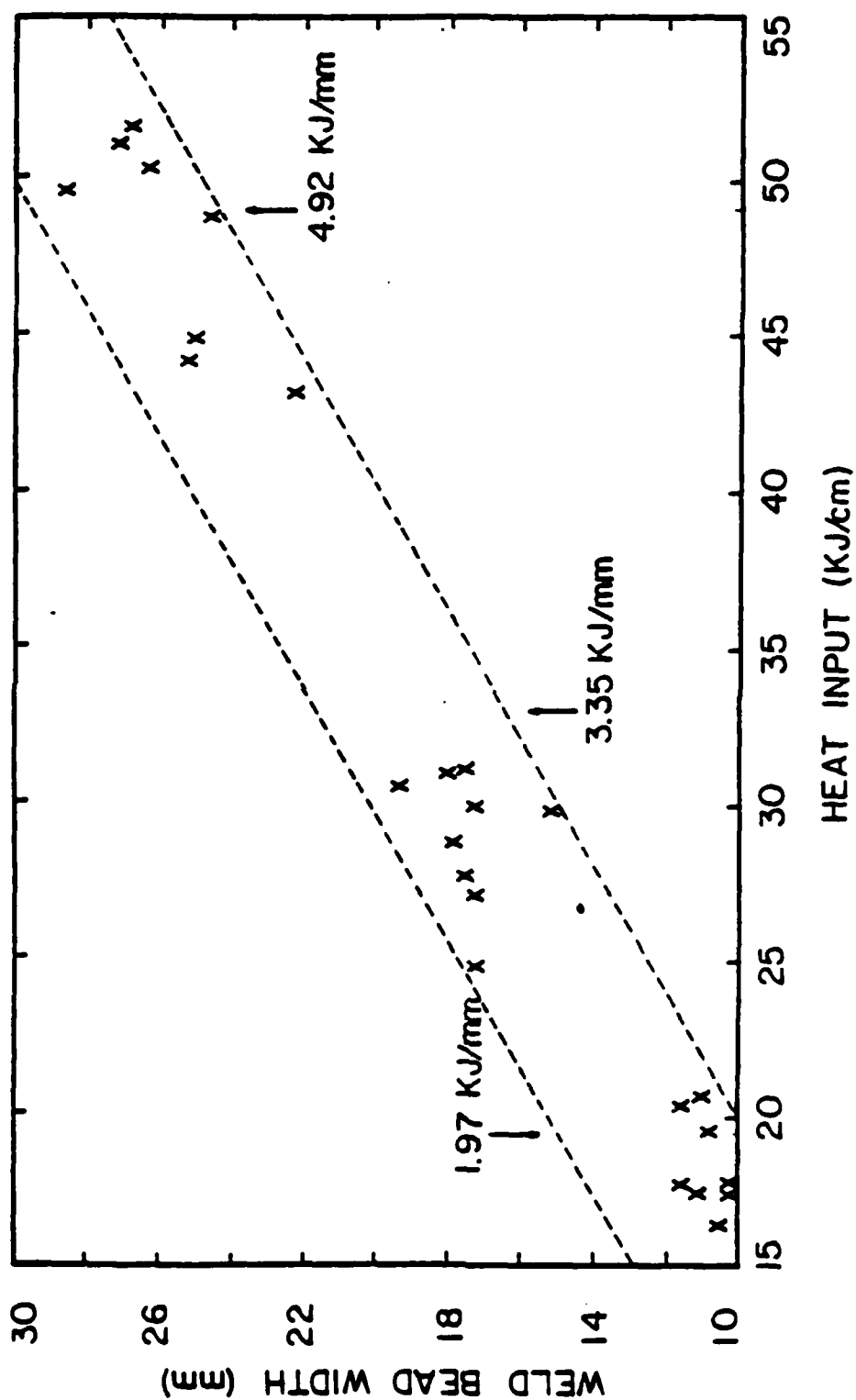
Figure 31.   Summary of weld bead width as a function of
heat input:
WBW = 23.4 + 0.49 • (H.I as KJ/mm)
Coefficient of determination = 0.958
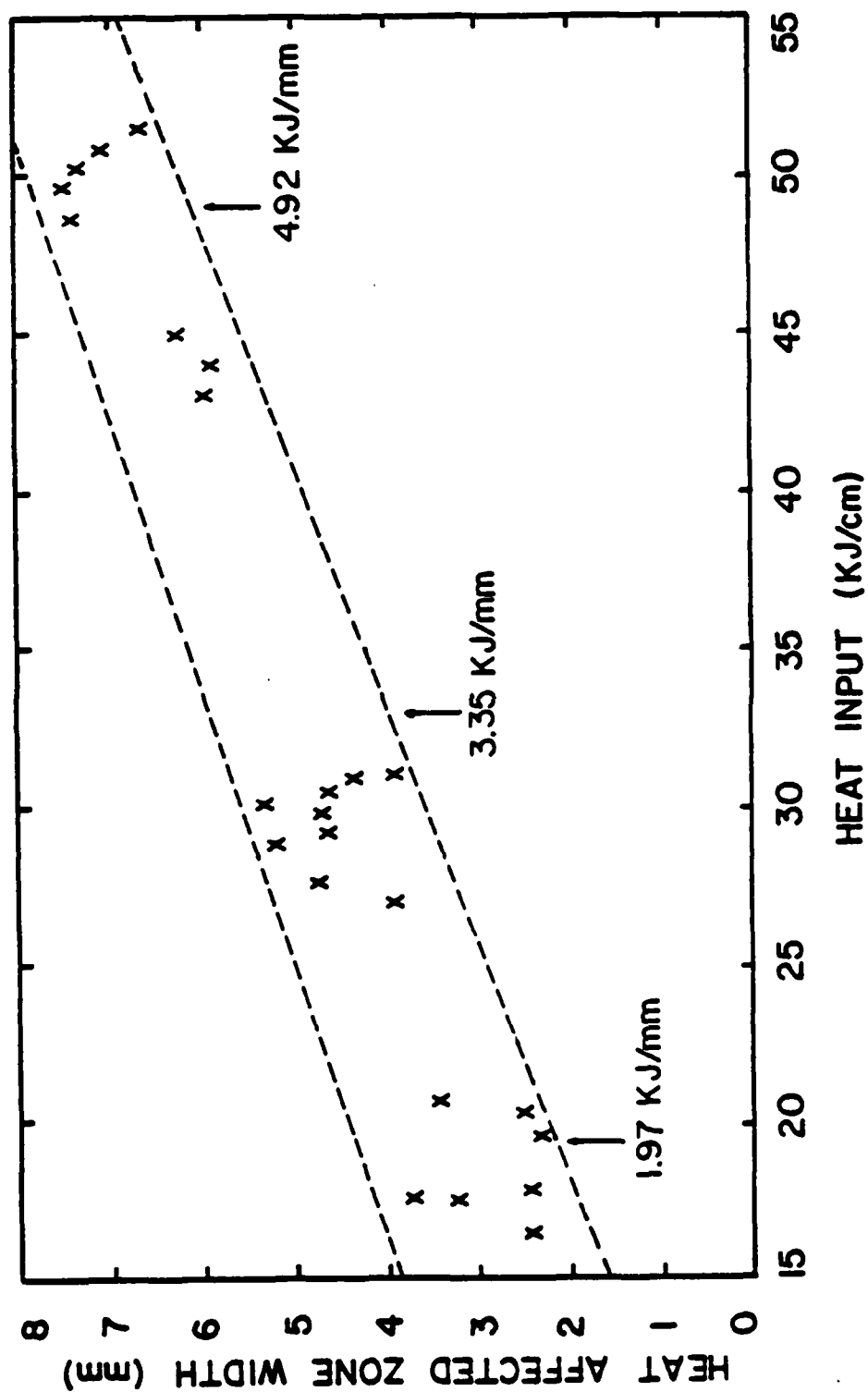
Figure 32.   Summary of heat affected zone width as a
             function of heat input:
             HAZW = 6.18 + 0.129 * (H.I as KJ/mm)
             Coefficient of determination = 0.887

4.5.2. Microstructural Characterization of the HAZ Region

The near fusion zone regions of the HAZ are associated
with an austenite grain coarsened microstructure. The
austenite grains are generally delineated by
allotriomorphic ferrite rims. The austenite grains of this
region are not as coarse at 1.97 KJ/mm   (50 KJ/in.),
Figure 33 as for 3.35 KJ/mm (85 KJ/in.), Figure 34 or 4.92
KJ/mm (125KJ/in.), Figure 35. In addition, the coarse
grained austenite region is very narrow in the 1.97 KJ/mm.
weld, consistent with the diminished overall HAZ width at
low heat input.

The microstructural zone of the coarse austenite grain
is consistant with the high hardness observed.

With increasing distance from the fusion zone boundary,
the prior austenite microstructure becomes refined.
Refinement manifests itself in an inability to distinguish
prior austenite grains via proeutectoid ferrite rims.

The variation in austenite grain size with distance
from the fusion zone boundary for the three nominal heat
inputs is illustrated in Figure 36.

The prior austenite microstructural refinement
associated with increasing distance from the fusion zone
boundary for the three heat-inputs is correlated with the

Figure 33.   Light micrograph of the Martensitic
             microstructural region in the near fusion zone
             of the HAZ for low heat input, 1.97 KJ/mm.
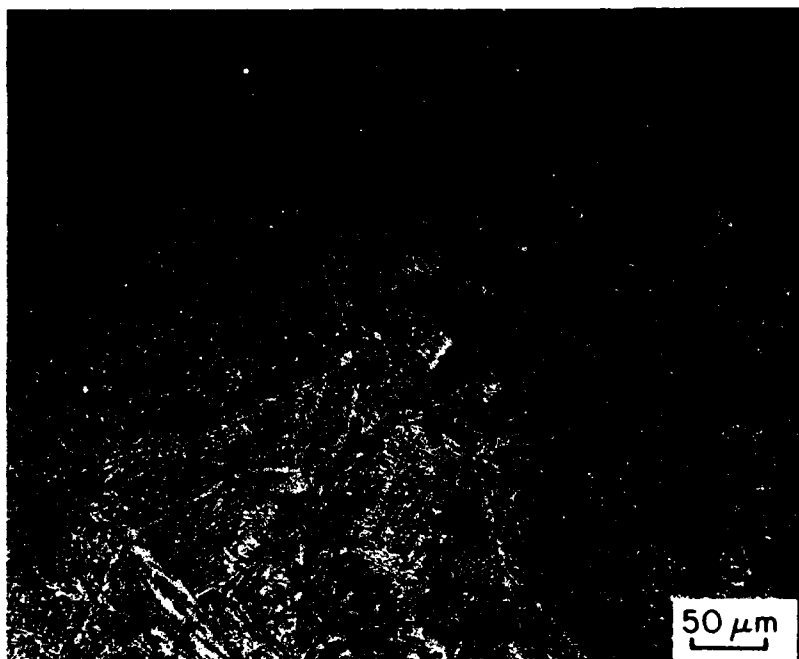
Figure 34.   Light micrograph of the Bainitic
             microstructural region in the near fusion
             zone of the HAZ for medium heat input,
             3.35 KJ/mm.
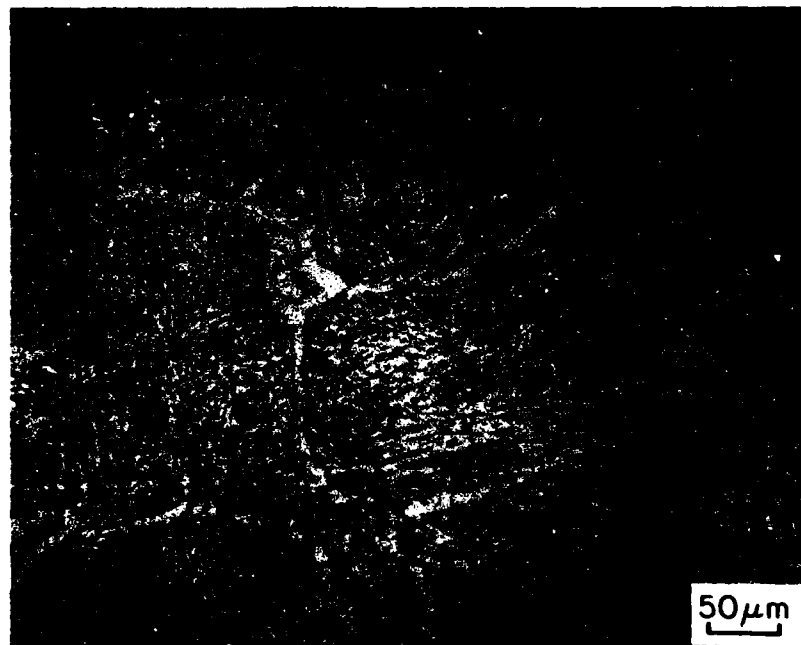
Figure 35.   Light micrograph of the Bainitic
              microstructural region in the near fusion zone
              of the HAZ for high heat input, 4.92 KJ/mm.
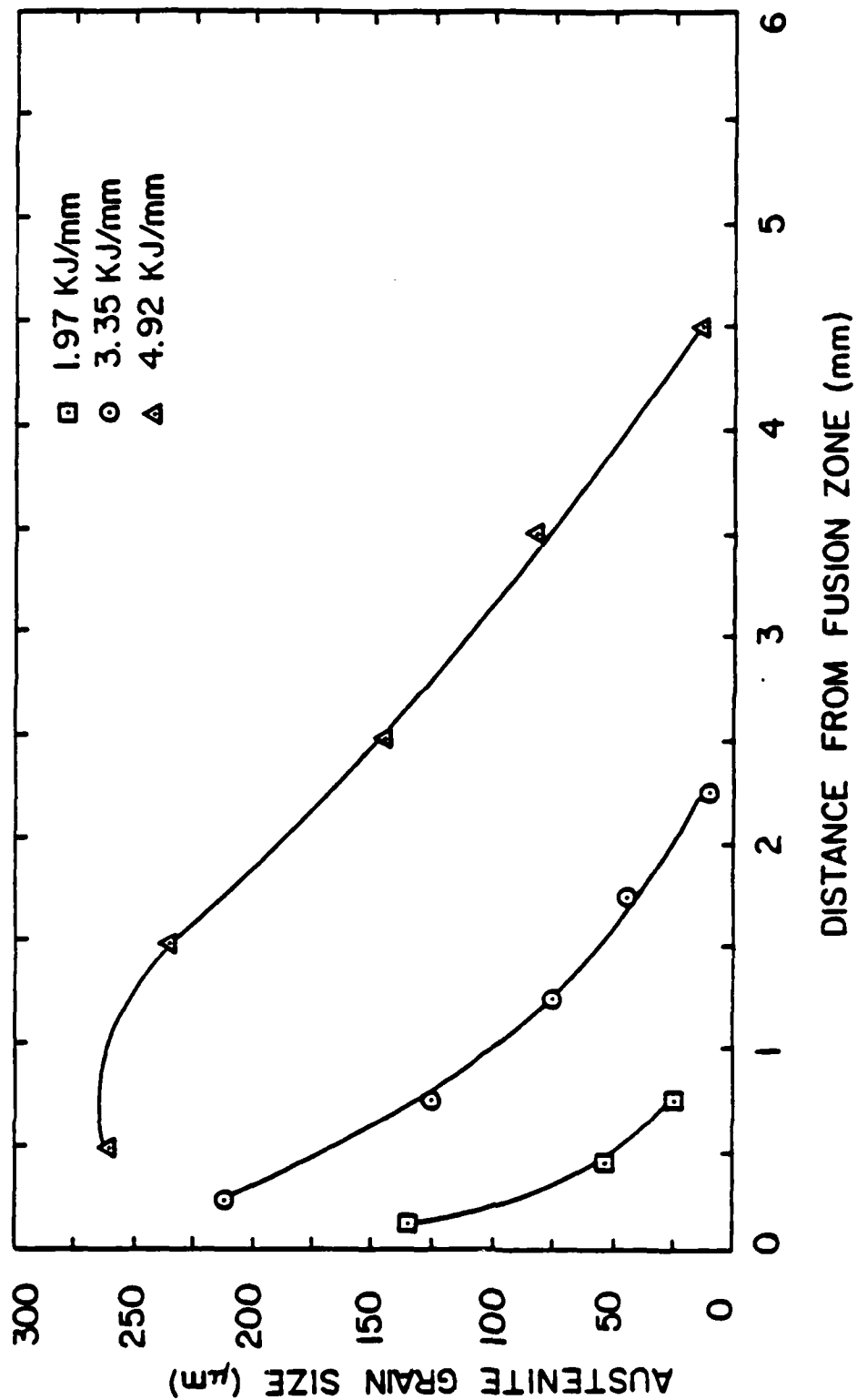
Figure 36. Summary of prior austenite grain size in the coarse grain region of a weld HAZ as a function of distance from the fusion zone for various nominal heat inputs.

evolution of higher temperature transformation product microstructures, Figures 37-39. Also, the microstructure in this region becomes finer as the cooling rate increases (ie. the heat-input decreases).

A distinct microstructural zone associated with a hardness decrease for locations further from the fusion zone boundry is characterized by dark etching bands. The dark-etching bands are a complex mixture of extremely fine ferrite, pearlite small patches of martensite, Figure 40. These bands indicate some sort of inheritance of the chemical and structural banding of the base-plate that results in heterogeneity in the transformation product microstructure.

At still greater distances from the fusion zone boundary, coarse grained polygonal ferrite on the same scale as the base-plate ferrite is distributed between the abovementioned dark-etching bands and the base-plate.

Diffuse pearlitic banding occurs beyond the polygonal ferrite region and increases until the banding becomes defined and is longer in the HAZ temperature range, Figure 41.

The variation of ferrite grain size with distance from the fusion zone boundary for the three nominal heat inputs is described in Figure 42.
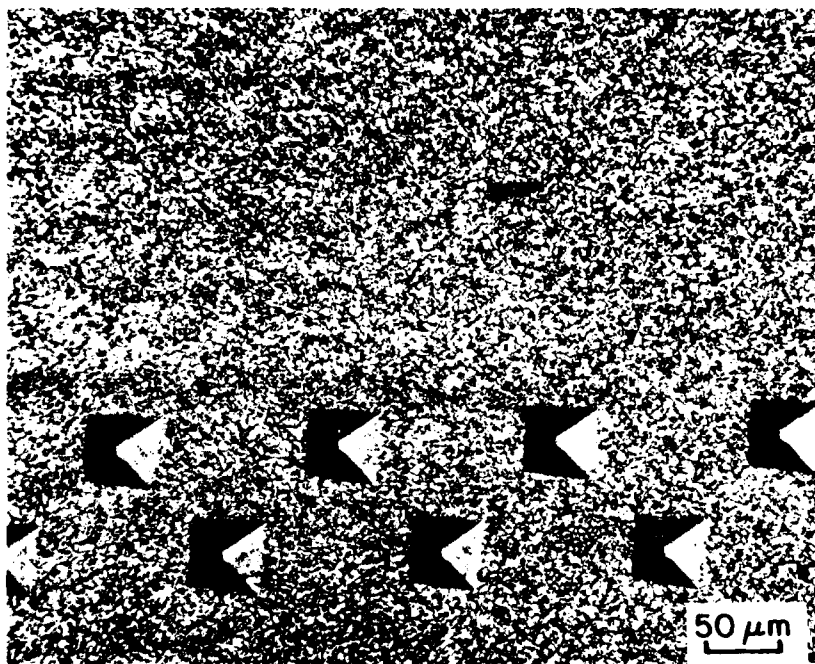
Figure 37. Light micrograph of the grain refined ferritic
            region of the HAZ for low heat input,
            1.97 KJ/mm.
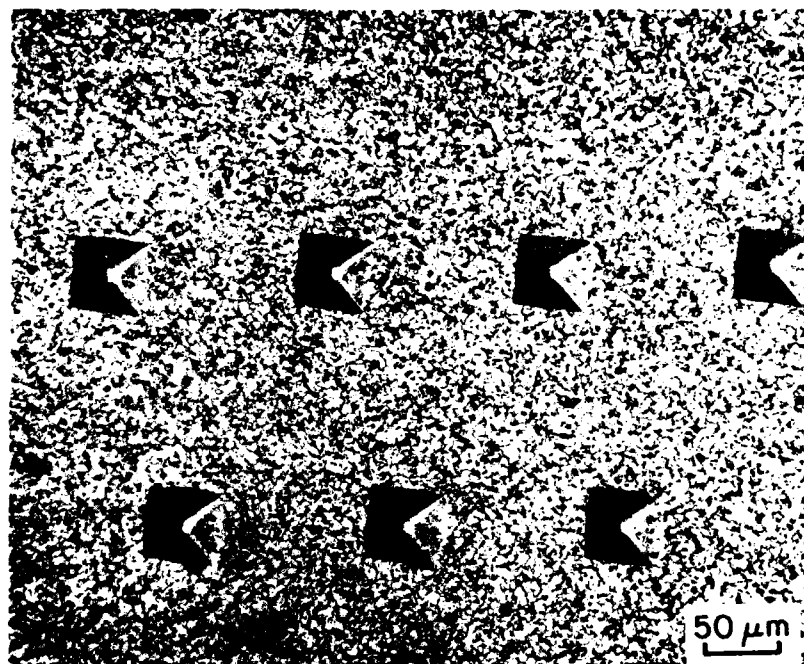
Figure 38. Light micrograph of the grain refined ferritic
region of the HAZ for medium heat input,
3.35 KJ/mm.
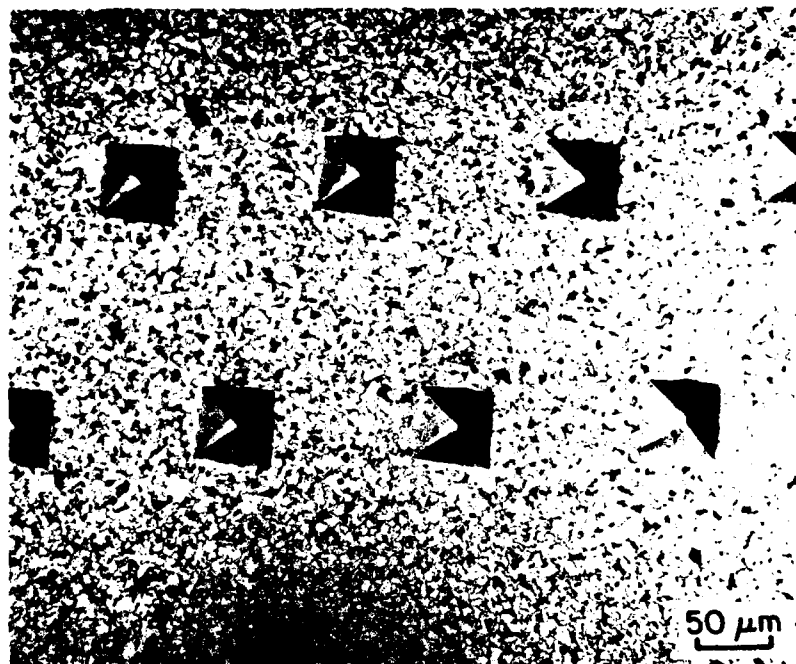
Figure 39.   Light micrograph of the grain refined ferritic
             region of the HAZ for high heat input,
             4.92 KJ/mm.
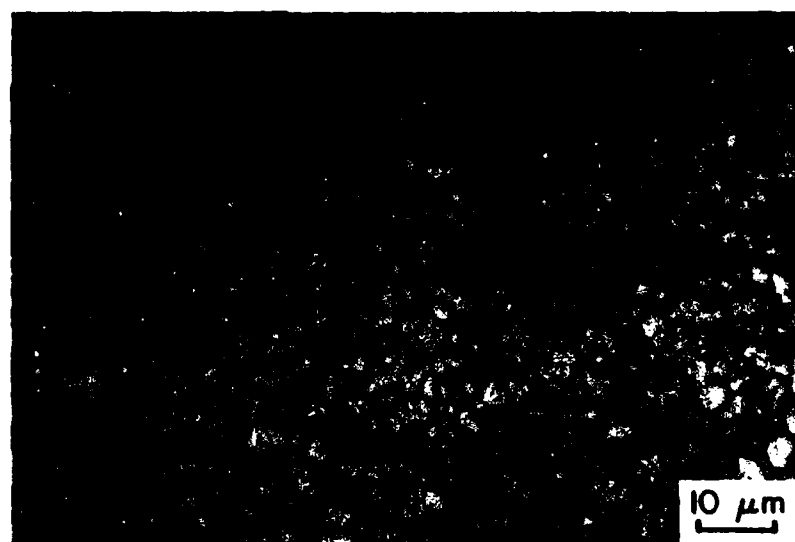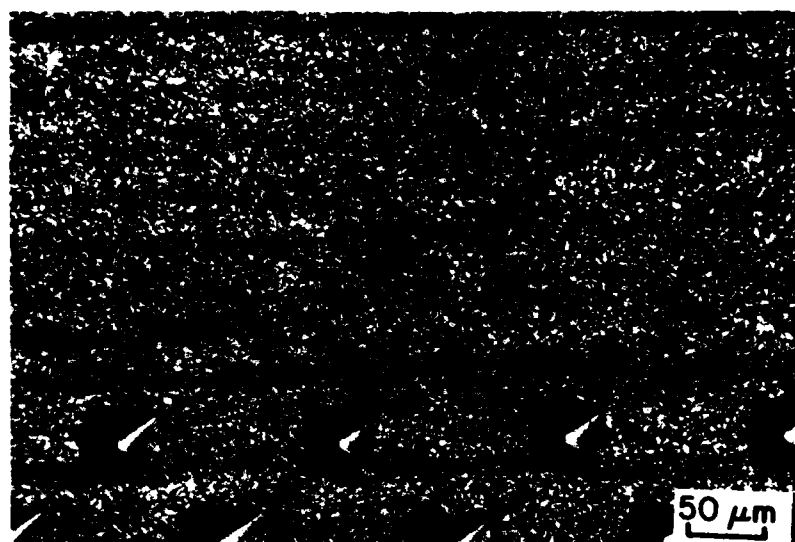
Figure 40.   Light micrograph of the dark etching band in
              the HAZ, composed of extremely fine ferrite,
              pearlite and small patches of martensite.
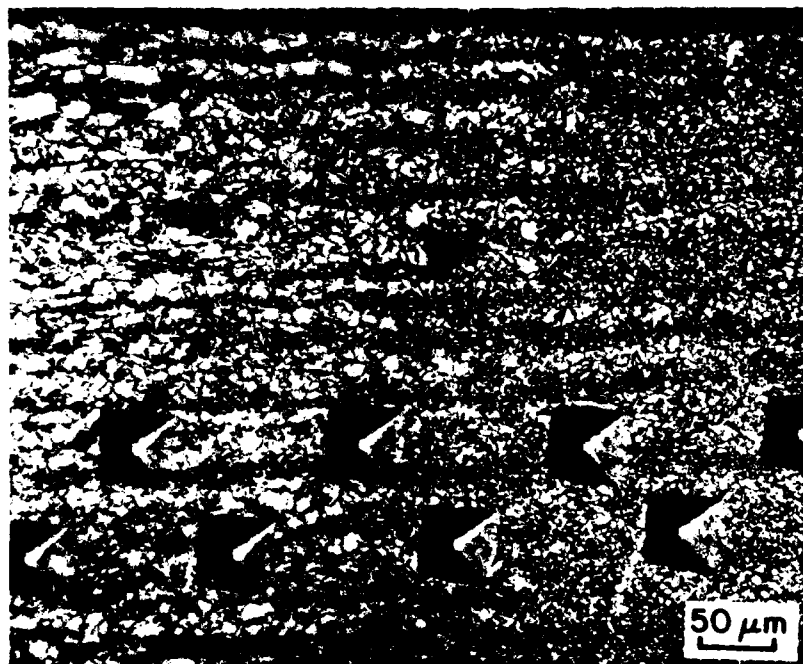
Figure 41.   Light micrograph of diffuse pearlite, banded
             microstructure common in all three heat input
             welds.
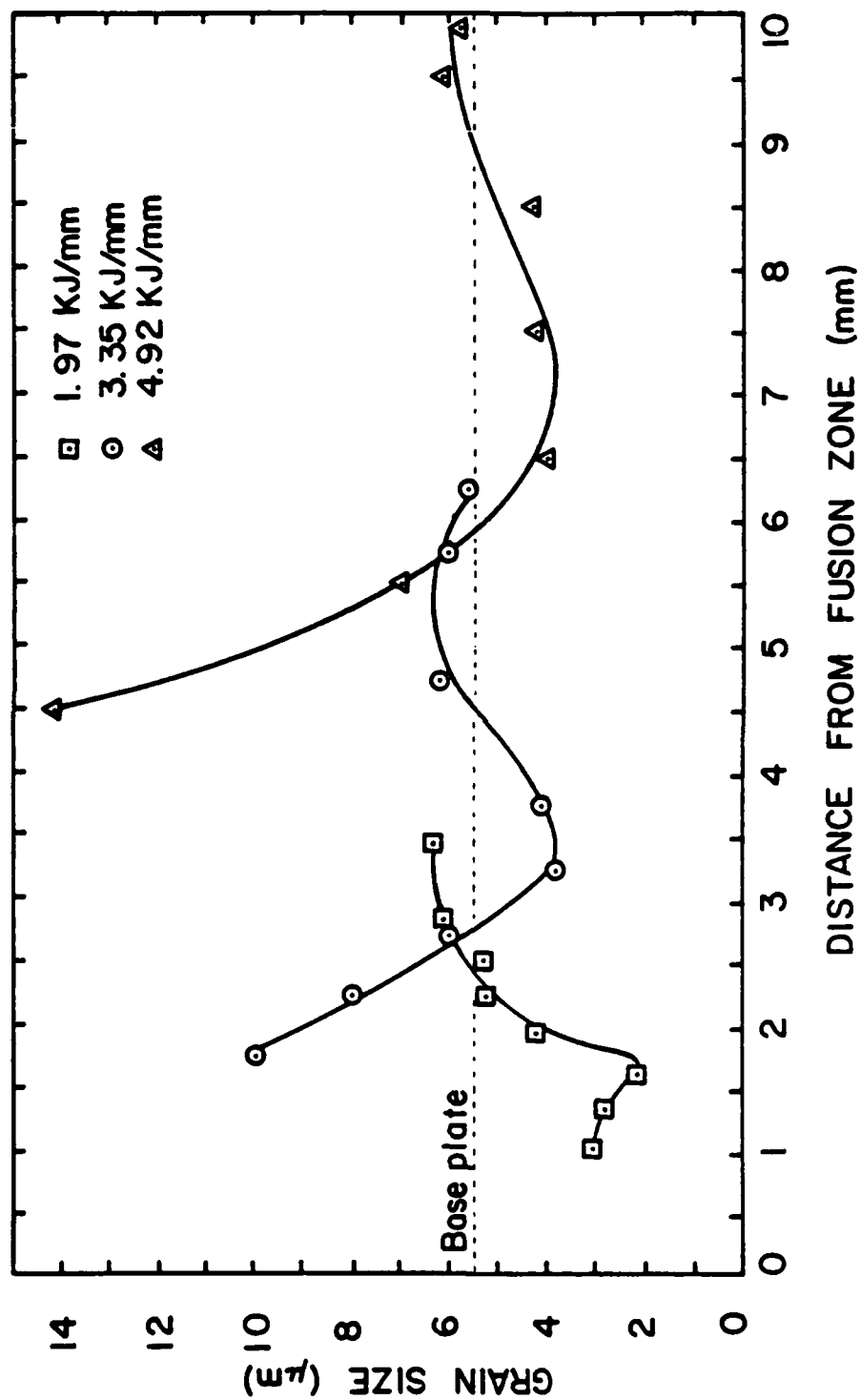
Figure 42. Summary of ferrite grain size in the weld HAZ
as a function of distance from the fusion zone
for various nominal heat inputs.

4.5.3. Microstructural Evolution in Weld HAZ/ Light Microscopy

The high heat input (4.92 KJ/mm) weld HAZ is characterized by many microstructures. The region next to the fusion zone (0.0-mm to 3.5-mm) experiences peak temperatures well into the austenite region. This region exhibits coarse grained austenite characterized by distinct and continuous allotriomorphic ferrite outlining the grain boundaries. The austenite grain size in the near fusion zone ranges from 75μm to 300μm in diameter, Figure 35.

The larger austenite grain sizes and the relatively rapid cooling rates in this region result in the typical transformation product of a Widmanstatten- Bainitic microstructure in the austenite grain interior, Figure 35. The relatively fast cooling rate also results in some suppression of the amount of allotriomorphic ferrite found in this region of the HAZ.

At distances of 3.5-mm to 4.3-mm from the fusion zone, the HAZ remains in the temperature range required for complete austenitization and exhibits a mixed microstructure of pearlite with decreasing amounts of bainite as the distance from the fusion zone increases. Extremely fine pearlite colonies with grain sizes on the order of 25μm to 75μm were observed.

The regions beyond 4.3-mm from the fusion zone, are
heated just above the temperature required for complete
austenitization and exhibit a refined equiaxed austenite
grain structure. The austenite grain size is a minimum
where a maximum temperature in the neighborhood of the
effective upper criticle temperature A_{c3} is realized.
The ferrite grains in this region are on the order of 2µm
to 10µm and are located approximately 5.8-mm from the
fusion zone line, Figure 39.

Beyond the region of refinement and extending outward
from the fusion zone is a region of partial refinement that
is produced by partial austenitization. The regions
richest in carbon exhibit an extremely fine transformation
structure of martensite and pearlite while the lower carbon
content ferritic regions are less affected as the maximum
temperature attained diminishes, Figure 41. The
microstructure as a whole approaches the base-plate
structure of pearlite and ferrite.

The microstructural characteristics at the medium heat
input (3.35 KJ/mm) weld HAZ are slightly different than
those at high heat input. The transformation product can
be regarded as being essentially the same as that at high
heat input, but with slight differences. The HAZ was
narrower and the transformation products finer. The

bainitic transformation product near the fusion zone is associated with large prior austenite grains with allotriomorphic ferrite rims 50μm to 250μm in diameter, Figure 34. The coarse grained austenite of the medium heat input weld is under half the size of the corresponding region in the high heat input weld with a distance approximately 0.0-mm to 1.4mm from the fusion zone.

A bainitic/martensitic structure with allotriomorphic ferrite surrounding prior austenite grains of 20μm to 50μm was observed at a distance of 1.4mm to 2.0mm from the fusion zone.

The austenitic grain refined region consisted of an equiaxed ferrite grain microstructure with a grain size of 1.0μm to 5μm) at a distance of 2.0-mm to 3.8-mm, Figure 38. The refined region tended to have smaller equiaxed grains than observed in the corresponding region of the high heat input welds.

At distances beyond 3.8-mm from the fusion zone a banded microstructure is observed to gradually evolve. The microstructure is composed of martensite/pearlite bands in the partially austenitized regime and is similar to the high heat input microstructure, Figure 41. Finally, the microstructure becomes banded as in the base plate microstructure.

The low heat input welds exhibit a drastic reduction in the overall width of the HAZ as well as for various microstructural regions within the HAZ. In the low heat input weld, the transformation product microstructure of the coarse austenite region is characterized by indistinct, discontinuous allotriomorphic ferrite rims on prior austenite grain boundaries. In fact, in this instance the allotriomophic ferrite microconstituent can be more accurately associated with Widmanstatten side-plates and sawteeth. In addition, more rapid cooling near the fusion zone in comparison to the high and medium heat input, produce an austenite grain interior substantially martensitic in structure for this region, (0.0mm to 0.3mm from the fusion zone). The prior austenite in this grain coarsened region is on the order of 100μm to 175μm, Figure 33. Presumably, the martensitic component of this microstructure is what imparts the higher hardness to this region at 1.97 KJ/mm heat input.

The region next to the grain coarsened region, was also composed of martensite, but with a grain size of 50μm to 100μm in diameter and contained very thin allotriomorphic ferrite at the prior austenite grain boundaries. This region extended from 0.3-mm to 0.75-mm.

The grain refined region contained extremely fine

ferrite grains and small regions of martensite. Ferrite

grain sizes ranged from 0.5μm to 5.0μm in the region

0.75mm to 1.3mm from the fusion zone, Figure 37.

The last region of interest, 2.5mm to 3.3mm from the

fusion zone, exhibited clustering of small ferritic grains

to form a diffuse banded microstructure. Many of the

grains in this region of diffuse banding were 5.0μm and

smaller, Figure 40. As the unaffected metal of the base

plate was approached, pearlitic banding became more

apparent.

4.5.4. Hardness Measurements in Weld HAZ

Hardness measurements were conducted on transverse

sections of the HAZ for welds, typical of the three nominal

heat inputs. Measurements were made along a line extending

from the fusion zone/HAZ interface to the HAZ/base-plate

interface.

Hardness profiles for the three nominal heat-inputs are

depicted in Figure 43, 44, 45.

A hardness maximum was observed in the vicinity of the

fusion zone boundary for all three heat inputs. The

hardness associated with this maximum is significantly

greater for the 1.97 KJ/mm heat input, Figure 43 than for
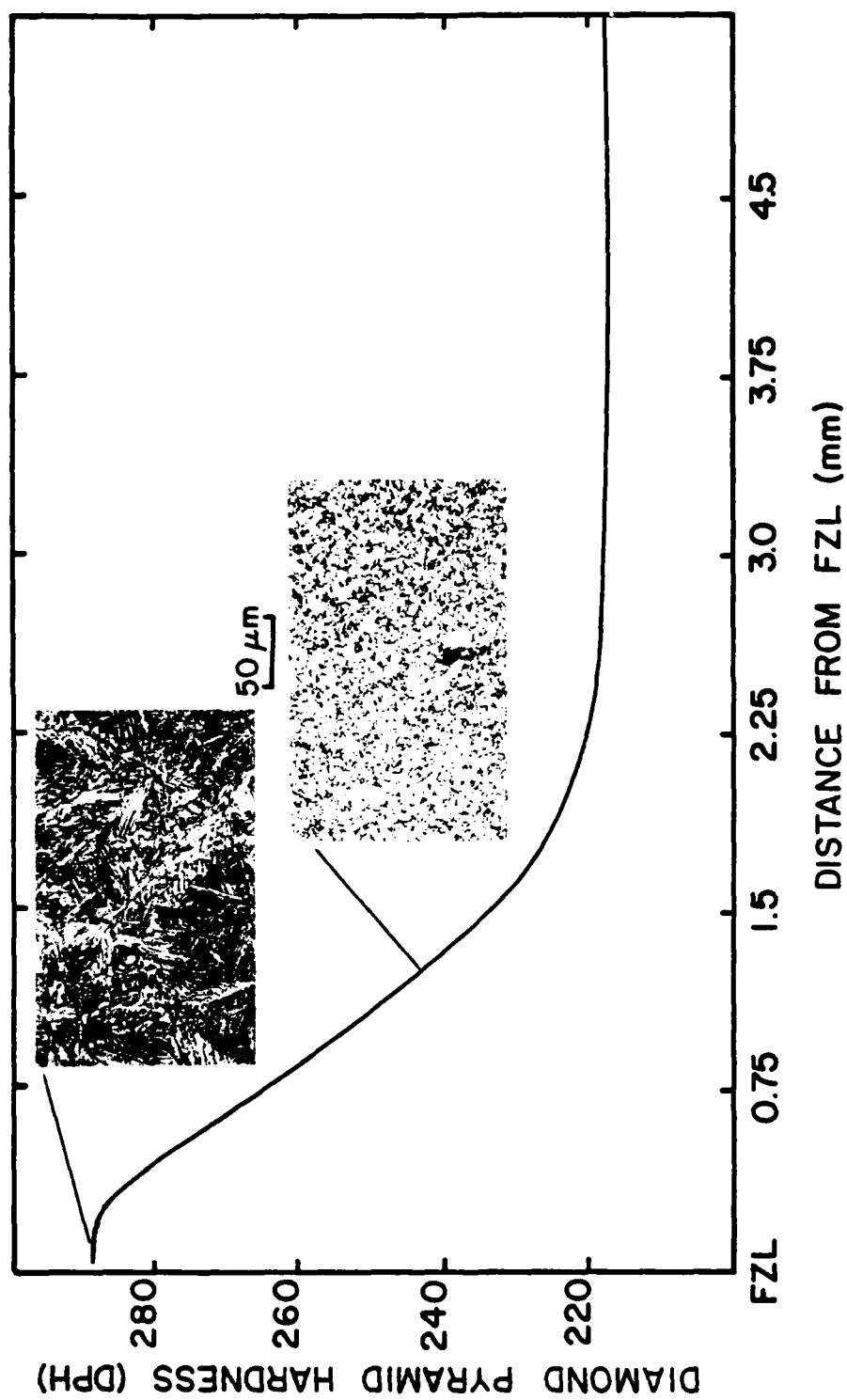
Figure 43. Diamond pyramid hardness as a function of distance from the fusion zone boundry in the HAZ for a nominal heat input of 1.97 KJ/mm.
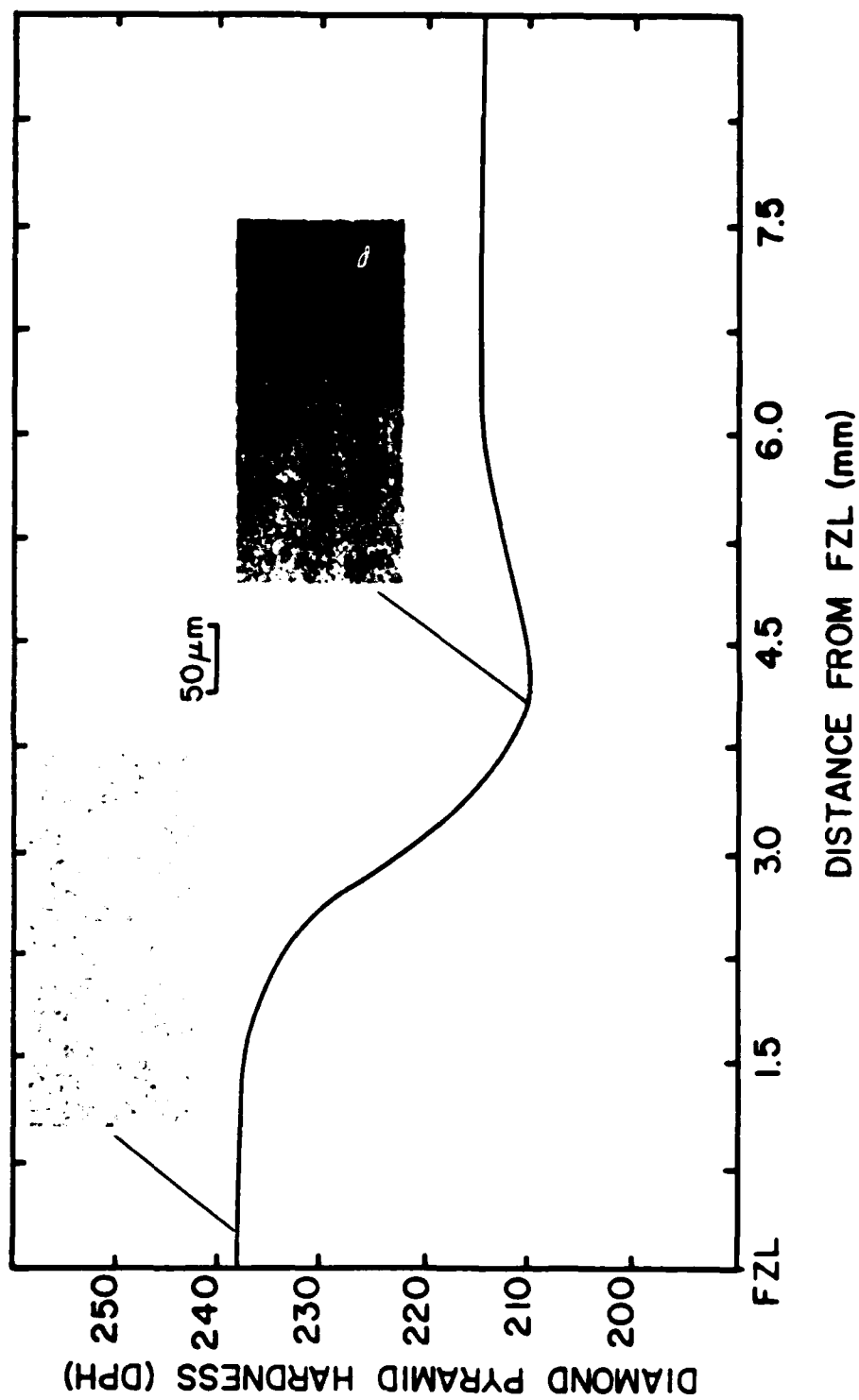
Figure 44. Diamond pyramid hardness as a function of
distance from the fusion zone boundry in the
HAZ for a nominal heat input of 3.35 KJ/mm.
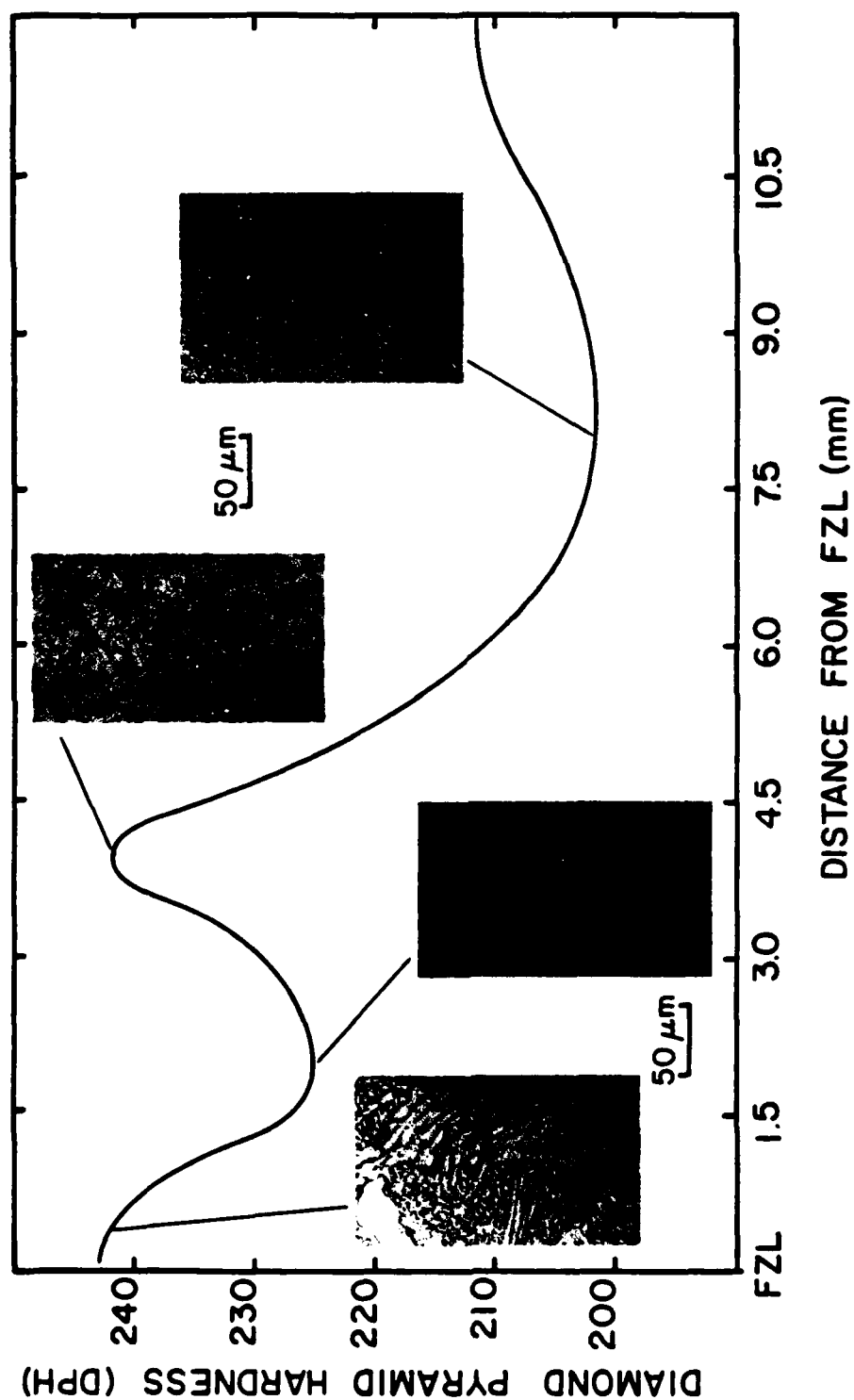
Figure 45. Diamond pyramid hardness as a function of
distance from the fusion zone boundry in the
HAZ for a nominal heat input of 4.92 KJ/mm.

either the 3.35 KJ/mm heat input, Figure 44 or 4.92 KJ/mm

heat input, Figure 45 (~290 DPH vs. ~240 DPH).

At 1.97 KJ/mm and 3.35 KJ/mm the hardness decreases

continuously with distance from the fusion zone boundary.

For 1.97 KJ/mm heat input a continuous decrease in hardness

to that of the base-plate occurs whereas a shallow minimum

in hardness occurs for the 3.35 KJ/mm weld in the vicinity

of 4mm from the fusion zone boundary.

The 4.92 KJ/mm. weld is distinctive in that after the

initial hardness decrease from the near fusion zone maximum

there is an increase hardness to a second maximum in the

vicinity of 4-mm from the fusion zone boundary. The

microstructure associated with the second hardness maximum

is similar to that described previously for this location.

Recall that the location 4-mm from the fusion zone boundry

in this weld represents a polygonal ferrite/pearlite

microstructure and is associated with a different thermal

history .

4.5.5. Charpy Impact Toughness in Weld HAZ

Charpy impact data was derived from two sources.

Specimens of actual weld HAZ's, and specimens of simulated

HAZ's were tested. The latter corresponded to selected

positions in the HAZ.

Results of Charpy V-notch impact energy tests on actual weld and simulation HAZ specimens for various position/heat input combinations in the HAZ are depicted in Figures 46, 47, 48.

The microstructures and thermal cycles that correspond to simulation impact energy transition curves of Figure 46 are displayed in Appendix 2.

The impact energy versus impact temperature data for actual welds exhibited significant scatter. To determine potential sources of this variability, charpy specimens were sectioned normal to the fracture surface and parallel to the direction of crack propagation. In this way the crack profile could be observed to determine the microstructure of the HAZ through which fracture occurred.

These observations indicated that actual weld impact toughness data was derived from several microstructures at a given heat input. Therefore, variations in toughness were due to variation in microstructure as well as variation in impact temperature.

The impact specimens for the high heat input welds have microstructures that are characteristic of two approximate positions (0.0--2.5mm and 2.5--3.5mm) in the HAZ. The microstructure and the transition curve for these positions
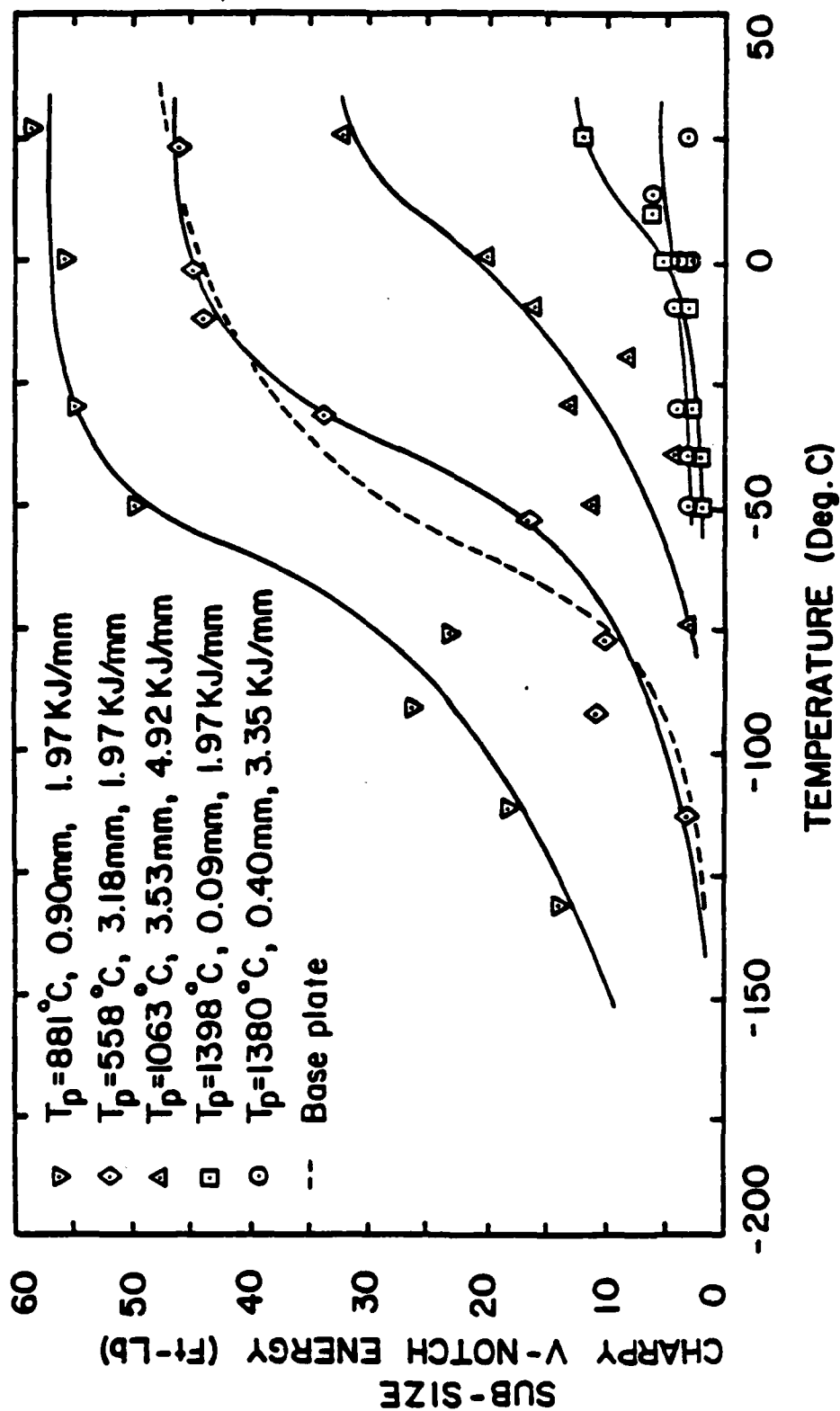
Figure 46.   Summary plot of charpy impact energy for
             sub-size specimens as a function of temperature
             for various simulated HAZ thermal cycles.
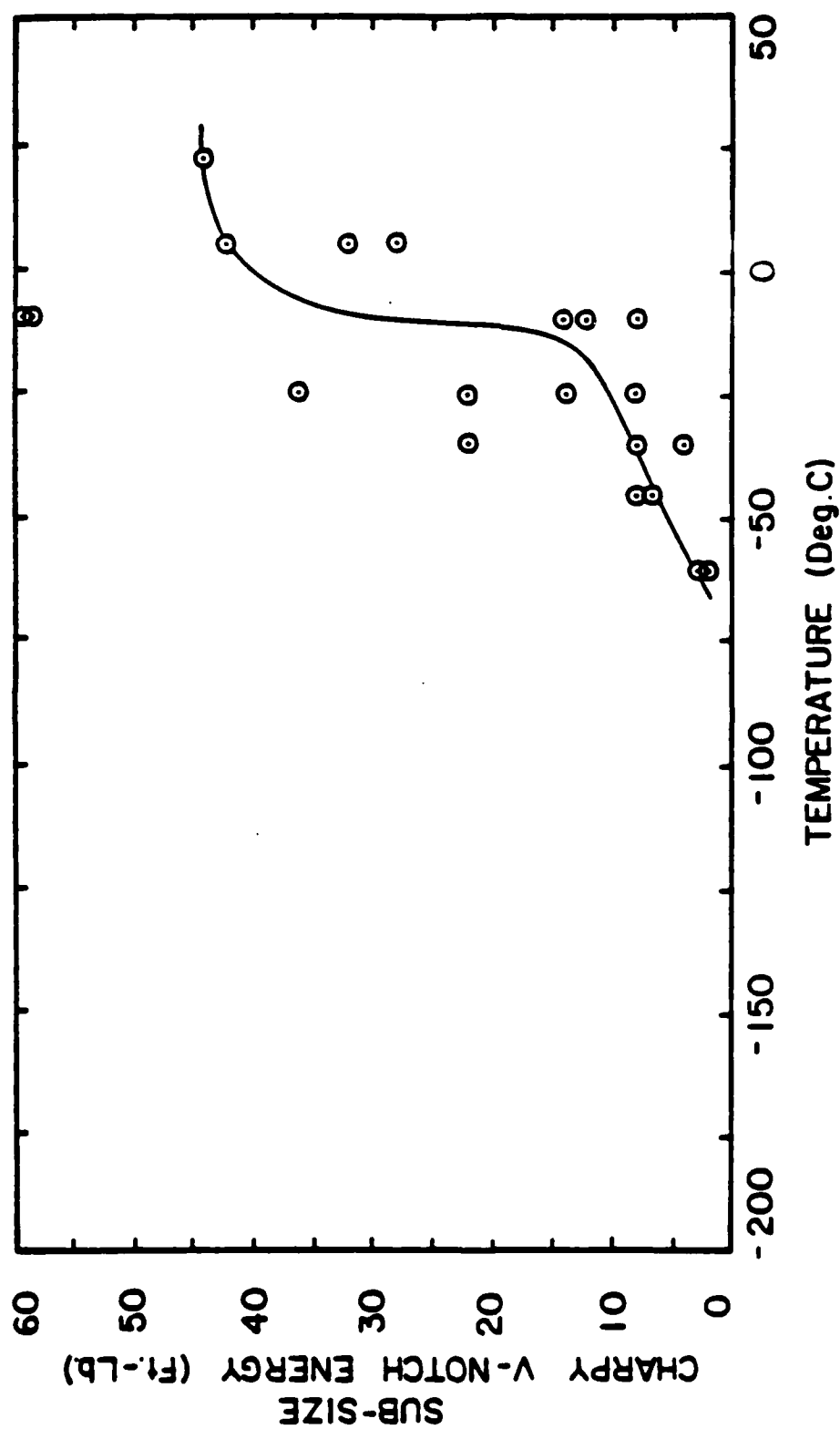
Figure 47. Summary plot of charpy impact energy for sub-size specimens as a function of temperature composed of a nominal heat input of 3.35 KJ/mm with variations in notch location within actual weld HAZ.
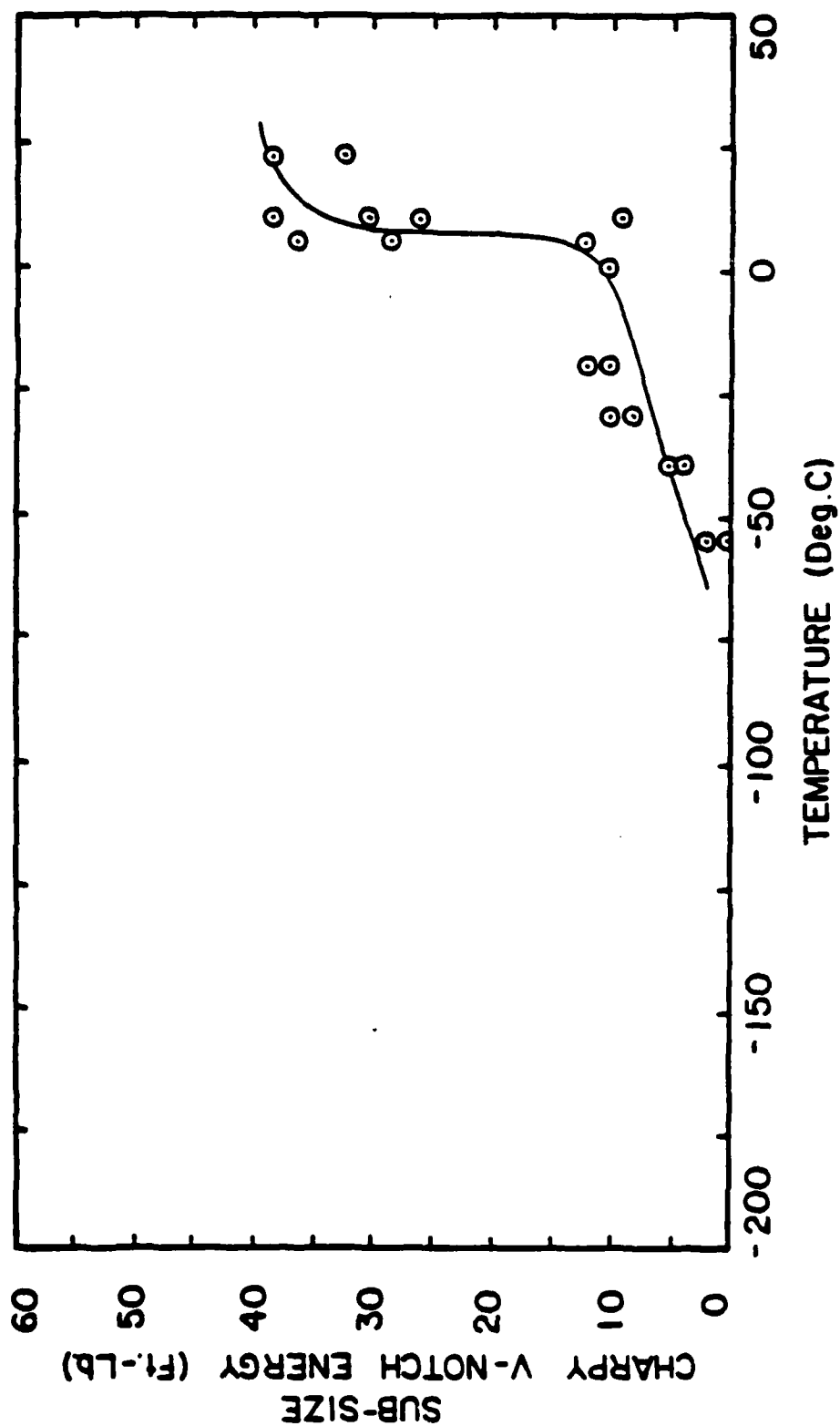
Figure 48.   Summary plot of charpy impact energy for
              sub-size specimens as a function of temperature
              composed of a nominal heat input of 4.92 KJ/mm
              with variations in notch location within actual
              weld HAZ.

is shown in figures 49 and 50. A bainitic microstructure
was associated with the region next to the fusion zone and
a ferrite/pearlite microstructure in the region removed
from the fusion zone.

The medium heat input impact specimens can be
associated with three positions (0.0--1.4mm; 1.4--2.0mm;
2.0--3.0mm) in the HAZ. Three impact transition curves
with corresponding micrographs are shown in figure 51, 52,
and 53. The microstructures for these locations are
bainitic, bainitic/martensitic/pearlitic, and
ferritic/pearlitic, respectively.

If the actual weld data is separated according to
microstructure, some of the scatter can be removed and data
from actual welds for a given microstructure can be coupled
with simulation data for that microstructure. In addition,
HAZ impact results from actual weld and simulation
specimens have been plotted together for a constant
microstructure and are compared directly in Appendix 3.

Plots of upper shelf impact energy and impact
transition temperature as a function of position in the HAZ
are depicted in figures 54 and 55 and include simulation
and actual weld data. Summary data for these curves have
been tabulated in Tables 11 and 12.

Generally speaking, the transition temperatures for all
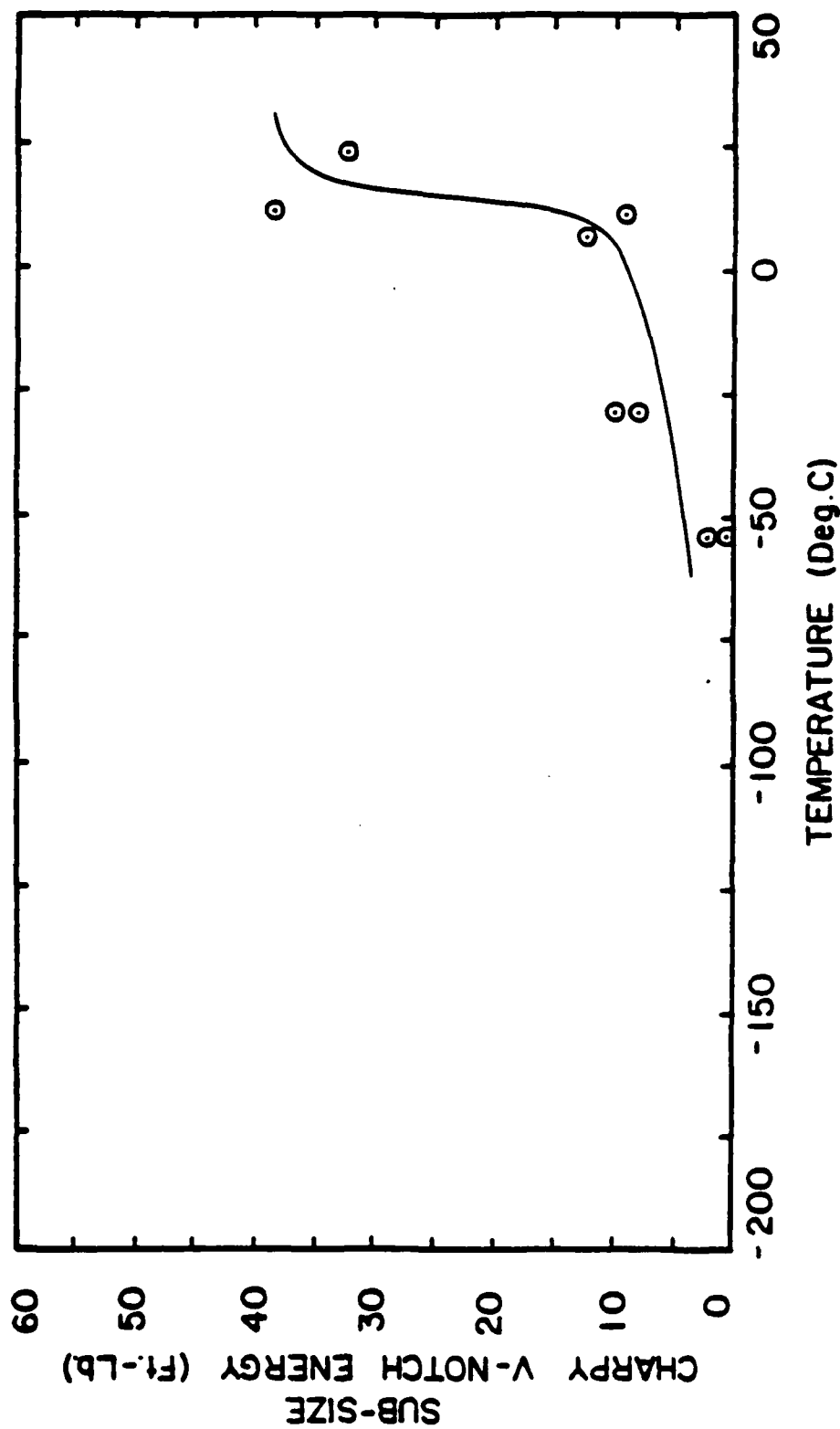
Figure 49. Charpy impact energy for sub-size specimens as
a function of temperature for the nominal heat
input of 4.92 KJ/mm for the location of
D_{FZL}= 0.0-2.5mm in actual weld HAZ.
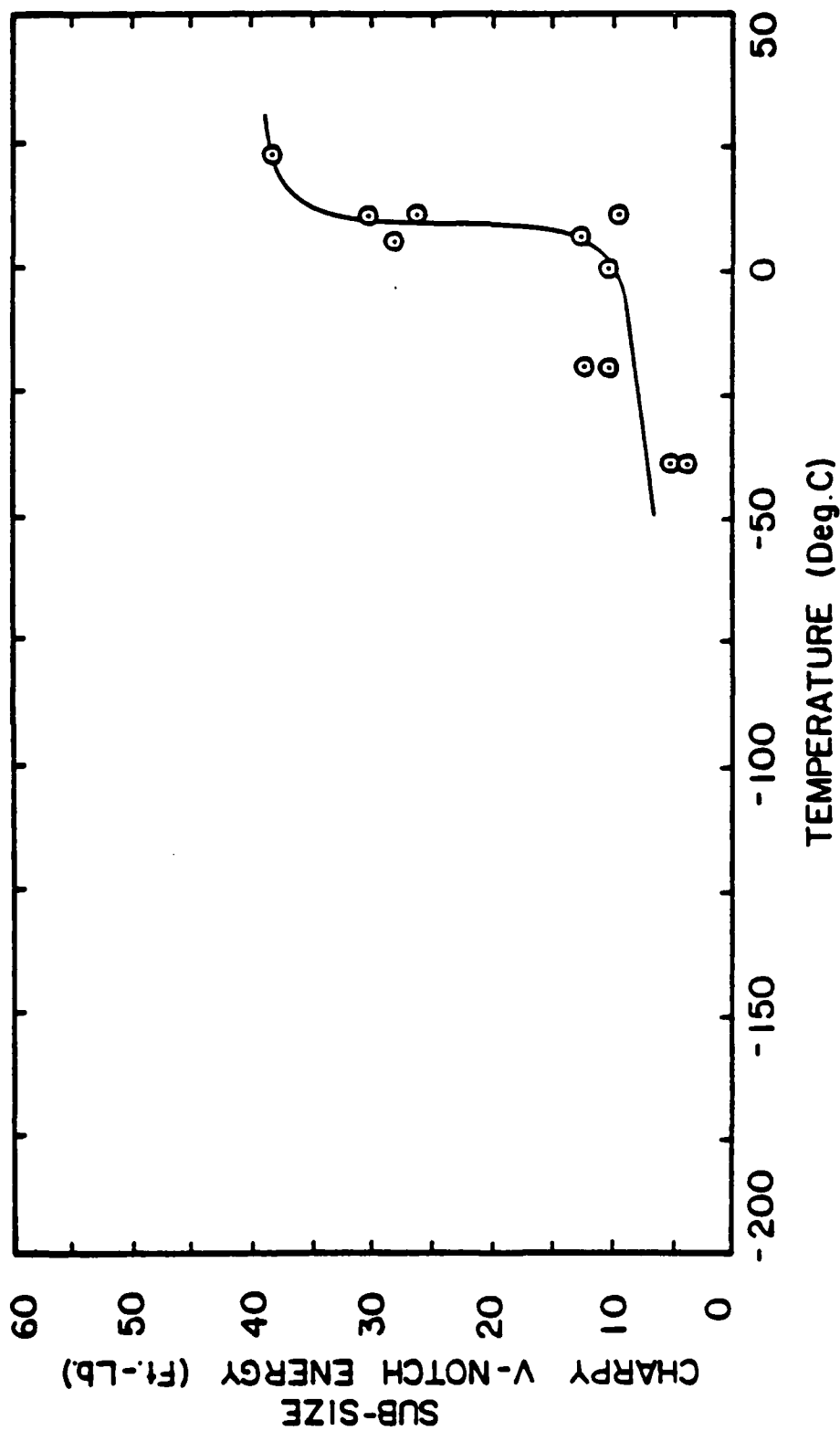
Figure 50. Charpy impact energy for sub-size specimens as a function of temperature for the nominal heat input of 4.92 KJ/mm for the location of D_{FZL} = 2.5-3.5mm in actual weld HAZ.
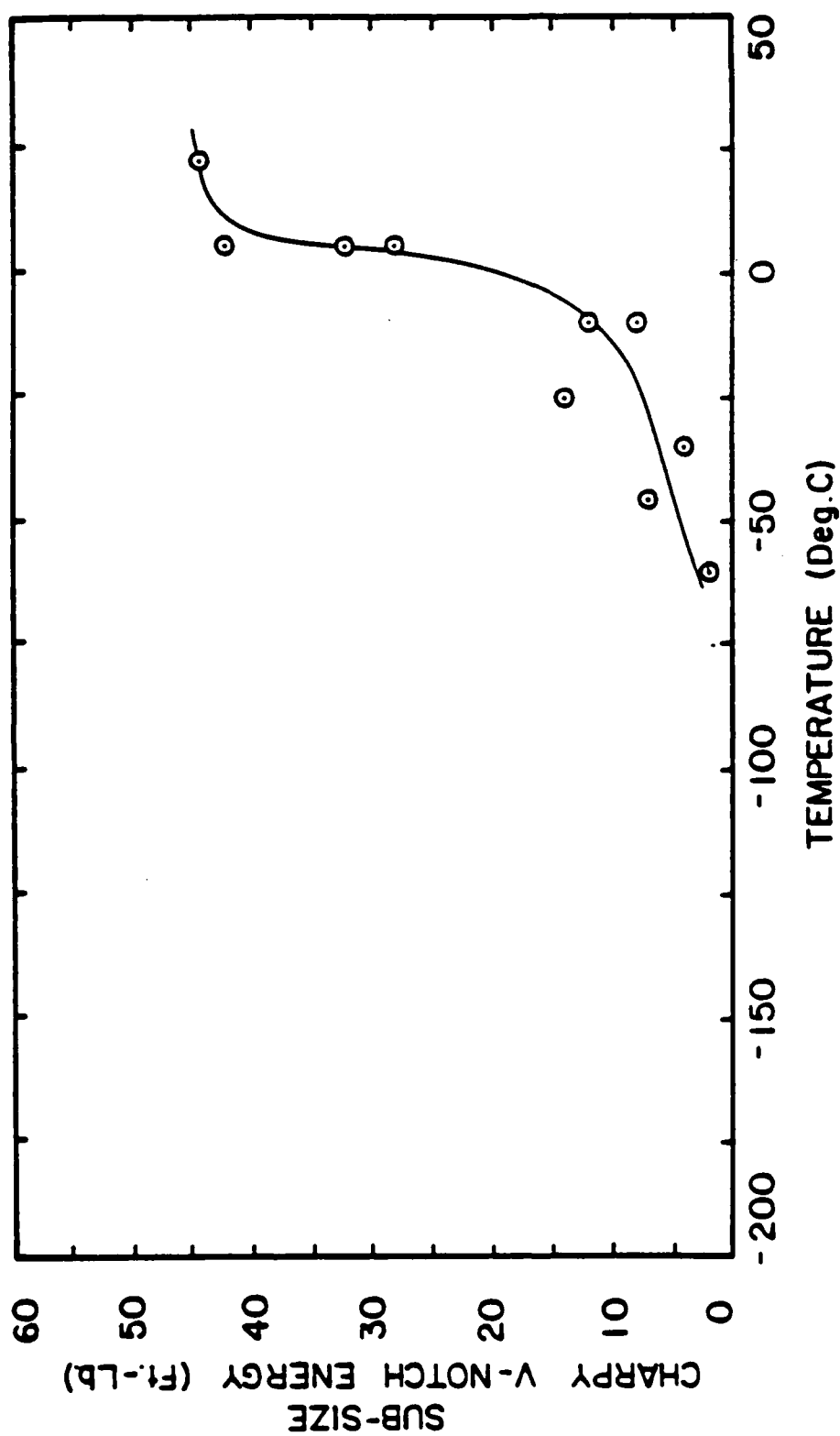
Figure 51.   Charpy impact energy for sub-size specimens as a function of temperature for the nominal heat input of 3.35 KJ/mm for the location of D_{FZL} = 0.0-1.4mm in actual weld HAZ.
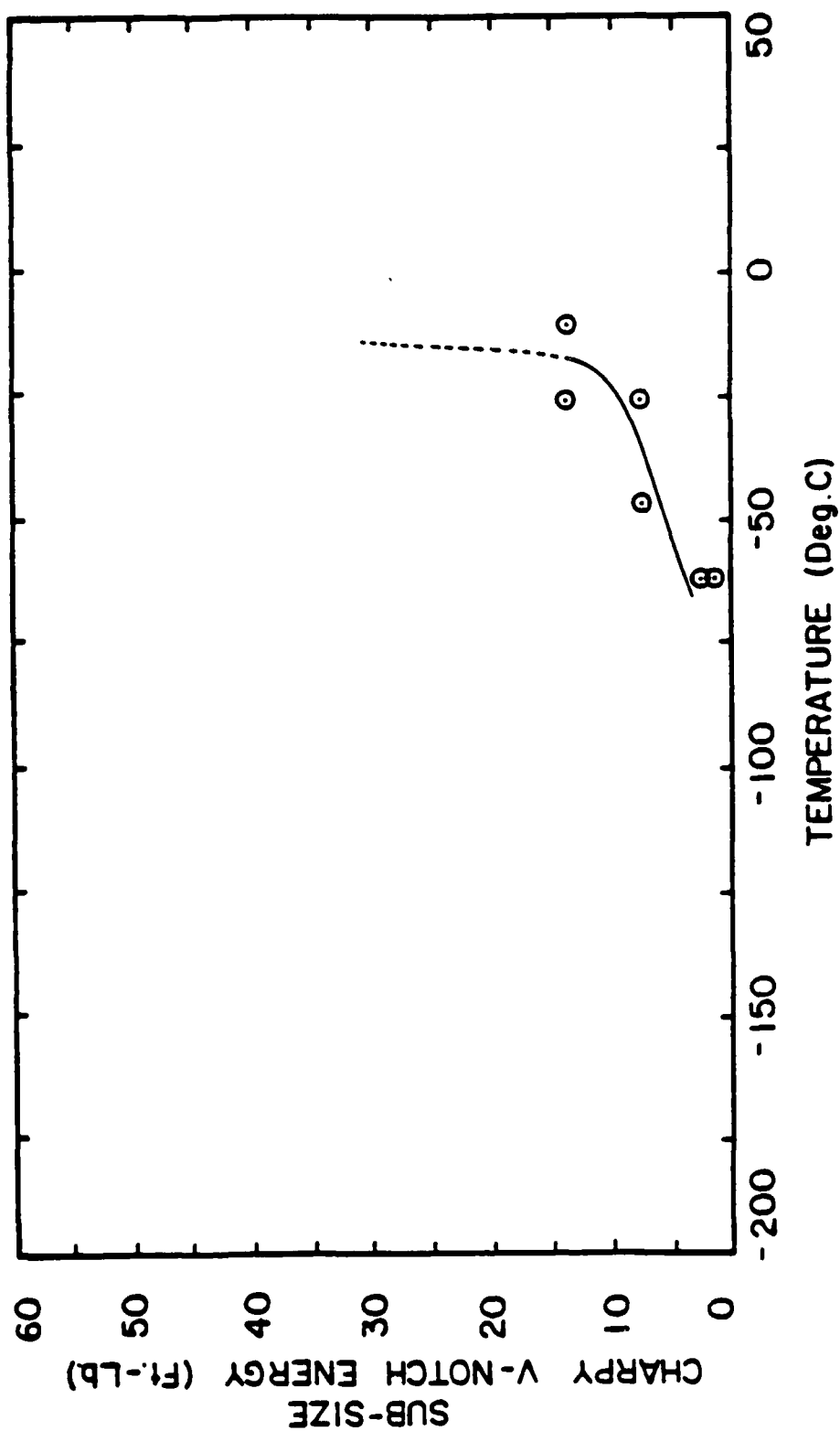
Figure 52. Charpy impact energy for sub-size specimens as
            a function of temperature for the nominal heat
            input of 3.35 KJ/mm for the location of
            D_{FZL}= 1.4-2.0mm in actual weld HAZ.
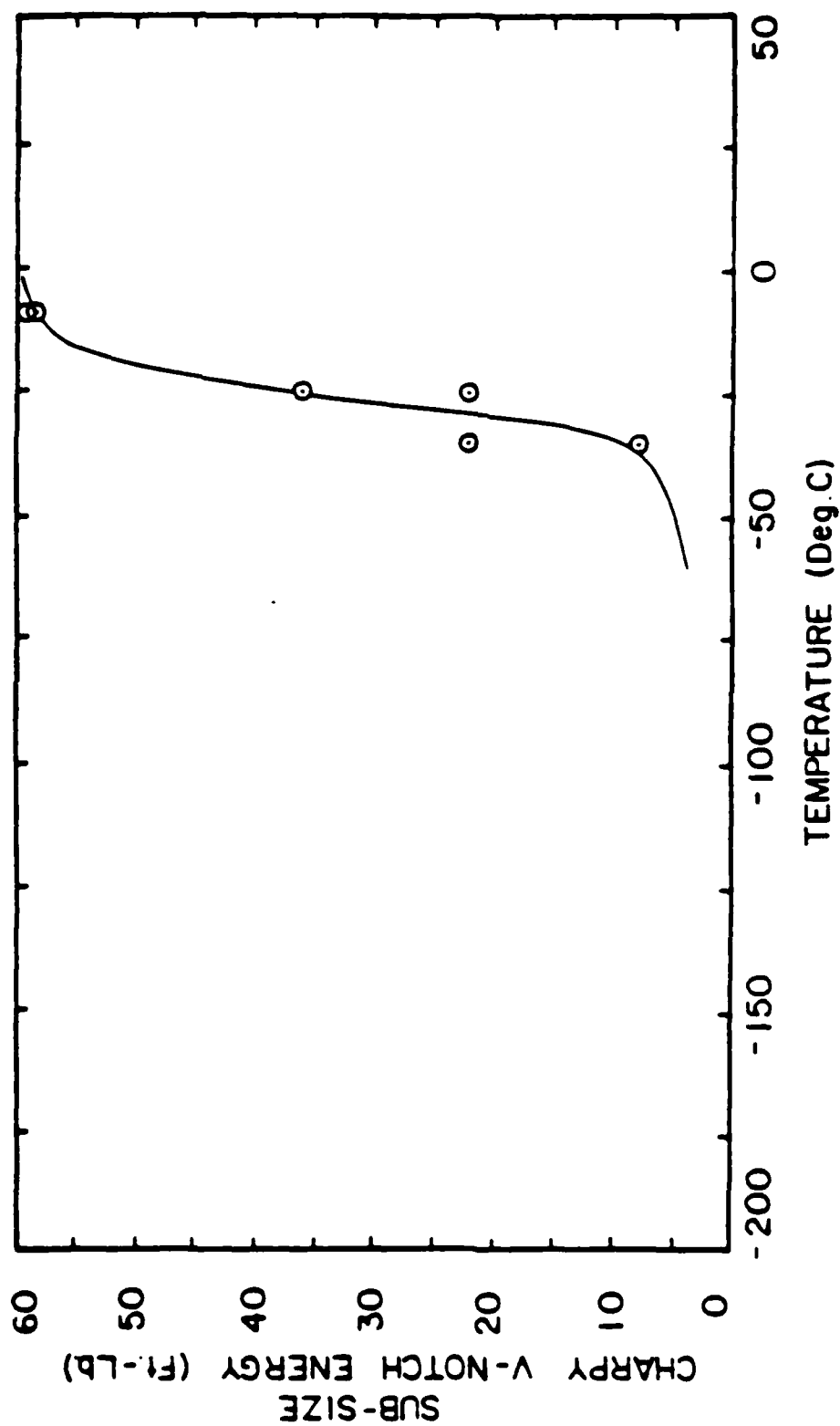
Figure 53. Charpy impact energy for sub-size specimens as
a function of temperature for the nominal heat
input of 3.35 KJ/mm for the location of
D_{FZL}= 2.0-3.0mm in actual weld HAZ.
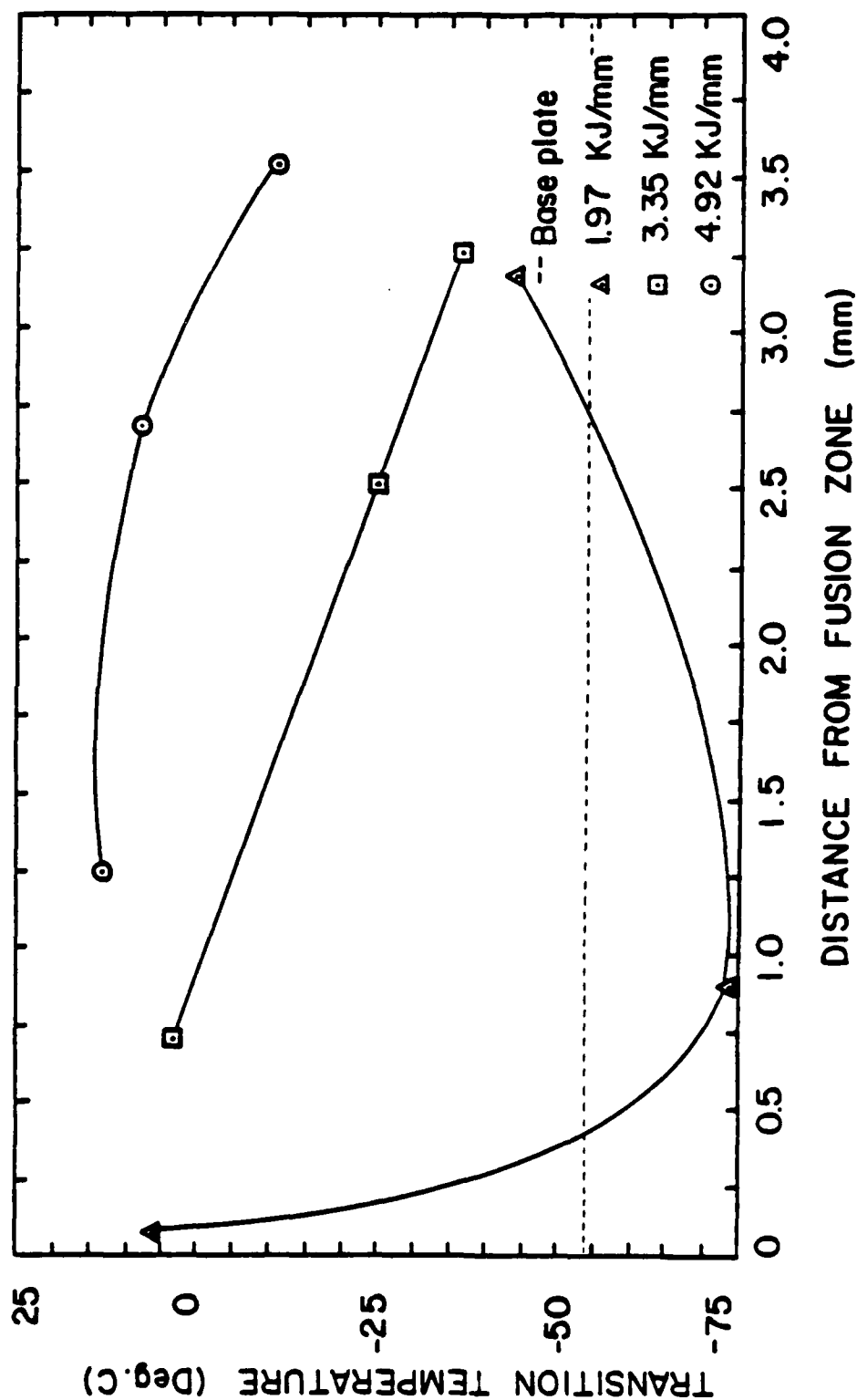
Figure 54. Summary of transition temperature for subsize charpy specimens as a function of distance from the fusion zone boundary for various nominal heat inputs of both experimental and simulated HAZ specimens.

DISTANCE FROM FUSION ZONE (mm)

UPPER-SHELF IMPACT ENERGY (Ft-Lb.)

-- Base plate
▲ 1.97 KJ/mm
▣ 3.35 KJ/mm
⊙ 4.92 KJ/mm
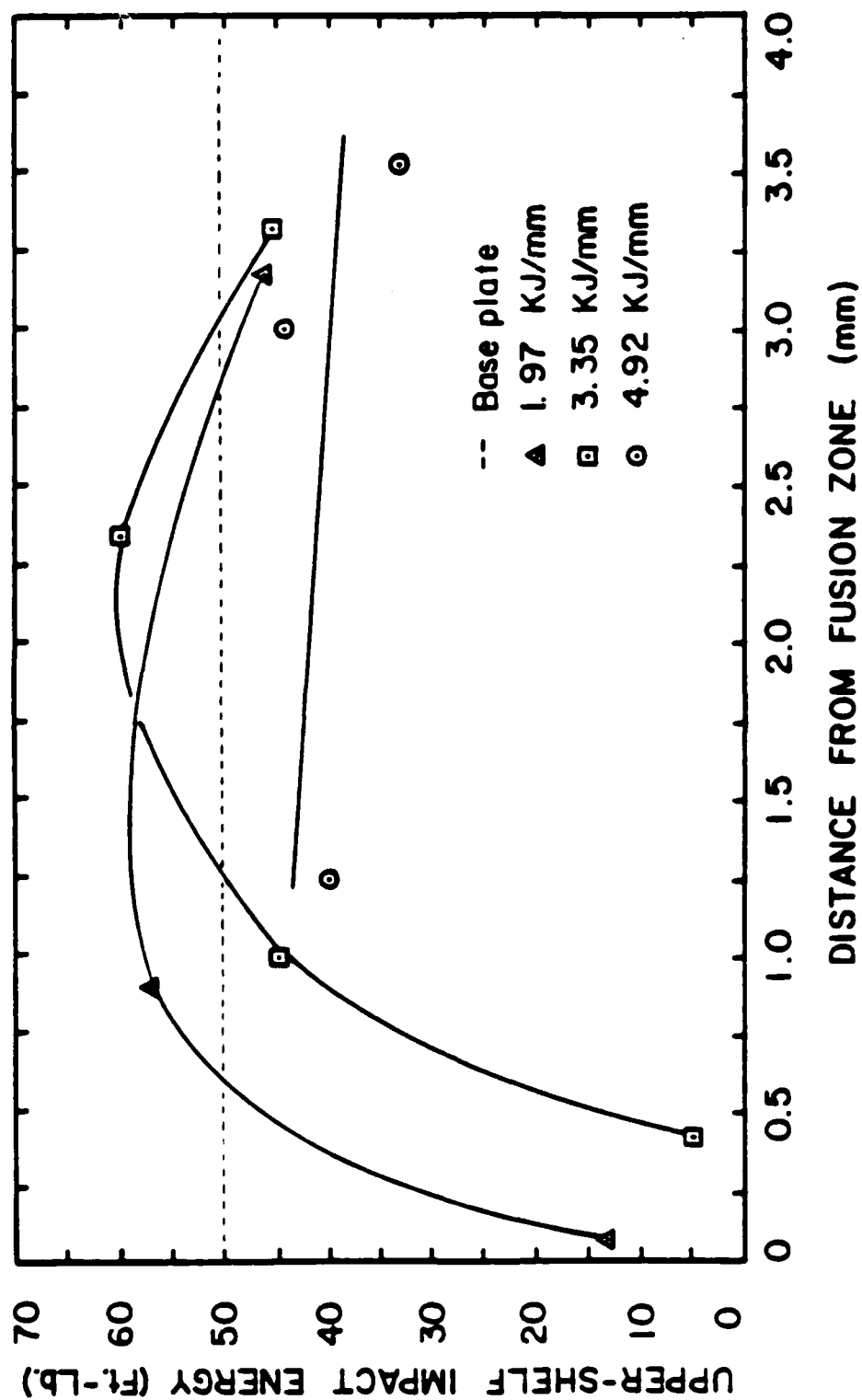
Figure 55.   Summary of upper shelf impact energy for
             subsize charpy specimens as a function of
             distance from the fusion zone boundary for
             various nominal heat inputs of both
             experimental and simulated HAZ specimens.

Table 11

Charpy Impact Results for Actual Weld HAZ Specimens

Distance From FZL (mm)	*Impact Transition Temperature (deg.C)	Absorbed Energy 0 deg.C (ft.-lb)	Upper Shelf Impact Energy (ft.-lb)
Nominal Heat Input---3.35 KJ/mm			
0.0--1.4	+1	20	45
1.4--2.0	-15**	--	--
2.0--3.0	-25	60	60+
Nominal Heat Input---4.92 KJ/mm			
0.0--2.5	+15	9	38
2.5--3.5	+10	11	43

* Transition Temperature at 50% maximum impact energy at the highest temperature (25 deg.C)

** Approximation, due to incomplete data curve

Table 12

Charpy Impact Results for Simulated Specimens

Peak Temperature (deg.C)	Distance From FZL (mm)	*Impact Transition Temperature (deg.C)	Absorbed Energy 0 deg.C (ft.-lb)	Upper Shelf Impact Energy (ft.-lb)
Nominal Heat Input---1.97 KJ/mm				
1398	0.09	+6	4	13
881	0.9	-75	56	58
558	3.18	-44	45	48
Nominal Heat Input---3.35 KJ/mm				
1380	0.4	N/A	3	5
Nominal Heat Input---4.92 KJ/mm				
1063	3.53	-11	20	33
Base-plate as-recieved		-54	43	50

* Transition Temperature at 50% maximum impact energy at the highest temperature (25 deg.C)

N/A---Not Applicatible

positions in the HAZ increase as the heat input increases.
Figure 54 also indicates that transition temperature
increases as the fusion zone is approached. In addition,
the transition temperature data for all heat-inputs appear
to approach the same value of approximately 5 deg.C at the
fusion boundary. Also, as would be expected, the data
approach the value of the base-plate with increasing
distance from the fusion zone. However, the variation of
transition temperature for the lowest heat input exhibits a
minimum at approximately 1mm from the fusion zone. No
minima in the transition temperature exists for the higher
heat inputs in this range of data.

There is generally less variation in upper shelf energy
with heat input, Figure 55. At a given heat input, the
upper shelf energy exhibits a maximum. This maximum is
located at increasing distance from the fusion zone with
increasing heat input. Overall, the upper shelf energy
increases with decreasing heat input.

The fracture surfaces of actual weld HAZ and simulated
HAZ specimens can be characterized by the same basic
morphology types through the unifying factor of
microstructure as a function of heat input and position in
the HAZ. Knowledge of this allows correlations to be made
between fracture surface morphology, microstructure

associated with fracture and charpy V-notch toughness as a
function of impact temperature.

Three microstructures were identified for correlation
with toughness results. These microstructures are coarse
bainite and martensite that are located in the near fusion
zone region of the HAZ, and fine ferrite located in the
grain refined region of the HAZ.

Characterization of fracture morphology was
accomplished for lower shelf, transition and upper shelf
impact temperature regimes when applicable. The fracture
surfaces of lower shelf specimens were characterized at a
test temperature from -75 deg.C to -50 deg.C and those of
upper shelf specimens, at room temperature (+25 deg.C).

The fracture surface of the bainitic microstructure at
-50 deg.C possessed no apparent fibrous initiation zone but
was characterized by a fairly flat surface composed of
facets, Figure 56(a). Higher magnification observations
indicated a cleavage micro-fracture morphology with large
cleavage facets approximately 100μm to 200μm in
diameter, Figure 56(b). Striations approximately 10μm in
width were observed on the large facets and a small amount
of ductility assocaited with microvoid coalescence was
detected on tear ridges between the large facets,
Figure 56(b).
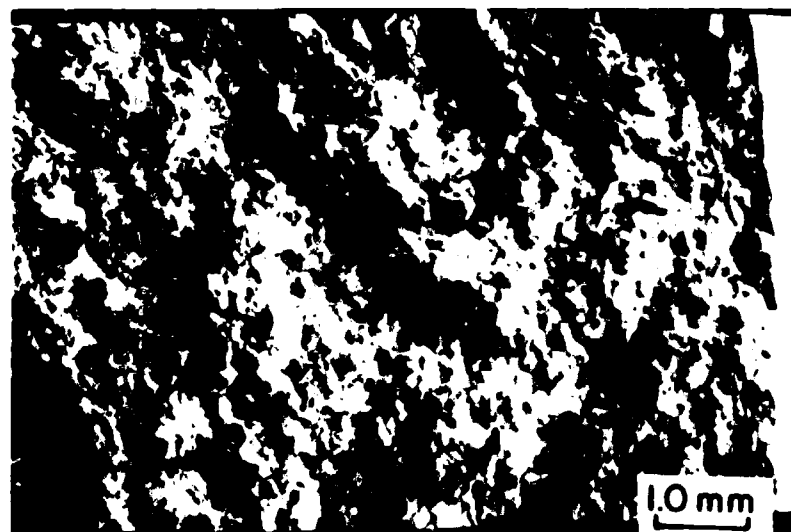
(a)
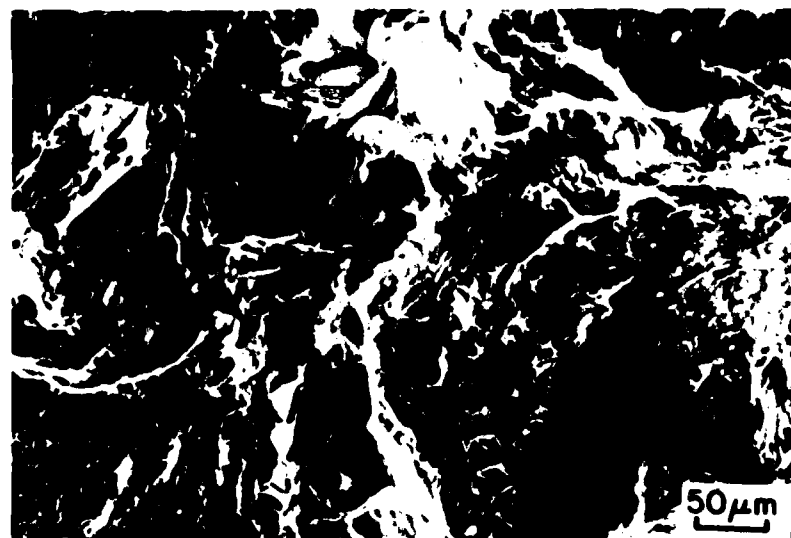
(b)

Figure 56.   Scanning electron micrographs of sub-size
              charpy impact specimens; Temp = -50 deg.C
              Bainitic microstructure.
              (a) Topographic macrograph of specimen
              (b) Cleavage facet morphology

Micro-crack profiles were observed to be translathwith respect to the bainitic packets. Small deviations in crack direction occured at packet boundaries and allotriomorophic ferrite along prior austenite boundaries, Figure 57. Little or no deviations were observed within bainitic packets.

A rise in temperature to 25 deg.C did not produce an upper impact energy shelf or any significant changes in fracture morphology. A slight increase in impact energy was produced due to small increases in the amount of microvoid coalescence. Also, some shear lips were observed along the sides of the specimens, Figure 58.

Macro-features of the martensitic fracture at -50 deg.C were similar to bainitic fracture characteristics. The surface profile was essentially flat with no fibrous initiation zone, Figure 59(a). Fracture was cleavage with cleavage facets approximately 100μm in diameter. Microvoid coalescence was present in addition to secondary cracking, Figure 59(b). Finer striations, 5μm to 10μm wide, were observed on the facets.

Crack propagation was through martensitic packets with major changes in propagation direction occuring at martensitic packet boundaries and allotriomorphic ferrite at prior austenite boundaries. Smaller changes in crack

Figure 57.   Light micrographs of sub-size charpy impact
              specimens; Temp = -50 deg.C, Bainitic
              microstructure.
              (a) Profile macrograph of specimen
              (b) Transgranular crack profile through
                  Bainitic microstructure
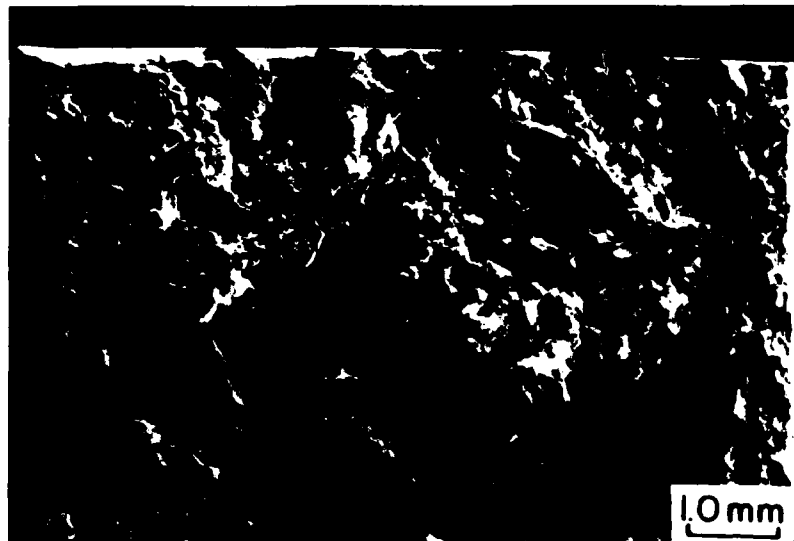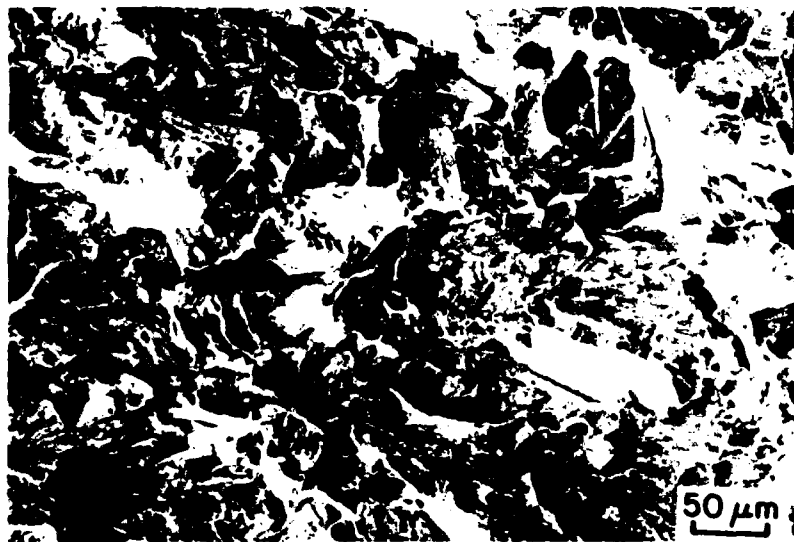
Figure 58.   Scanning electron micrographs of sub-size
             charpy impact specimens; Temp = +25 deg.C
             Bainitic microstructure.
             (a) Topographic macrograph of specimen
             (b) Cleavage facet morphology with small amount
                 of microvoid coalescence.

(a)

1.0 mm

(b)

50 μm
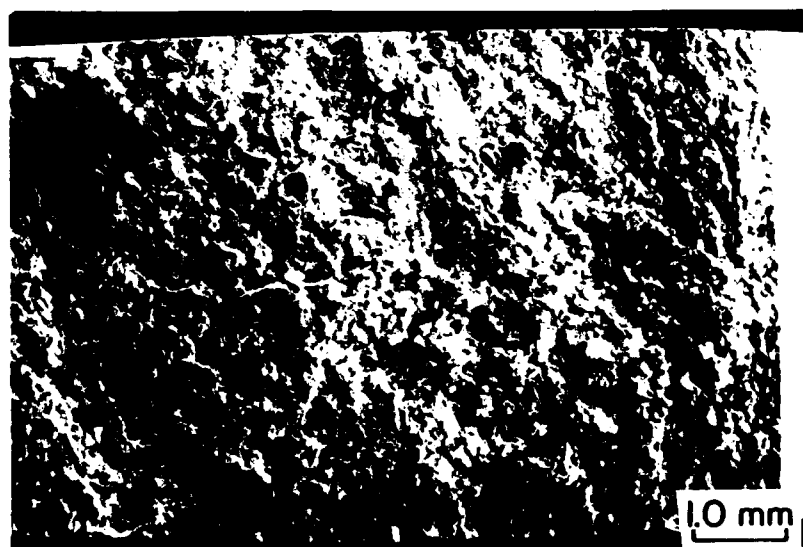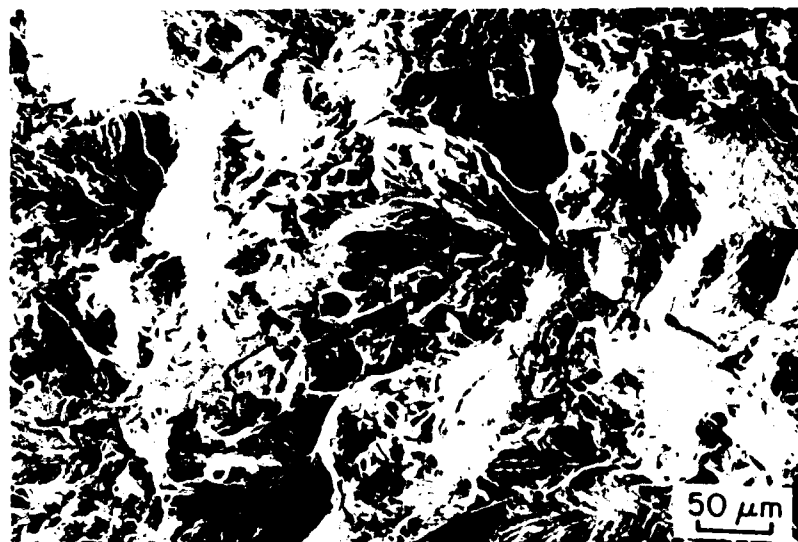
Figure 59.   Scanning electron micrographs of sub-size
charpy impact specimens; Temp = -50 deg.C
Martensitic microstructure.
(a) Topographic macrograph of specimen
(b) Cleavage facet morphology with secondary
cracking.

direction were observed at the laths within each packet, Figure 60.

As observed in the bainitic specimens, no significant changes in fracture morphology were produced with an increase in temperature to 25 deg.C. Although the start of the impact transition temperature was observed, the overall fracture surface morphology is not very different than the -50 deg.C specimen, however, tear ridges with associated microvoid coalescence occur in greater number, Figure 61.

The fine ferritic microstructural fracture appearence at a temperature of -75 deg.C is quite different from the appearence of the banitic and martensitic fractures presented previously. A macrograph is shown in Figure 62(a).

Ductile shear lips can be observed along the sides of the specimen and a "thumbnail" fibrous crack initiation zone observed at the notch root. A ductile hinge is located at the back of the specimen. Both the thumbnail region and hinge region are characterized by a microvoid coalescence fracture morphology. The area between these two regions is characterized by regions of small cleavage facets with large areas of ductile tear ridges, Figure 62(b). The cleavage facets are approximately 5μm in diameter, Figure 62(c).
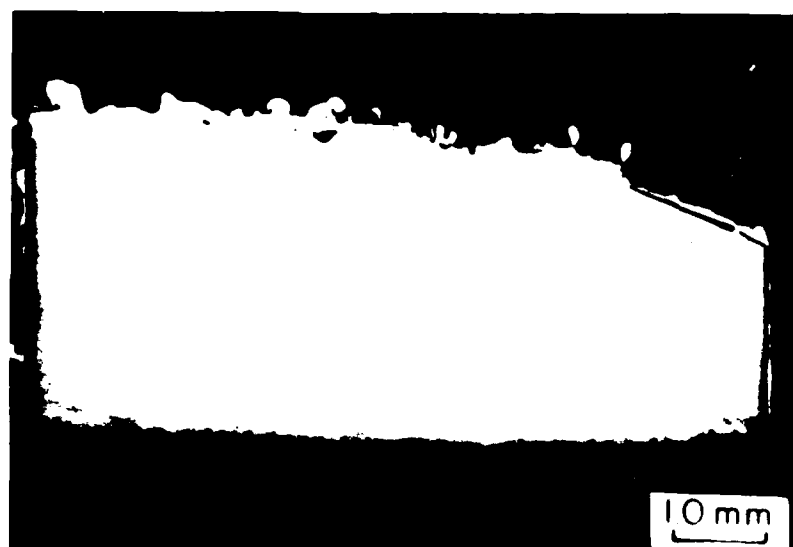
Figure 60.   Light micrographs of sub-size charpy impact
             specimens; Temp = -50 deg.C.
             Bainitic/Martensitic microstructure.
             (a) Profile macrograph of specimen
             (b) Crack tip profile through
                 Bainitic/Martensitic microstructure
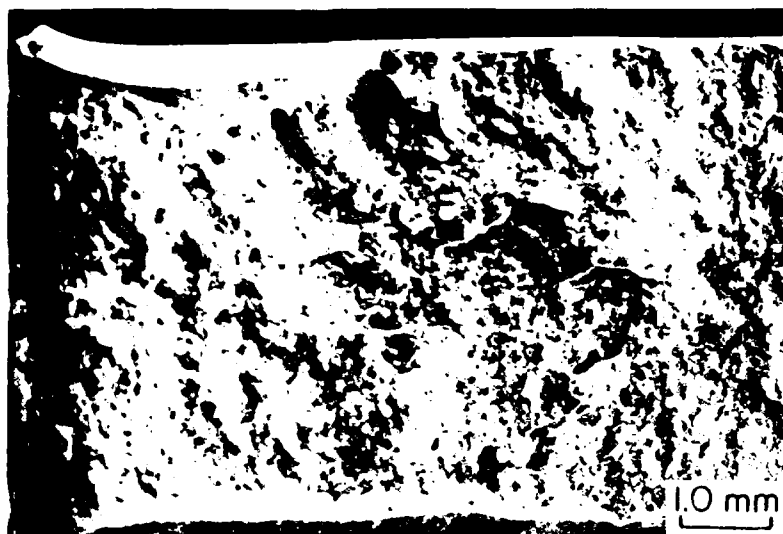
(a)
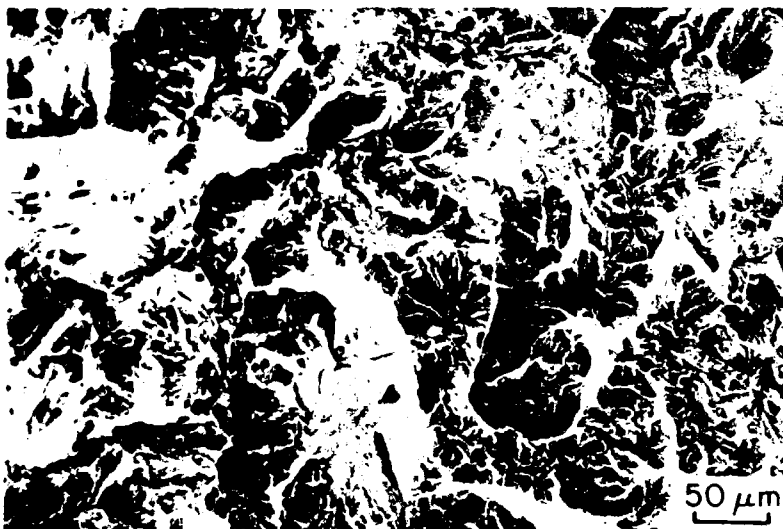
(b)

Figure 61.   Scanning electron micrographs of sub-size
              charpy impact specimens; Temp = +25 deg.C
              Martensitic microstructure.
              (a) Topographic macrograph of specimen
              (b) Cleavage facet morphology with secondary
                  cracking.
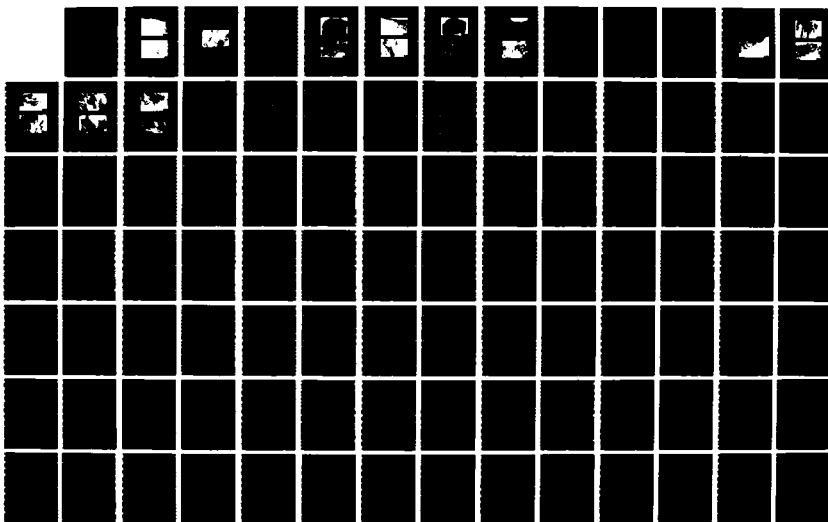
MICROCOPY RESOLUTION TEST CHART
NATIONAL BUREAU OF STANDARDS-1963-A

(a)

1.0 mm

(b)

50 μm

Figure 62.   Scanning electron micrographs of sub-size
             charpy impact specimens; Temp = -75 deg.C
             Ferritic microstructure.
             (a) Topographic macrograph of specimen
             (b) Small cleavage facet morphology with large
                 regions of microvoid coalescence.
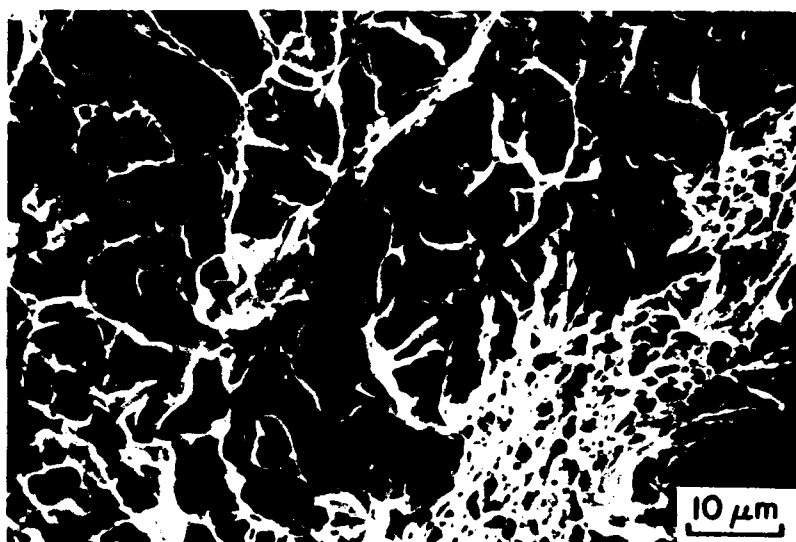
(c)

Figure 62.   Scanning electron micrographs of sub-size
              charpy impact specimens; Temp = -75 deg.C
              Ferritic microstructure.
              (c) High magnification of ferrite cleavage
                  facets

A microstructural profile of the ferritic fracture indicates that crack propagation was intergranular. Secondary internal cracks and tears were observed in both macrographs and micrographs, Figure 63.

The ferritic specimen at room temperature is irregular in shape. A thumbnail crack initiation zone is present and extends toward the center of the specimen length, Figure 64(a). In addition to large shear lips with lateral expansion toward the rear of the specimen are present. The entire fracture surface is characterized by a microvoid coalescence fracture morphology, Figure 64(b). Large shallow dimples with small inclusions are present.

The microstructure of the crack profile remains intergranular with secondary cracking. The crack profile indicated significant ductility along the crack surface, Figure 65.

4.6. HAZ Microstructure and Simulation Experiments

The Gleeble was employed to simulate HAZ microstructures utilizing one of the experimentally determined thermal cycles described previously. The actual welds and weld simulations employing the Gleeble. The characterization of actual welds has involved the
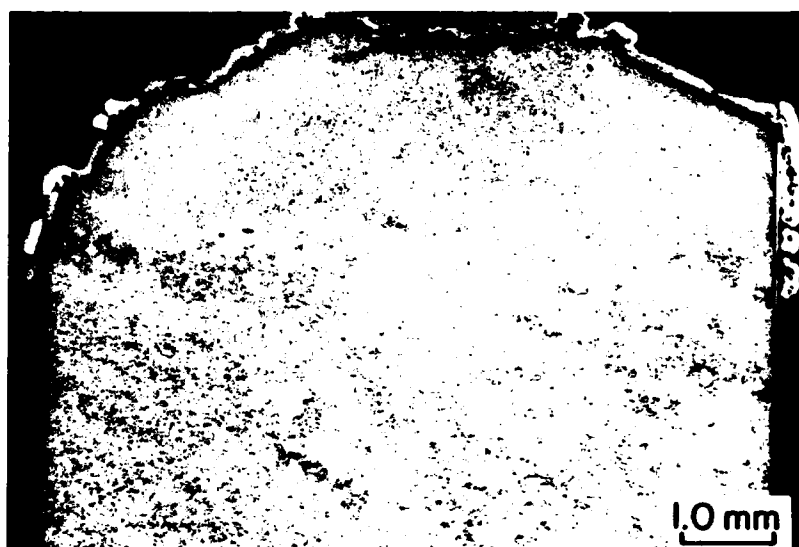
(a)

(b)

Figure 63.   Light micrographs of sub-size charpy impact
             specimens; Temp = -50 deg.C, Ferritic
             microstructure.
             (a) Profile macrograph of specimen
             (b) Intergranular crack profile through
                 Ferritic microstructure
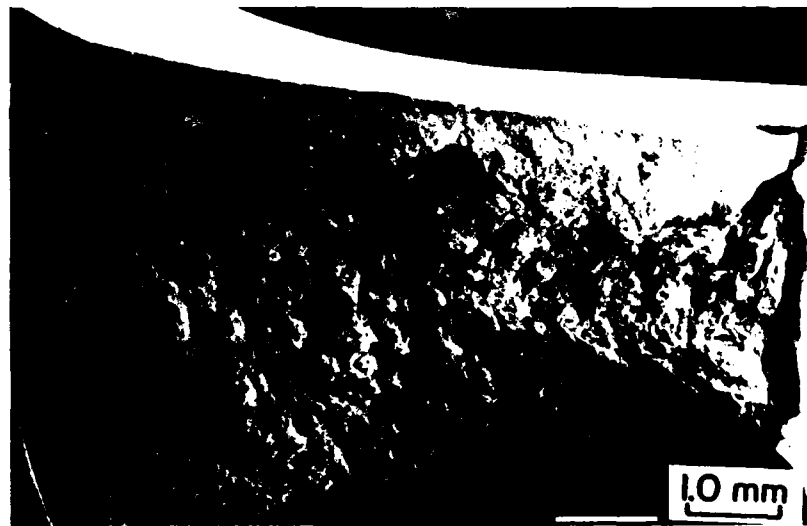
(a)
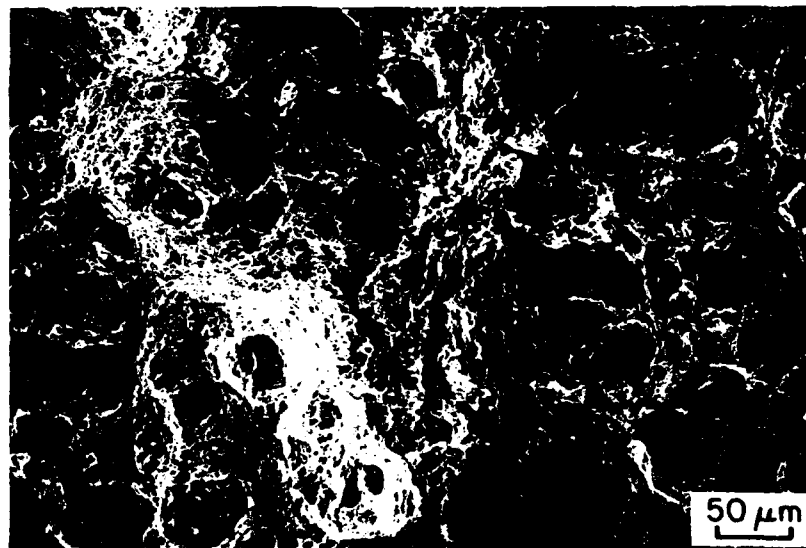
(b)

Figure 64.   Scanning electron micrographs of sub-size
             charpy impact specimens; Temp = +25 deg.C,
             Ferritic microstructure.
             (a) Topographic macrograph of specimen
                 illustrating a "thumbnail" crack initiation
                 zone.
             (b) Surface morphology characterized by
                 microvoid coalescence.
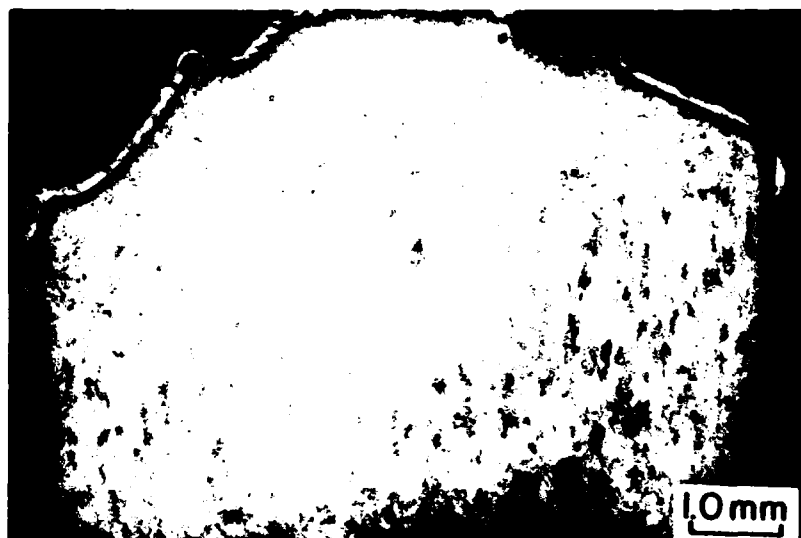
(a)

(b)

Figure 65.   Light micrographs of sub-size charpy impact
              specimens; Temp = +25 deg.C, Ferritic
              microstructure.
              (a) Profile macrograph of specimen illustrating
                  an irregular surface
              (b) Intergranular crack profile through
                  Ferritic microstructure with significant
                  ductility

(a)
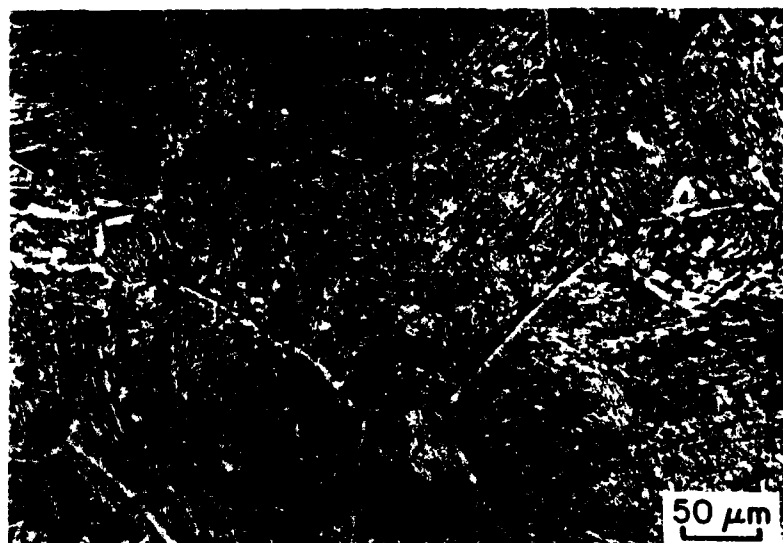
(b)

Figure 66. Light micrograph of HAZ microstructures;
            T_p = 1380 deg.C, D_{FZL} = 0.39mm
            (a) Actual weld HAZ microstructure
            (b) Gleeble simulation HAZ microstructure

determination of microhardness and microstructure as a function of position in the HAZ. The Gleeble simulations results of this simulation are displayed in Figure 66 for a location in the austenite grain coarsened region of a nominally 3.35 KJ/mm (85 KJ/in.) weld. The prior austenite grain size for the actual HAZ and the HAZ simulation are virtually identical as are the transformation products.

This would seem to indicate that the Gleeble can adequately simulate local HAZ microstructures for which a specific thermal cycle is available.

The characterization and analysis of transformation product evolution during welding has been accomplished on have been accomplished for positions in the HAZ of various heat input welds for which a thermal cycle has been determined. Microstructural and microhardness correlation with corresponding positions in actual welds was accomplished to establish the validity of the weld simulation. In addition, the transformation behavior was investigated during the simulation experiments via dilatometry.

4.6.1. Microstructure of HAZ Simulations

Specimens were subjected to thermal cycle simulations

for HAZ locations. Heat input parameters are specified in Table 10 for the thermal transient data. Thermal transient curves for all heat input HAZ locations are illustrated in Appendix 1.

The microstructures and hardness values produced in weld simulation specimens generally compared favorably with the corresponding locations in the actual weld HAZ's. Minor problems were encountered in specifying the location of the thermocouple with respect to the fusion zone boundary in the actual welds. This resulted in slight relative shifts of microstructure and hardness between simulation and actual weld.

The close correspondence between actual HAZ and HAZ simulation microstructures allowed for TEM thin foil observations to be made on selected HAZ microstructures in simulation specimens. Obtaining thin foil specimens was facilitated by the homogeneous microstructure of the simulation specimens.

4.6.2 TEM Foil Results of Simulated Specimens.

Simulation specimens with large volumes of homogeneous microstructures enabled various locations in the HAZ to be investigated via TEM thin foil. TEM observations confirmed

the presence of precipitation, dislocation substructure and microstructural characteristics for various comparisons and correlations in hardness data.

A thin foil was made from a location in the HAZ pertaining to the second hardness peak for the high heat input. At this location, extensive iron carbide precipitation and degenerate pearlite colonies were observed, Figure 67.

TEM specimens taken from the near fusion zone location of the medium heat input confirmed the microstructure as consisting of bainitic laths. Bainitic laths with an array of dislocations and large carbides are shown in Figure 68.

In the specimen for the low heat input at a position near the fusion zone, the microstructure consisted of bainite and martensite with auto tempered carbides in the lath, Figure 69. At small distances from the fusion zone in the banded region, regions containing martensite with pearlite are observed, Figure 70(a). In addition, transformation twins are present in the martensitic lath and are shown in Figure 70(b).

Figure 71(a) illustrates an area next to the region in Figure 70 containing ferrite and martensite. Also, a precipitate dispersion of iron carbide was observed within the ferritic grains at high magnification, Figure 71(b).

0.13 μm

Figure 67. Transmission electron micrograph of a thin foil
containing degenerated pearlite colonies with a
dispersion of iron carbide precipitates.

(a)
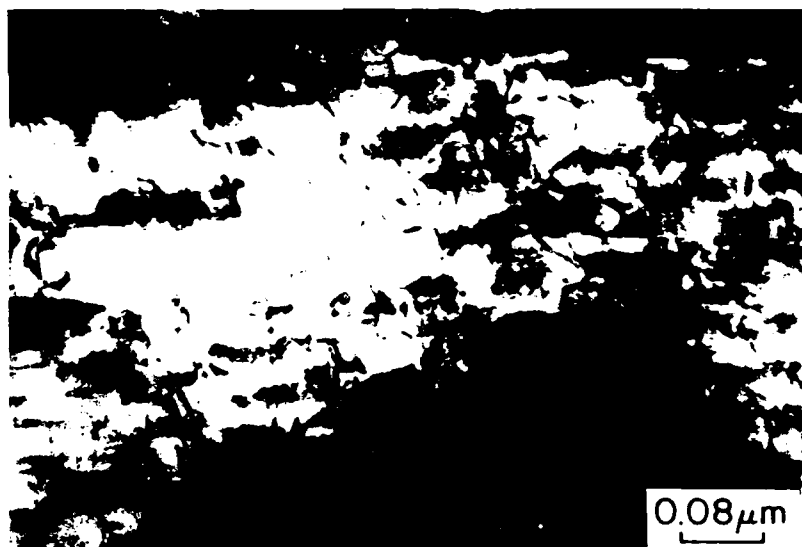
(b)

Figure 68.   Transmission electron micrograph of thin foil
              in the near fusion zone of the HAZ for medium
              heat input.
              (a) Bainitic lath microstructure.
              (b) Large carbides with an array of
                  dislocations.

(a)

0.35 μm

(b)

0.13 μm
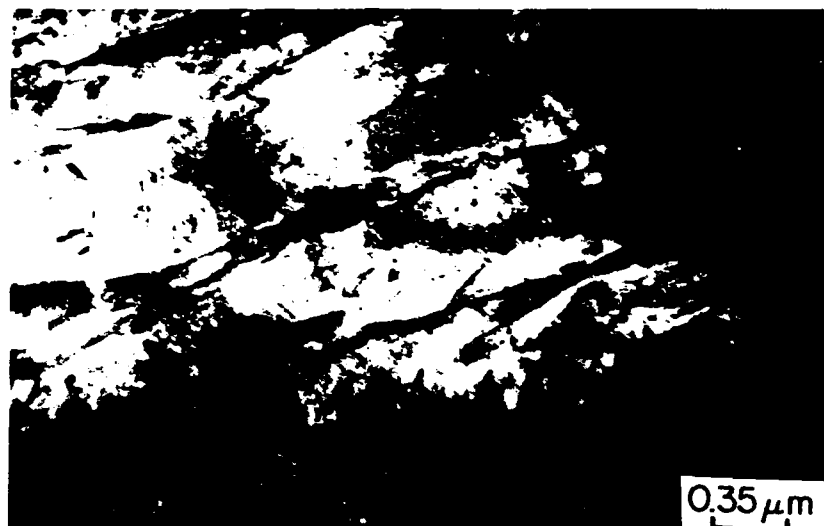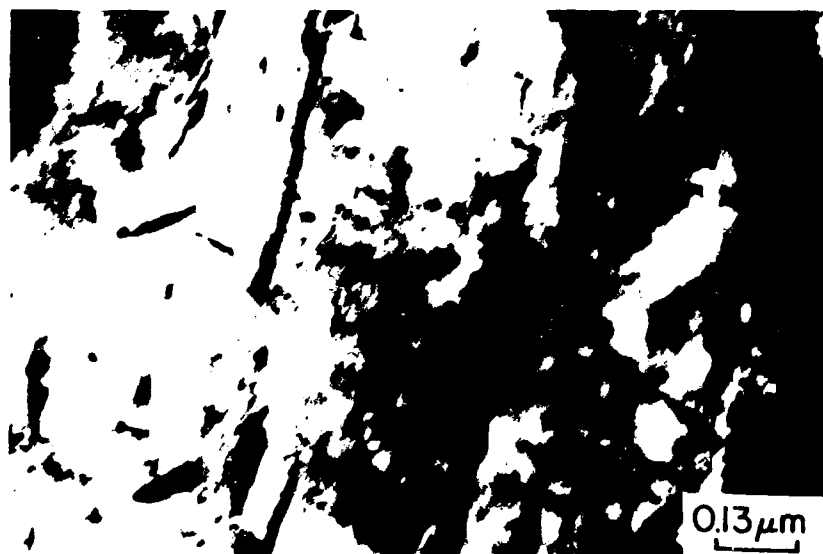
Figure 69.   Transmission electron micrograph of thin foil
in the diffuse banded region of the HAZ for low
heat input weld.
(a) Bainite and martensite with auto tempered
    carbides in the lath.
(b) High magnification of martensite laths with
    carbides.
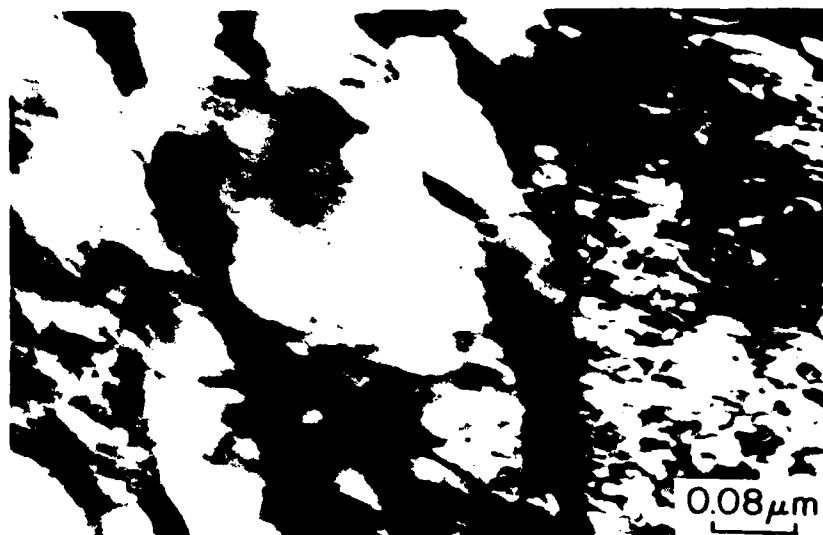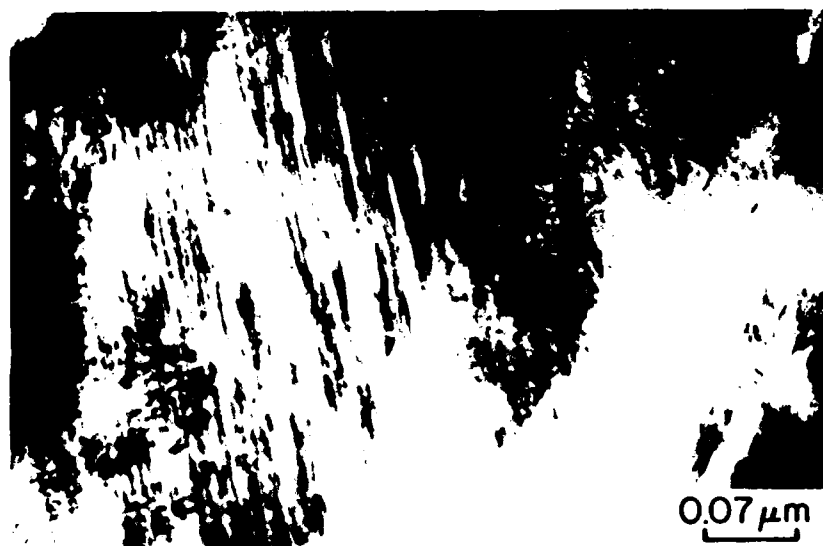
Figure 70.   Transmission electron micrograph of thin foil
              in the diffuse banded region in the HAZ for a
              low heat input weld.
              (a) Martensitic and pearlitic microstructure.
              (b) Transformation twins within martensitic
                  lath.

(a)

2.0 μm

(b)

0.07μm
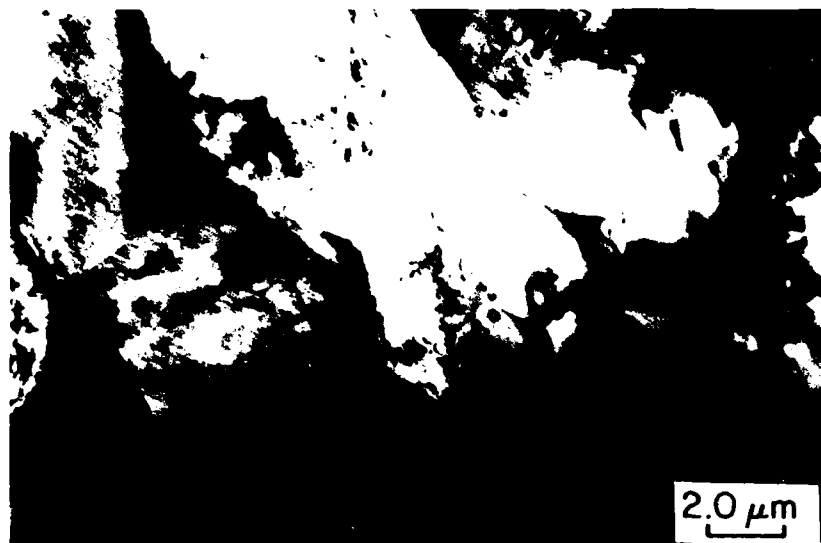
Figure 71.   Transmission electron micrograph of thin foil
             in the diffuse banded region in the HAZ of low
             heat input weld.
             (a) Martensitic and ferritic microstructure.
             (b) Iron carbide precipitation within ferritic
                 grain.

4.6.3 Continuous Cooling Transformation Temperatures

Transformation start and finish temperatures and times were obtained from diametral strain data by methods outlined by Eldis [94] Transformation start and finish temperatures determined via dialatometer are depicted in Figure 72. Transformation temperature is plotted versus the logarithm of time. The number adjacent to individual data points represent peak temperatures for the thermal cycles involved. Implicit in this data is also a variation of position in the HAZ.

As heat input was increased from 1.97 KJ/mm (50 KJ/in.) to 4.92 KJ/mm (125 KJ/in.) the transformation start was generally pushed to slightly higher temperatures and longer times. The transformation end was generally just pushed to longer times.

For a given heat input the transformation temperatures appear to vary discontinuously with peak temperature. Low peak tempertures are associated with high transformation temperatures and high peak temperatures with lower transformation temperatures.

A continuous cooling transformation diagram is derived from figure 72 for transformation temperatures that are approximately within a relatively narrow temperature band,
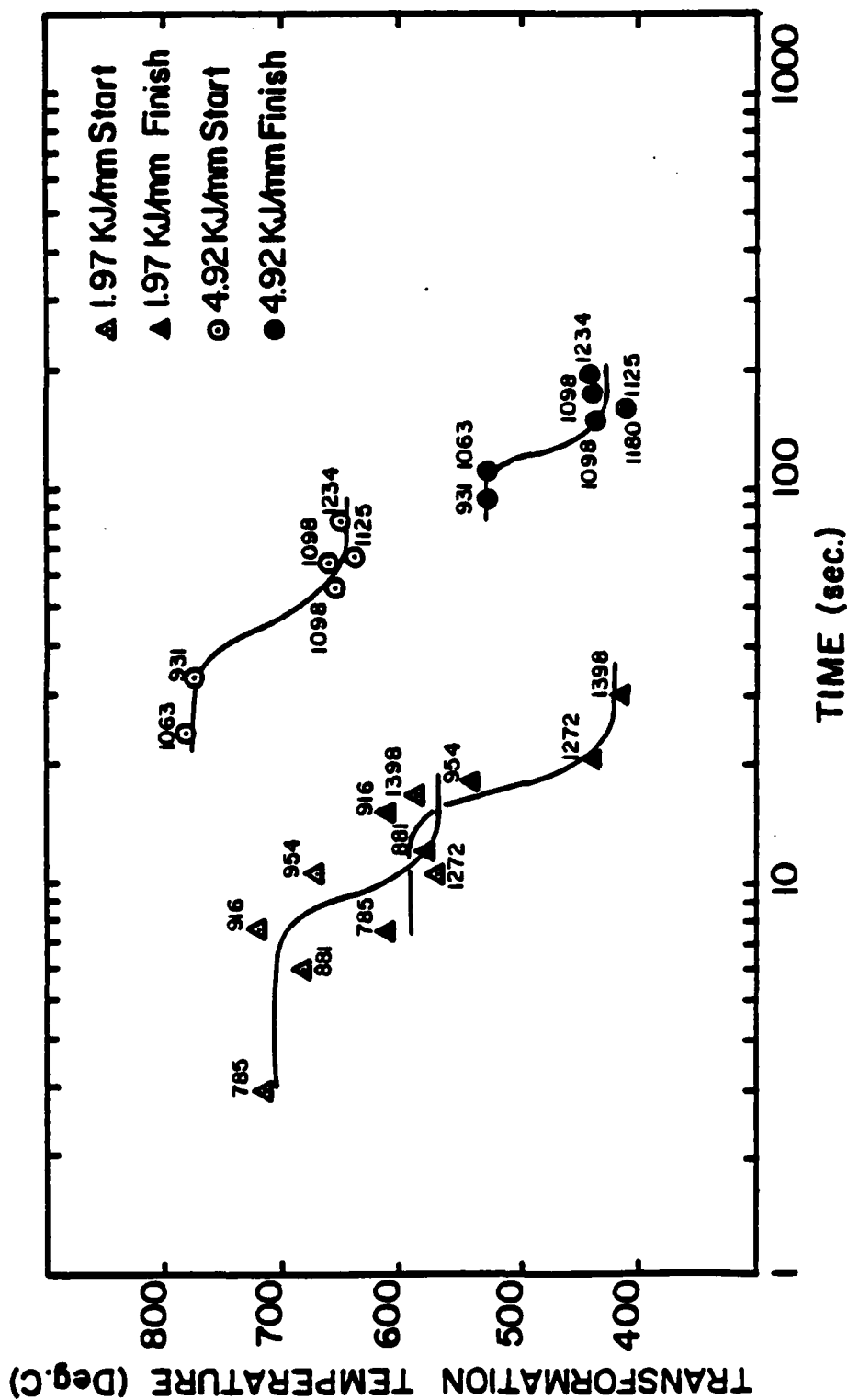
Figure 72. Summary of transformation start and finish temperature as a function of cooling time for experimental weld cycles via time-temperature curves.

Figure 73. Transformation curves indicate start and finish time-temperature for coarse and fine austenitic grain microstructure.

A plot of transformation start temperatures versus the time to cool between 800 Deg.C and 500 Deg.C ($\Delta t_{800/500}$) is shown in Figure 74. The parameter $\Delta t_{800/500}$ is inversely proportional to cooling rate. The shaded groupings within the plot refer to different heat inputs and $\Delta t_{800/500}$ increases with increasing heat input. The cooling rate decreases with increasing heatinput. The observed scatter in transformation start temperature is associated with peak temperature. Low peak temperatures are associated with high transformation temperatures and high peak temperatures with low transformation temperatures. The plot indicates that transformation temperature is a generally weak function of cooling rate and as shown in the previous plot, a strong function of peak temperature.

4.6.4. Isothermal Precipitate Studies

4.6.4.1. 900 Degrees C.

Fine precipitates are observed at all times. Size
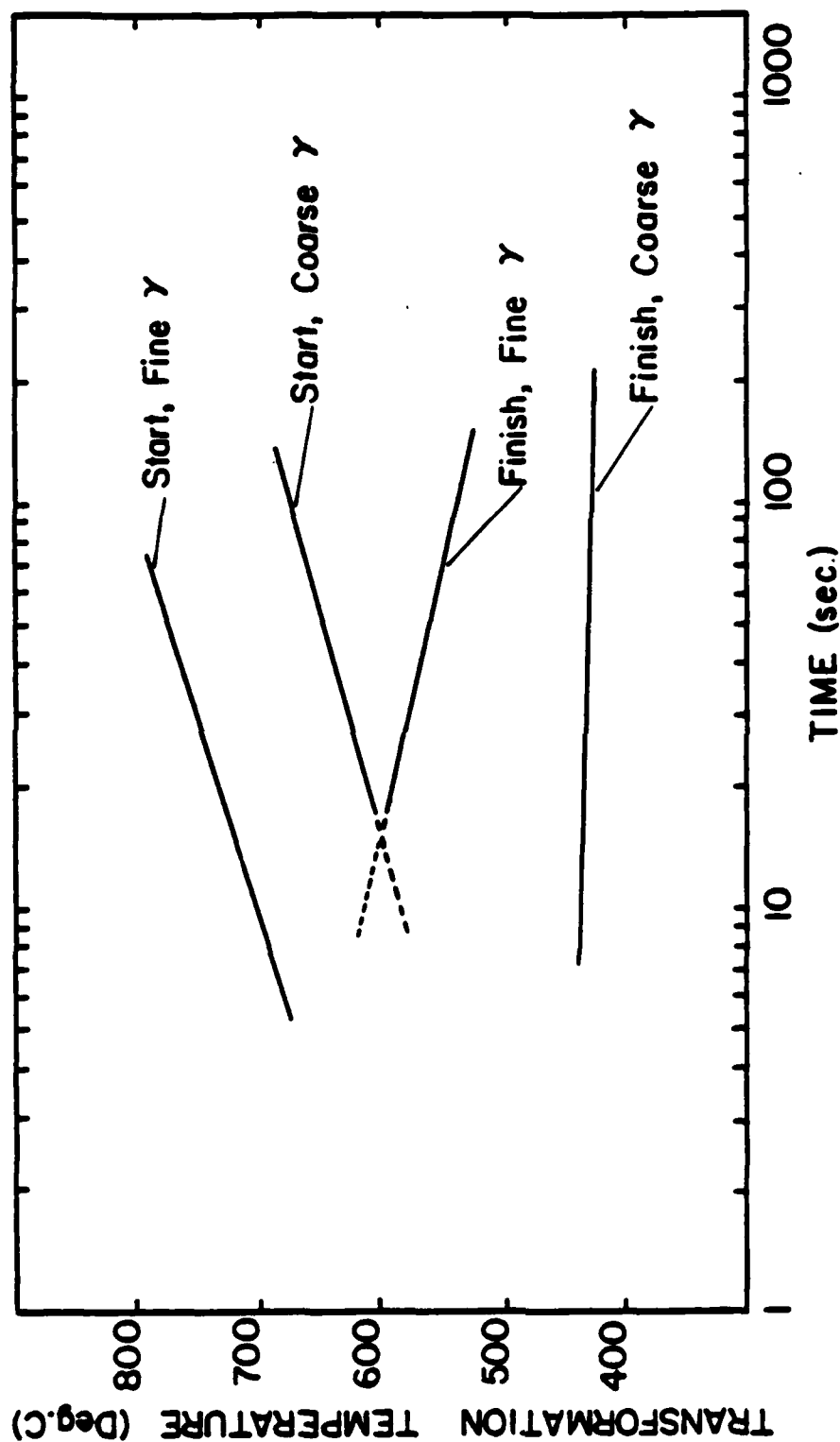
Figure 73. Continuous cooling transformation diagram for various heat input weld thermocycles indicating start and finish time-temperatures for coarse and fine austenitic grain microstructure.
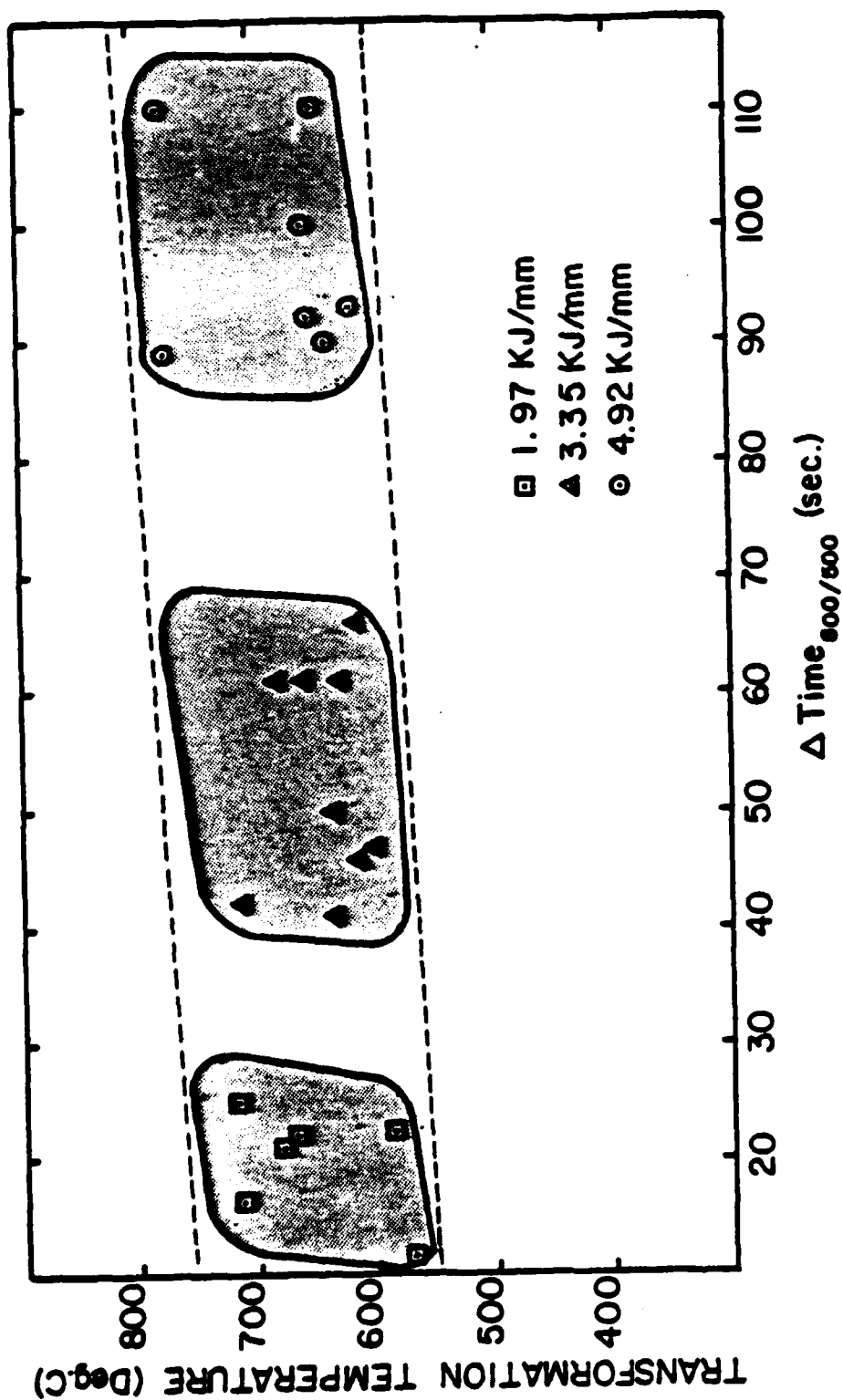
Figure 74. Transformation temperature as a function of cooling time interval for continuous cooling 800 deg.C to 500 deg.C.

distributions of the fine V(C,N) are plotted in

Figures 75-78.   In addition a dispersion of coarse cuboidal

precipitates are observed.   The size distribution for the

coarse precipitates is plotted in Figure 79.   The fine

precipitates were identified as V(C,N) via TEM selected

area diffraction.   The coarse particles were not positively

identified.   The precipitate particles were not uniformly

distributed in the matrix.   It appeared that there were

more densely precipitated regions associated with a thin

carbon film.   It is possible that more than one monolayer

of precipitates was extracted in these regions so that only

tenuous statements can be made of interparticle spacing.

However, the carbon films in these regions were present at

low temperatures and short times so that they could be a

manifastation of chemical inhomogeneities associated with

the base-plate and the ferrite to austenite

transformation.   One might expect banded regions of the

base-plate to be enriched in manganese and carbon,

accounting for the denser precipitation and the carbon

films.

These carbon films may be amorphous due to dissolution

in the etching acid of carbon in solid solution and

iron-carbide.   Formation of amorphous carbon has been noted

in descriptions of bulk extraction of microalloy
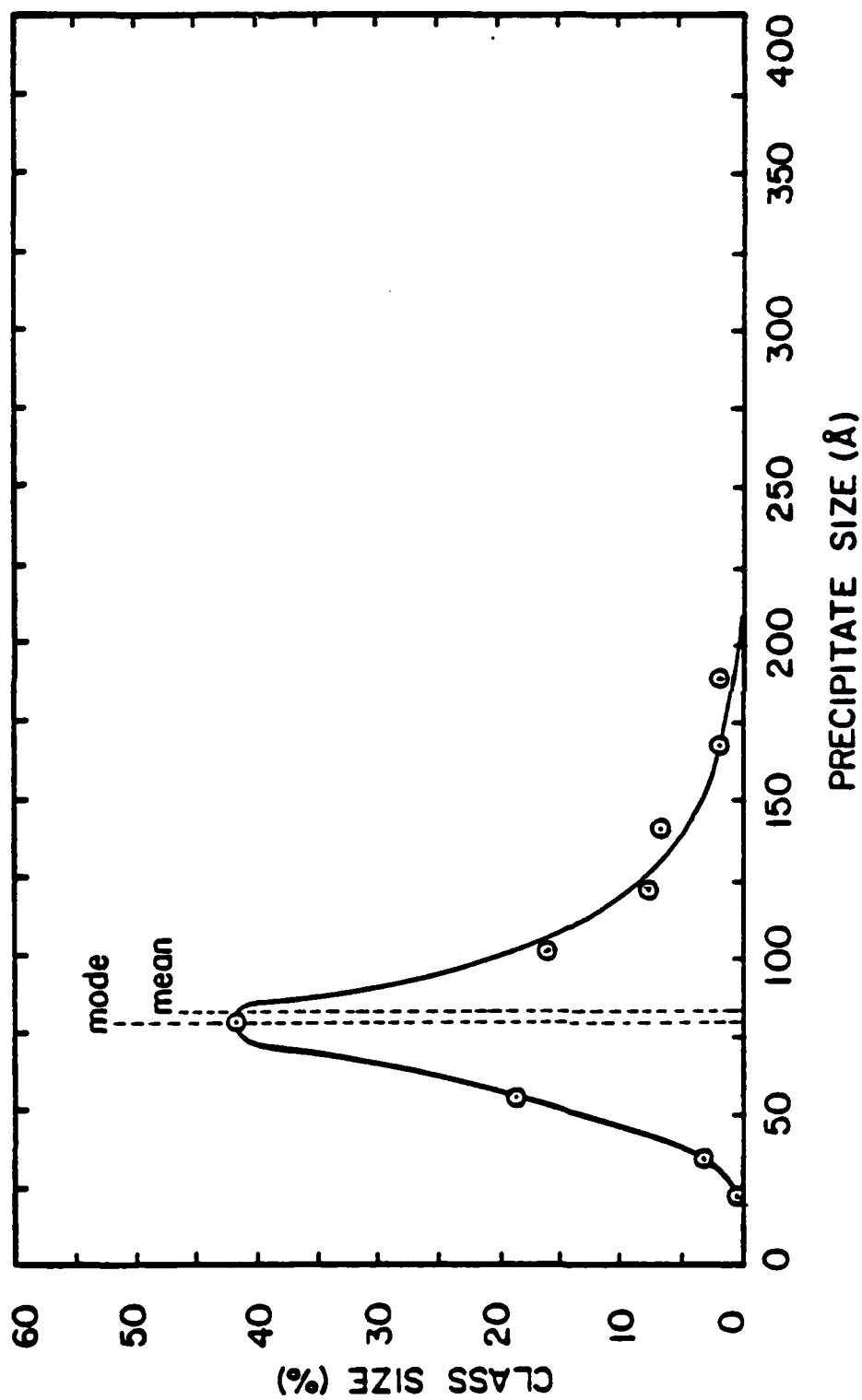
Figure 75.   Fine V(C,N) precipitate size distribution, short time heat treatment-- 5 seconds at 900 degrees C.
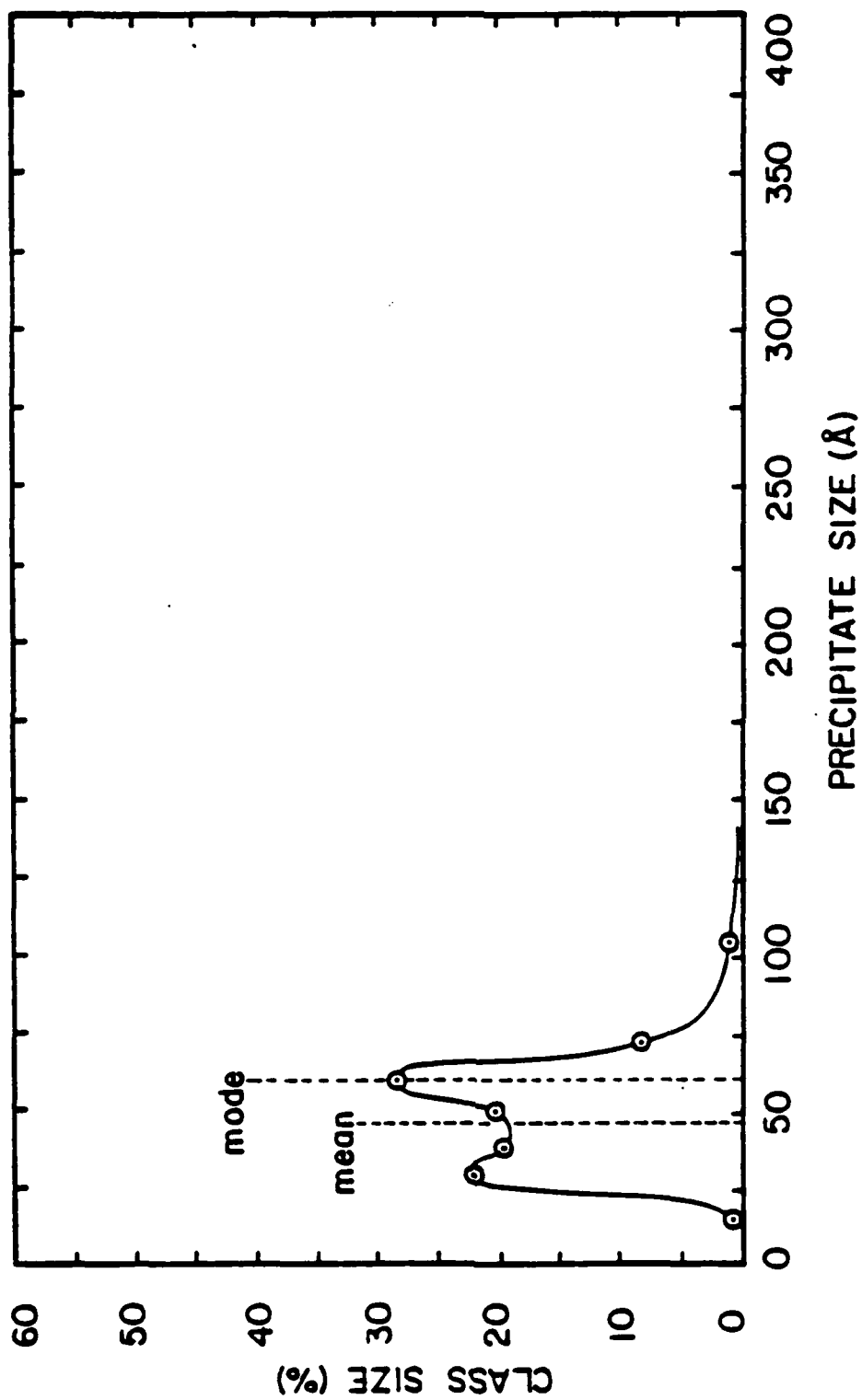
Figure 76. Fine V(C,N) precipitate size distribution, short time heat treatment--10 seconds at 900 degrees C.
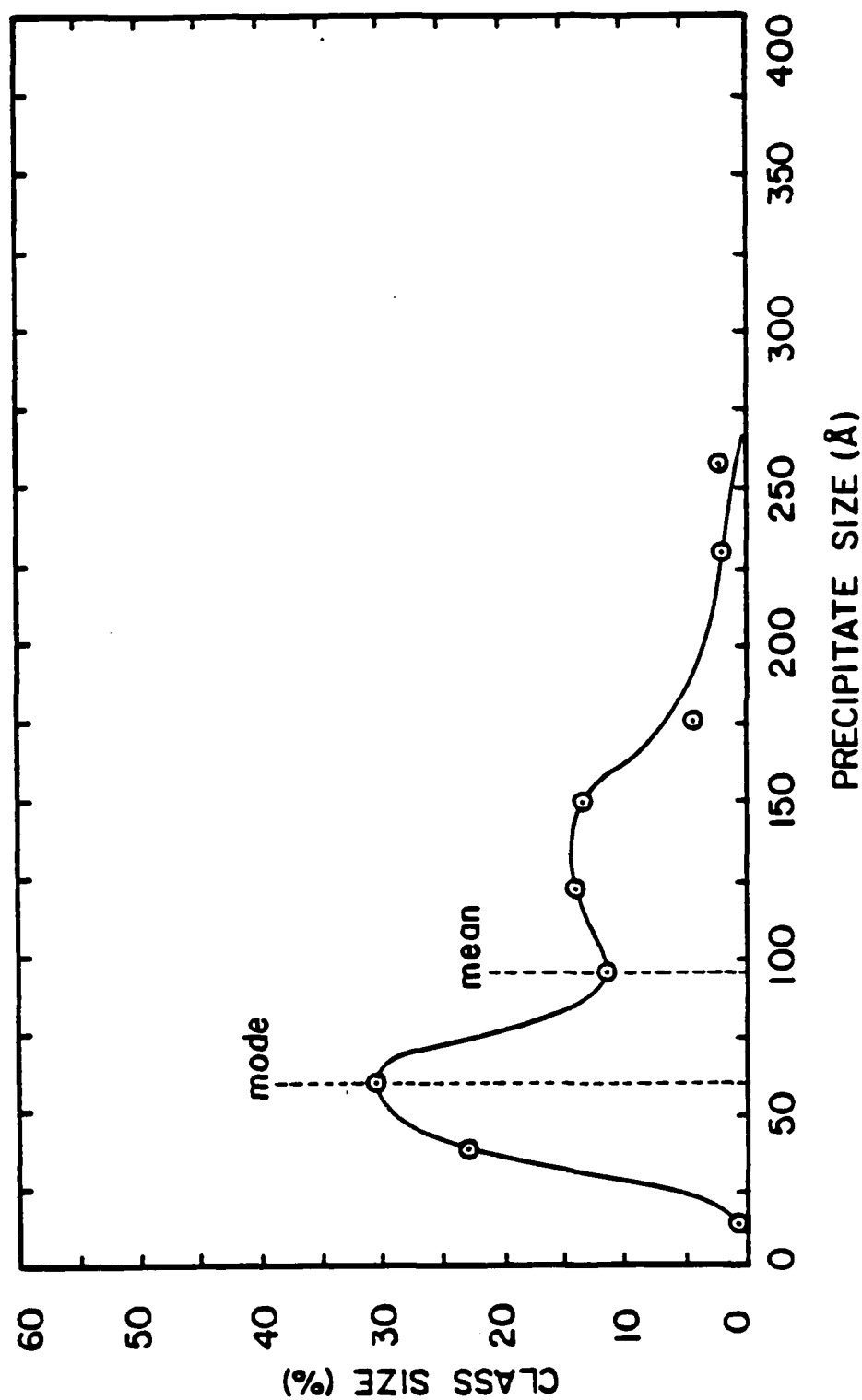
Figure 77. Fine V(C,N) precipitate size distribution, short time heat treatment--20 seconds at 900 degrees C.
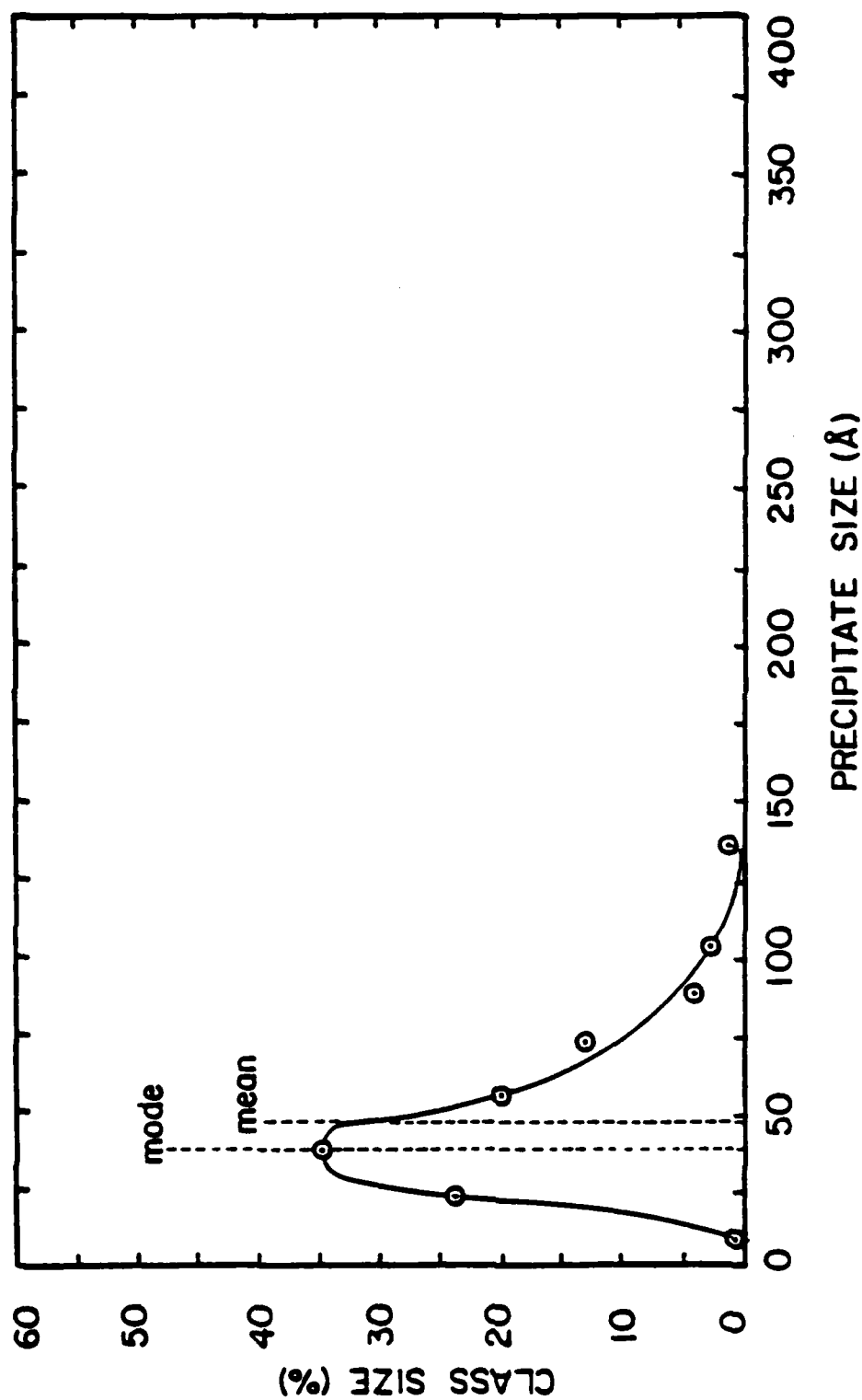
Figure 78. Fine V(C,N) precipitate size distribution, short time heat treatment--40 seconds at 900 degrees C.
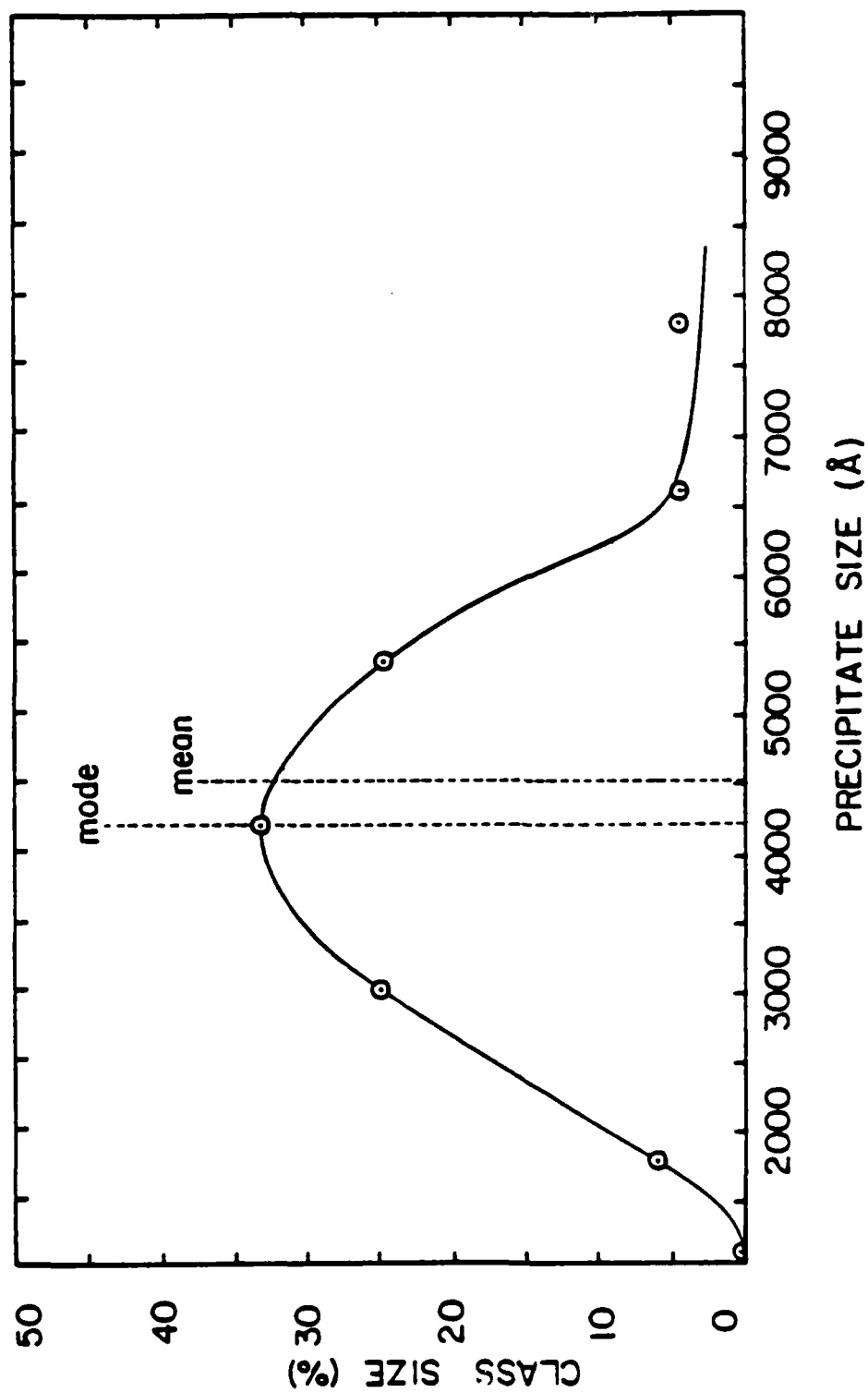
Figure 79. Coarse cuboidal precipitate size distribution, short time heat treatment--40 seconds at 900 degrees C.

precipitates via matrix dissolution in a dilute acid. In
these descriptions the amorphous carbon is cited as an
agent in agglomerating fine precipitate particles and is
similar to the agglomeration of precipitates observed in
carbon extraction replicas.

The microstructure appeared to change between 10 and 20
seconds. The mean precipitate size decreases from
approximately 80Å at 5 seconds to approximately 50Å at
20 seconds. At 40 seconds the mean precipitate size has
once again decreased to approximately 30Å.

In examining the individual size distributions the 5
seconds condition appears unimodal. However at 10 and 20
seconds bimodal distributions appear to have developed. At
10 seconds the two modes are closely spaced; the finer
particle mode is at 30Å to 40Å and the coarser particle
mode is located in the vicinity of 60Å. At 20 seconds
the fine and coarse particle modes have separated further.
The fine particle mode has increased slightly to
approximately 60Å, but the coarse particle mode has
increased significantly to approximately 125Å. At 40
seconds the distribution once again appears unimodal.

It would appear that that the evolution of an austenite
microalloy precipitate dispersion at 900 deg.C is quite
complex. Initially a prior base-plate precipitate

dispersion exists that is modified by the ferrite to austenite phase transformation. Dissolution of precipitates must occur on phase transformation as well as chemical inhomogeneities. The latter appear to be manifested in the carbon film observations described above.

Dissolution of precipitates to establish the equilibrium volume fraction results in a decreasing size for all precipitates. This would result in an initial decrease in the mean precipitate size, Figure 80. However, as finer precipitates dissolve completely, only coarser precipitates are left to size and count for a size distribution. Therefore, one would expect that with time the mean precipitate size might increase due to presence of coarser particles that may in fact be shrinking as well. Implied in this rationale is more rapid dissolution of finer particles. Theory would indicate an increasing rate of dissolution for a single particle. The formation of a bimodal intermediate distribution implies the coarsening of some particles while others are shrinking and this would seem reasonable in light of the explanation made above.

There also appears to be two stages associated with the evolution of microalloy precipitation state. Initially, the precipitate dispersion is modified while the phase transformation of ferrite to austenite is occuring.
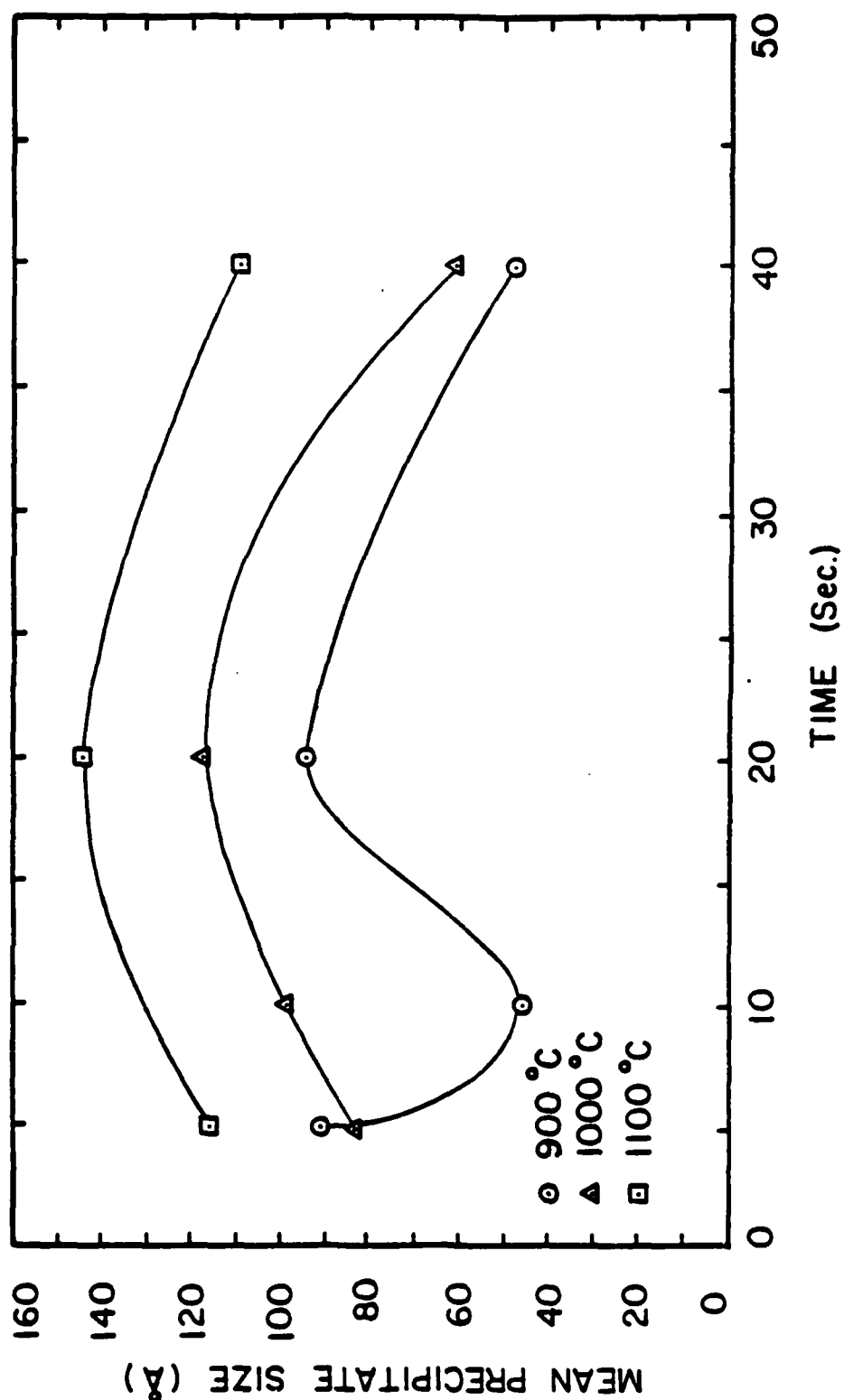
Figure 80. Summary of the mean precipitate size for short
time heat treatments at various temperatures
and times.

Indications are that this occurs rapidly at 900 deg.C but
it may require at least 10-20 seconds. Edmounds and Law
[30] indicate that vanadium carbides dissolve at the
transformation front and then reprecipitate in austenite.
The decrease in mean precipitate size may then involve the
dissolution of a more uniform precipitate dispersion in a
stable fully formed austenite structure.

4.6.4.2. 1000 Degrees C.

Fine precipitates, identified as V(C,N) by SAD, are
present for all times at 1000 deg.C. The size
distributions are shown in Figures 81-84. Coarse
precipitates are also present that could not be positively
identified by SAD, the size distribution is shown in Figure
85. The microstructure has changed to a lath martensite or
bainitic matrix and precipitates still appear segregated in
association with carbon films.

The mean precipitate size first increases to a maximum
in the vicinity of 20 seconds and then decreases. The mean
size at 5 seconds and at 40 seconds is comparable to that
measured at 900 deg.C. The precipitate sizes at 1000 deg.C
are greater for intermediate times. (10 and 20 seconds)

All individual distributions appear unimodal but do
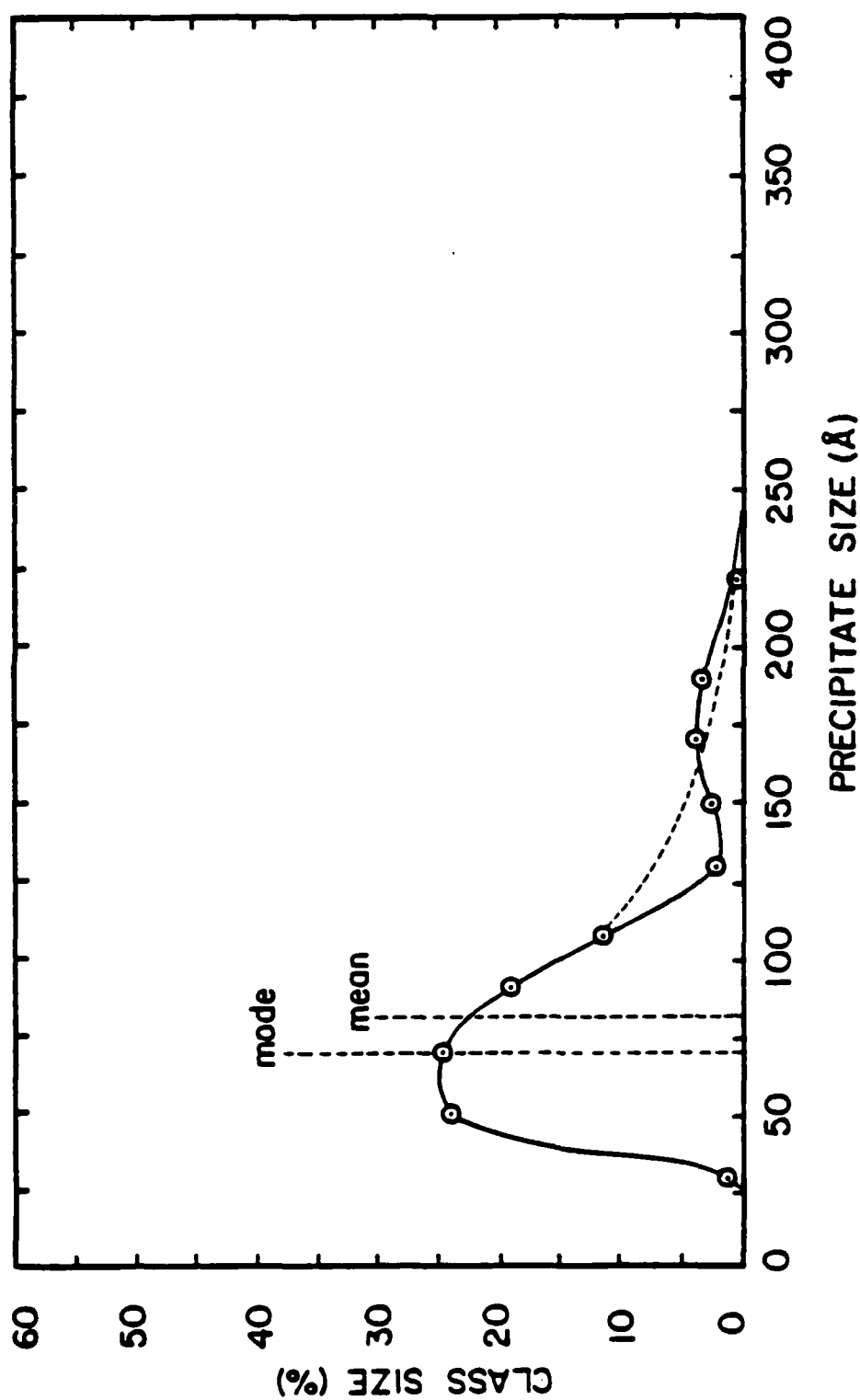
Figure 81. Fine V(C,N) precipitate size distribution for short time heat treatment-- 5 seconds at 1000 degrees C.
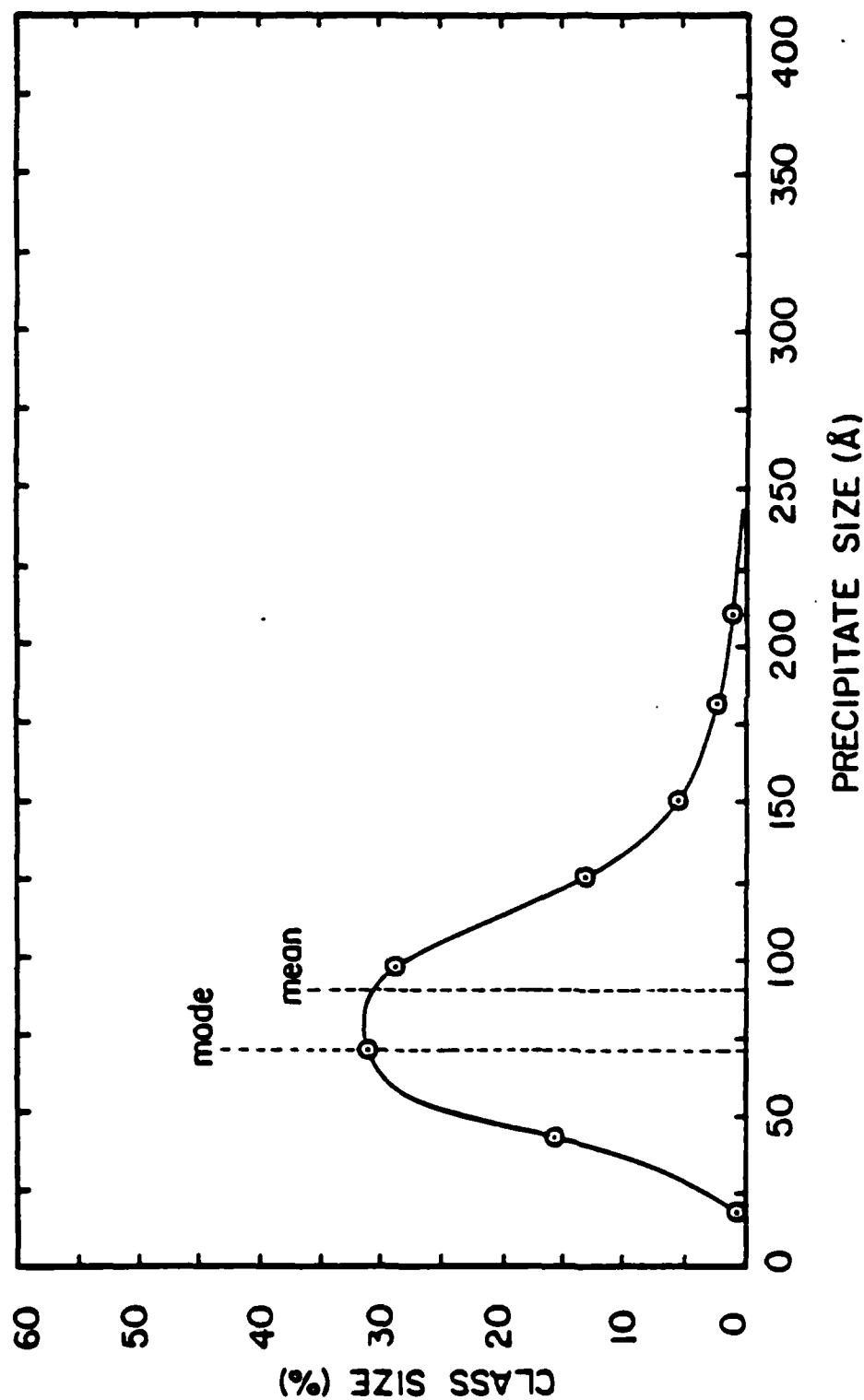
Figure 82. Fine V(C,N) precipitate size distribution for short time heat treatment--10 seconds at 1000 degrees C.
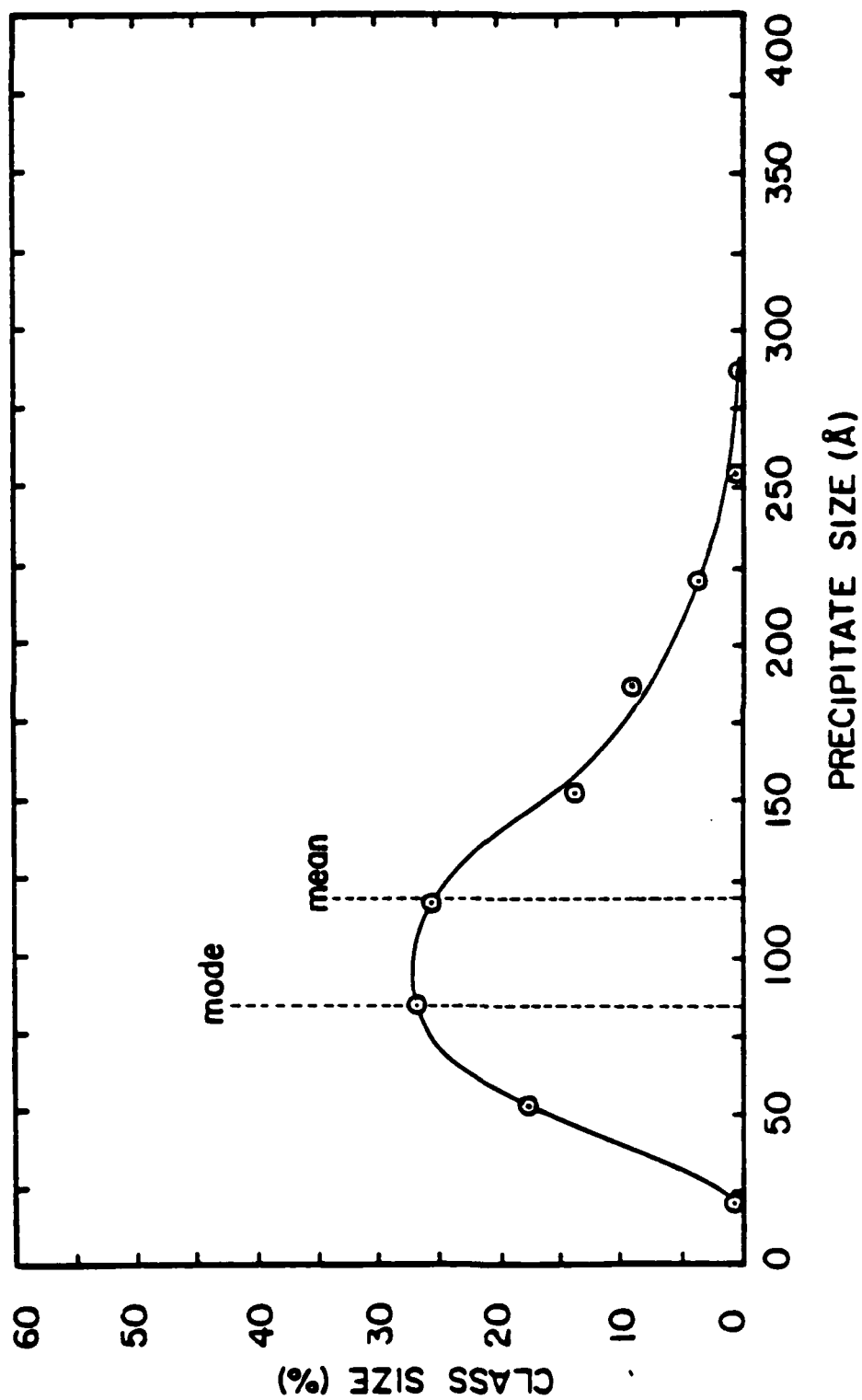
Figure 83. Fine V(C,N) precipitate size distribution for short time heat treatment--20 seconds at 1000 degrees C.
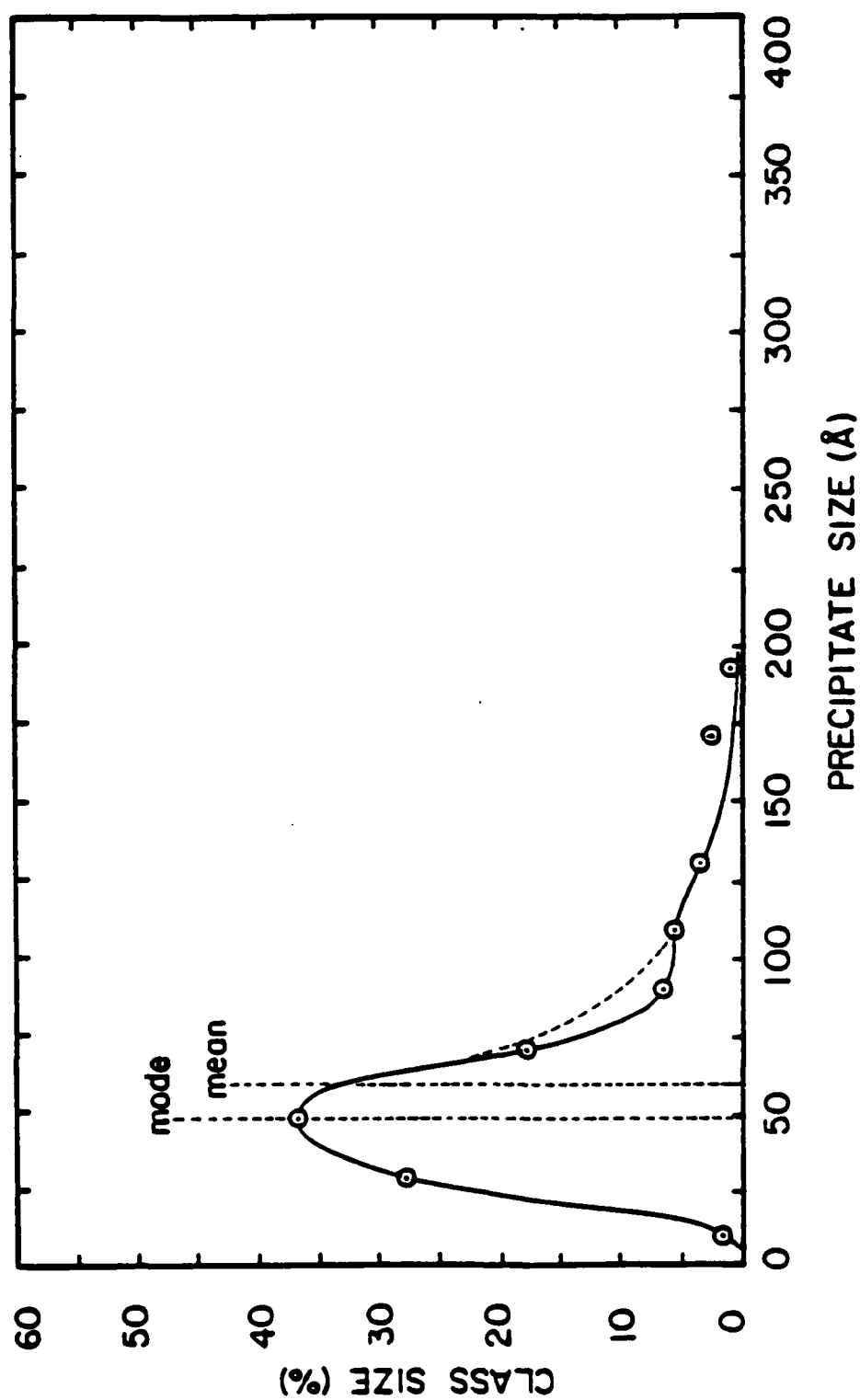
Figure 84.   Fine V(C,N) precipitate size distribution for short time heat treatment--40 seconds at 1000 degrees C.
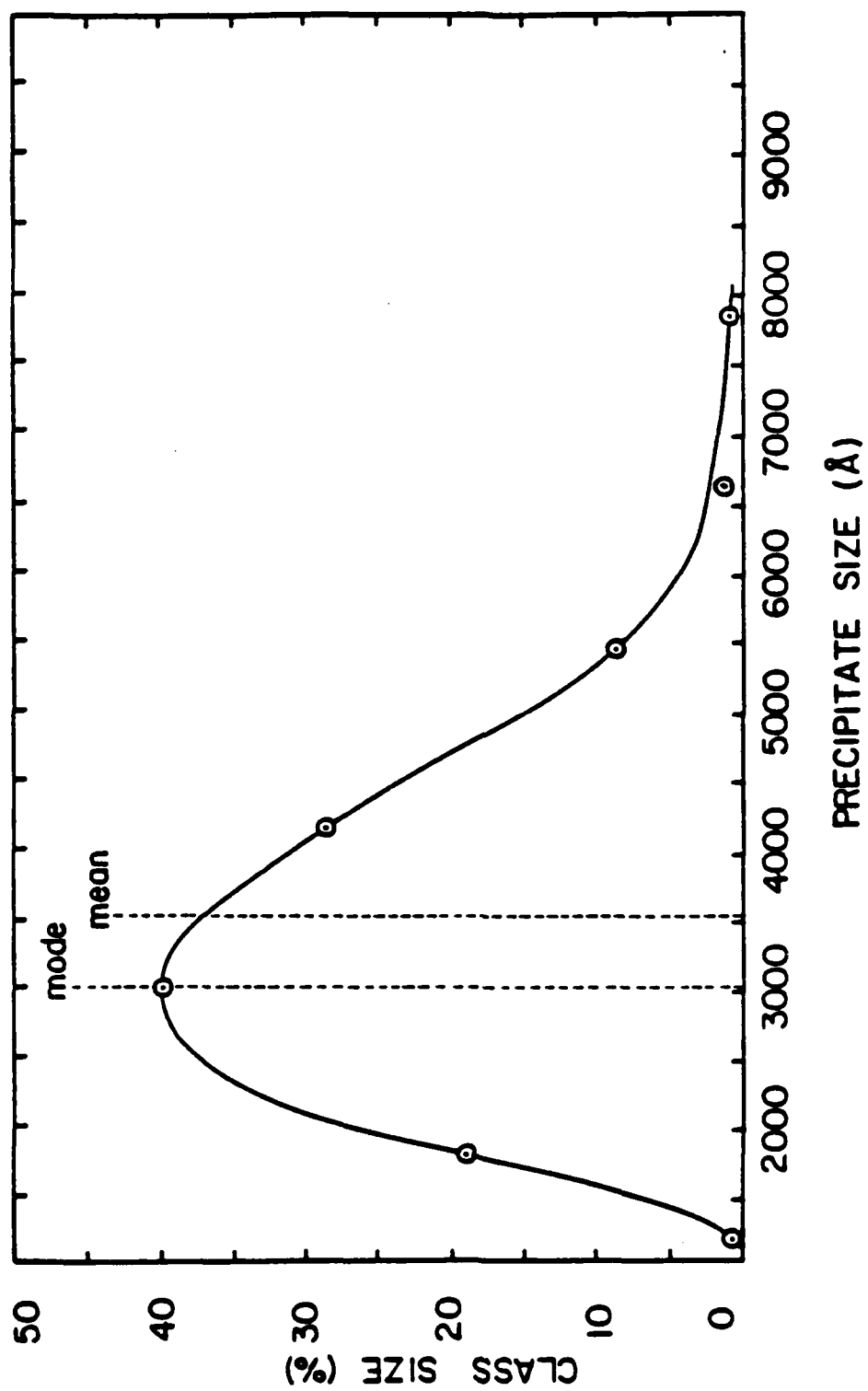
Figure 85.   Coarse cuboidal precipitate size distribution
             for short time heat treatment--40 seconds at
             1000 degrees C.

appear to broaden with time up to 20 sec. In addition
to possessing a smaller mean precipitate size, the
size distribution for the 40 seconds condition is
narrower.

The underlying processes here are the same as
those obtaining at 900 deg.C except that the processes
occuring in conjunction with austenite formation
probably occur at times less than 5 seconds. The
variation of mean precipitate size therefore occurs in
association with a size distribution dissolving in
austenite to attain an equilibrium volume fraction of
precipitates.

The initial increase in precipitate size is then
correlated with preferential dissolution of fine
precipitates. This is followed by a decrease in mean
particle size as even the coarser particles start
dissolving rapidly.

4.6.4.3. 1100 Degrees C.

The coarse precipitates were identified by SAD
as Nb(C,N) and the distribution is shown in Figure 86.
In addition, finer Nb(C,N) precipitates, some with
a rod morphology were observed. The distribution
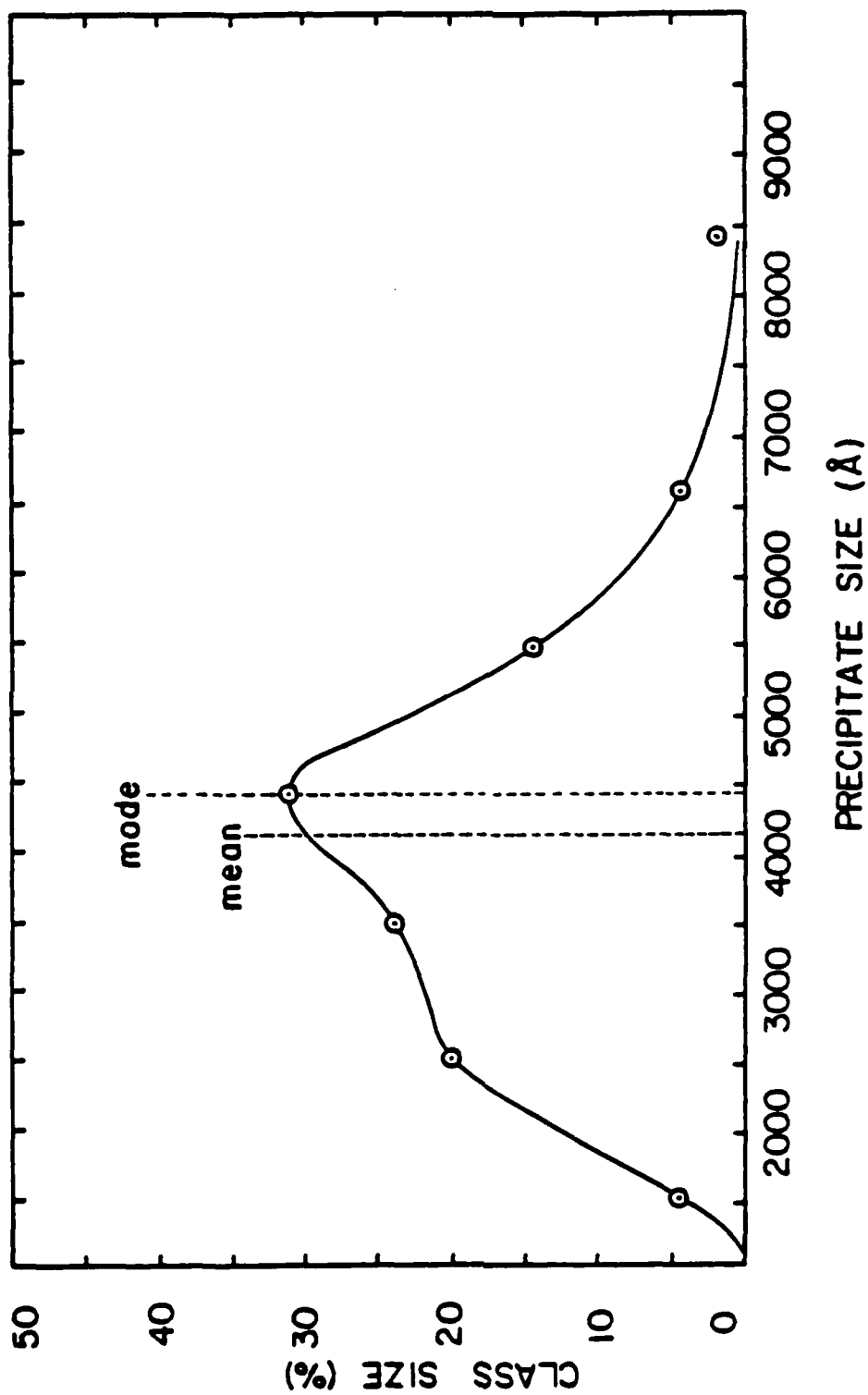
Figure 86. Coarse cuboidal precipitate size distribution
for short time heat treatment-- 5 seconds at
1100 degrees C.
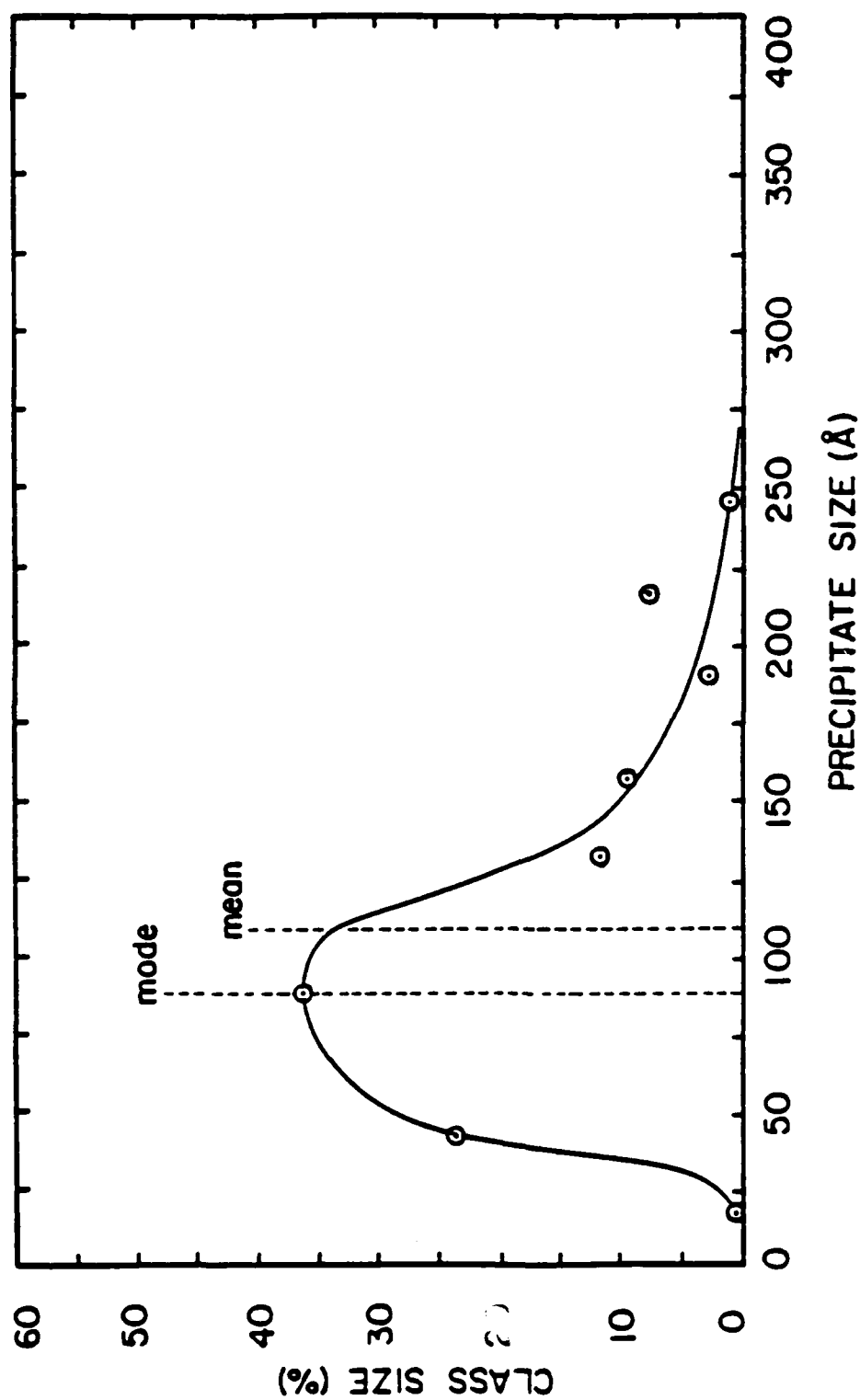
Figure 87. Fine Nb(C,N) precipitate size distribution
for short time heat treatment-- 5 seconds at
1100 degrees C.
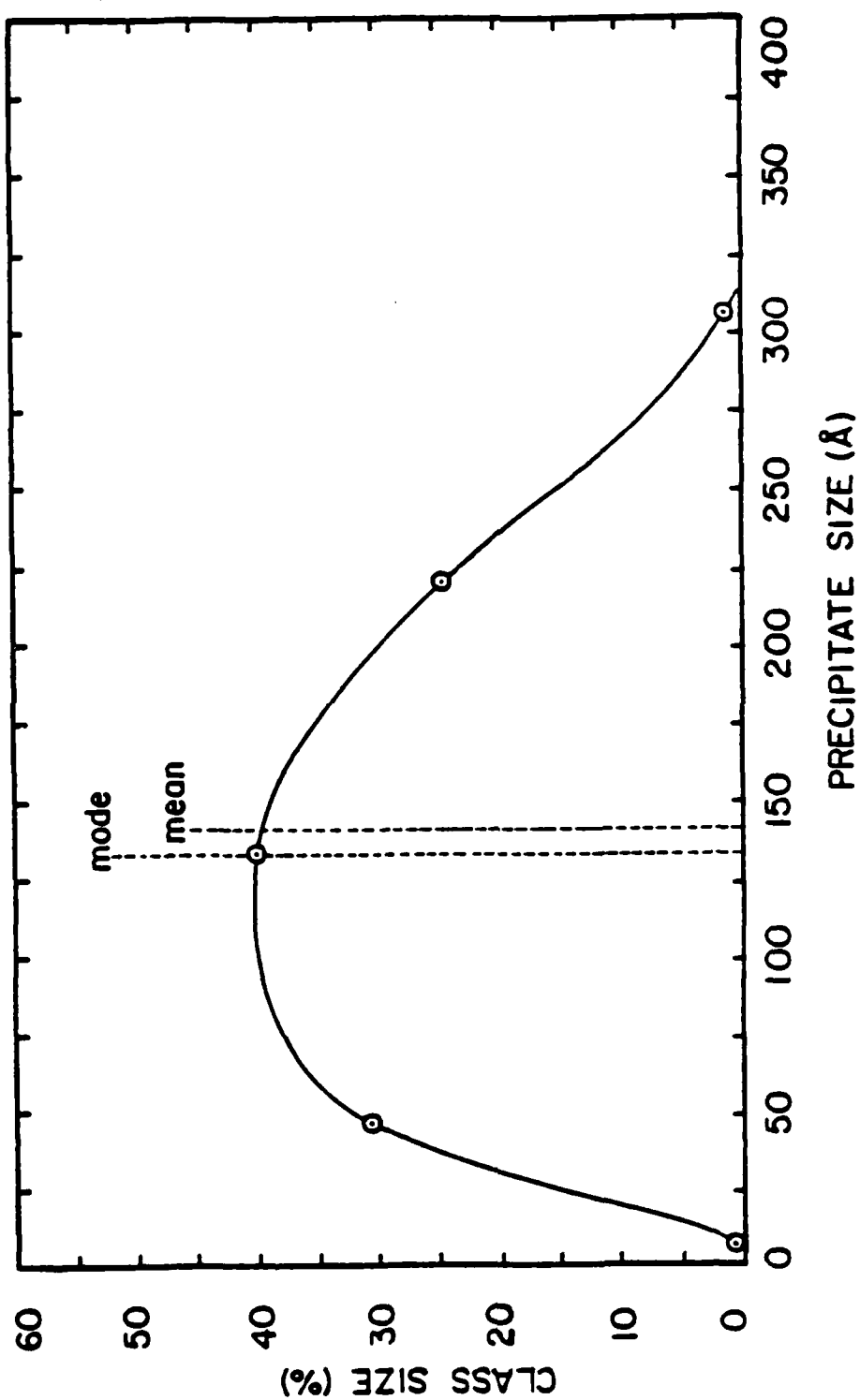
Figure 88. Fine Nb(C,N) precipitate size distribution
for short time heat treatment--20 seconds at
1100 degrees C.
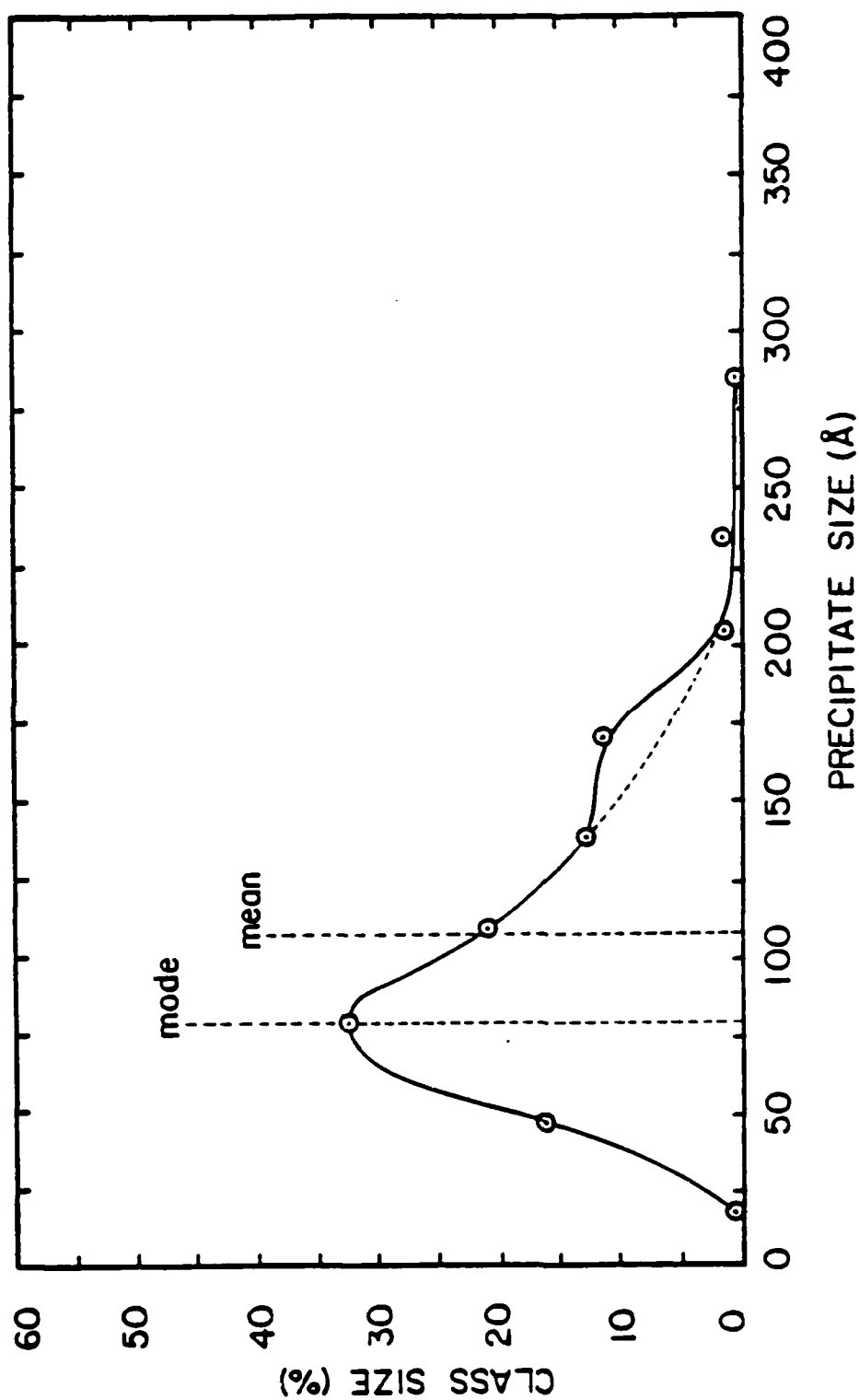
Figure 89.   Fine Nb(C,N) precipitate size distribution
for short time heat treatment--40 seconds at
1100 degrees C.

of the fine precipitates are seen in Figures 87-89.
No fine precipitates were observed at 10 seconds and
no SAD evidence for V(C,N) was found. Once again, the
mean precipitate size exhibits a maximum in the vicinity
of 20 seconds and all particles for this hold time are
coarser than those observed at lower temperatures.
All individual size distributions are broad and
unimodal.

It appears that at 1100 deg.C the V(C,N) has gone
into solution although these may be fine V(C,N) at 5
seconds.

The fine Nb(C,N) precipitates probably form due
to coarsening of Nb(C,N) precipitates that were
probably part of the fine dispersion present at
lower temperatures rather than nucleation and
growth of Nb(C,N) precipitates at 1100 deg.C. The
initial mean precipitate size variation was probably
due to initially preferential dissolution of fine
precipitates or coarsening of Nb(C,N) prior to
dissolution of Nb(C,N).

4.6.4.4. 1200 Degrees C.

The mean particle size of Nb(C,N) increases with
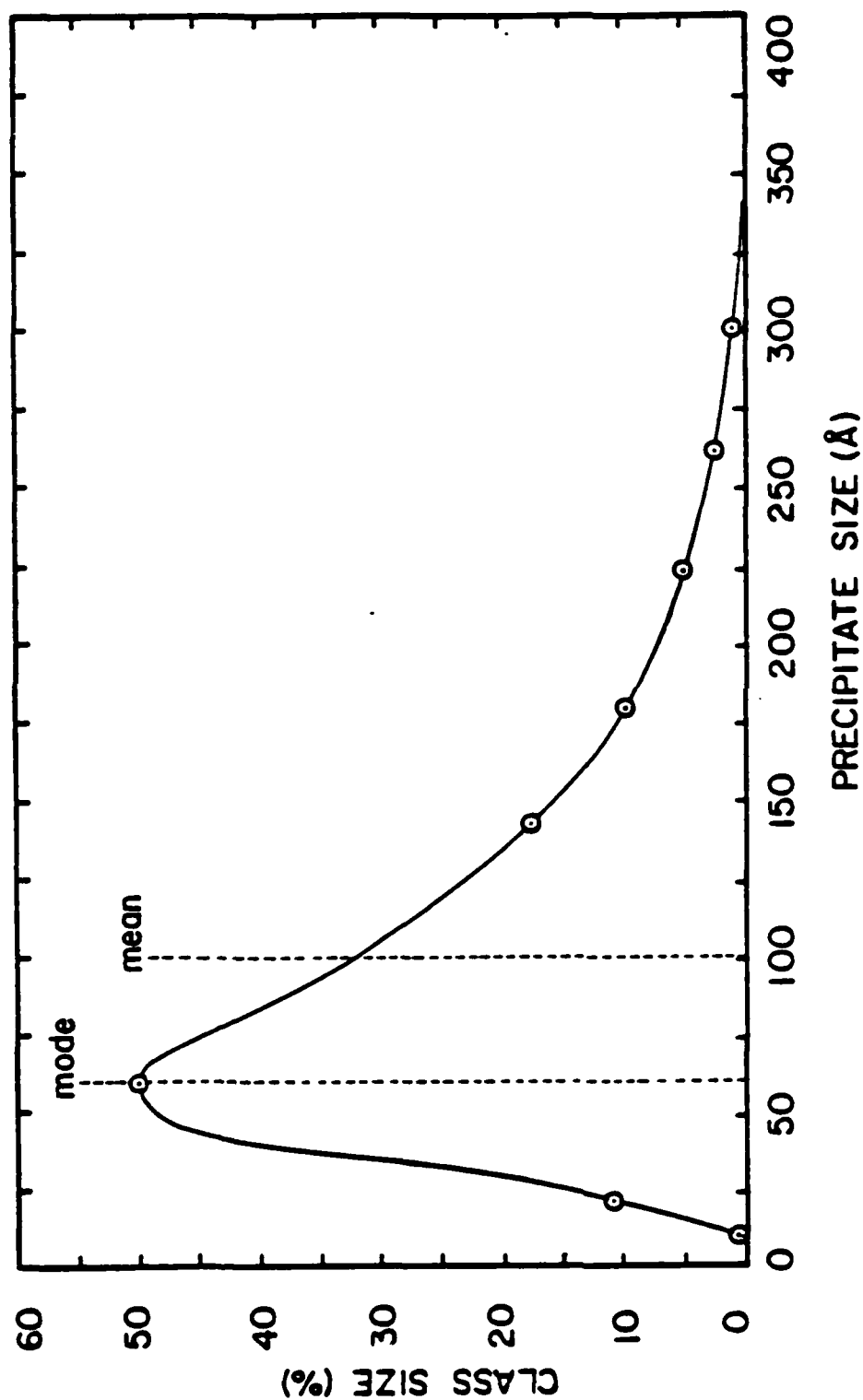
Figure 90.   Fine Nb(C,N) precipitate size distribution
for short time heat treatment-- 5 seconds at
1200 degrees C.
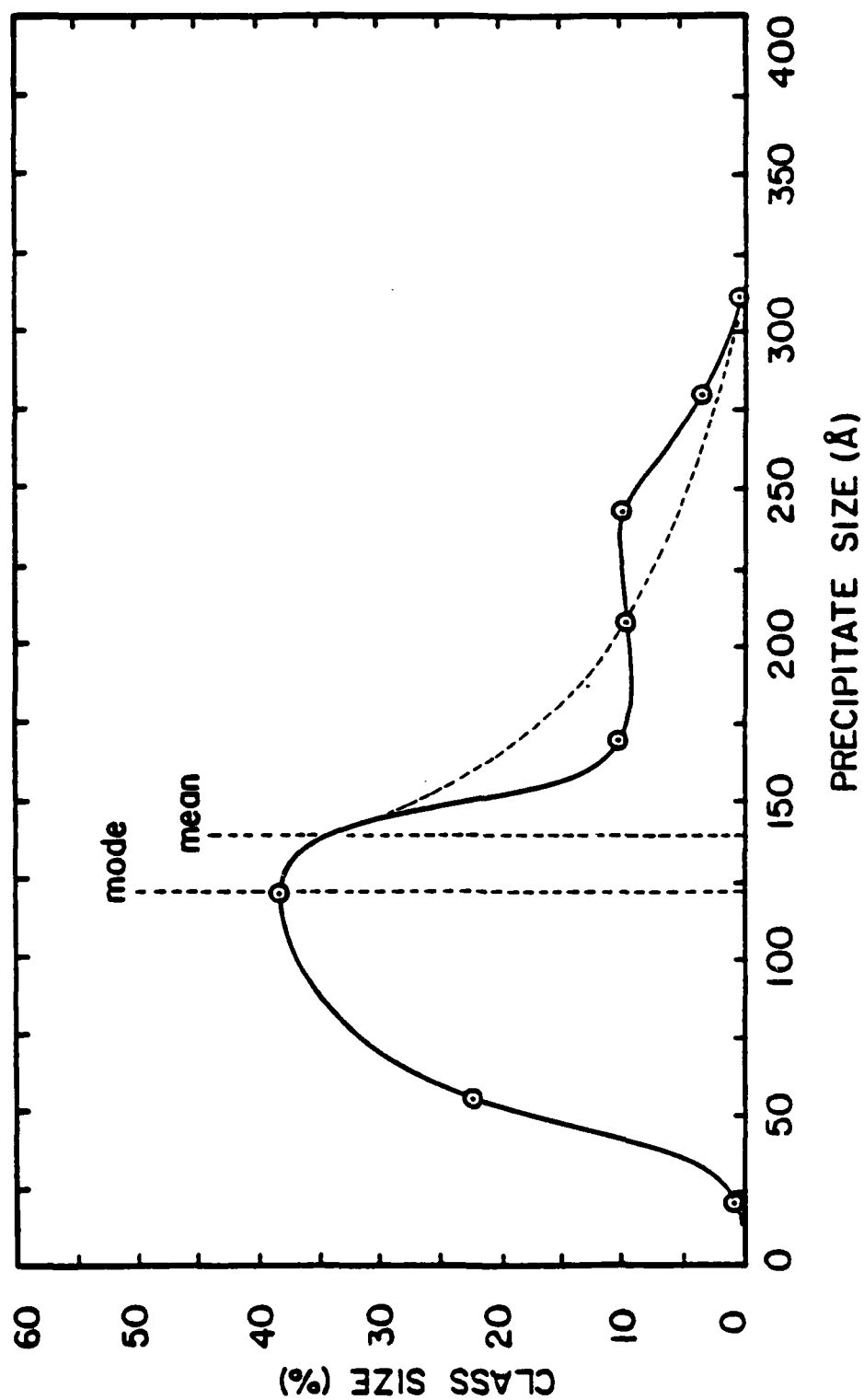
Figure 91. Fine Nb(C,N) precipitate size distribution for short time heat treatment--10 seconds at 1200 degrees C.

time to 10 seconds after which no particles are
observed, Figures 90 and 91.   This may be due to
particle coarsening and then very rapid dissolution.

4.6.4.5. 1300 Degrees C.

All precipitates are in solution.

4.6.5. Microalloy Precipitation During A Simulated Weld
        Thermal Cycle

Recall from Table 11 the thermal cycle from weld
Plate 12. TC2 is a nominal heat input of 3.35 KJ/mm
(85 KJ/in.) located in the near fusion zone region
of the heat affected zone.   This is a region of coarse
grained austenite. Specimen heat treatment conditions
were produced by rapidly quenching specimens that were
heated to various points along the thermal cycle via
Gleeble 1500.

Fine V(C,N) precipitates persisted to
temperatures between 1000 deg.C and 1100 deg.C.   Some
fine precipitates were present at 1100 deg.C but, it
is uncertain whether these precipitates are V(C,N) or
Nb(C,N).

Coarse cuboidal Nb(C,N) precipitates were observed in significant number density and persisted to temperatures between 1200 deg.C and 1300 deg.C.

5. Discussion

The welding of steel produces a fusion zone that cools primarily by the conduction of heat through the material being welded. It is this heat from the fusion weld, flowing outward that produces changes in the size, microstructure and properties of the HAZ.

The size of the HAZ is determined by weld parameters such as heat input, joint geometry and base-plate thickness. Within this region, portions are fully austenitized while others are partially austenitized or just heated. The transformation products of the HAZ for a particular steel are the result of prior austenite structure and cooling rate which is also dependent on weld parameters.

This study is an attempt to understand the interrelationship of welding parameters, microstructure, and properties. Microstructure is deemed the fundamental factor relating welding parameters to HAZ mechanical properties.

To understand these fundamental relationships, heat flow in the HAZ is related to weld parameters and in turn, austenite and transformation product microstructural evolution. Finally the relationships between structure and mechanical properties is investigated.

In order to model microstructural evolution in the HAZ
during arc welding, a thermal model for the welding process
must be established. This model can then be utilized in
conjunction with kinetic equations that describe thermally
activated microstructural processes to rationalize
microstructural evolution over the weld thermal cycle.

Heat flow in welds as mentioned in section 2, can be
modeled by an analytical approach after Rosenthal.[7]
This method involves solution of a differential equation
in closed form. Achieving the solution in closed form
requires a number of simplifying assumptions which are
the primary weaknesses of the approach. These
assumptions include (a) thermal properties and boundary
conditions are temperature independent, (b) weld
plates have infinite or semi-infinite dimensions,
(c) convection and radiation are ignored, (d) infinite
temperatures are computed at the source, (e) weld bead
characteristics are ignored and (f) simple heat source
characteristics.

Realistically, the thermal parameters vary with
temperature, distribution of the heat sources for
different processes can have different geometries such
as a point source, a linear line source, a circular
plane source, in addition to the electrode

characteristics. Weld preparation concerning joint design
and finite plate dimensions also affect the boundary
conditions.

Although the Rosenthal closed form solution approach
has several weaknesses it does, however, predict the
general functional relationship between thermal cycle, heat
input and position in the HAZ.

Heat flow in welding has also been represented by
numerical method solutions, such as finite element
methods (FEM) and finite difference methods (FDM). These
are somewhat more sophisticated in that they can account
for temperature and time variations of thermal
parameters, more complex boundary conditions, i.e.
radiation and convection, more complex heat sources, e.g. a
molten metal pool that is undergoing solidification.
[6,20-25,95]

These numerical method approaches are cumbersome and
costly. However, more sophisticated, volumetric approaches
to the heat source that include variable flux density have
been developed to more closely approximate actual welding
conditions.

The following sections are presented in an effort to
explain the basis for which a heat flow model of a
temperature distribution has been developed.

5.1. Theoretical Thermal Cycle Modeling

Initially, the following heat flow models were chosen
for modeling the experimental data:

(a)   moving point source; semi-infinite slab

(b)   rapidly moving point source approximation

These were chosen on the basis of observed weld pool
and HAZ cross-section geometries.

The differences between the various theoretical models
were investigated for the welding conditions employed in
this study.   The thermal parameters utilized are listed in
Table 13.   Rykalin [15] has recommended thermal diffusivity
and conductivity values at approximately 500 deg.C for use
in the theoretical equations.   The higher temperature
parameters were examined to see if better fits to
experimental data could be obtained in the vicinity of the
peak temperatures.

A comparison of models (a) and (b) indicated that the
largest differences occurred during the heating period for
all heat inputs.   Small differences in peak temperature and
even smaller differences in temperature during the cooling
period existed for all the heat inputs.   The differences
were greater for the higher heat inputs (lower welding
speeds).   Despite the relatively small differences between

Table 13

Heat Flow Parameters for Various Theoretical Thermal Cycles

Appendix 4 Fig.	Theoretical Temperature (deg.C)	Thermal Diffusivity cm^2-sec-C	Thermal Conductivity (cal/cm-sec-C)	Arc Efficiency n
Plate 9 TC 2 : Nominal Heat Input---1.97 KJ/mm Experimental Temperature---881 deg.C Position from FZL---0.88 mm				
141	1160-1163	0.08	0.10	0.9
142	1140-1141	0.06	0.08	0.9
143	1120-1123	0.06	0.08	0.8
Plate 12 TC 2 : Nominal Heat Input---3.35 KJ/mm Experimental Temperature---1380 deg.C Position from FZL---0.39 mm				
144	1355-1373	0.08	0.10	0.9
145	1353-1362	0.06	0.08	0.9
146	1339-1353	0.06	0.08	0.8
Plate 2 TC 1 : Nominal Heat Input---4.92 KJ/mm, Experimental Temperature---1098 deg.C Position from FZL---1.52 mm				
147	1156-1177	0.08	0.10	0.9
148	1146-1164	0.06	0.08	0.9
149	1131-1146	0.06	0.08	0.8

models (a) and (b) it was not deemed feasible to use them interchangeably.

In order to compare the various heat flow models with experimental data, an account must be taken of the different datum to which position is referenced. In the theoretical models, position is referenced to the center line of the weld whereas in the experimental data it is referenced to the fusion line by means of metallograph. Therefore, the position(s) associated with the melting point isotherm must be specified as a function of heat input and the particular theoretical model being employed. This position vector is then added to the experimentally determined position vector, referenced to the fusion line. The total position vector, thus obtained, is referenced to the weld center line and is associated with the experimentally determined thermal cycle. This total position vector is utilized to calculate the theoretical thermal cycle for that position.

Consider model (a) whose governing equation is:

$$(5.1) \qquad T - T_o = \frac{q}{2\pi\lambda R} \cdot \exp(\frac{-v}{2a} \cdot (R + \varepsilon))$$

where,

$$R = (\varepsilon^2 + Y_O^2 + Z_O^2)$$

$$\varepsilon = x_O - \nu t$$

(5.2) $$T - T_O = (A/D \cdot \exp(-D \cdot B)$$

$$A = q/2\pi\lambda$$

$$B = \nu/2a$$

$$C = Y_O^2 + Z_O^2$$

$$D = ((x_O - \nu t)^2 + c)^{0.5}$$

It is necessary to define the locus of points of maximum temperature by differentiating equation (5.1) with respect to time and setting the expression equal to zero:

(5.3) $$\frac{\partial T}{\partial t} = \frac{A (x_O - \nu t)\nu}{((x_O - \nu t)^2 + C)^{1.5}} \cdot \exp (D) \cdot$$

$$\frac{AB}{((x_O - \nu t)^2 + C)^{0.5}} \cdot \frac{-(x_O - \nu t)\nu}{((x_O - \nu t)^2 + C)^{0.5} - \nu} \cdot \exp (D)$$

Equation (5.3) reduces to:

(5.4) $(x_o - \nu t) \cdot ((1 + B) \cdot ((x_o - \nu t) + C^2))^{.5} + B((x_o - \nu t) + C^2) = 0$

Since

$\varepsilon = x_o - \nu t:$

(5.5) $\varepsilon + \varepsilon B(\varepsilon^2 + C)^{0.5} + B(\varepsilon^2 + C) = 0$

This equation was solved numerically to determine the time
to maximum temperature at a given position. Substitution
in Equation (5.1) results in the maximum temperature,
T_{max}. An iterative procedure was then employed to
determine the position vector associated with
$T_{max} = T_{melting\ point}$, the required quantity. The
melting temperature was experimentally determined as 1465
Deg.C by melting an instrumented specimen in a programmed
thermal cycle test apparatus (Gleeble).

Consider model (b) whose governing equation is:

(5.6) $T - T_o = \dfrac{q/\nu}{2\pi\lambda t} \cdot \exp(\dfrac{-r^2}{4at})$

where,

$$r^2 = Y_O{}^2 + Z_O{}^2$$

(5.7) $T - T_O = (A/t) \cdot \exp(-B/t)$

where,

$A = (q/\nu)/(2\pi\lambda)$

$B = r^2/4a$

Differentiating (5.6) and setting the result equal to zero:

(5.8) $-\dfrac{\partial T}{\partial t} = \dfrac{A}{t^2} \cdot \left(\dfrac{B}{t} - 1\right) \cdot \exp\left(\dfrac{-B}{t}\right) = 0$

$\partial T/\partial t = 0$ when $(B/t) - 1 = 0$

(5.9) $t_{max} = r^2{}_{max}/4a$

Substituting in (5.6)

(5.10) $T_{max} - T_O = (A/B) \cdot 1/e$

Setting T_{max} = $T_{melting\ point}$:

(5.11) $r_{fusion\ line}$ = $\dfrac{2qa}{[\ \pi\nu\lambda e(T_{mp}-T_{o})\ ]^{0.5}}$

To reiterate, these calculated fusion line positions
are referenced to the centerline and can therefore be added
to the positions associated with experimental data that are
referenced to the fusion line. The total position vector
obtained is utilized in the pertinent theoretical model to
model the thermal cycle at the given thermocouple
position.

The experimental data for several thermal cycles in
nominally 1.97, 3.35, 4.92 KJ/mm (50, 85, 125 KJ/in.) welds
are depicted in Appendix 4 along with the theoretical
determined thermal cycles. The local heat inputs were
employed for the theoretical calculations and due to the
relatively small differences between models (a) and (b) on
the scale of these plots a single theoretical curve was
utilized in each plot.

At nominally 1.97 KJ/mm (50 KJ/in.) and a distance from
the fusion line of 0.88-mm the theoretically predicted peak
temperature ranges from approximately 1120 deg.C to 1160
deg.C as the arc efficiency and thermal parameters were
varied within reasonable values. The experimentally
determined peak temperature is 880 deg.C, significantly

less than the theoretical value. In addition, the

theoretical models substantially underestimated temperature

in the cooling regime. Reasonable variations in the model

parameters were obviously unable to account for the

differences between theory and experiment. It would seem

that in this instance the theoretical models are

inadequate. Also, utilization of a more sophisticated

numerical method approach in which variable thermal

parameters are possible would not produce an adequate fit

between theory and experiment.

At nominally 3.35 KJ/mm (85 KJ/in.) and 0.39 mm from

the fusion line the theoretically predicted peak

temperatures ranged from 1340 deg.C to 1373 deg.C. The

experimentally determined peak temperature is 1380 deg.C so

that the peak temperature is more accurately predicted for

this set of conditions. However, once again the

theoretical models underestimate temperatures during the

cooling period. The models would appear inadequate in this

instance, as well.

At nominally 4.92 KJ/mm (125 KJ/in.) and 1.52 mm from

the fusion line the range of theoretically predicted peak

temperatures is approximately 1130 deg.C to 1180 deg.C, and

the measured peak temperature is 1098 deg.C, significantly

lower. The temperatures in the cooling regime are again

significantly underestimated by the theoretical equations.

The measured peak temperature is plotted against
distance from the fusion line for the various nominal heat
inputs in Figures 92-94. The scatter in data for each heat
input is probably due to the scatter about the nominal heat
input. However, the trends are consistent in that peak
temperature decreases with distance from the fusion line at
a given heat input and increases with heat input at a given
distance from the fusion line. The measured peak
temperatures are compared to the theoretically determined
peak temperatures as a function of distance from the fusion
line in Figure 92-94. It is interesting to note that as
heat input increased the theoretical models at first
overestimate and then generally underestimate the peak
temperature. At an intermediate nominal heat input of 33.5
KJ/cm the theoretical models appear to adequately predict
the peak temperature

Christensen, and others [16, 96] cite the fact that the
Rosenthal point source equation adequately predicts the
thermal cycle for locations near the plate surface, i.e.
those that will closely approximate a semi-infinite slab.
The measurements in the present study were made well below
the surface. It is also possible that the weld pool
solidification and the effects of finite plate thickness
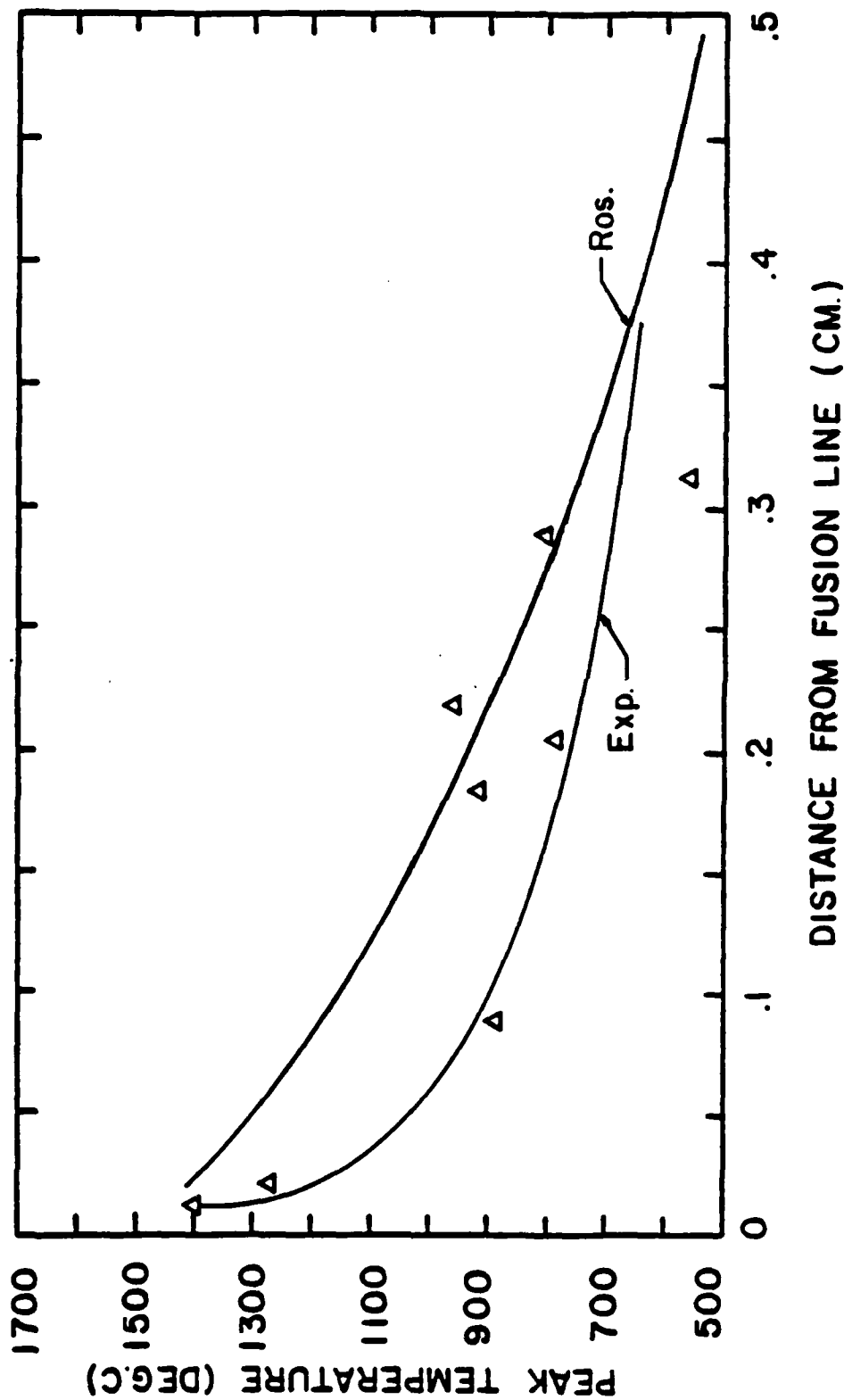
Figure 92. Comparison of experimental to theoretically determined (Rosenthal Equations) peak temperatures as a function of distance from the fusion zone in the HAZ for nominal low heat input weld, (1.97 KJ/mm).
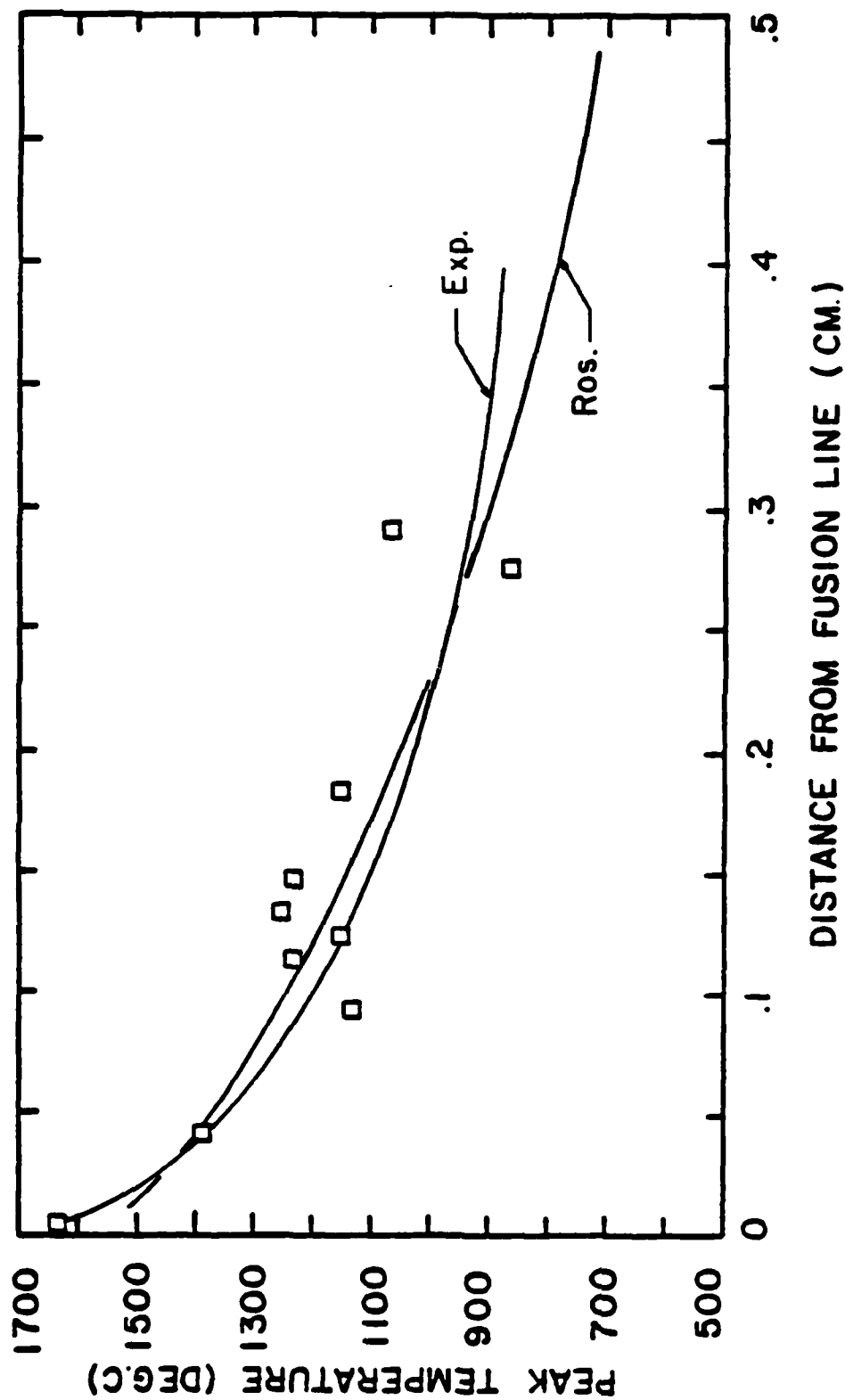
Figure 93. Comparison of experimental and theoretically
determined (Rosenthal Equations) peak
temperatures as a function of distance from the
fusion zone in the HAZ for nominal low heat
input weld, (3.35 KJ/mm).
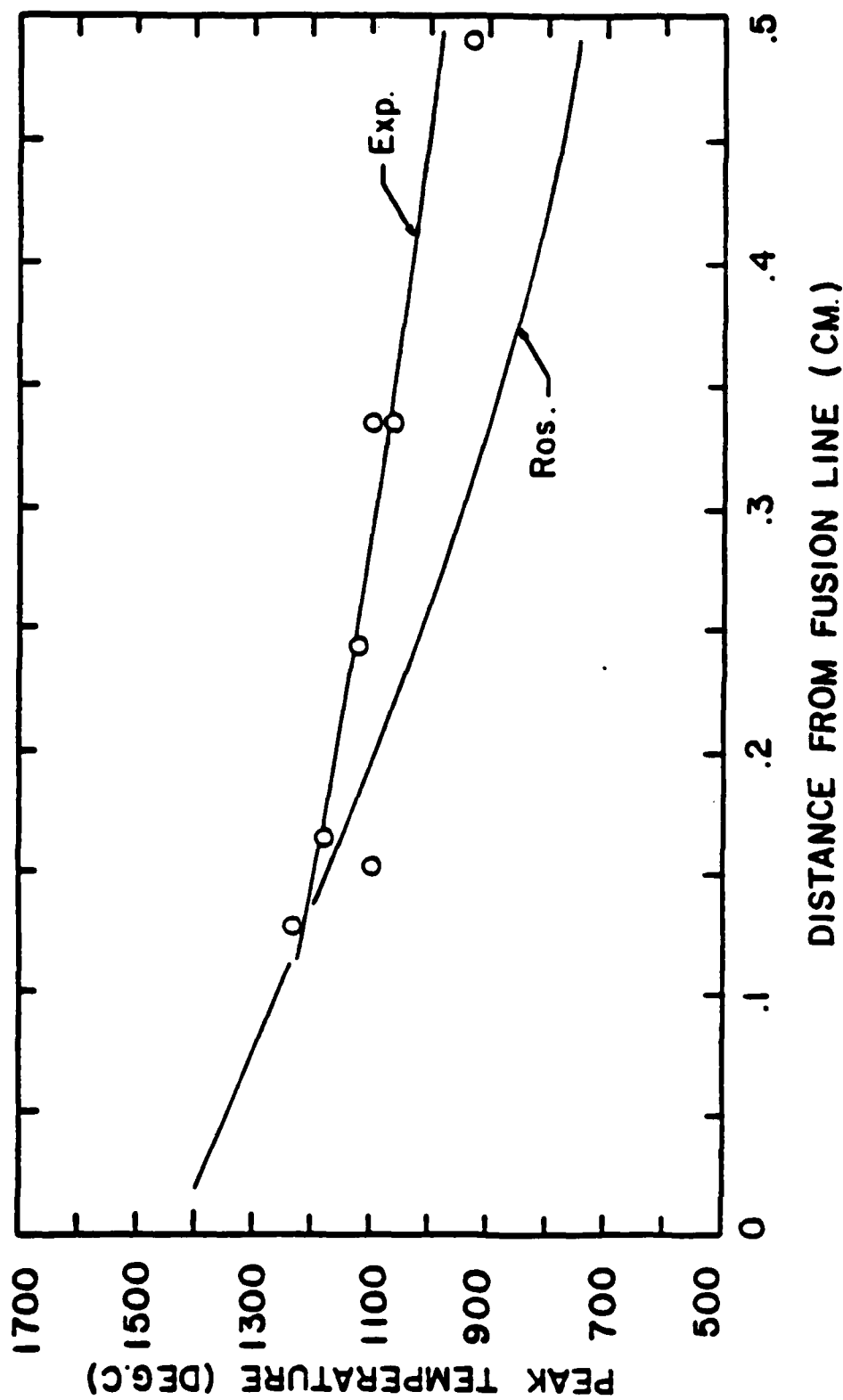
Figure 94.   Comparison of experimental and theoretically
determined (Rosenthal Equations) peak
temperatures as a function of distance from the
fusion zone in the HAZ for nominal low heat
input weld, (4.92 KJ/mm).

could account for the observed discrepancies.

Substitution of extremum in thermal parameters could not create an envelope sufficiently wide to account for differences between models and actual data.

In general, it would appear that the Rosenthal-type theoretical equations for a moving point source on a semi-infinite slab are inadequate for modeling thermal cycles under these conditions. However, they still predict the correct, general form of the thermal cycle and the proper functional realationships between the thermal cycle, heat input and distance from the fusion zone. As a result they will be employed as empirical fitting equations in section 5.2 for overall data reduction to provide a thermal model for subsequent microstructural modeling of HAZ evolution.

5.2 Empirical Model

The Rosenthal-type equations were discussed in the previous section and it was concluded that they do not quantitatively predict the thermal transient as a function of heat input and position in the HAZ. However, the Rosenthal-type equations do predict the general shape of the thermal transient.

In view of this, efforts were made to establish a
statistically based interpolation scheme for submerged arc
welding of this geometry. Fitting of the data was
accomplished, via a least-squares scheme. Four variables
are employed in developing the model for this fit: heat
input, position, time and temperature. Although fitting is
based on a model equation similar to Rosenthal-type
equations the fitting is persued on a purely empirical
basis.

The method for modeling consists of dividing the
thermal cycle into three regions of interest; a heating
region, a peak temperature region, and a cooling region.
Each region from numerous thermal transient curves are then
plotted together and empirical constants are found. These
constants result from the correlation of various weld
parameters and are placed into a form of the Rosenthal
rapidly moving point source, thereby achieving an empirical
fit for each region of interest.

The rapidly moving point source was chosen for the
heating and cooling cycle of the thermal data because of
the equation's ability to predict the general shape of the
experimental thermal transient curve and to qualitatively
relate welding parameters with the time and temperature
data.

Assume the overall data could be fitted by the general equation:

(5.12) $T = A/t \cdot \exp(-B/t)$

This is the Rosenthal rapid point source except that A and B are now being allowed to assume any value to fit data instead of the values:

$$A = \frac{(q/v)}{4\pi\lambda}$$

$$B = \frac{r^2}{4a}$$

The general equation above could be separated into two parts. One part of the equation dominates the heating side and the other part dominates the cooling side of the thermal cycle.

The data from the heating side of empirical temperature curves was plotted as the log temperature versus the inverse time function to yield a linear function according to equations (5.13) and (5.14) below:

(5.13) $T = A'\exp(-B'/t)$

(5.14) $\text{Log } T = \text{Log } A' - B'/(2.303t)$

A' and B' are therefore specified for each set of
experimental conditions of heat input and position . These
empirical coefficients were then statistically correlated
to welding parameters making the A' and B' terms functions
of heat input and position.   In this case the position in
the HAZ is referenced from the fusion line.   The fit
parameters A' and B' from equation (5.13) were correlated
via a least squares fit.

(5.15) $A' = 1.599 - 0.891(r)$

(5.16) $B' = 5.61 + 0.038\dfrac{(q/v)}{r}$

(5.17) $\text{Log } T = 1.599 - 0.891(r) - \dfrac{[5.61 + 0.038(q/v)]}{r \cdot t}$

(5.18) $T = \dfrac{39.72}{\exp\left(2.049\, r^2 t + 12.903\, r + 0.087(q/v)\right)}$

where,

r = distance from the fusion zone (cm)

q/v = heat input (KJ/cm)

T = temperature (deg.C)

t = time (sec.)

Equation (5.18), empirically derived above, produces a
heating curve profile which is characteristic of the actual
thermal transient data and should strictly be used for the
welding parameters used in this investigation.

As previously stated, the empirically determined thermal cycles, when compared with the Rosenthal-type equation, were underestimated in the cooling region. However, the form of this equation does predict the general shape for HAZ cooling. The cooling portion of the thermal cycle could be fitted by the equation:

$$(5.19) \qquad T = C'/t^n$$

$$(5.20) \qquad \log T = \log C' - n \log t$$

The fitting parameters C' and n are specified for each set of conditions of heat input and position. Slight variations in the n value are found to occur for various thermal cycles but are contained within a small range of values about 0.5. The value n = 0.5 will be assumed for all conditions.

Correlation of the C' term with heat input and position yields:

$$(5.21) \qquad \log C' = 2.047 + 1.069 \log(q/v)$$

$$(5.22) \qquad T = \frac{111.43 \ (q/v)}{t^{0.5}}$$

An empirical fit of the data for the peak temperature

was performed as a function of heat input and position.

(5.23) $T_p = K_{(\frac{q/v}{r})}^n$

(5.24) $\text{Log } T_p = \text{Log } K + n \text{ Log }_{(\frac{q/v}{r})}$

(5.25) $\text{Log } T_p = 2.656 + 0.16 \text{ Log }_{(\frac{q/v}{r})}$

(5.26) $T_p = 452.9 \cdot _{(\frac{q/v}{r})}^{0.16}$

A temperature 100 deg.C below the peak temperatures was
assumed to be the boundary of the peak temperature region.
This boundary temperature was chosen on the basis of
inflection points in the plotted experimental data that
indicated the onset of the peak region.

A parabolic function was assumed for the peak
temperature region with the peak temperature at the maximum
of the parabola. The choice of a parabola as the function
was somewhat arbitrary but provided a reasonable
apprroximation to the shape of typical thermal cycles.

The fit parameters A′,B′,and C′ all represent the
results of individual fits in the various regimes,
Figure 95 rather than those that would result from an
overall fit of the general equation:

(5.27) $T = (A/t^n)\exp(-B/t)$
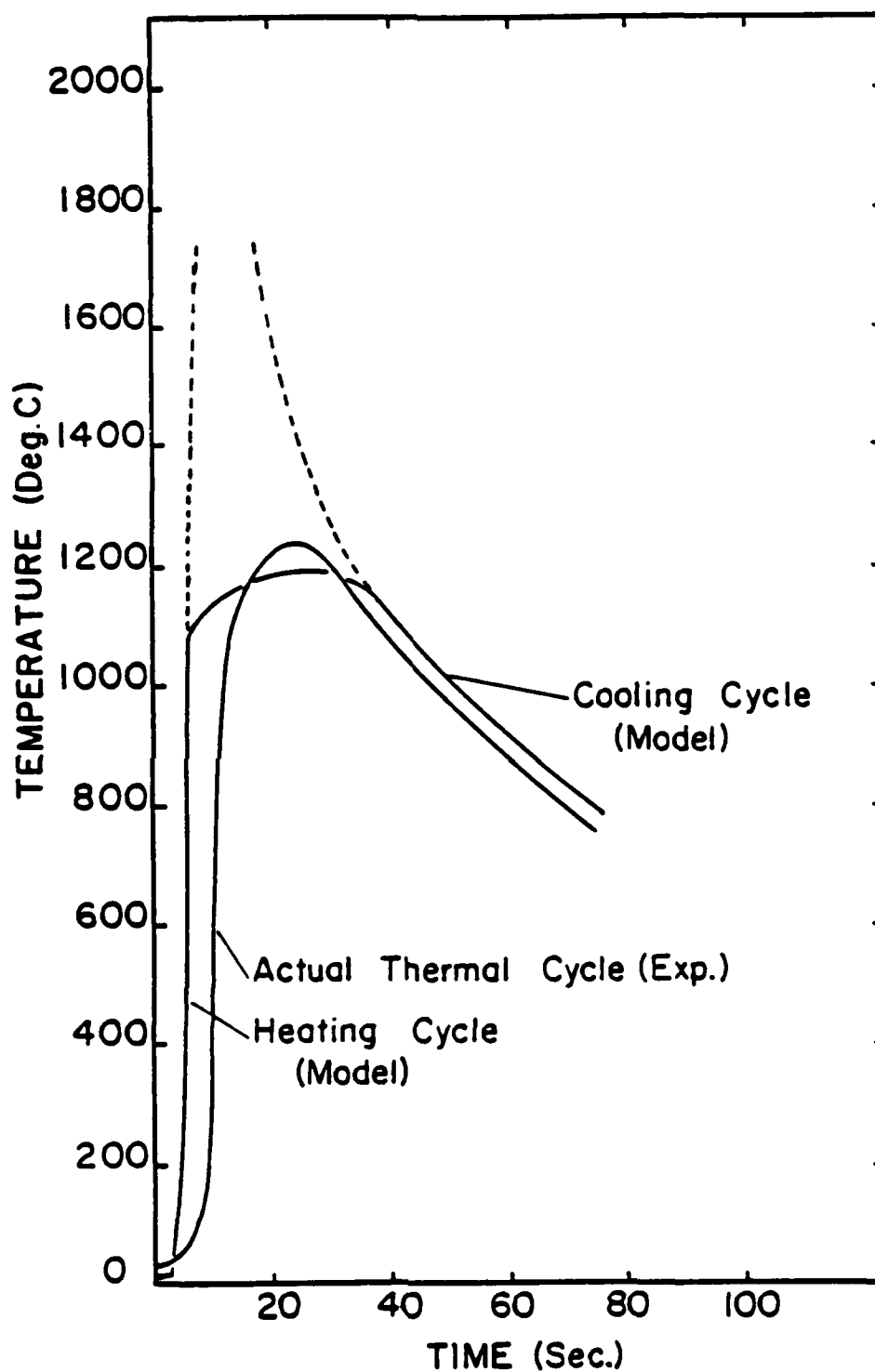
Figure 95.   Comparison of experimental thermal transient
             curve to the three regimes (heating regime.
             peak regime, cooling regime) of theoretically
             determined thermal curves.

Therefore, each fitting equation can only be utilized in the regime from which it was determined and multiplication of the heating and cooling equations together to obtain an overall fit is not appropriate.

A more sophisticated and comprehensive fitting approach based on the results described above would be to statistically fit the general equation and therefore the entire thermal cycle at once. The present approach was deemed appropriate to obtain an adequate thermal model for subsequent microstructural modeling.

With an overall empirical fit of the data, utilizing the general form:

(5.27) $T = (A/t^n) \cdot exp(-B/t)$

The correlations between A, B, n, and welding parameters (heat input, position) may be compared with those theoretically derived. This comparison might indicate, in more detail, the nature of deficiencies in theoretical modeling and suggest as well as additional important parameter more appropriate general approaches.

It should also be noted that the greatest scatter in the various data correlations occurred for conditions of high heat-input and positions close to the fusion line. This suggests that for these conditions, weld pool effects

may be significant. Potential sources of variations from
the weld pool are discussed in the next sub-section.

In a similar investigation using the same temperature
acquisition techniques developed in this research project,
Muth [97] obtained similar results when comparing
experimental results with a Rosenthal-type equation. Also,
a statistical correlation of heat input and position by
Muth was shown to be in agreement with the results of this
investigation.

5.3 Weld Pool Configuration and Thermal Transients

The considerations mentioned previously do not account
for all the discrepancies in the mismatch of experimental
and theoretical thermal cycles. These discrepancies must
be discussed in relation to material properties and weld
pool characteristics. In the theoretical equations the
thermal diffusivity and conductivity are the only means for
describing heat flow rates thru the material. However weld
pool interactions, material orientation and chemistry are
other considerations in heat flow in the HAZ. Although
complex, weld pool shape and interactions at the
liquid-solid metal interface have a large effect on heat
transport from the weld pool.[98,144] Processes in the

weld pool can produce variations in solidification time,
heat evolution from phase changes, and a non-planar heat
front associated with the "weld bay" effect.

Consideration of weld pool effects in the heat
transport problem does simplify the conceptual
understanding of detailed response in the peak temperature
region of the thermal cycle and explains the slower cooling
rate in the HAZ. However, quantitative modeling is very
complex. Although the understanding of the shape of the
temperature curves may be improved, complications still
exist in expressing the boundary conditions for
mathmatically modeling various parameters and applications.

Due to the digging effects of arc pressure and weld
pool stirring, a deep center penetration and wide surface
weld bead may develope. Heat isotherms are conducted along
lines perpendicular to the fusion zone and at positions in
the bay region, indicated in Figure 96(a), heat is received
along a non-planar front. At distances removed from the
bay region, the isotherms approach a hemispherical shape.
The thermal cycle measured in the bay region is
characterized by an inflection in the heating portion of
the cycle in the curve, Figure 96(b). The inflection
results from heat flow to the bay region from different
directions and possibly at different times. Anomalies such
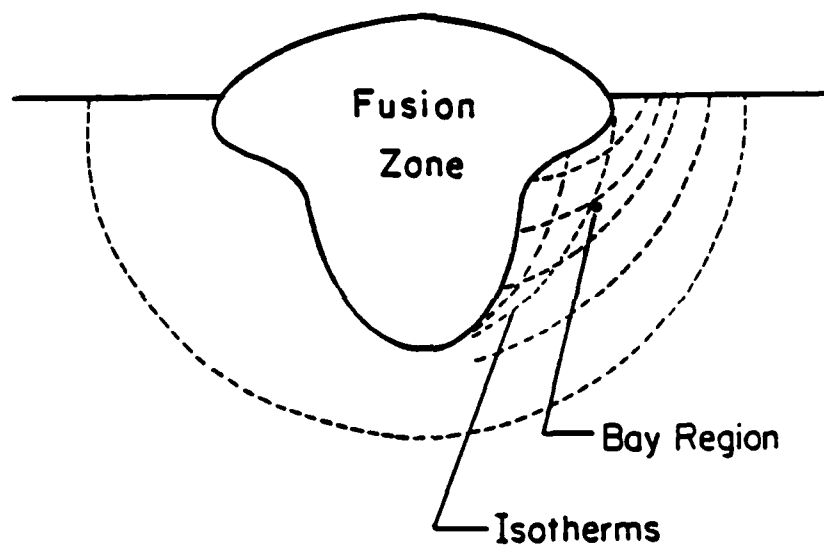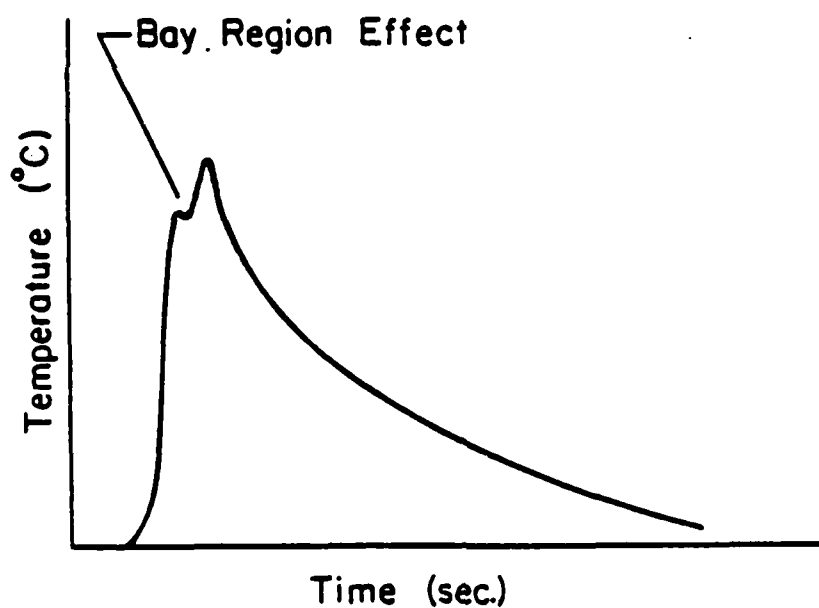
Figure 96.   Schematic representation of weld pool
              configuration and interaction.
              (a) Location of bay region with respect to
                  fusion zone and movement of isotherms.
              (b) An inflection in the thermal cycle
                  with reference to a location in the bay
                  region.

as the bay region and thermal cycle effect has been
observed by other investigators.[5,99,100,101,102,144]

The bay region was observed in most of the experimental
welds. Excellent correlations of the bay region and
inflections in the thermal transient curves, were
observed. The greatest effects of the bay region were
noted in thermal couple positions near the fusion zone with
large weld shape bays. In contrast, a lesser effect of the
bay region was seen at distances removed from the fusion
zone bay and under conditions in which an eliptical weld
shape was produced.

Position of the thermocouple near the fusion zone
appeared to have the largest effect on the thermal
transient curve. The start and finish time of the
inflection increased as the fusion zone was approached.

In general, heat input for the various welds changed
the size and configuration of the bay region. High heat
inputs produced greater weld bays and lower heat inputs
produced more elipitical shaped welds. Also, as heat input
increased, thermal peaks for the temperature curve
broadened with an increased number of inflections noted
along the peak of the curve. These effects may account for
some of the previously noted data scatter for these
conditions.

Peak temperatures in the thermal transient data appeared to have little to no effect on the formation of the bay region, but the probability of formation of the bay region is dependent upon the heat input. Therefore, the correlation and the degree of inflection in thermal data appear to be solely dependent on position in the HAZ. It should be noted that the thermocouple itself did not play a role in the formation of a bay.

To summarize, the heat flow in the HAZ of a single pass submerged arc weld could not be adequately modeled via a Rosenthal-type closed form solution. Evidence suggests that heat source and weld pool effects in addition to finite plate dimensions are the primary reasons for difficulties. It is possible that numerical method solutions to the heat flow problem, currently available, could provide a fundamentally-based thermal model.

Nevertheless an empirical thermal model was determined that predicts the thermal cycle as a function of heat input and position and will be employed in subsequent microstructural modeling.

5.4 Microstructure in the HAZ

It would be desirable to formulate a model of HAZ

microstructural evolution with which predictions could be made based on such parameters as weld geometry, base-plate chemistry and heat input. A complete model actually consists of three parts.

The first part is a thermal model in which the thermal history is specified for each location in the HAZ as a function of welding conditions. Establishment of the thermal model was discussed in the previous section.

The second part involves modeling of austenite microstructural evolution at each location as a function of thermal history. In the case of microalloyed HSLA steels this necessitates consideration of coarsening/dissolution behavior of various microalloy precipitate dispersions and their effect upon austenite grain coarsening behavior.

Usually the information on thermally activated processes such as grain growth, precipitate coarsening and precipitate dissolution are modeled and data obtained under isothermal conditions. The weld thermal cycle represents athermal conditions so that the validity of integral procedures to utilize the isothermal data needs to be investigated.

Austenite microstructural evolution in the HAZ is an important aspect of welding microalloyed steel since it, in part determines the nature of transformation product

microstructure and therefore mechanical properties in the
HAZ.

Finally, in the third part, some means for predicting
the transformation product microstructure must be
specified. This could prove difficult, on a strictly
fundamental basis since prior austenite microstructure,
local composition and cooling rate are all factors in
determining the nature of transformation products. In
fact, theoretical approaches to hardenability under
isothermal and continuous cooling conditions have met with
only limited success. In this work only indications of the
important parameters with regard to transformation product
microstructural evolution were studied and will be
discussed.

In summary, to formulate a model
microstructural evolution, specification of several
important parameters is required.

(a) Base-plate microstructure: important, this
includes the state of microalloy precipitation and
inclusion population. In general, the particle
dispersions present in the HAZ during welding are
derived from those present in the base-plate.

(b) Thermal history: The establishment of thermal
history as a function of position in the HAZ and welding

parameters such as heat input is required. By having an adequate thermal model, the athermal nature of the weld thermal cycle is fully described.

(c) Austenite microstructural evolution and associated thermally activated processes: In this regard kinetic equations of state as a function of temperature are required for grain growth and precipitate coarsening/dissolution.

(d) Transformation product microstructural evolution: The relative effects of prior austenite microstructure and cooling rate on transformation product microstructure must be specified.

Parts (a) and (b) have already been described and discussed. The following sections address austenite and transformation product microstructural evolution.

5.5 Austenite Microstructural Evolution

The overall objective is the decription of austenite grain growth, over the weld thermal cycle. A function of the following form needs to be specified and rationalized.

$$(5.28) \qquad D_\gamma = D_\gamma(T, t)$$

where,

D_γ= austenite grain size.

The thermal history can then be substituted into Equation (5.28) to derive austenite grain size as a function of time. Integration of grain growth can then be accomplished over the weld thermal cycle. As it stands, this represents an empirical approach to the modeling in that the underlying mechanisms involved with grain growth are not considered. The validity of the integrative technique for all kinetic equations of state will be examined in a subsequent section.

The presence of microalloy precipitates and inclusions in the austenite microstructure serves to complicate the description of austenite grain growth by the pinning of grain boundaries and thus the retarding of grain growth. It is then necessary to specify the conditions under which boundaries are pinned and therefore, the limiting grain size, in the presence of a particle dispersion. It is also necessary to describe the conditions under which boundary unpinning and grain growth can occur in order to fundamentally base the microstructural model.

Simple isothermal reheating experiments were performed to indicate the general austenite microstructural response

to reheating and to elucidate the fundamental mechanisms underlying austenite grain coarsening in this Nb-V microalloyed steel. In addition, quantitative kinetic equations derived from this data are necessary to test integral techniques for predicting microstructural evolution over a weld thermal cycle.

The isothermal austenite grain coarsening results are summarized in Figures 97(a) and 97(b). The data may be characterized by abrupt grain coarsening in the temperature range 1000 to 1100 deg.C and regimes of slow and rapid grain growth. The grain coarsening behavior is associated with the state of microalloy precipitation.

Various theoretical approaches have been made to grain growth in the presence of second phase particles.[36,37,146,147] The theories indicate that the limiting grain size of the microstructure is dependent upon the parameters of the particle dispersion, i.e. volume fraction (f) and particle size (r). Conditions for boundary unpinning have been described in terms of reduction in volume fraction due to dissolution and increases in particle size due to particle growth or coarsening.[37,48-50,148-153] Furthermore, boundary unpinning can result in normal or abnormal grain growth. The latter is particularly insidious in that several large
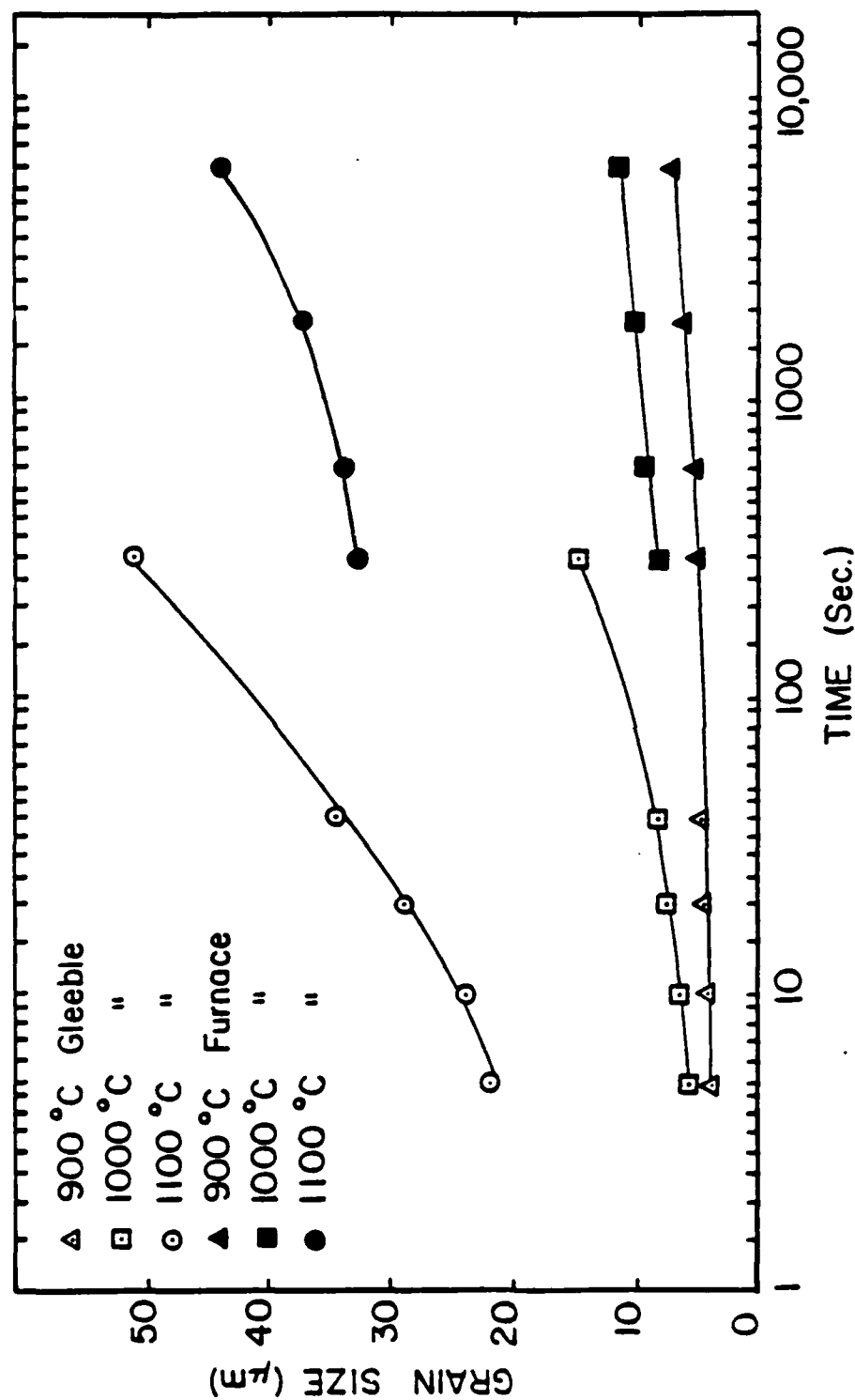
Figure 97(a). Summary of austenite grain size as a function of time for Gleeble and Furnace heat treatments.
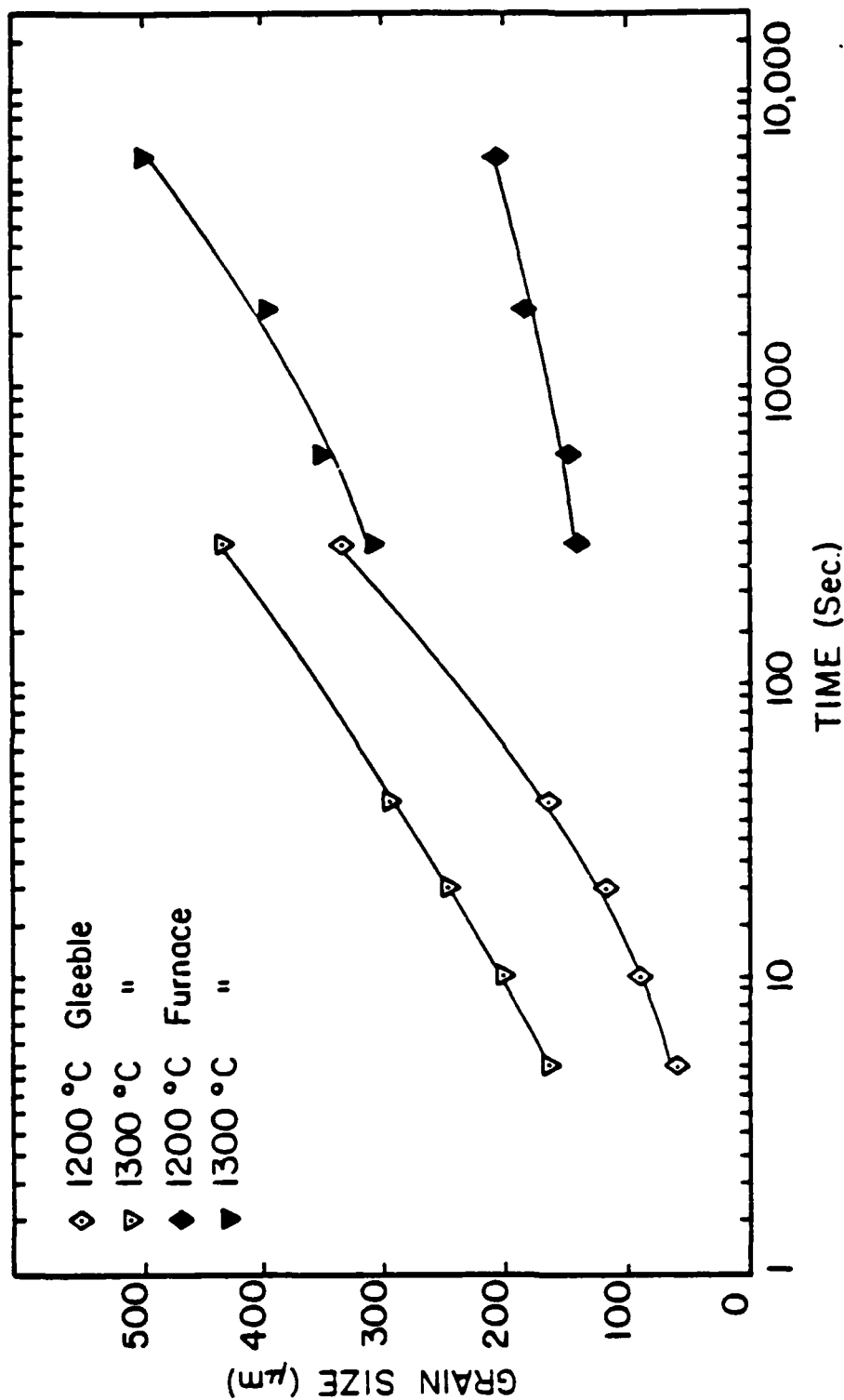
Figure 97(b). Summary of austenite grain size as a function
of time for Gleeble and furnace heat
treatments.

grains can grow catastropically at the expense of a fine
grained matrix. Thus, the nature of austenite grain growth
is intimitely associated with the scale of the particle
dispersion present.

In the Nb-V steel employed in this heat treatment
study, a fine dispersion of interphase V(C,N) precipitates,
and a coarser dispersion of Nb(C,N) precipitates were
confirmed by X-ray diffraction of an extracted precipitate
residue. One might then expect that if precipitate
dissolution is controlling grain coarsening the grain
coarsening temperature is correlated with an appropriate
precipitate solution temperature.

The solubility of NbC and VN microalloy precipitates
[161-164] in austenite is examined in Figure 98. This
figure indicates that VN completely dissolves at
approximately 1075 deg.C and NbC at approximately 1150
deg.C. It would appear that dissolution of the Nb based
precipitate is not responsible for austenite grain
coarsening behavior. Complete dissolution of VN occurs at
a slightly higher temperature than the onset of grain
coarsening but this could be accounted for by the greater
solubility of a carbonitride versus pure VN. In fact X-ray
diffraction of extracted precipitate residues from reheated
specimens showed the V-based precipitate completely
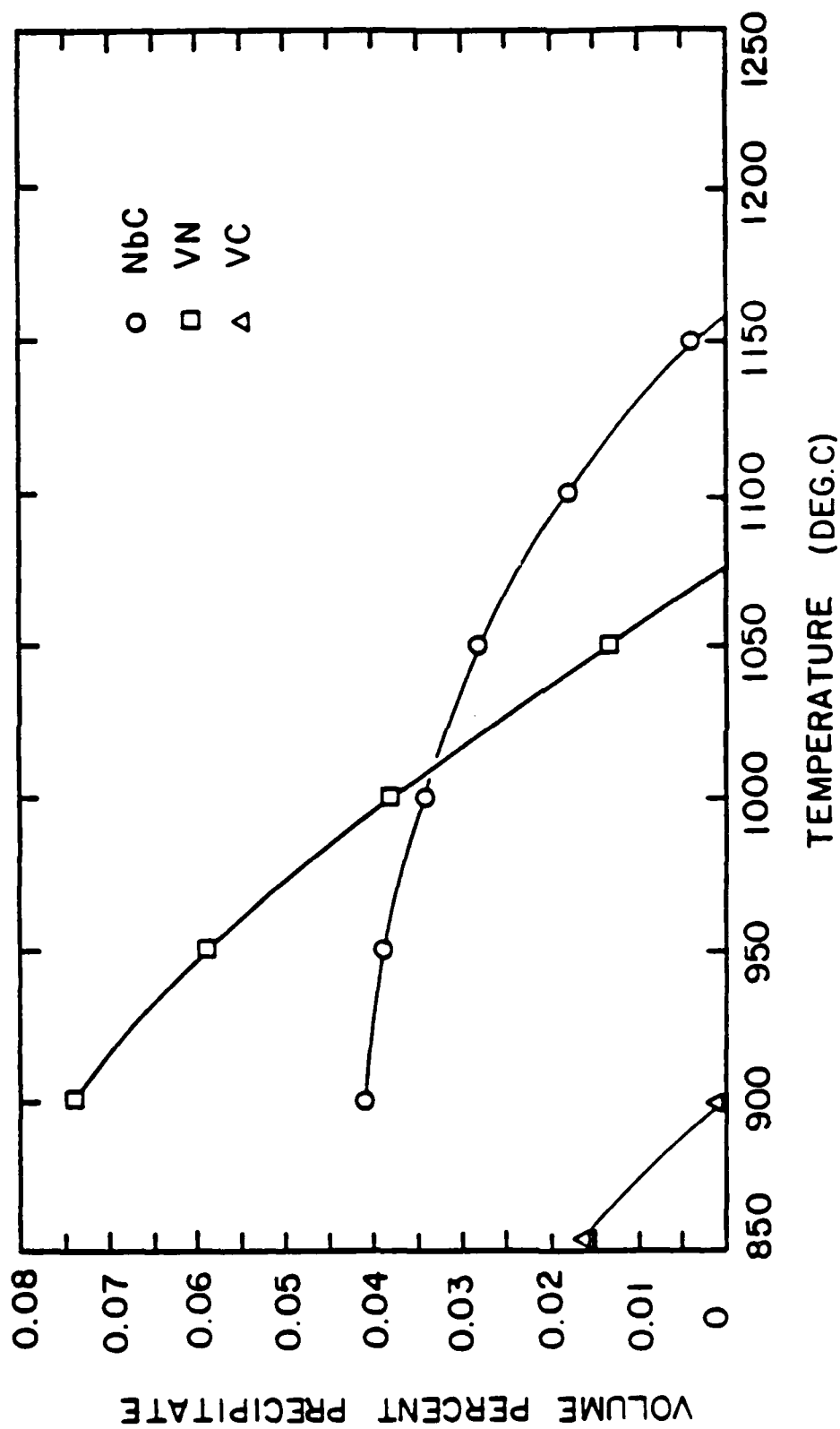
Figure 98.   Summary of theoretical precipitate volume
             percent as a function of temperature.

dissolved between 900 deg.C and 1000 deg.C. TEM
observations of extracted replicas also supports this
asertion. This would seem to support a vanadium
carbonitride with a lower solution temperature than VN as
the species controlling grain coarsening. It is unclear
whether the coarsening phenomena is soley due to particle
dissolution.

Gladman's criterion [37] is embodied in the following
equation:

$$(5.29) \qquad d_p crit = \frac{6D_o f}{\pi} \cdot (\frac{3}{2} - \frac{2}{Z})$$

where,

$d_p crit.$ = is a critical particle size for pinning.

D_o = matrix grain size

f = volume fraction of particles.

Z = ratio of the size of the largest grain to D_o

Actual particle sizes greater than $d_p crit.$ imply grain
boundary unpinning.

The criticle particle size may be calculated as a
function of temperature for the V(C,N) precipitate with the
following assumptions. The Z factor value may be
reasonably assumed to be 1.5. The limiting matrix grain

size is approximately 20μm. The volume fraction is the
equilibrium volume fraction at a given temperature,
calculated from solubility relationships. [84]

The assumption of an equilibrium volume fraction may be
invalid especially at short times. One might then expect
that specification of an equilibrium volume fraction of
precipitate is an underestimate of the actual volume
fraction. In addition, the presence of a carbonitride
results in a further ambiguity in calculation of the
equilibrium volume fraction.

Nevertheless the calculation was made for VN. The
minimum critical particle size prior to precipitate
dissolution is approximately 300Åm. Reference to
Figure 99 indicates the actual particle size prior to
complete dissolution of V-based precipitates is always less
than 300Åm. Therefore, particle coarsening is definitely
not controlling austenite grain coarsening.

The minimum critical particle size at any temperature
would be expected to decrease for a carbonitride since the
latter is less stable than VN. However, the critical
particle size would still not be diminished sufficiently
prior to complete dissolution for precipitate coarsening
control.

The variation in mean precipitate size depicted in
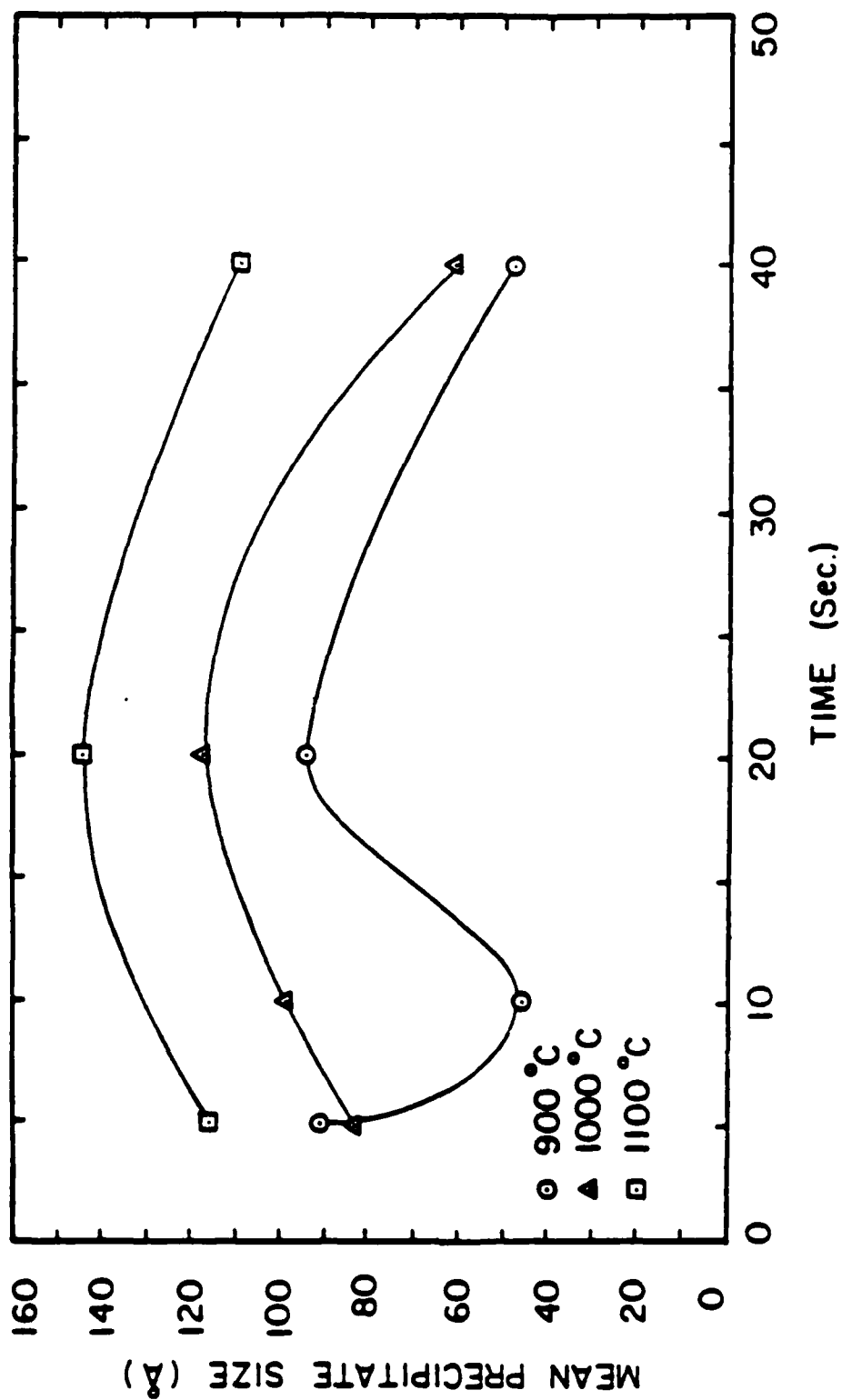
Figure 99.   Summary of mean precipitate size distributions
             as a function of heat treatment time for
             various times and temperatures.

Figure 99 is interesting. It would appear from the mean particle size data that the average particle size increases initially with time at temperature and then decreases and generally increases with temperature.

The increase in particle size at temperature is difficult to rationalize since all particles are probably dissolving to attain the equilibrium volume fraction, especially at short times. Also, the previous analysis indicated that particle dissolution controls grain growth. It may be rationalized in the following manner.

A particle size distribution exists from which the mean particle size is calculated. During particle dissolution under an overall driving force to attain equilibrium, all particles are shrinking. However, diffusion controlled particle dissolution theory indicates that the rate of dissolution is faster for small particles in the distribution, especially a very small sizes where capillarity effects enhance dissolution. [150] This means that small particles can be removed from the distribution preferentially. When the mean particle size is computed from the coarser, remaining particles the mean size can increase. Eventually, the large particles shrink sufficiently due to dissolution, for the mean particle size to decrease.

It is only after the equilibrium volume fraction at a given temperature is attained that particles coarsen via Ostwald ripening. The driving force here is capillarity and is much lower than chemical driving forces needed to attain equilibrium.

Particle coarsening, i.e. Ostwald ripening, is only applicable to a situation where the equilibrium volume fraction of precipitate has been obtained. That is, there is no longer any chemical driving force (super-saturation or under-saturation) in the matrix. Ostwald ripening is then just a change in the state of aggregation of stable precipitates wherein large particles grow at the expense of small particles via a capillarity driven reaction. If an equilibrium volume fraction is achieved, precipitation growth occurs by Ostwald ripening, Figure 100. The attainment of an equilibrium volume fraction during a fairly rapid thermal transient is questionable.

In summary, grain coarsening of this Cb-V steel during reheating is due to dissolution of the V-based precipitate. In addition, particle coarsening is only likely to be a factor for higher stability precipitates that resist complete dissolution to temperatures where coarsening is appreciable.

The results of Figures 97(a) and 97(b), indicate that
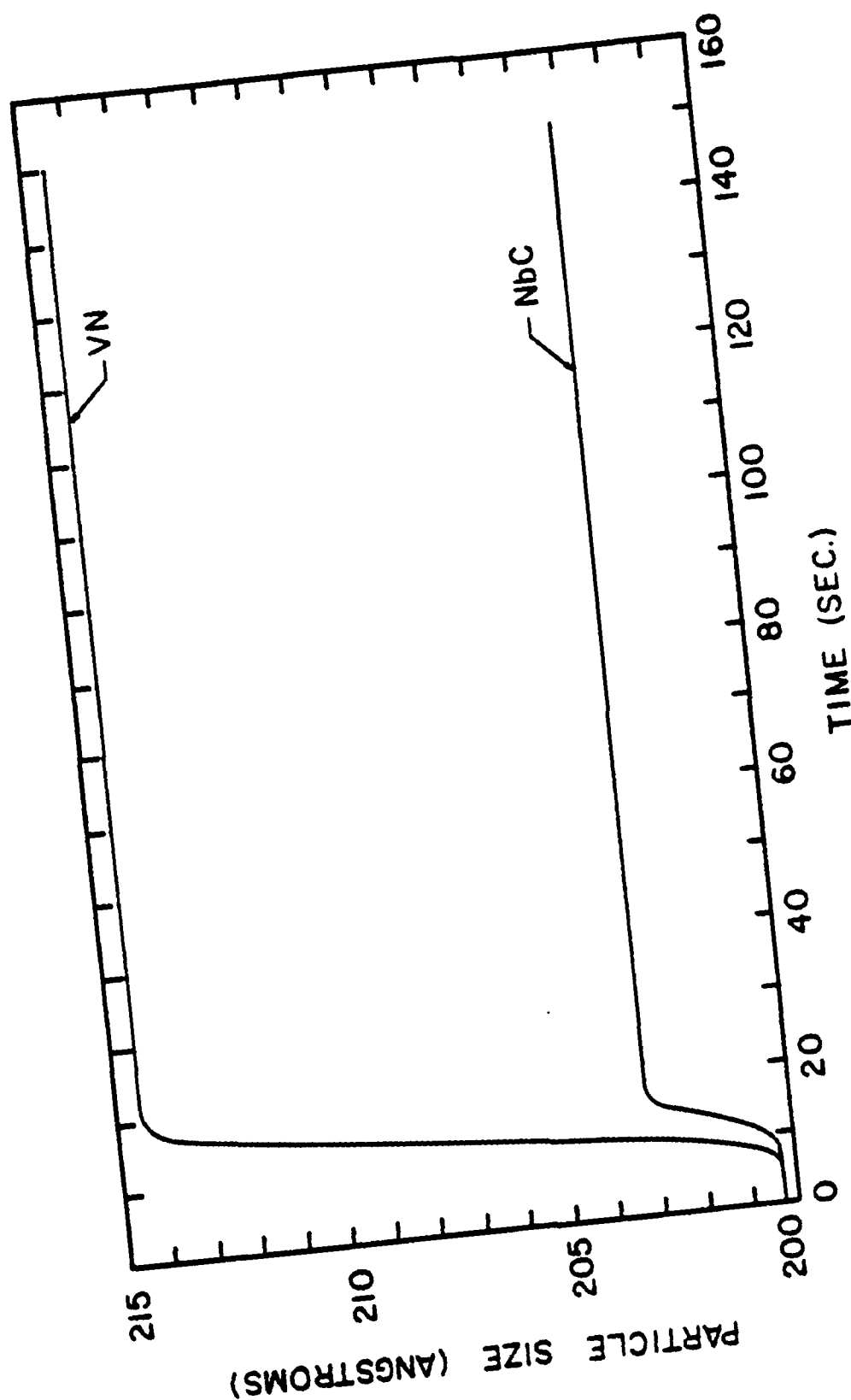
Figure 100.   Summary of theoretically determined
precipitate size as a function of time for
Ostwald ripening where conditions of
equilibrium volume fraction of precipitates
have been attained.

the rate of grain growth observed in Gleeble reheating
experiments at short times is significantly greater than
the rate observed for furnace experiments at longer times.
Note the greater austenite grain size for the 300 second
Gleeble specimen compared to the corresponding furnace
specimens at all temperatures greater than 900 deg.C. This
may be rationalized by considering the significantly
greater heating rate to the test temperature in the
Gleeble. First, an increased heating rate raises the
transformation temperature [154] and therefore delays the
onset of a fully stable austenite for growth during
heating. Second, growth of austenite during heating is
diminished by a higher heating rate. Therefore, when the
test temperature is reached, the austenite grain size in
the Gleeble specimen would be less than that in the
corresponding furnace treated specimen. Theory indicates
that the instantaneous rate of grain growth, dD/dt, is
inversely proportional to the instantaneous grain size:

(5.30) $dD/dt = 1/D_x$ [128]

Therefore,

$\quad\quad$ if $D_{\gamma(Gleeble)} < D_{\gamma(Furnace)}$ then

$\quad\quad$ $(dD_{\gamma}/dt)_{Gleeble} > (dD_{\gamma}/dt)_{Furnace}$

The higher initial rate of grain growth for the Gleeble
treated specimen causes a difference in austenite grain
size that persists throughout the treatment time regime,
Figure 101.

This phenomena would certainly have implications with
regards to austenite microstructural evolution in the HAZ
during welding. The heating rates during HAZ welding
thermal cycles are significantly greater those of a typical
furnace. Therefore, utilization of austenite grain growth
equations derived from furnace experiments might yield
significant errors in modeling austenite evolution over the
weld thermal cycle. It was for this reason that the
Gleeble results were employed to generate isothermal
austenite grain growth kinetic equations for modeling
procedures to be discussed subsequently. Furthermore,
these results indicate that the heating rate during welding
may be an important variable in correlating HAZ austenite
microstructural evolution with the thermal cycle. In the
past the peak temperature was deemed to be the most
significant parameter in determining austenite
microstructure in the HAZ.

If abrupt grain coarsening is defined in association
with average austenite grain size greater than 20μm, then
an inverse relation between austenite grain coarsening
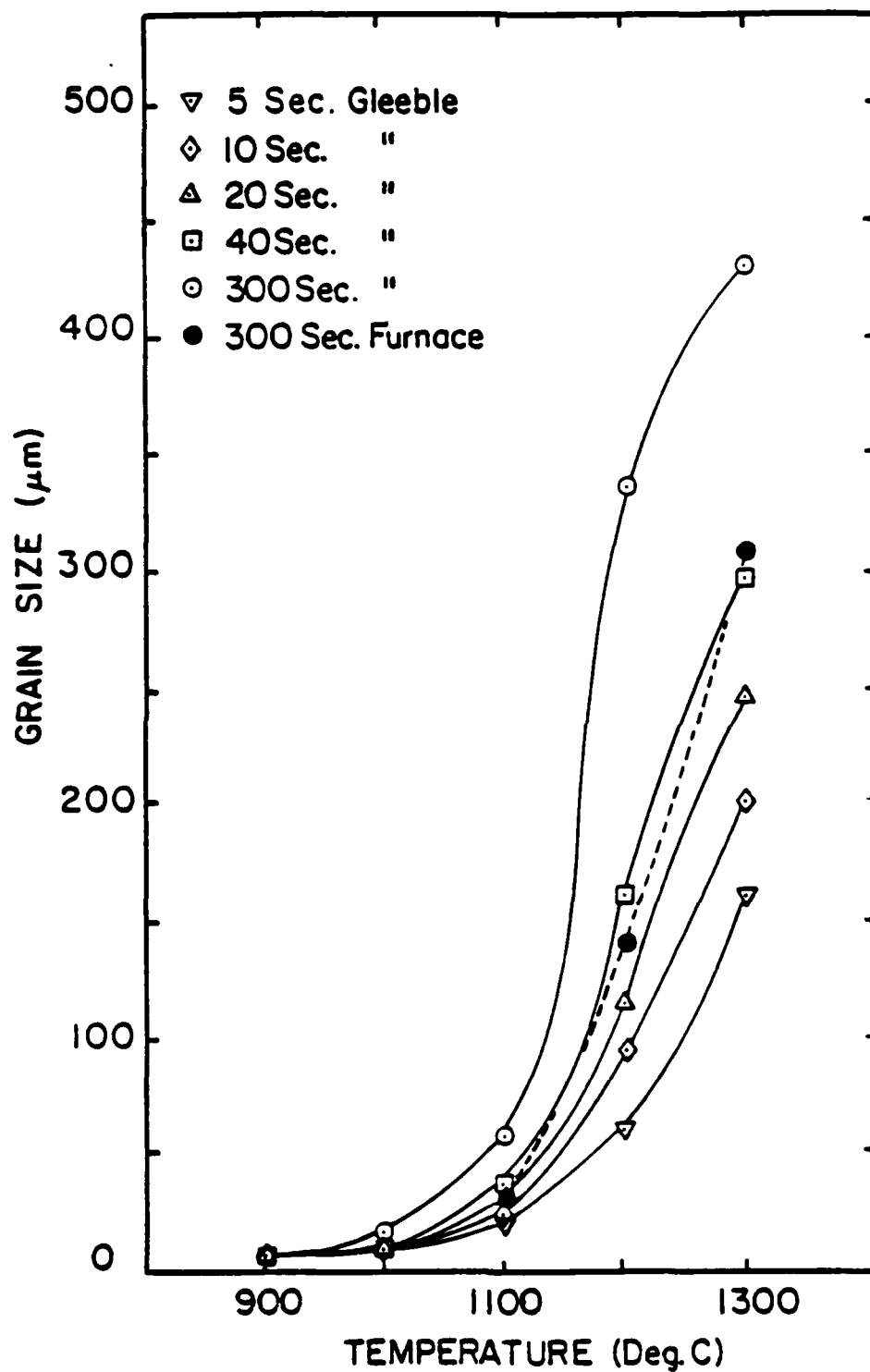
Figure 101.   Summary of austenite grain size as a function
of temperature for short heat treatment times.

temperature and time exists such that austenite grain
coarsening temperature increases as time decreases. This
means that for welding athermal treatments, abrupt grain
coarsening might be delayed to higher temperatures in the
thermal cycle than would be indicated from isothermal
kinetics.

The approach in modeling athermal grain growth will be
to associate the onset of rapid grain growth with
attainment of a grain size of approximately 20μm.

The following approach to modeling isothermal grain
growth may be taken:

(5.31) $D_Y = (Kt)^n$

(5.32) $\log(D_Y) = n\log(K) + (n\log(t))$

where,

$$\log(K) = fn(T)$$

$$n = fn(T)$$

$$K = K_0 \cdot \exp(-nQ/RT)$$

$$\log(K) = \log(K_0) - (nQ/(2.3RT))$$

$$D_Y = [K_0 \cdot \exp(-nQ/RT)] \cdot t^n$$

Approach (5.31) has yielded the following plots,
Figures 102,103,104 for Gleeble heat treated specimens.
The value n increases to a maximum in the vicinity of 1200
degrees C. and there appears to be three regimes of
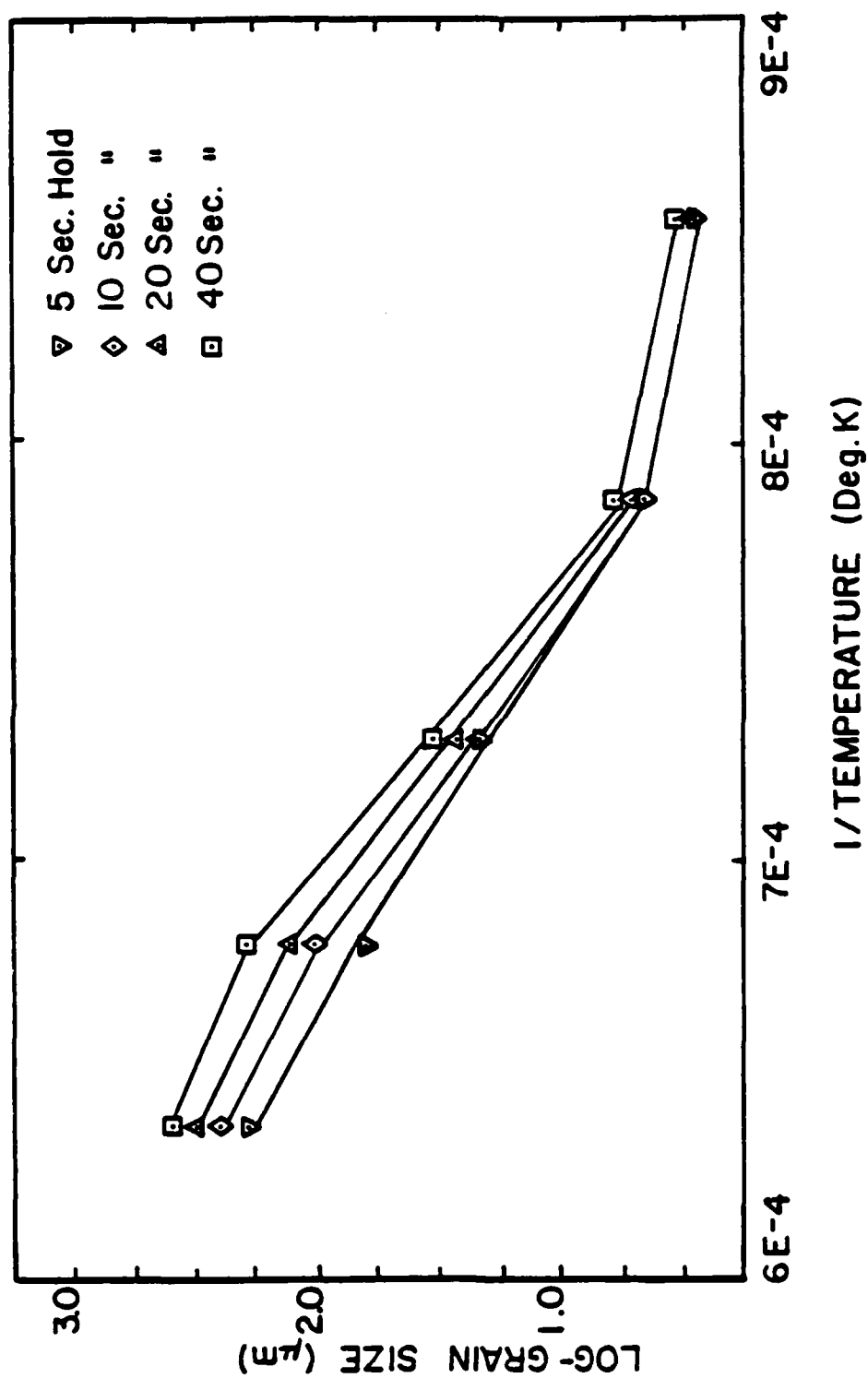
Figure 102. Summary of log-grain size as a function of inverse temperature for short time heat treatments.
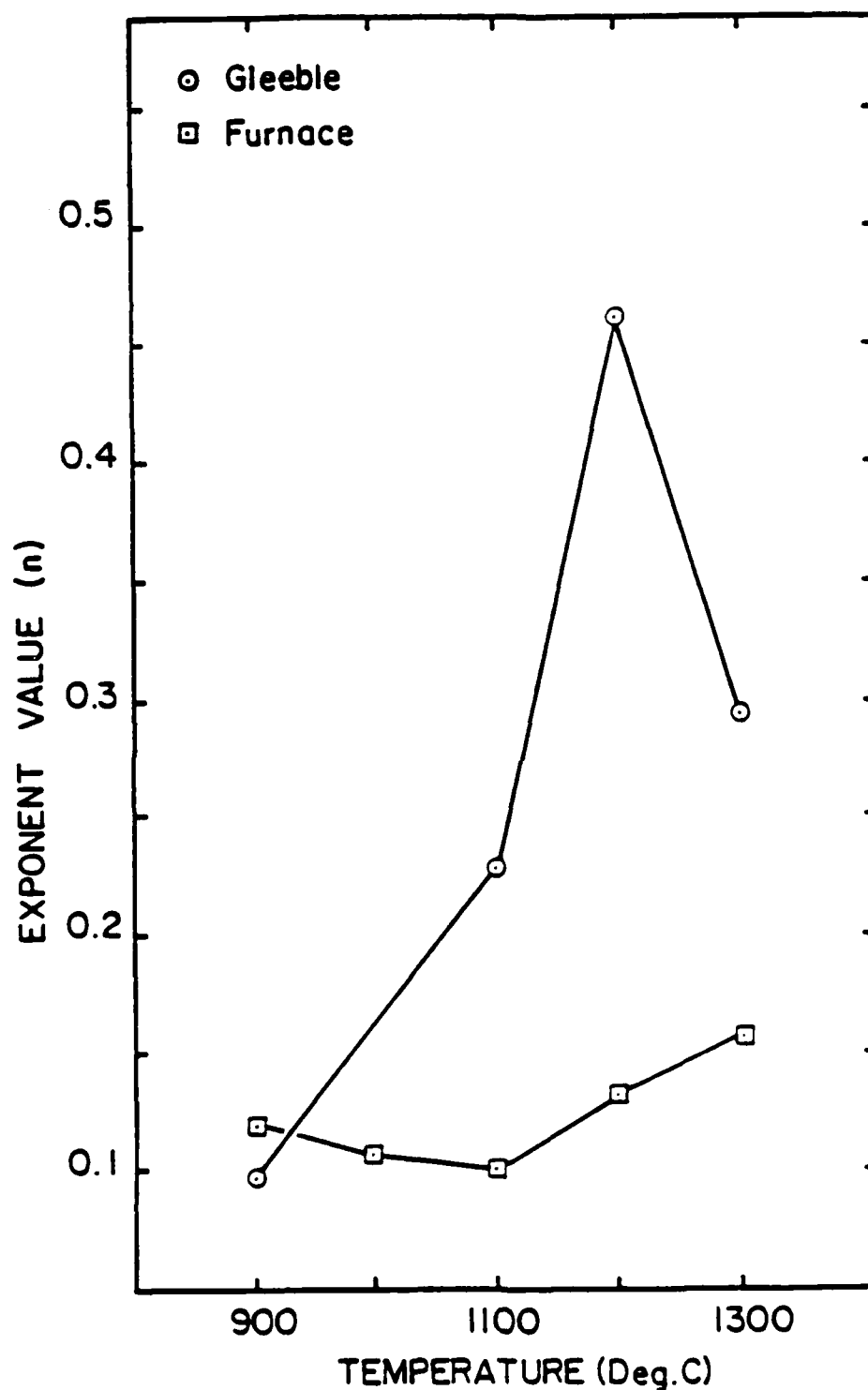
Figure 103.   Comparison of empirically determined Gleeble
and furnace exponent values for grain size
calculations as a function of temperature.
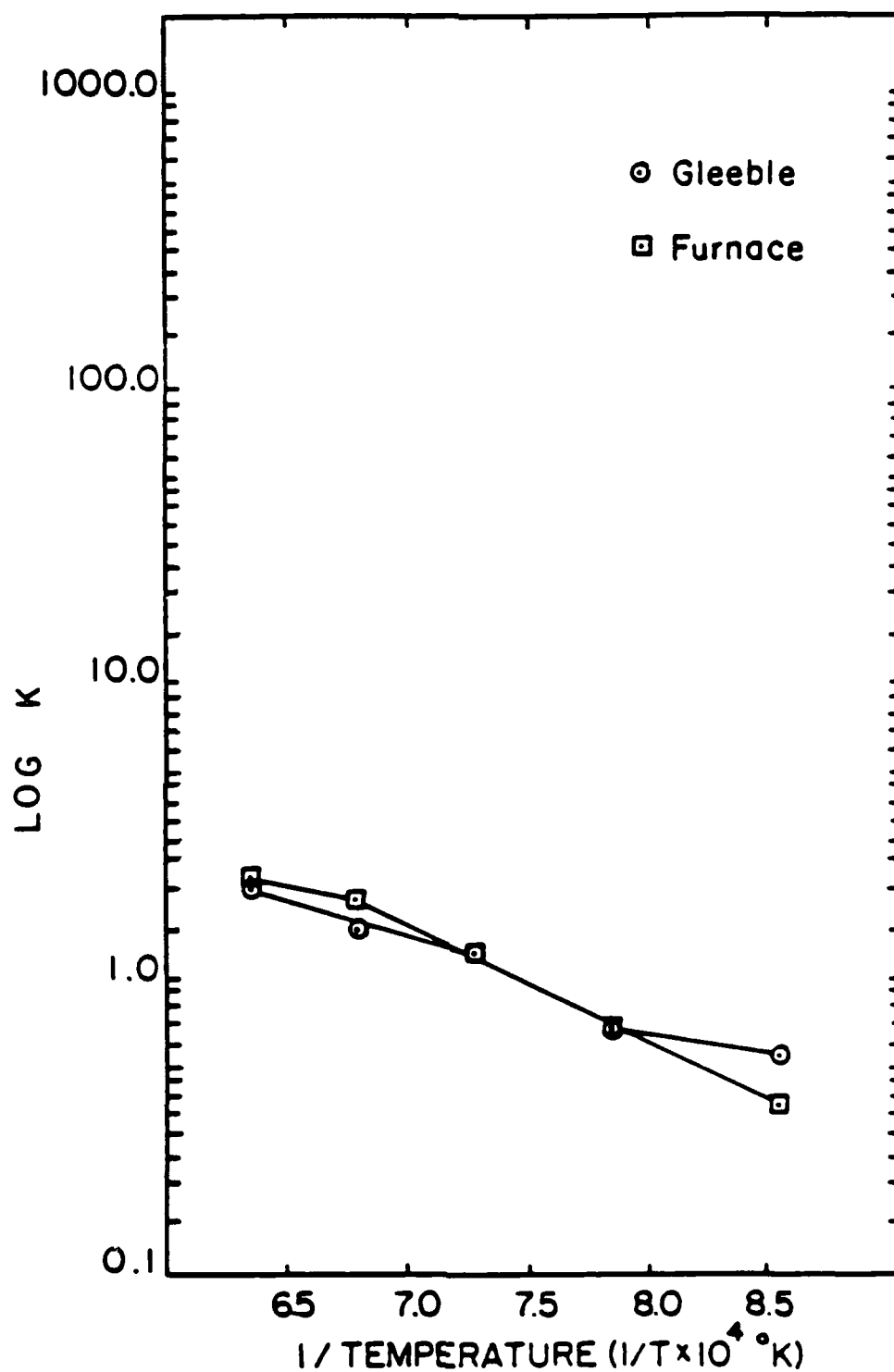
Figure 104.   Comparison of empirically determined Gleeble
               and furnace log K values for grain size
               calculations as the inverse function of
               temperature.

behavior for Q.

    To utilize isothermal kinetic equations to predict
athermal grain growth one breaks the thermal cycle into
short isothermal increments. Then one utilizes isothermal
equations to integrate over the thermal cycle
for Eq:

(5.31): $D_\gamma = (Kt)^n$

(5.32): $\log(K) = \log(K_0) - (nQ/(2.3R) \cdot 1/T$

Table 14 contains the individual values for n and log K.

    The Gleeble results were utilized to generate equations
describing austenite grain growth as a function of time and
temperature. Different equations were required for the
various regimes of slow and rapid grain growth.

    These grain growth kinetic equations were employed to
investigate the evolution of HAZ austenite microstructure
during welding by integrating them over the weld thermal
cycle. The latter was established from temperature
measurements and discussed previously. The thermal
for a particular HAZ position and heat input was
into small increments of time over which the
isothermal growth equation could be
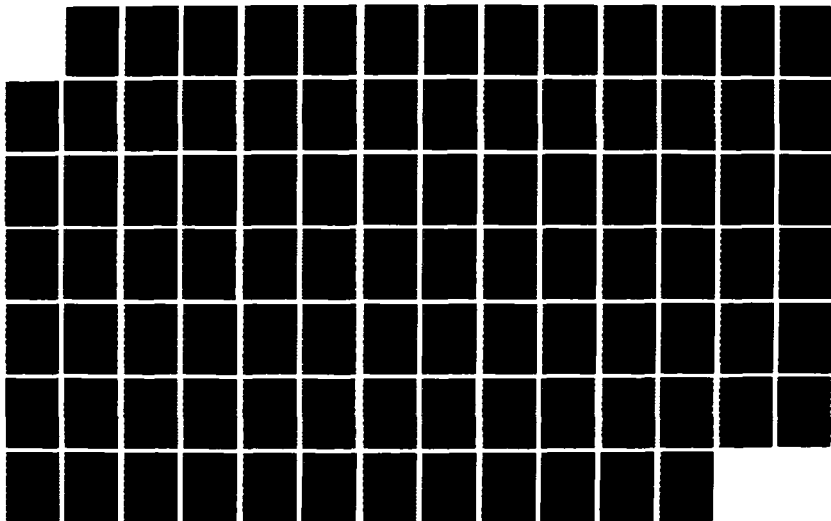
MICROCOPY RESOLUTION TEST CHART

NATIONAL BUREAU OF STANDARDS-1963-A

Table 14

Athermal Grain Growth Kinetic Parameters

For three regime behavior:

900-1100 deg.C:	$n = (6.7 \times 10^{-4}) \cdot T - 0.506$
1100-1200 deg.C:	$n = (2.37 \times 10^{-3}) \cdot T - 2.381$
1200-1300 deg.C:	$n = (-1.7 \times 10^{-3}) \cdot T + 2.503$
900-1000 deg.C:	$\log(K) = 1.73 - 1402.99/T_{abs}$
1000-1100 deg.C:	$\log(K) = 8.07 - 9473.69/T_{abs}$
1100-1300 deg.C:	$\log(K) = 7.85 - 9088.33/T_{abs}$

of these incremental isothermal calculations were summed

over the cycle to yield the total austenite grain growth.

The integration process has been investigated fundamentally

with regard to the so-called "rule of additivity"[51-53].

Cahn has stated that the rule strictly applies when the

thermally activated process being summed has only one

temperature dependent parameter. It is unclear whether the

process of grain growth and the related processes of

particle coarsening or dissolution fulfill this

requirement.

To investigate the efficacy of applying the rule of

additivity, austenite grain size measurements were made on

quenched specimens obtained at various points during a

thermal cycle. The thermal cycle chosen was one associated

with relatively high heat input and a position near the

fusion zone, i.e. one of high peak temperature. This was

done in order to obtain austenite grain size measurements

over all the temperature regimes of grain growth,

Figure 105. The expermental data is compared with the

variation in grain size predicted by integrating empirical

kinetic equations over the thermal cycle, Figure 106.

Several points are obvious from this figure. First,

the excellent match between experimental data and predicted

variation indicates that the integral technique is
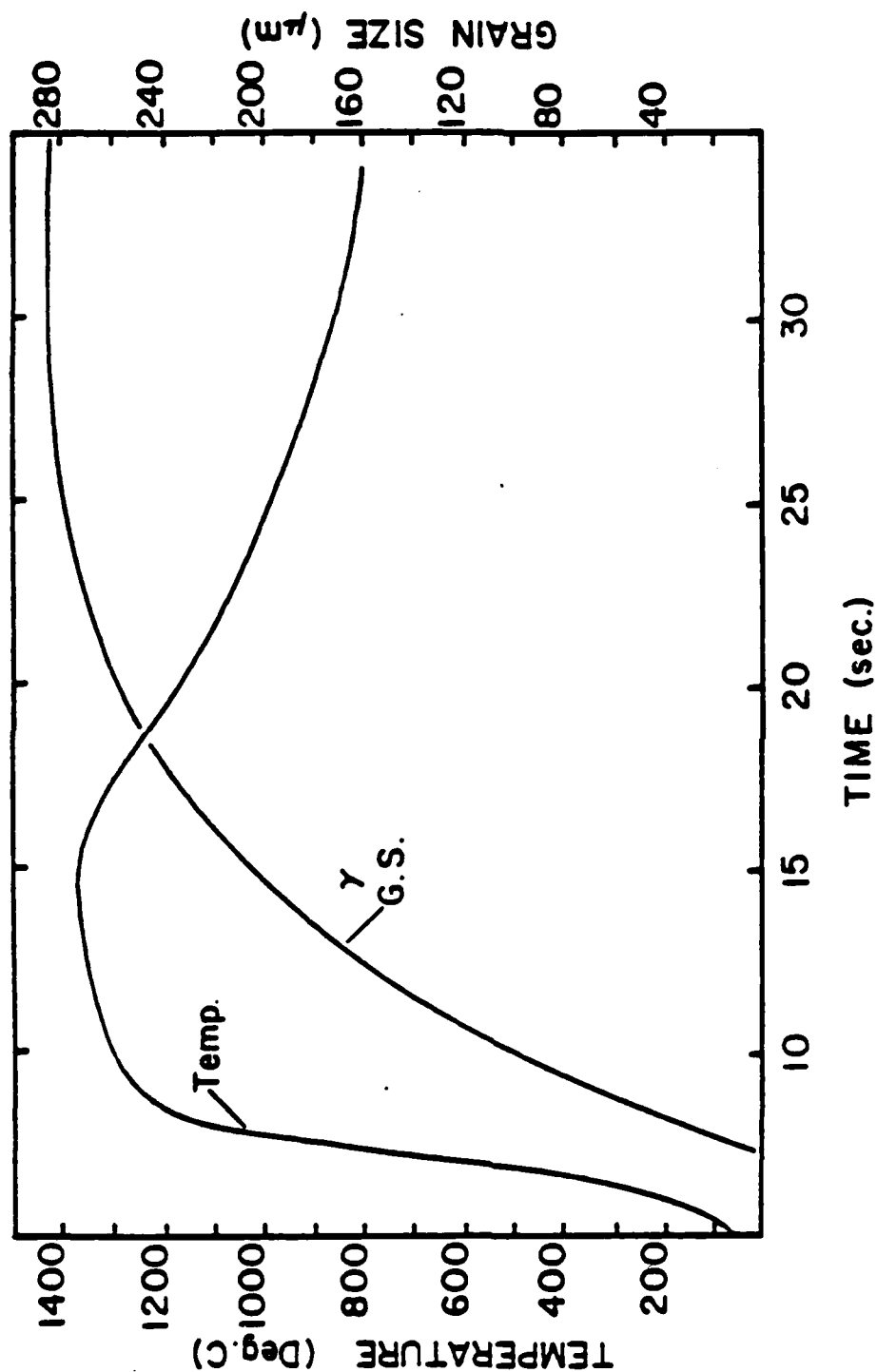
Figure 105. Weld thermal cycle and austenite grain size growth data as a function of time for medium nominal heat input (3.35 KJ/mm), T_P = 1380 deg.C, D_{FZL} = 0.39mm.
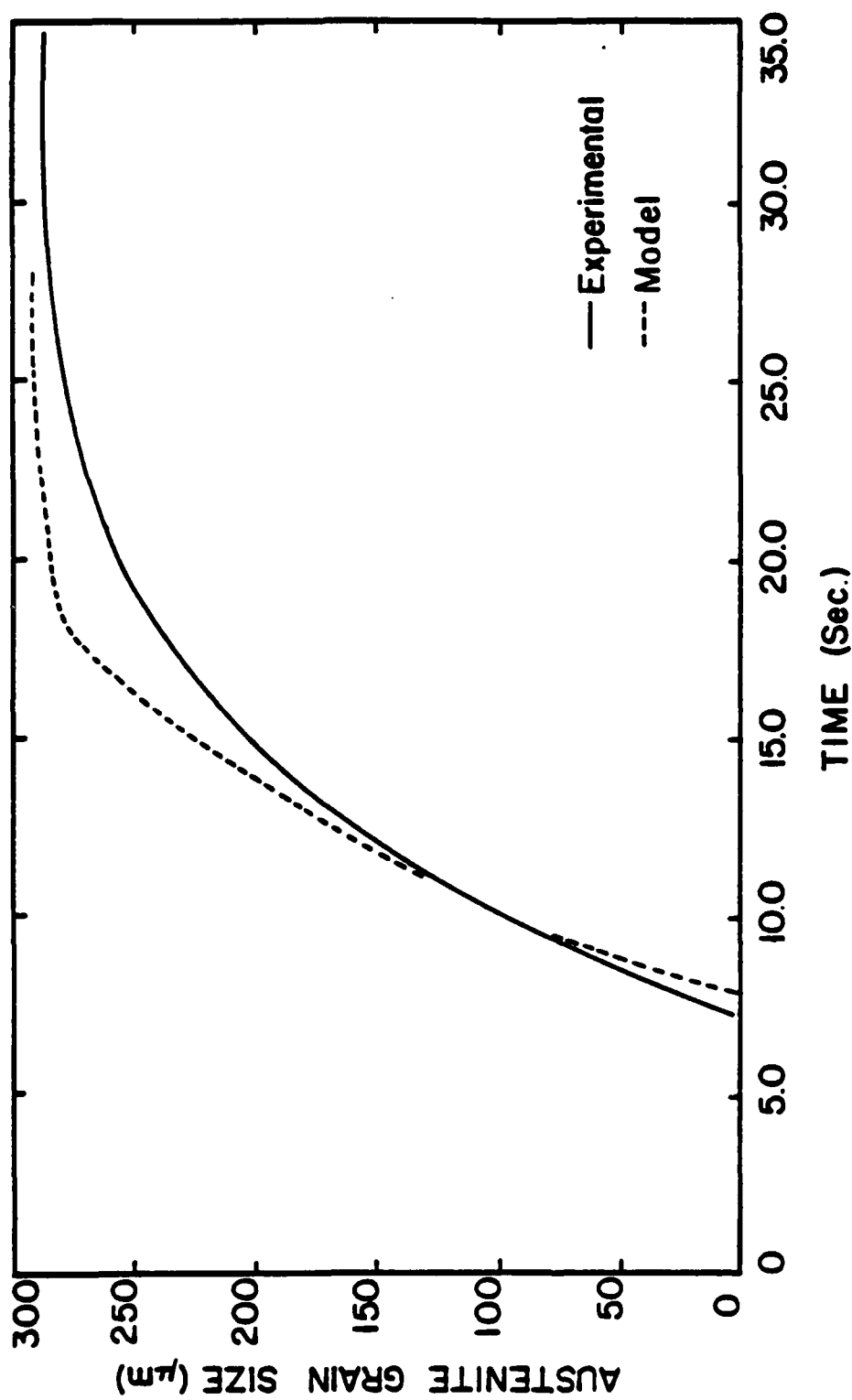
Figure 106.   Comparison of experimental austenite grain
               size to theoretically predicted austenite
               grain size, as a function of time.

adequate, regardless of whether the rule of additivity is strictly adhered to. Thus, isothermal kinetic equations for grain growth, determined from relatively simple treatments, may be utilized to predict austenite grain growth in the HAZ. Measurements of austenite grain size as a function of distance from the fusion line in acutal welds compare favorably with predicted grain sizes utilizing the integrative technique, Figure 107.

Most of the austenite grain growth occurs during heating and in the vicinity of the peak temperature for this set of conditions, Figure 105. Note that the rate of grain growth slows significantly after the peak temperature is attained. For the state of precipitation, TEM confirmed that the precipitates in the athermal treated specimens were dissolved at 1300 deg.C. This was much higher in temperature when compared to the state of precipitation in isothermal treated specimens.

These results imply that the fundamental mechanism of precipitate dissolution that controls austenite grain coarsening observed in the course of isothermal experments, may also be inferred for austenite microstructural evolution during a thermal cycle. Importantly, this allows the austenite microstructural response in the HAZ to be placed on a fundamental basis derived from the observed
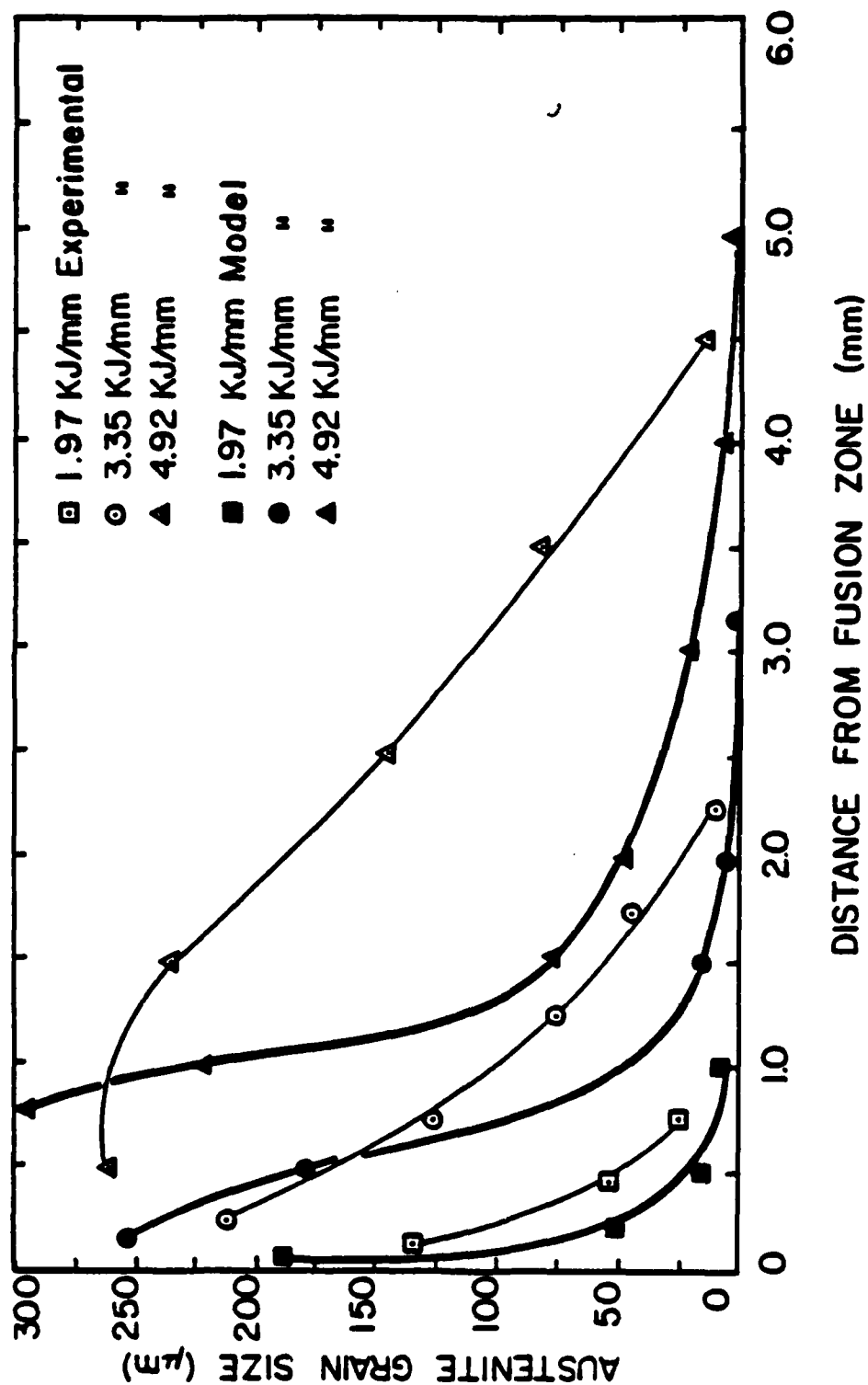
Figure 107. Comparison of experimental austenite grain
size to theoretically predicted austenite
grain size, as a function of distance from the
fusion zone boundary.

response of the base-plate to reheat treatment. The latter
has been established for many types of microalloyed HSLA
base-plate.

To summarize, the austentite grain coarsening behavior
during reheating of this Nb-V steel is characterized by
abrupt grain coarsening that is controlled by precipitate
dissolution of V(C,N). The decription of behavior during
isothermal treatment may be successfully extended to the
athermal treatment during welding. Therefore, a knowledge
of the isothermal grain growth kinetics and their
fundamental basis should allow for prediction of
microstructural evolution during welding if proper
precautions regarding heating are taken.

More specifically the onset of the coarse grained
austenite region of the HAZ could be reasonably predicted
for any set of welding conditions within the constraints of
the accuracy of the thermal model.

5.6   Transformation Product Microstructure

The tranformation product microstructure of steels has been studied extensively in the course of investigations of hardenability [53,155].   These investigations have ~~have~~ empirically quantified the important effects of steel composition, prior austenite microstructure, state of precipitation and cooling rate.   They have also indicated the complexity of interaction between these controlling parameters and therefore underlined the difficulties in theoretical modeling of hardenability.   In fact, no completely satisfactory theoretical modeling of hardenability has been accomplished.

The problem of modeling transformation product microstructural evolution in the HAZ during welding is further complicated by the added complexity of the thermal conditions in comparision to those associated with the majority of hardenability investigations.   This complicates specification of prior austenite microstructure, cooling rate and state of precipitation for welding conditions even if an adequate thermal model for welding can be determined. Difficulties with the latter have been cited in previous discussion.   This means that even utilization of the existing, empirically derived isothermal and continuous

cooling transformation database can be very complicated for welding conditions. It would certainly be desirable to ascertain the conditions under which this is possible, since to generate transformation data specifically for welding would be time consuming and costly.

The HAZ of a weldment represents a gradient in transformation product microstructure that evolves due to gradients in prior austenite microstructure, cooling rate and possibly steel composition. The sources of these gradients have been described and discussed previously with regard to a thermal model and model for austenite microstructural evolution as a function of position in the HAZ and the welding parameter of heat input. Observations of transformation product microstructure in this study have been made to identify the parameters of the thermal and austenite microstructural models that control transformation product microstructure.

The transformation product microstructure varied significantly across the HAZ for all welds (heat inputs). The most drastic microstructural variation could be correlated with the onset of austenite grain coarsening in the vicinity of the fusion zone. Of course, the width of the austenite grain coarsened region increased with heat input, as might be expected from the variation of peak

temperture with position and heat input described by the thermal model.

The transformation product microstructure of the austenite grain coarsened region varied with heat input but differences occurred for comparable peak temperatures and prior austenite grain size, Figures 33-35. This indicates a variation of transformation product microstructure due to cooling rate. The lowest heat input weld (1.97 KJ/mm)in this region is apparently associated with a cooling rate greater than the critical cooling rate for martensite formation whereas the cooling rates of this region associated with the higher heat inputs yield coarse, upper bainitic microstructures. Both of these microstructures are low temperature transformation products associated with the coarse prior austenite grains. The formation of autotempered martensite with higher cooling rate has been observed by other investigators of welded low carbon steel.[109,120,156-159] It is significant that no microalloy precipitates were detected by TEM in either the martensitic or upper bainitic microstructures. The martensitic microstructure only contained a matrix of autotempered carbides and no appreciable proeutectoid ferrite, Figure 69, that could contain microalloy precipitation.

No interlath austenite was detected as detected by others.[165] The auto tempering is due to the low carbon content induced high Martensitic start temperature. Only the large interlath Fe_3C precipitates characteristic of upper bainite were present in the high heat input microstructures even though appreciable levels of proeutectoid ferrite were detected by light microscopy. In addition no retained austenite was detected here either. Other investigators have detected very little in the way of retained austenite in comparable martensitic/bainitic microstructure.[117]

Apparently, the cooling rate in this region for all heat inputs is sufficiently high to preclude reprecipitation of microalloy carbonitrides that were placed in solution during the heating portion of the thermal cycle. It is expected that since interphase microalloy precipitation [139,156] is governed by C-curve kinetics a regime of cooling rate exists that is higher than a critical rate for precipitate nucleation. Therefore, the higher hardness in this region is soley due to the intrinsic hardness of the microstructures produced. Re-precipitation would require slower cooling rates and/or higher heat inputs.

The second maximum in hardness, detected for the high

heat input weld (4.92 KJ/mm), was surprising because the associated transformation product microstructure is ferrite/pearlite, and would be associated with lower hardness, Figure 45. That is, based on microstructure alone, the hardness should continuously decrease as for the lower heat inputs. Precipitation was suspected as the source of the hardness maximum. TEM confirmed the presence of a fine dispersion of Fe_3C precipitates rather than microalloy precipitates, Figure 67. These precipitates are very similar to those produced by quench aging [107] and could produce the observed hardness maximum.

A distinctive microstructure regime in all welds, but especially obvious at low heat input, is a fine grained ferrite/pearlite region located in the low peak temperature austenite portion of the HAZ, Figure 37. These ferrite grains are significantly finer than those present in the base-plate and in regions closer to the fusion zone. In fact, a minimum in ferrite grain size was measured for all welds that varied in HAZ location with heat input, Figure 42 . This region of fine ferrite grains is produced by a corresponding region of very fine austenite grains that are produced by a thermal experience near the A_3 temperature, Figure 36.

The ferrtic grain size was directly related to the

prior austenite grain size. This is consistent with
studies of the relationship between these two
microstructures during thermomechanical treatment of
base-plate.[32-35,84]

The microstructure of the HAZ near the base-plate, in
the intercritical and subcritical peak temperature, is
characterized by a banded microstructure in which the
original base-plate ferrite is interspersed amongst the
transformation products of the regions original pearlite,
Figure 41. The nature of the transformation products
derived from the original pearlilte vary from spheroidized
pearlite, to pearlite/martensite mixtures, to extremely
fine ferrite grains as the fully stable austenite region is
approached. The presence of martensite in this region was
confirmed by TEM, Figure 71, and is due to the higher
carbon austenite that exists in the intercritical
temperature regime.

The dilatometric transformation temperature data
provided an informative summary of transformation product
data, Figures 72-74 The transformation temperature for the
start and end of tranformation is very sensitive to peak
temperature, i.e. prior austenite grain size. Coarse
austenite grain sizes are directly correlated with low
transformation temperature and vice versa. This data is

convoluted with regard to heat input and position. The
data relating transformation temperature to cooling rate
indicates a generally low sensitivity response with respect
to this parameter. The apparently large scatter in the
data is due to variations in prior austenite grain size.
Therefore, except at the lowest heat input with the highest
cooling rates the HAZ transformations in this steel are
controlled mainly by prior austenite microstructure.

This would appear to be at odds with ascertains made in
the literature regarding the importance of cooling rate.
However, perusal of the literature indicates cooling rate
to be significant in controlling microstructure,
precipitation and related properties such as toughness, at
the low and high ends of the range of cooling rate.
[9,62,63,126] This does not negate the use of cooling rate
control to minimize hydrogen induced cold cracking.
[11,120,157-159]

In regard to utilization of the empirically derived
continuous and isothermal transformation literature, it
would seem one must take precautions in doing so. The work
of Nippes and Nelson [86] indicates that predictions from
continuous cooling transformation data can be made with a
knowledge of the weld thermal cycle. However, these
workers cite problems with the thermal model employed at

high heat inputs, consistent with thermal model problems
cited in the current study.

The use of isothermal data adds a complication due to
conversion of this data to continuous cooling data. This
requires application of the rule of additivity. Problems
in utilizing this concept have already been discussed with
regard to austenite microstructural evolution. [94]

Other attempts have been made to synthesize the large
continuous cooling thermal data base [160] in the form of
statistical regressions that correlate transformation
behavior with steel composition and a parameter defining
different austenitization conditions. It would seem, based
on the results of this study and other studies of
microalloyed steels that more than one austenization
parameter is necessary. That is, a different parameter for
each temperature regime of austenite grain growth. This
would be sensitive to steel composition and state of
precipitation in austenite. It would seem, based on our
results that some discontinuous, varying austenitization
parameter is required to account for the abrupt grain
coarsening.

The display of continuous cooling transformation data
related specifically to welding conditions is complicated
because of the coupling between peak temperature and

cooling rate via the thermal model and welding parameters.

5.7   Notch Toughness of the HAZ

Microstructure is the key and unifying aspect of a thermal response. Welding parameters place a given microstructure at a given location in the HAZ. In fact, they determine whether the microstructrure occurs at all.

To a first approximation, a given microstructure might be expected to yield the same toughness response regardless of its position in the HAZ, its volume fraction of the HAZ, or the microstructures that are adjacent to it in the HAZ.

In fact, one might expect that the toughness response of a given microstructure in a HAZ would be the same as that of a Gleeble simulation of that microstructure and the same as that of a specimen homogeneous in that microstructure.[109,118] Therefore, the fracture characteristics of a HAZ microstructure might be discussed soley on the basis of toughness versus structure and impact temperature.

Toughness depends upon several factors, namely, solid solution alloying, dislocation substructure, state of precipitation, inclusion disperison, pearlite content and ferrite grain size.[104-106,129,132,133] Several of these

factors also affect strength in a recipical manner.

The lowest toughness invariably occurred in the austenite grain coarsened region in the vicinity of the fusion zone. In this region of low temperature transformation products, such as auto-tempered martensite and upper bainite form due to the coarse austenite microstructure. It is notable that the higher cooling rate for the low heat input weld resulted in auto-tempered martensite, a slightly higher toughness microstructure, for a comparable austenite grain size. The microstructural analysis indicated that the low toughness in this region was primarily due to the transformation products since no appreciable microalloy precipitation was observed. The low toughness associated with the upper bainitic microstructure is due to the ease of crack nucleation at large interlath carbides and the ease of propagation through the similarly oriented laths of a single packet.

Recall that cleavage facets correlate with packet and austenite grain size rather than lath width. The enhanced ductility in crack propagation through allotriomorphic ferrite is offset by the low volume fraction of this constituent.

The added strength due to transformation induced dislocations also accounts for diminished toughness. The

slightly higher toughness of the auto-tempered martensite
is probably due to the overall finer lath structure and
finer intralath carbide dispersion. This accentuates the
need for low carbon contents to produce high martensite
start temperatures.[109,120,157-159]

In this regard, the literature generally has cited
Niobium and Vanadium carbonitride precipitation as the
cause for HAZ embrittlement in these steels.
[30,94,117,118,124-126] However, in the investigations for
which this effect has been observed, higher heat inputs and
therefore slower cooling rates, prevail. The slower
cooling rates are condusive to microalloy precipitation,
higher strength and therefore lower toughness.

A large portion of the toughness was obtained from
tests on simulation specimens produced with the Gleeble.
The microstructure of the thermal cycle in the simulated
specimen matched that of the corresponding position in the
actual weld, Figure 66. It has generally been assumed that
toughness measurements would be comparable between the two
types of specimens and, infact this is the case. No
drastic changes in toughness or fracture mechanism is
observed for a particular microstructure. This justifies
the combination of data from simulation specimens and
actual weld specimens, Figures 54,55. However, it is

interesting to note small systematic differences in impact
energy between the two specimen types, Appendix 3.   The
impact energy appears to be slightly higher in actual weld
specimens for tests performed in the lower shelf impact
temperature regime.

The actual weld specimens are characteristic of an
overall microstructure in which a relatively thin
embrittled region is located between regions of lower
strength and higher toughness.   The simulation specimens
are probably characterized by a shallower microstructural
gradient, i.e. a thicker embrittled region.   It would then
be expected that the constraint in the vicinity of the
crack tip is less for the actual weld specimens which
results in higher toughness for the same microstructure.
Japanese workers [127] have systematically investigated the
effect of embrittled region thickness on crack opening
displacement (COD) toughness in model specimens and have
shown that, that indeed greater toughness results with thin
embrittled regions compared to specimens with a homogeneous
microstructure.

The lack of systematic differences at higher impact
temperatures is probably due to overall higher plasticity
and toughness at these temperature.

This has potentially important implications with regard

to assessment of weldment toughness utilizing simulation specimens. Also the fracture behavior in an actual weld HAZ is somewhat dependent upon the width of the embrittled region in addition to the type of microstructrure in the embrittled region. This has been observed in other investigations of HAZ toughness, as well. [120,139,156]

This study underlines the precautions necessary in utilizing charpy toughness data obtained from actual welds. This data could contain significant variations due to microstructure and notch sampling as well as impact temperature.

The toughness of the austenite grain refined region of the HAZ was generally very high. In fact a maximum in toughness was observed for this region in the low heat input weld. Toughness in this case was higher than the base-plate toughness, Figures 46,55. The toughness maximum could be correlated directly with the fine ferrite grain size produced in association with the fine austenite grain size. The correlation between austenite and ferrite microstructure has been well established in this and other investigations[103-108]]. The fine austenite grain size is facilitated by the low peak temperatures in this region and by presence of microalloy precipitates that refine austenite grain size. In this instance then, Nb and V in

the form of microalloy precipitates refine the prior austenite microstructure and hence the transformation product microstructure to yield very high toughness.

In summary, the lowest toughness in the HAZ for all heat inputs invariably occurs in the vicinity adjacent to the fusion zone boundary. Auto-tempered martensite and upper bainite form in this region and are due to the coarse austenite microstructure.

In contrast to the brittle region of the HAZ, the austenite grain refined region of the HAZ generally possesses high toughness, more so than the base-plate in some cases. The austenite grain refinement is due primarily to microalloy additions.

Although literature cites that precipitation effects markedly decrease impact resistance, fast cooling rates associated with single pass welds as seen in this study, prevent reprecipitation from occurring in the grain coarsened region of the HAZ. Therefore, precaution must be exercised to prevent reprecipitation subsequently induced during a weldment or heat treatment.

6. CONCLUSIONS

Thermal Model

1.   The thermal cycle as a function of heat input and position in the HAZ of a single pass SAW weld could be predicted with an empirically determined equation of the same form as the theoretically based Rosenthal equation.

2.   Differences between simple theory and experiment are probably due to the temperature dependence of thermal parameters and weld pool (finite heat source) effects. Theoretical prediction of the HAZ thermal cycle for these welding conditions requires a more sophisticated modeling approach.

Austenite Microstructural Evolution

1.   Austenite grain growth in this steel is associated with abrupt grain coarsening that appears to be predominantly controlled by the dissolution of V(C,N) microalloy precipitates. This is the controlling mechanism in specimens isothermally treated and in the grain coarsened region of high heat-input SAW welds.

CONCLUSIONS (cont.)

2.   All heat-inputs utilized in this study result in a
coarse grained austenite microstructure in the near fusion
zone region of the HAZ.

3.   Kinetic equations that describe austenite grain growth,
and developed with simple isothermal treatment studies
could be employed via the rule of additivity and thermal
cycle data to reasonably predict austenite grain growth in
the HAZ during welding

4.   Austenite microstructural evolution at specific
locations in the HAZ could be adequately simulated with
experimentally derived thermal cycle data and a Gleeble
1500 programmed thermal cycle test apparatus.

5.   Nb(C,N) precipitation does not appear to play a major
role in austenite microstructural evolution.

Transformation Product Microstructural Evolution

1.   Microstructures in the coarse grained austenite region
consist of mixtures of upper bainite and autotempered

CONCLUSIONS (cont.)

martensite. A larger volume fraction of martensite is associated with the faster cooling rates at low heat input.

2. No reprecipitation of dissolved microalloying constituents occurred in the coarse grained region due to the relatively fast cooling rates of this study.

3. An extremely fine grained ferrite region developed for thermal cycles with peak temperatures just above the A_{c3}. This ferrite microstructure is associated with a minimum in austenite grain size and is finer than the base-plate microstructure.

4. Transformation from austenite in the HAZ appears to be mainly controlled by prior austenite grain size in this heat input range.

HAZ Toughness

1. Minimum charpy impact toughness in all heat inputs is associated with the low temperature transformation products of the coarse grained HAZ.

CONCLUSIONS (cont.)

2.   A maximum in toughness is associated with the fine grained ferrite region of the HAZ.

3.   Data from simulated microstructures correlated well with data from actual welds after the latter were separated according to structure.   The slightly higher toughness of actual weld specimens at low impact temperatures could be explained on the basis of less constraint at the crack tip for the thin embrittled region in actual HAZ's.

REFERENCES CITED

1.   George Schaffer, "Welding Report No. 698," American
       Machinist, September, (1977).

2.   K. Easterling, Introduction to the Physical
       Metallurgy of Welding, Butterworth & Co. Pub.,
       Boston, MA, pp.1-9, (1983).

3.   A. J. DeArdo, Thermomechanical Processing of
       Microalloyed Austenite, Conf. Proc. August 1981,
       G.A. Ratz, P.J. Wray, AIME, (1981).

4.   The Hot Deformation of Austenite, J. B. Balance,
       Cincinnati, Ohio, TMS-AIME (1975).

5.   P.S. Meyers, O.A. Uyehara, G.L. Borman, "Fundamentals
       of Heat Flow in Welding," Welding Research Council
       Bulletin No.123, pp. 1-46, (1967).

6.   J.Goldak, A.Chakravarti, M.Bibby, "A New Finite
       Element Model for Welding Heat Sources," Met. Trans.,
       pp. 299-305, (1964).

7.   D. Rosenthal, "Mathematical Theory of Heat
       Distribution During Welding and Cutting," Welding J.,
       20, pp. 2205-2345, (1941).

8.   N. Christensen, L. Davies, K. Gjermundsen,
       "Distribution of Temperatures in Arc Welding,"
       British Weld J., 12, pp. 54-75, (1965).

9.   C.M. Adams Jr.,"Cooling Rates and Peak Temperatures
       in Fusion Welding," Welding J. AWS, 37, No.5, pp.210,
       (1958).

10.   P. Jhaveri, W. G. Moffat, C.M.Adams Jr.,"The Effect
       of Plate Thickness and Radiation on Heat Flow in
       Welding and Cutting," Welding J., 41, No.1, pp.12,
       (1962).

11.   B. A. Graville, The Principles of Cold Cracking
       Control in Welds, Dominion Bridge Co., Montreal,
       April, 1975).

12.   S. Tanaka, "Temperature Distribution in a Finite
       Thick plate Due to a Moving Heat Source," Journal of
       Japan Welding Soc., 13, pp.347, (1943).

13.   K. Kohira, T. Yataka, N. Yurioka, "A Numerical
       Analysis of the Diffusion and Trapping of Hydrogen in
       Steels and Steel Weldments," Journal of Japan Welding
       Society, 43, No.9, pp.921, (1974).

14.   K. Kohira, T. Yataka, N. Yurioka, "A Numerical
       Analysis of the Diffusion and Trapping of Hydrogen in
       Steels and Steel Weldments," II World International
       Institute of Welding, Doc. IX-951-76,(1976).

15.   N. N. Rykalin, Calculation of Heat Flow in Welding,
       Moscow, (1951).

16.   N. Christensen, "Welding Metallurgy," Welding
       Metallurgy Compendium, Linkoping, Sweden, (1976).

17.   British Iron & Steel Research Association, Physical
       Constants of Some Commercial Steels at Selected
       Temperatures, Butterworths, London, (1953).

18.   A. C. Nunes, "Computer Modeling in Welds," Welding
       J., 62, pp. 165s-170s, (1983).

19.   N. D. Malmuth, "Computer Analysis of Heat Flow,"
       Welding J., 53, pp.388s-400s, (1974).

20.   J. Goldak, M. Bibby, J. Moore, R. House, B. Patel,
       Computer Modeling of Heat Flow in Welds, Department
       of Mechanical and Aeronautical Engineering, Carleton
       University, Ottawa, Canada, K1S 5b6, (1985).

21.   K. Masubuchi,"Analysis of Welded Structures,"
       Pergamon press, International Series on Materials
       Science and Technology, 33, pp. 61-87, (1980).

22.   O. Westby, Temperature Distribution in the Workpiece
       by Welding, Department of Metallurgy and Metals
       Working, The Technical University, Trondheim,
       Norway, (1968).

23.   V. Pavelic, R. Tanbakuchi, O. A. Uyehara,P. S.
       Myers,"Experimental and Computed Temperature
       Histories in Gas Tungsten-Arc Welding Thin Plates,"
       Welding Journal Res. Suppl., 48, pp.
       295s-305s,(1969).

24. J. H. Argyris, J. Szimmat, K. J.
     Willan,"Computational Aspects of Welding Stress
     Analysis," Computer Methods in Applied Mechanics and
     Engineering, 33, pp. 635-666, (1982).

25. M. Ushio, F. Matsuda, "Mathematical Modeling of Flow
     Field and Heat Transfer of Welding Arc," Fourth
     International Symposium of the Japanese Welding
     Society, Japanese Welding Society, Osaka, Japan,
     paper 4JWS-I-4, November, 1982.

26. E. P. Nippes, E. C. Nelson, "Continuous Cooling
     Transformation Characteristics of Three Types of
     Weld Metal," Research Suppl., pp.30-36s, (1958).

27. Y. C. Hirsch, B. A. Parker, "Advances in the Physical
     Metallurgy and Application of Steels," Advances in
     the Physical Metallurgy and Applications of Steel,
     Proc. of Int'l Conf., The Metals Soc., Univ. of
     Liverpool, Liverpool, England, Univ. of Liverpool,
     pp.26, September, 1981.

28. R. A. Grange, "Effect of Microstructural Bonding in
     Steel," Met. Trans, 2, pp. 417-426, February, (1971).

29. G. R. Speich, A. Szirmae, "Formation of Austenite
     From Ferrite and Ferrite-Carbide Aggregates," Trans.
     AIME, 245, pp.1063, (1969).

30. N. C. Law, D. V. Edmonds, "The Formation of Austenite
     In a Low Alloy Steel," Met. Trans. A., 11a, pp.33-46,
     January, (1980).

31. C. I. Garcia, A. J. DeAndo, "Formation of Austenite
     in 1.5 Pct. Mn Steels," Met. Trans. A., 12a, pp. 521,
     (1981).

32. A. Roosz, Z. Gacsi, E. G. Fuchs, "Isothermal
     Formation of Austenite in Eutectoid Plain Carbon
     Steel," Acta Met., 31, No. 4, pp. 509-517, (1983).

33. G. R. Speich, V. A. Demerest, R. L. Miller,
     "Formation of Austenite During Intercritical
     Annealing of Dual Phase Steels," Met. Trans. 12a, pp.
     1419-1428, (1981).

34. R. F. Mehl, W. C. Hagel, "The Austenite-Pearlite
     Reaction," Progress in Metal Physics, pp.74-134,
     (1956).

35.   D. P. Datta, and A. M. Gokhale,"Austenitization
      Kinetics of Pearlite and Ferrite Aggregates in a Low
      Carbon Steel Containing 0.15 wt. Pct. C," Met. Trans.
      A., _12a_, pp.443-450, (1981).

36.   M. Hillert, "On the Theory of Normal and Abnormal
      Grain Growth," Acta. Met., _13_, pp. 227, (1965).

37.   T. Gladman, "Grain Growth Kinetics," Proc. Roy. Soc.,
      _294A_, pp.298, (1966).

38.   N. A. Naroun, "Grain Growth in Isothermal
      Treatments," J. Materials Science, _15_, pp. 281,
      (1980).

39.   V. Y. Novikov, "Austenite Grain Growth," Acta. Met.,
      _29_, pp. 883, (1981).

40.   C. J. Simpson, K. T. Aust and W. C. Winegard,
      "Austenite Microstructural Evolution," Met. Trans.,
      _2_, pp. 987, (1971).

41.   C. Zener, Private Communication to C. S. Smith,
      Trans. AIME, _175_, pp. 15, (1949).

42.   E. L. Brown, "The Microstructural Behavior of
      Austenite Due to Hot Rolling," Ph.D. Dissertation,
      Univ. of Pittsburgh, (1979).

43.   M. L. Santella, "Grain Growth and High Temperature
      Hot Rolling Behavior of Low Alloy Steel Austenite,"
      Ph.D. Dissertation, Univ. of Pittsburgh, (1981).

44.   H. Ikawa, S. Shin, H. Oshige, "Grain Coarsening of
      Austenite,' Trans. Jap. Welding Soc., _4_, (2), pp. 35,
      (1973).

45.   H. Ikawa, S. Shin, H. Oshige, "Grain Growth During
      Welding," Trans. Jap. Welding Soc., _6_, (1), pp. 17,
      (1975).

46.   H. Ikawa, H. Oshige, S. Noi, K. Kanda, "Grain Growth
      Kinetics During a Weld Thermal Cycle," Trans. Jap.
      Welding Soc., _9_, (1), pp. 41, (1978).

47.   H. Ikawa, H. Oshige, S. Noi, H. Date, K. Uchikawa,
      "Austenite Grain Growth in Weld HAZ," Trans. Jap.
      Welding Soc., _9_, (1), pp.47, (1978).

48.   P. J. Alberry, W. K. C. Jones, "A Computer Model for
       the prediction of HAZ Structures in Mechanised
       Tungsten Inert Gas Multipass Weld Deposits," TMS-AIME
       Paper Selection, F79-12, (1979).

49.   P. J. Alberry, W. K. C. Jones, "Computer Model for
       Prediction of HAZ Microstructures in Weldments,"
       Metals Technology, 9, pp. 419, (1982).

50.   M. F. Ashby, K. E. Easterling, "Grain Growth in
       Welds," Acta Met, 30, pp. 1969, (1982).

51.   M. Avrami, "Transformation-Time Relations for Random
       Distribution of Nuclei," J. Chem. Phys., 8 , pp. 212,
       (1940).

52.   J. W. Cahn, "Transformation Kinetics During
       Continuous Cooling," Acta Met., 4, pp.572, (1956).

53.   J. S. Kirkaldy, Written Discussion of Paper by G. T.
       Eldis: Hardenability Concepts with Applications to
       Steel, D. V. Doagne and J. S. Kirkadly eds.,
       Warrendale, PA, TMS-AIME, pp. 155-157, (1977).

54.   E. Orowan, Reports of Progress in Physics, 12, pp.
       185, (1948).

55.   A. S. Tetelman and A. J. McEvily Jr., Fracture of
       Structural Materials, John Wiley, (1967).

56.   N. P. Allen, W. P. Rees, B. E. Hopkins, H. R. Tipler,
       "Tensile and Impact Properties of Iron-Carbon and
       Iron-Carbon-Manganese alloys of Low Carbon Content,"
       J. Iron and Steel Inst., pp. 108-120, June, 1953.

57.   G. T. Hahn, M. Cohen, B. L. Averbach, "The Yield and
       Fracture Behaviour of Mild Steel, with Special
       Reference to Manganese," J. Iron and Steel Inst., pp.
       634-644, (1962).

58.   J. D. Baird and R. R. Preston, "Relationships Between
       Processing Structure and Properties in Low Carbon
       Steels," Processing and Properties of Low Carbon
       Steel, J. M. Gray, Warrendale, PA, AIME, pp. 1-45.

59.   R. W. K. Honeycombe, "Structure and Strength of Alloy
       Steels," Climax Molybdenum Co., pp.3-33.

60.   A. R. Rosenfield, G. T. Hahn, J. D. Embury, "Fracture
       of Steels Containing Pearlite," Met. Trans., 3, pp.
       2797-2804, (1972).

61.   J. M. Gray, "Strength-Toughness Relations for
       Precipitation-Strengthened Low Alloy Steels
       Containing Columbium," Met. Trans., 3, pp. 1495-1500,
       (1972).

62.   F. H. Samuel, "Interrelations of Cooling Rate,
       Microstructure, and Mechanical Properties in Four
       HSLA Steels," Met. Trans. A., 15A, pp. 1807-1817,
       (1984).

63.   M. T. Miglin, J. P. Hirth, A. R. Rosenfield, "Effects
       of Microstructure on Fracture Toughness of a
       High-Strength Low Alloy Steel," Met. Trans. A., 14A,
       pp. 2055-2061, (1983).

64.   C. Crussard, R. Borione, J. Plateau, Y. Morillon, F.
       Maratray, "A Study of Impact Tests and the Mechanism
       of Brittle Fracture," J. Iron and Steel Inst.,
       pp.146-177, (1956).

65.   N. J. Petch, "Cleavage Strength of Polycrystals," J.
       Iron and Steel Inst., pp. 25-28, (1953).

66.   A. H. Cottrell, "Theory of Brittle Fracture in Steel
       and Similar Metals," Trans. AIME, pp. 194-203,
       (1958).

67.   J. A. Hendrickson, D. S. Wood, D. S. Clark, "The
       Initiation of Brittle Fracture in Mild Steel,"
       Chicago Conf. ASM 39th., pp.656-681,
       November, (1957).

68.   J. F. Knott, A. H. Cottrell, "Notch Brittleness in
       Mild Steel," J. Iron and Steel Inst., pp.249-260,
       March, (1963).

69.   T. Gladman, F. B. Pickering, "The Effect of Grain
       Size on the Mechanical Properties of Ferrous
       Materials," Sheffield Laboratories and Sheffield
       City Polytechnic, pp.1-69,(1981).

70.   F.B. Pickering ed., Proceedings of the Int. Symp. On
       HSLA Steels-Microalloying 1975, "High Strength, Low
       Alloy Steels- A Decade of Progress", ASM, Metals
       Park, OH,(1975).

71. L.F. Porter, S.J. Manganello, D.S. Dabkowski, J.H. Gross, Metal Engineering Quarterly, 6, pp.17, (1966).

72. T. C. Lindley, "The HAZ in Welds," Acta Met., 18, pp.1127, (1970).

73. E. F. Nippes, "Cooling Rates in Arc Welds," Welding J., 22, pp.531s, (1957).

74. W. F. Savage, W. A. Owlzarski, "The Microstructue and Notch Behavior of a Welded Structural Steel," Welding J., 31, pp. 55s, (1966).

75. E. F.Nippes, "The Heat-Affected Zone in Submerged Arc Welding," Welding J., pp. 1s, February, (1959).

76. R. E. Dolby and J. F. Knott, "Toughness of Martensite and Martensitic-Bainitic Microstructures with Particular Reference to Heat Affected Zones in Welded Low Alloy Steel," J. Iron and Steel Inst., pp. 857, (1972).

77. M. F. Gittos, R. E. Dolby, "Microstructures in the Heat Affected Zone," The Welding Institute- Members Report, May (1976)

78. M. F. Gittos, R. E. Dolby, "Heat Affected Zone Toughness in Welds," The Welding Institute-Members Report, June (1978).

79. T. G. Davey, "The Effect of Welding Parameter Changes on the Heat-Affected Zone Microstructure and Toughness of Single Pass Welds in 25mm Thick C-Mn Steels," The Welding Institute- Members Report, August (1981).

80. E. G. Signes, J. C. Baker, "Effect of Columbium and Vanadium on the Weldabiltiy of HSLA Steels," Welding J., pp. 179s-187s, (1979).

81. N. E. Hannerz, "Influence of Vanadium on the HAZ Properties of Mild Steel," Welding J., pp. 162s-168s, (1975).

82. E. Levine, D. C. Hill, "Structure Property Relationship in Low C Weld Metal," Metal Construction, pp. 346-353,August, (1977).

83. A. B. Rothwell, "CANMET Report 79-6", Summarised in Canadian Welder and Fabricator, pp. 20, May, (1980).

84. L. J. Cuddy, "Microstructures Developed During Thermomechanical Treatment of HSLA Steels," Met Trans A., 12A, pp. 1313- 1320, July, (1981).

85. E. F.Nippes, "The Weld Heat-Affected Zone," Welding Res. Supp., pp. 1s, January, (1959).

86. E. F. Nippes, E. C. Nelson, "Prediction of Weld Heat Affected Zone Microstructures from Continuous Cooling Transformation Data," Weld J. Res. Suppl., pp. 289s-294s, July, (1958).

87. R. Kohno, S. B. Jones,"An Initial Study of Arc Energy and Thermal Cycles in the Submerged Arc Welding of Steel," The Welding Institute Research Report, pp. 5, December (1978).

88. "Rapidly Changing Temperatures," Temperature-Its Measurement and Control in Science and Industry, 2, American Institute of Physics, (1962).

89. E. E. Underwood, "Applications of Quantitative Metallography," ASTM E562, E112, 8, 8th ed.

90. M. F. Ashby and R. Ebeling, "On the Determination of Number Size, Spacing and Volume Fraction of Spherical Second-Phase Particles from Extraction Replicas," Trans. AIME, 236, pp. 1396-1404, (1966).

91. G. A. Dibari, 43rd Annual Metal Finishing Guidebook and Directory, International Nickel Co. Inc., pp. 258, (1975).

92. Personal Communication from D. Anderson, David Taylor Naval Ship Research and Development Center, Annapolis, Maryland, (1984).

93. R. C. McNicol, "Correlation of Charpy Test Results for Standard and Non-Standard Size Specimens," Welding J., pp. 391s, September, (1965).

94. G. T. Eldis, "A Critical Review of Data Sources For Isothermal Transformation and Continuous Cooling Transformation Diagrams," Hardenability Concepts with Applications to Steel, D.V. Doagne and J. S. Kirkadly eds., Warrendale, PA, TMS-AIME, pp. 43-157, (1977).

95.   E. Friedman, "Analysis of Weld Puddle Distortion,"
        Weld J., Weld Res Supp Int, 6, No. 5, 6, (1976).

96.   N. Christensen, V. Del. Davies, K. Gjermumdsen,
        "Distribution of Temperatures in Arc Welding,"British
        Welding J., pp. 54, Februrary, (1965).

97.   T. Muth, "The Influence of Casting and Welding
        Processing Variables on the Structure and Properties
        of Cast Steel Overpack Containers for Nuclear Waste
        Disposal," Master of Science Thesis, Colorado School
        of Mines, (1986).

98.   J. F. Lancaster ed., The Physics of Welding ,
        International Institute of Welding, Pergamon Press,
        New York, pp. 241-246. (1984).

99.   N. Christensen, K. Gjermundsen, "Measurements of
        Temperature Outside and Inside the Welding Pool in
        Submerged Arc Welding," Report on Army Contract
        DA-91-591-EUC-1530, January, (1962).

100.   J. Heuschkel,"Development of a Steel Weld Metal, and
        Welding Procedure Capable of Producing 150 ksi Yield
        Strength in Heavy Sections," Westinghouse Research
        Labs, Final Report, U.S. Dept. of Navy Code 6348,
        No. BS-78823, Index SR007-01-01 (1962).

101.   C. M. Adams Jr., "Cooling Rates in Fusion Welding",
        Welding Journal, 37, (1958).

102.   C. M. Adams Jr., "Peak Temperatures in Fusion
        Welding", Weld J. Res. Supl., pp. 210s-215s, (1958).

103.   R. D. Stout, W. D. Doty, Weldability of Steels,
        S. Epstein, R. Somers ed., Welding Res. Council,
        New York, NY, (1978).

104.   R. D. Stout, W. D. Doty, Welding Handbook 1,
        Fundamentals of Welding, 7th ed., Charlotte Weisman,
        Miami, Flordia, American Welding Soc., (1976).

105.   K. Minoda, T. Kohno, N. Katayama, S.Kaihara,
        Y. Kaki, "Crack Opening Displacement Characteristics
        of Welded Joints on Low Temperature Service Steel for
        LPG Storage Tanks," Trans. Iron and Steel of Japan,
        22, No.12, pp.942-951, (1982).

106. R. E. Dolby, "HAZ Toughness of Structural and
     Pressure Vessel Steels - Improvement and Prediction,"
     Welding J. Res. Supl., 58, No.8, pp. 225s-238s,
     August, (1979).

107. W. C. Leslie, The Physical Metallurgy of Steels,
     McGraw Hill, New York, pp.166, (1981).

108. H. G. Pisarski, R. J. Pargeter, "Fracture Toughness
     of HAZ in Steels for Offshore Platforms," Metal
     Const., pp. 412, July, (1984).

109. G. Bernard, F. Faure, P. H. Maitrepierre, "Properties
     of Welds in Submerged Arc Welding," Proceedings of
     1976 ASM Int'l Conf. - Welding of HSLA Microalloyed
     Structural Steels, A.B. Rothwell and J. M. Gray eds.,
     Ohio, ASM, pp.187, (1976).

110. R. E. Dolby and J. F. Knott, "Toughness of Martensite
     with Particular Reference to Heat Affected Zones in
     Welded Low Alloy Steel," J. Iron and Steel Inst., pp.
     767, (1973).

111. H. Suzuki, "Welding of Modern Structural Steels,"
     1982 Houdremont Lecture, Welding in the World,
     20, No.7/8, pp. 121-148, (1982).

112. H. G. Pisarski, O. L. Towers A. A. Willoughby,
     "Guidelines for Fracture Toughness Testing of Heat
     Affected Zones," The Welding Institute Res. Bulletin,
     pp.188, June (1984).

113. M. Koso, M. Miura, Y. Ohmori, "Microstructure and
     Toughness of Weld Heat Affected Zone in 785 MN/m^2
     HSLA Steels," Metals Technology, 8, part 12,
     pp.482-487, December, (1981).

114. K. J. Irvine, F. B. Pickering, "Low-Carbon Steels
     with Ferrite-Pearlite Structures," Iron Steel Inst.,
     196, pp.518-531, (1963).

115. T. Kunitake, F. Terasaki, Y. Ohmori H. Ohtani, "The
     Bainite and Bainite-Martensite Duplex Structure in
     Low Carbon, Low Alloy, High Strength Steels," Iron
     and Steel, pp.647, December, (1972).

116. W. F. Savage, W. A. Owczarski, "The Microstructure
     and Notch Impact Behavior of a Welded Structural
     Steel," Welding Res. Supl., pp. 55s, February, 1966).

117. R. E. Dolby, "The Effect of Nb On The HAZ Toughness
      of High Heat Input Welds in C-Mn Steels," Proceedings
      of 1976 ASM Int'l. Conf. - Welding of HSLA
      Microalloyed Structural Steels, A. B. Rothwell and J.
      M. Gray eds., Ohio, ASM, pp. 212, (1976).

118. J. M. Sawhill, P. Boussel, J. W. Morrow, "Heat
      Affected Zone Toughness of High Heat Input HSLA
      Welds," Proceedings of 1976 ASM Int'l. Conf. -
      Welding of HSLA Microalloyed Structural Steels, A.B.
      Rothwell and J.M. Gray eds., Ohio, ASM, pp. 235,
      (1976).

119. J. P. Naylor, P. R. Krahe, "The Effect of Bainite
      Packet Size on Toughness," Met. Trans., 5,
      pp.1699, July, (1974).

120. J. A. Davidson, P. J. Konkol, J. F. Sovak, "Assessing
      Fracture Toughness and Cracking Susceptibility of
      Steel Weldments- A Review," United States Steel
      Corp.- Res., December, (1983).

121. R. E. Dolby, "Advances in the Welding Metallurgy of
      Steel," Advances in the Physical Metallurgy and
      Applications of Steel, Proc. of Int'l Conf., The
      Metals Soc., Univ. of Liverpool, Liverpool, England,
      pp. 111-125, September, (1981).

122. C. A. Hippsley, J. E. King, J. F. Knott, "Toughness
      Variations and Intergranular Fracture During the
      Tempering of Simulated HAZ Structures in a Mn-Mo-Ni
      Steel," Advances in the Physical Metallurgy and
      Applications of Steel, Proc. of Int'l Conf., The
      Metals Soc., Univ. of Liverpool, Liverpool, England,
      pp147-155, September (1981).

123. U. R. Lenel, R. W. K. Honeycombe, "Kinetics of
      Formation of Austenite During Intercritical Annealing
      of a Low Alloy Steel," Advances in the Physical
      Metallurgy and Applications of Steel, Proc. of Int'l
      Conf., The Metals Soc., Univ. of Liverpool,
      Liverpool, England, pp. 38-46, September, (1981).

124. J. K. Knott, "Strength and Toughness of Steels,"
      Advances in the Physical Metallurgy and Applications
      of Steel, Proc. of Int'l Conf., The Metals Soc.,
      Univ. of Liverpool, Liverpool, England, pp. 181-198,
      September, (1981).

125.   Y. Hirsch, B. A. Parker, "Microstructural Changes
       During the Reheating of Nb-Containing, HSLA Steels,"
       Advances in the Physical Metallurgy and Applications
       of Steel, Proc. of Int'l Conf., The Metals Soc.,
       Univ. of Liverpool, Liverpool, England, pp. 26-32,
        September, (1981).

126.   S. D. Bhole, J. Billingham, "Effect of Heat Input on
       HAZ Toughness in HSLA Steels," _Advances in the_
       Physical Metallurgy and Applications of Steel, Proc.
       of Int'l Conf., The Metals Soc., Univ. of
       Liverpool, Liverpool, England, pp. 156-161,
        September, (1981).

127.   Shuji Aihara, Toshiaki Haze, "Micro-Mechanical
       Inhomogeneity on Cleavage Fracture Initiation,"
       Nippon Steel Corp., Japan, 5-10-1, pp.1-12.

128.   Hsun Hu, B. B. Rath, "On the Time Exponent in
       Isothermal Grain Growth," Met. Trans., $\underline{1}$,
       pp.3181-3184, November, (1970).

129.   F. B. Pickering, _Physical Metallurgy and the Design_
       of Steels, Applied Science Pub., England, (1978).

130.   _Proceedings of 1976 ASM Int'l. Conf. - Welding of_
       HSLA Microalloyed Structural Steels, A.B. Rothwell
       and J.M. Gray, ASM, Ohio,. (1976).

131.   _Processing and Properties of Low Carbon Steel_, B. L.
       Bramfitt, A. R. Marder, AIME, New York, pp. 191,
       (1973).

132.   F. B. Pickering, "The Optimisation of Microstructures
       in Steel and Their Relationship to Mechanical
       Properties," _Hardenability Concepts with Applications_
       to Steel, D. V. Doane and J. S. Kirkaldy eds., New
       York, AIME, pp. 179-228, (1978).

133.   T. Gladman, "Strcucture-Property Relations in
       High-Strength Microalloyed Steels," _Microalloying_
       '75, International Symposium on High-Strength
       Low-Alloy Steels, Washington, D.C., Union Carbide
       Corp., pp. 3-24, (1975).

134.   _The Hot Deformation of Austenite Symposium_, J. B.
       Ballance, AIME, Cleveland, OH, (1977).

135.   Y.Z. Zheng, G. Fitzsimons, R.M. Fix, A.J. DeArdo,
        "Achieving Grain Refinement Through Recrystallization
        Controlled Rolling and Controlled Cooling in V-Ti-N
        Microalloyed Steels," ASM Metals Congress, (1983).

136.   Microalloying 80, PGH Conf., J.M. Gray, ASM, Ohio,
        (1980).

137.   Microalloying 83, Phil. Conf., J.M. Gray, ASM, Ohio,
        (1983).

138.   J.P. Pons, "Models and Methods for Calculations of
        Temperature Distribution in Welding," International
        Symposium on Calculation of Internal Stresses in Heat
        Treatment of Metallic Materials, Ewa Attebo Tortsen
        Ericsson ed., Sweden, Linkoping Univ., pp. 455, May,
        (1984).

139.   D. Uwer, "Factors Affecting HAZ Properties of
        Normalized and QT Steels,"Proceedings of 1976 ASM
        Int'l. Conf. - Welding of HSLA Microalloyed
        Structural Steels, A.B. Rothwell and J.M. Gray eds..
        Ohio, ASM, pp. 257, (1976).

140.   M. Hillert, K. Nilsson, L.E. Torndahl, "Effect of
        Alloying Elements on the Formation of Austenite and
        Dissolution of Cementite," J of Iron and Steel Inst.
        pp. 49-66, January, (1971).

141.   C.I. Garcia, A.J. Deardo, "Formation of Austenite in
        1.5 Pct. Mn Steels," Met Trans A., 12A, pp. 521-530,
        March, (1981).

142.   R.A. Grange, "The Rapid Heat Treatment of Steel," Met
        Trans, 2, pp. 65-78, January, (1971).

143.   G. R. Speich, A. Szirmae, "Formation of Austenite
        From Ferrite and Ferrite-Carbide Aggregates," Trans.
        AIME, 245, pp.1063, (1969).

144.   S. Lawson, H. Kerr, "Fluid Motion in GTA Weld
        Pools-Part 1 & 2," Welding Res, 6, No. 5, 6, (1976).

145.   D. Rosenthal, "The Theory of Moving Sources of Heat
        and Its Application to Metal Treatments," Trans AIME,
        68, pp. 849-865, (1946).

146. D.A. Porter, K.E. Easterling, _Phase Transformations In Metals and Alloys_, Van Nostrand Reinhold, UK, (1981).

147. P.G. Sherman, _Transformations In Metals_, McGraw-Hill, New York, (1983).

148. H.B. Aaron, D. Fainstein, G.R. Kotler, "Phase Transformations in Metals," J. Appl. Physics, 41, (11), pp. 4404, (1970).

149. H. B. Aaron, G.R. Kotler, "Coarsening and Dissolution Kinetics," Met Trans., 2, pp. 393, (1971).

150. G.W. Greenwood, "Particle Coarsening," _The Mechanism of Phase Transformation in Crystalline Solids, Report No. 33_, London, Inst. of Metals, pp. 103, (1969).

151. T. Healey, A.T. Brown, M.V. Speight, "Secondary Recrystallization in 20 Cr-25 Ni-Nb Stabilized Stainless Steel," CEGB Report RD/B/N3250, (1976).

152. C. Wagner, "Precipitation Coarsening and Dissolution,"Electro-Chem., 65, pp. 581, (1961).

153. I.M. Lifshitz, V.V. Slyozoz, "Second Phase Particles and Their Properties," J. Physics Chem. Solids, 19, pp. 35, (1961).

154. G. Huppi, Unpublished work, Colorado School of Mines, (1985).

155. C.A. Siebert, D.V. Doane, D.H. Breen, "HAZ Toughness and Properties,"_The Hardenability of Steels_, ASM, Ohio, (1977).

156. N. Hannerz, "Weld Metal and HAZ Toughness and Hydrogen Cracking Susceptibility of HSLA Steels As Influenced By Nb, Al, V, Ti, and N," _Proceedings of 1976 ASM Int'l. Conf. - Welding of HSLA Microalloyed Structural Steels_, A.B. Rothwell and J.M. Gray eds., Ohio, ASM, pp. 365, (1976).

157. American Assoc. of State Highway and Trans. Offic., _Guide Specifications for Fracture Critical Non-Redundant Steel Bridge Members_, American Assoc. of State Highway and Trans, Offic., Washington, D.C., (1978).

158. H.S. Pearson, P.F. Packman, "Fracture Testing
      Guidelines for Engineers," Proc. of Western Metal &
      Tool Expos. & Conf., D.W. Hoeppner ed., Los Angeles,
      CA, (1972).

159. M. Ciprandi, R. Trippodo, V. Wagner, "Crack Speed
      Preliminary Determination and Propagation Resistance
      Prediction for Steels Used in Aircraft Components,"
      La Metallurgia Italiana, No. 7/8, pp. 289-310,
      (1980).

160. P.H. Maynier, V. Dullet, P. Bastier, "Prediction of
      Microstructures Via Empirical Formula Based on CCT
      Diagrams," Hardenability Concepts with Applications
      To Steel, D.V. Doane and J.S. Kirkaldy eds.,
      TMS-AIME, pp. 163, (1973).

161. D. C. Houghton, G. C. Weatherly, J. D. Embury,
      "Microchemistry of Carbonitrides in the HAZ of
      HSLA-Steels," Proc. Int'l Conf., Advances of Physical
      Metallurgy and Application of Steels, Liverpool,
      September (1981).

162. A. J. Woodfield, J. M. Raison, M. H. Loretto, R. E.
      Smallman, R. C. Cochrane, "Stability of Carbonitrides
      in Steels,"Proc. Conf. on Heat Treatment,
      Shanghai,(1983), Met. Soc. Book No.310 (1984).

163. W. Roberts, A. Sandberg, "The Influence of Processing
      Route and Nitrogen Content on Microstructure
      Development and Precipitation Hardening in Vanadium
      Microalloy HSLA Steels," Swedish Institute for Metals
      Research, Report No. IM-1489 (1980).

164. B. Loberg, A. Nordgren, J. Strid, K. E. Easterling,
      "The Role of Alloy Composition on the Stability of
      Nitrides in Ti-Microalloy Steels during Weld Thermal
      Cycles," Met. Trans. A. 15, pp.33-41, (1984).

165. Gareth Thomas, "Retained Austenite and Tempered
      Martensite Embrittlement," Met. Trans., 9A,
      pp.439-450, March (1978).

APPENDIX

APPENDIX 1

Experimental thermal cycle data for nominal heat input
welds:

    1.97 KJ/mm   (50 KJ/in.)

    3.35 KJ/mm   (85 KJ/in.)

    4.92 KJ/mm   (125 KJ/in.)
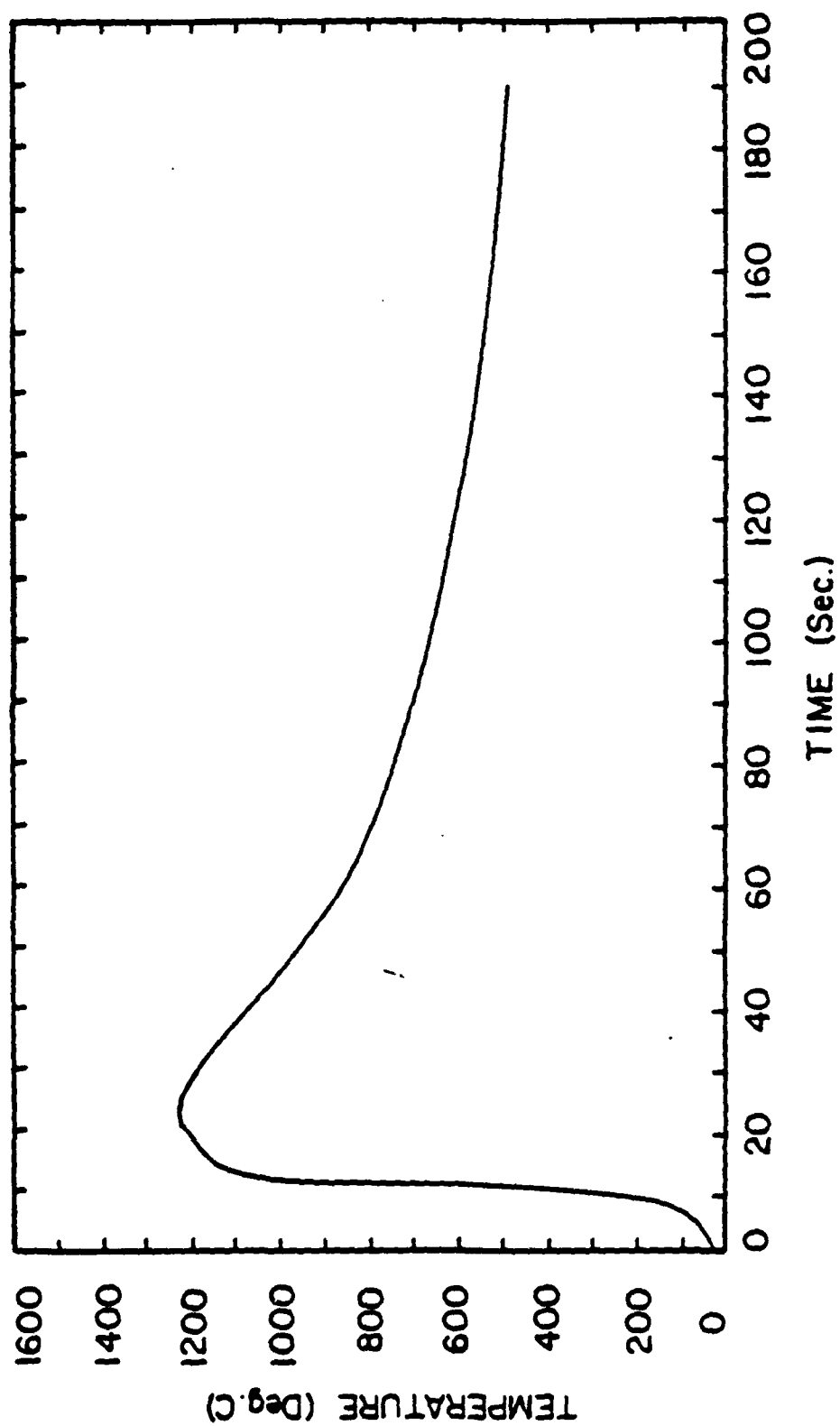
Figure 108. Experimental weld thermal cycle for
Plate 1.TC1; nominal heat input=4.92 KJ/mm,
T_P=1234 deg.C, D_{FZL}=1.27mm.
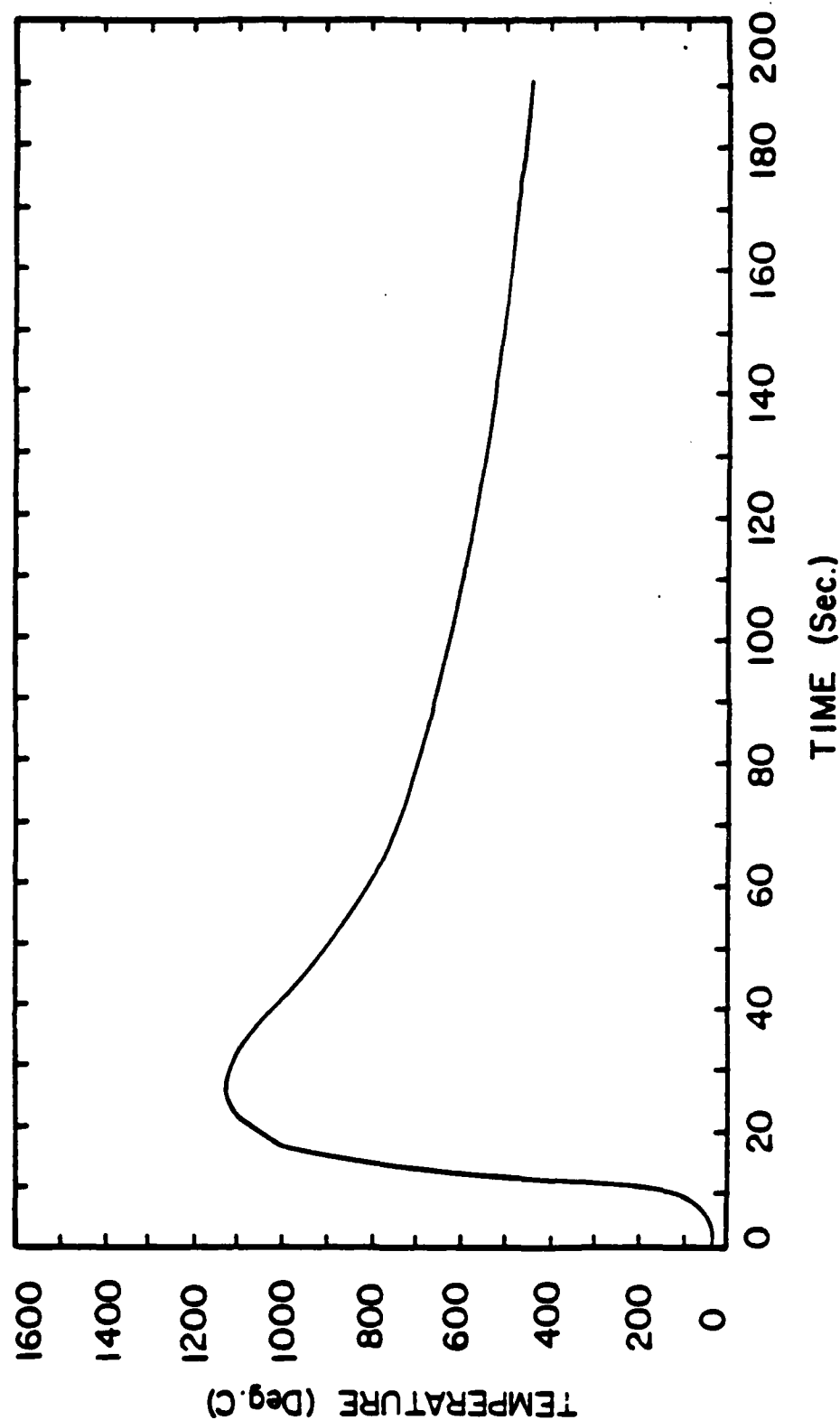
Figure 109. Experimental weld thermal cycle for Plate 1,TC2;
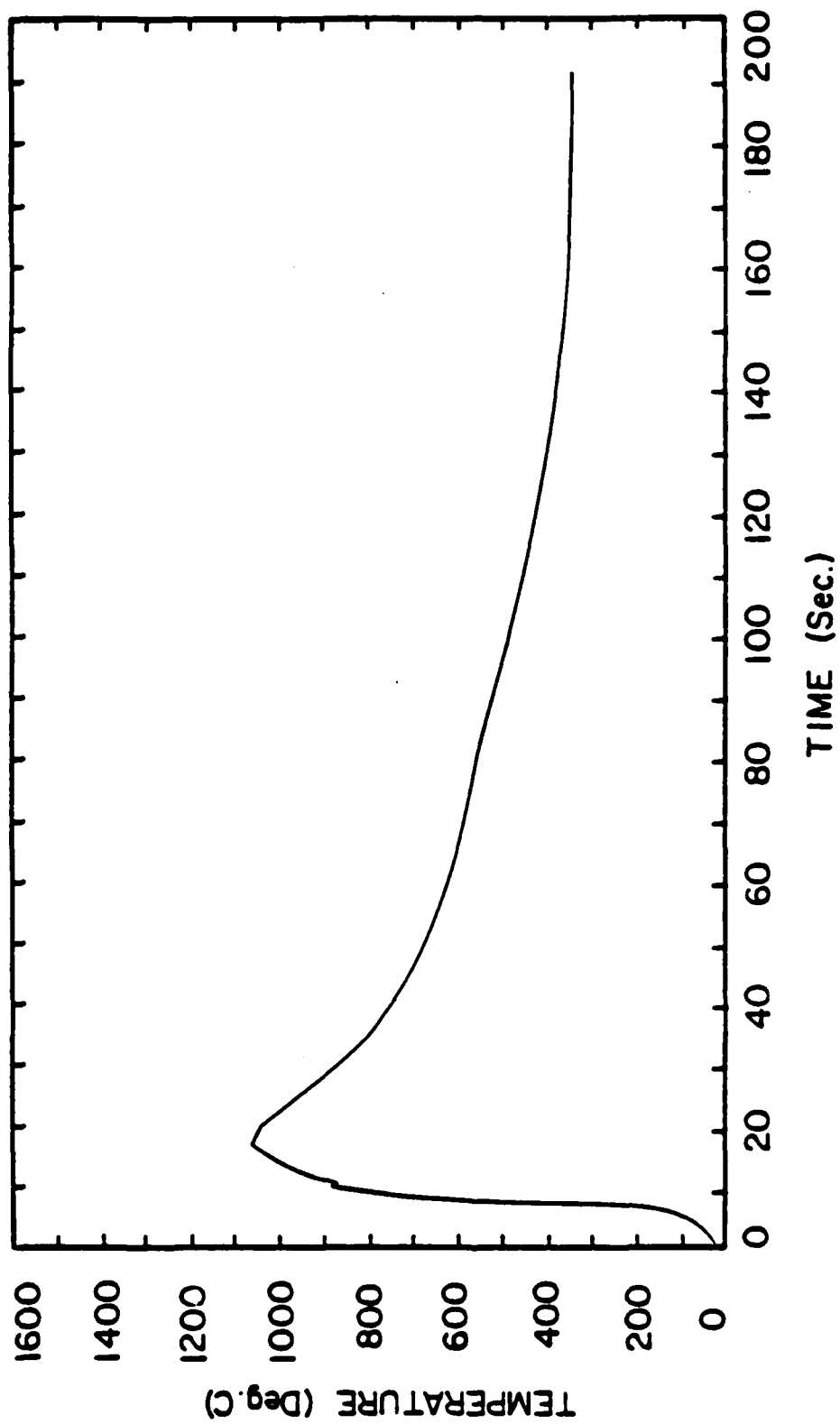nominal heat input=4.92 KJ/mm, Tp=1125 deg.C,
DFZL=2.43mm.
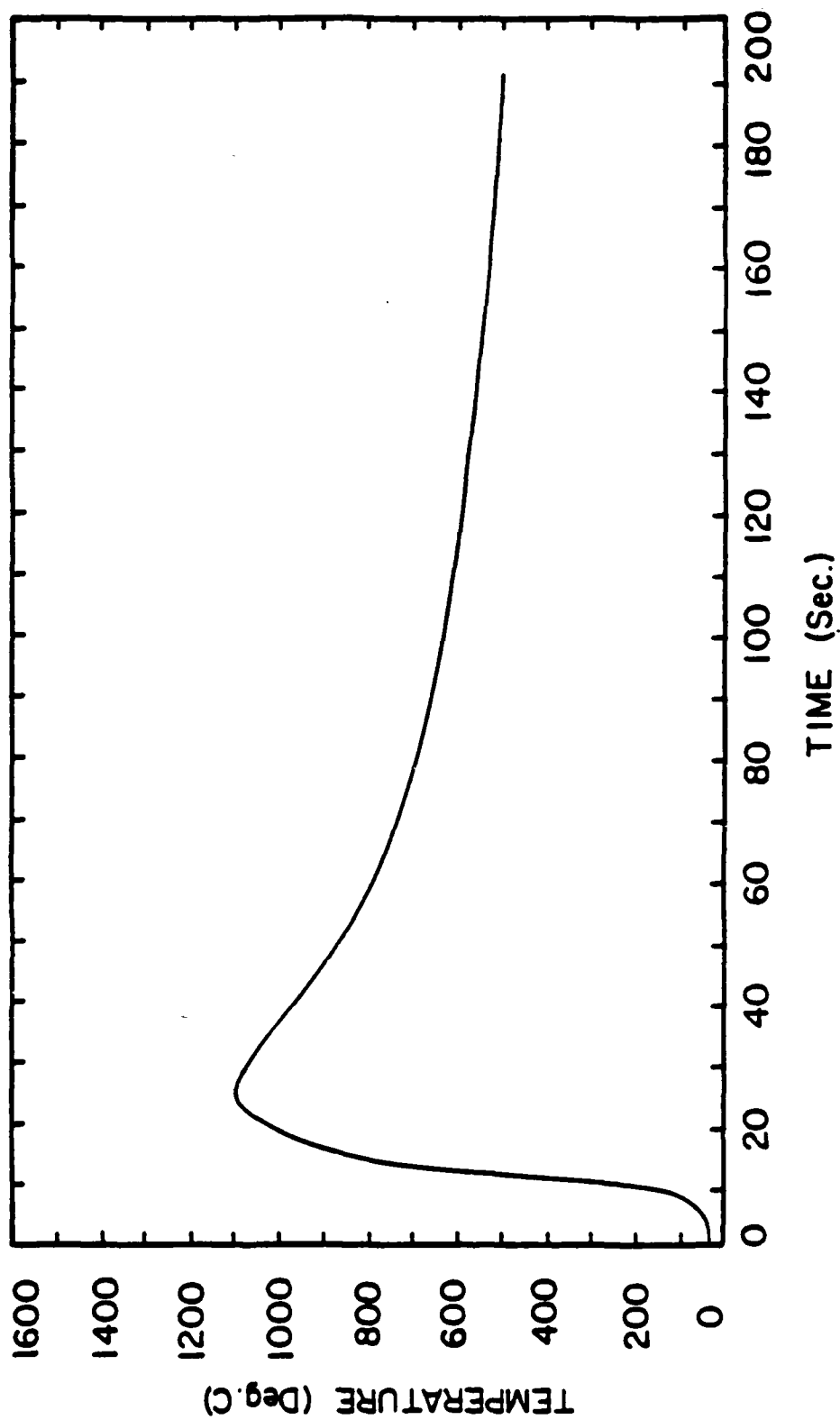
Figure 110. Experimental weld thermal cycle for Plate 2.TCI; nominal heat input=4.92 KJ/mm, Tp=1098 deg.C, $D_{FZL}=1.52mm$.
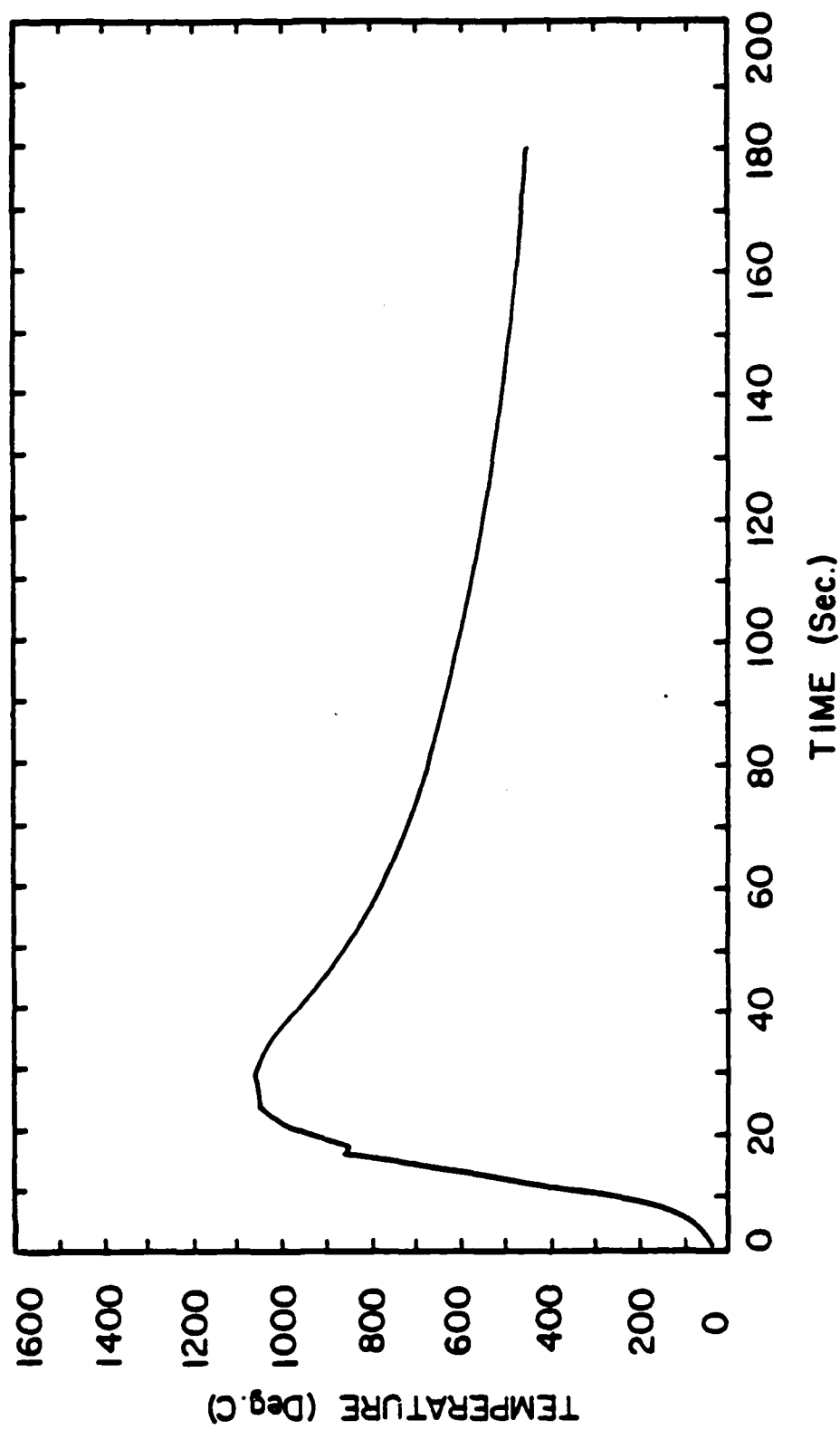
Figure 111. Experimental weld thermal cycle for Plate 4.TC1; nominal heat input=4.92 KJ/mm, Tp=1063 deg.C, D_{FZL}=3.35mm.
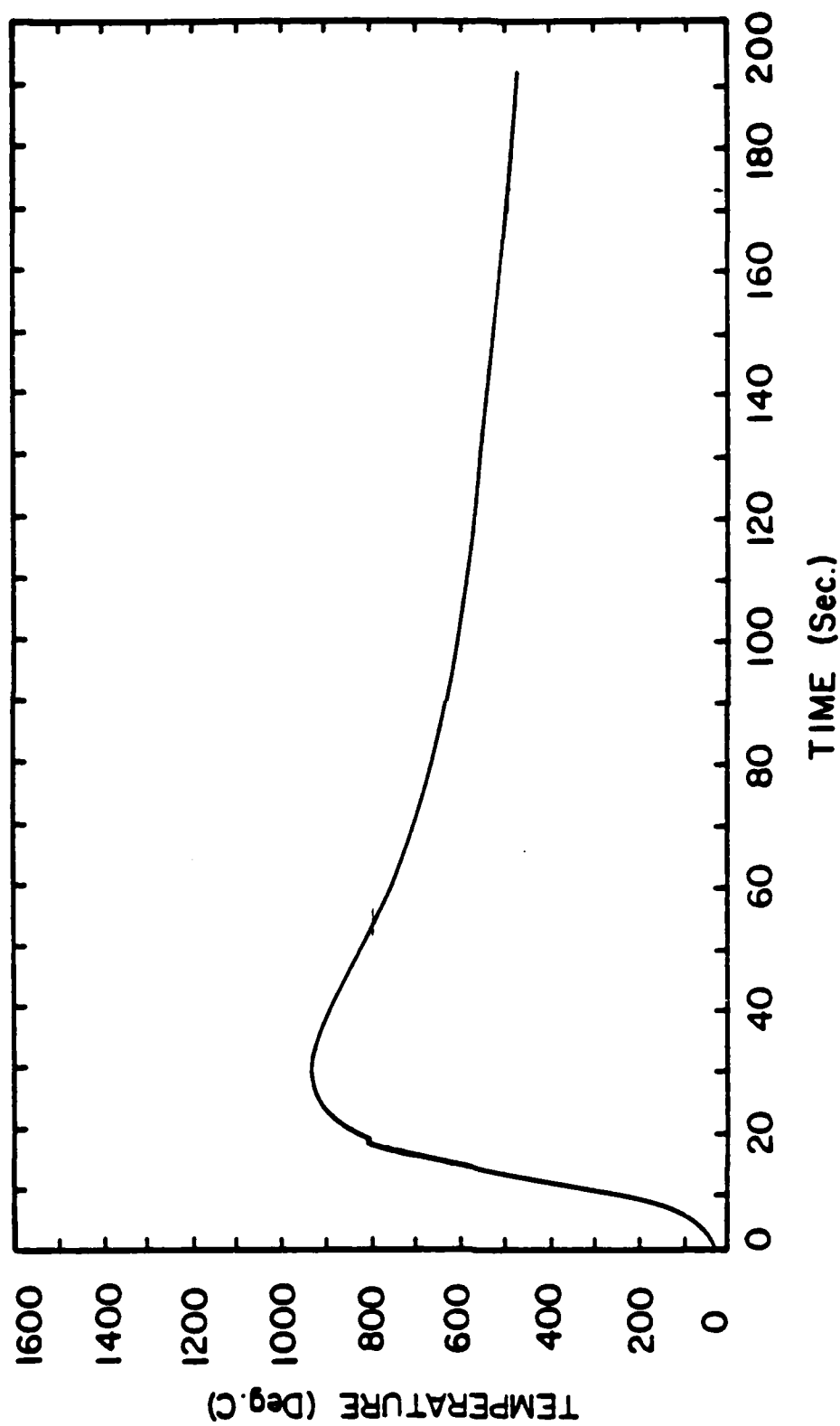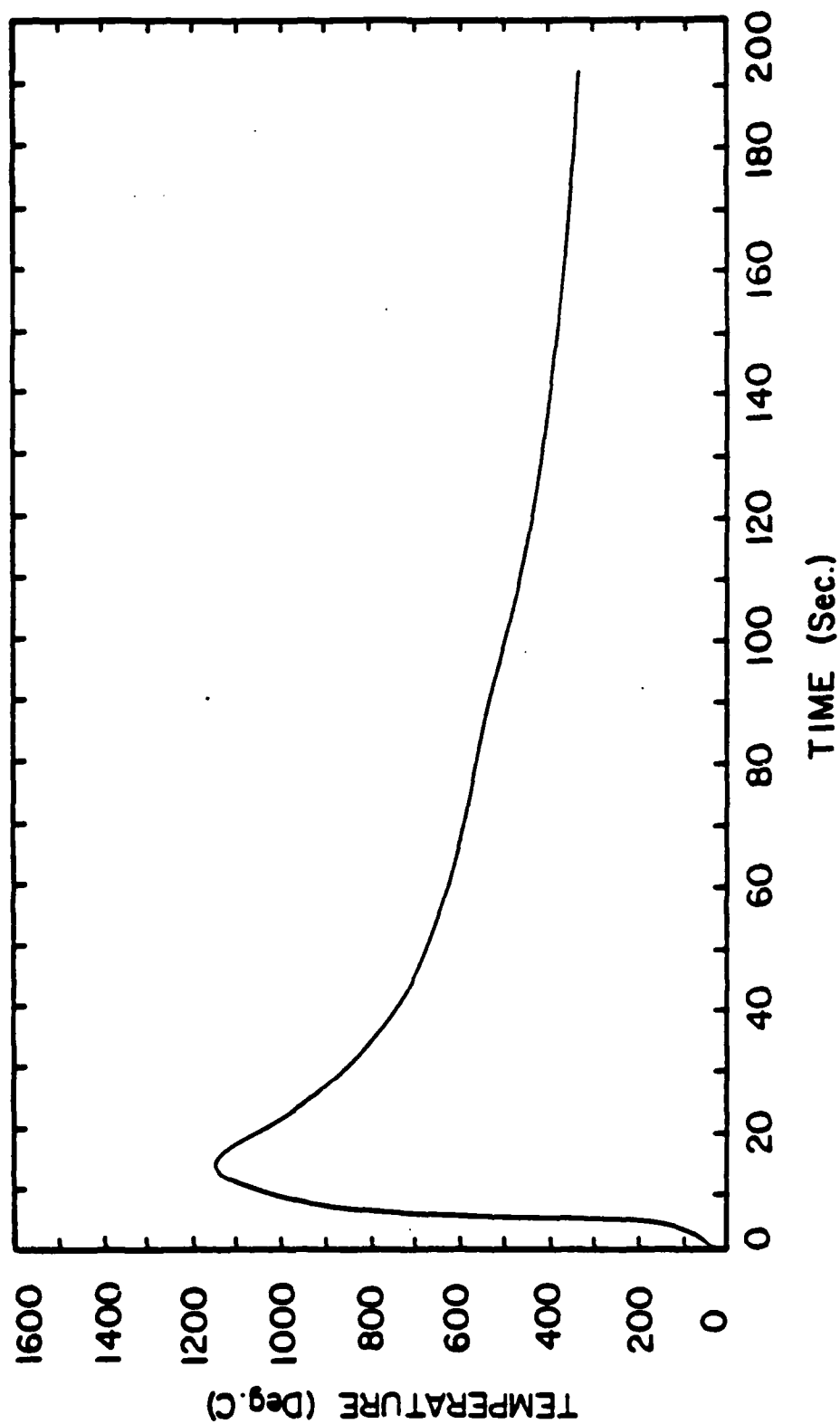
Figure 112.   Experimental weld thermal cycle for Plate 4.TC2;
nominal heat input=4.92 KJ/mm, Tp=931 deg.C,
D_{FZL}=4.92mm.
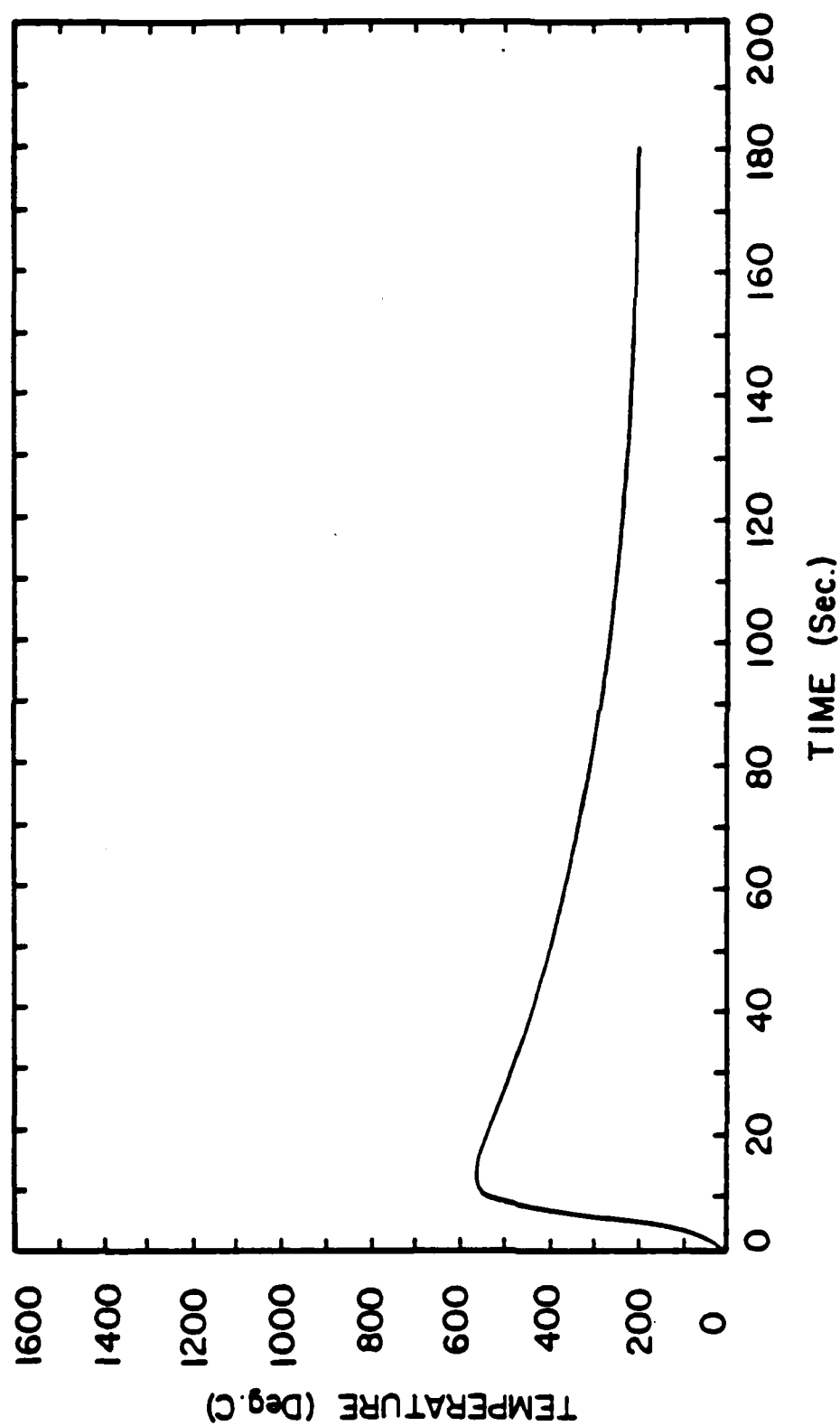
Figure 113.   Experimental weld thermal cycle for Plate 5.TC1;
               nominal heat Input=1.97 KJ/mm, Tp=558 deg.C
               D_{FZL}=3.12mm.
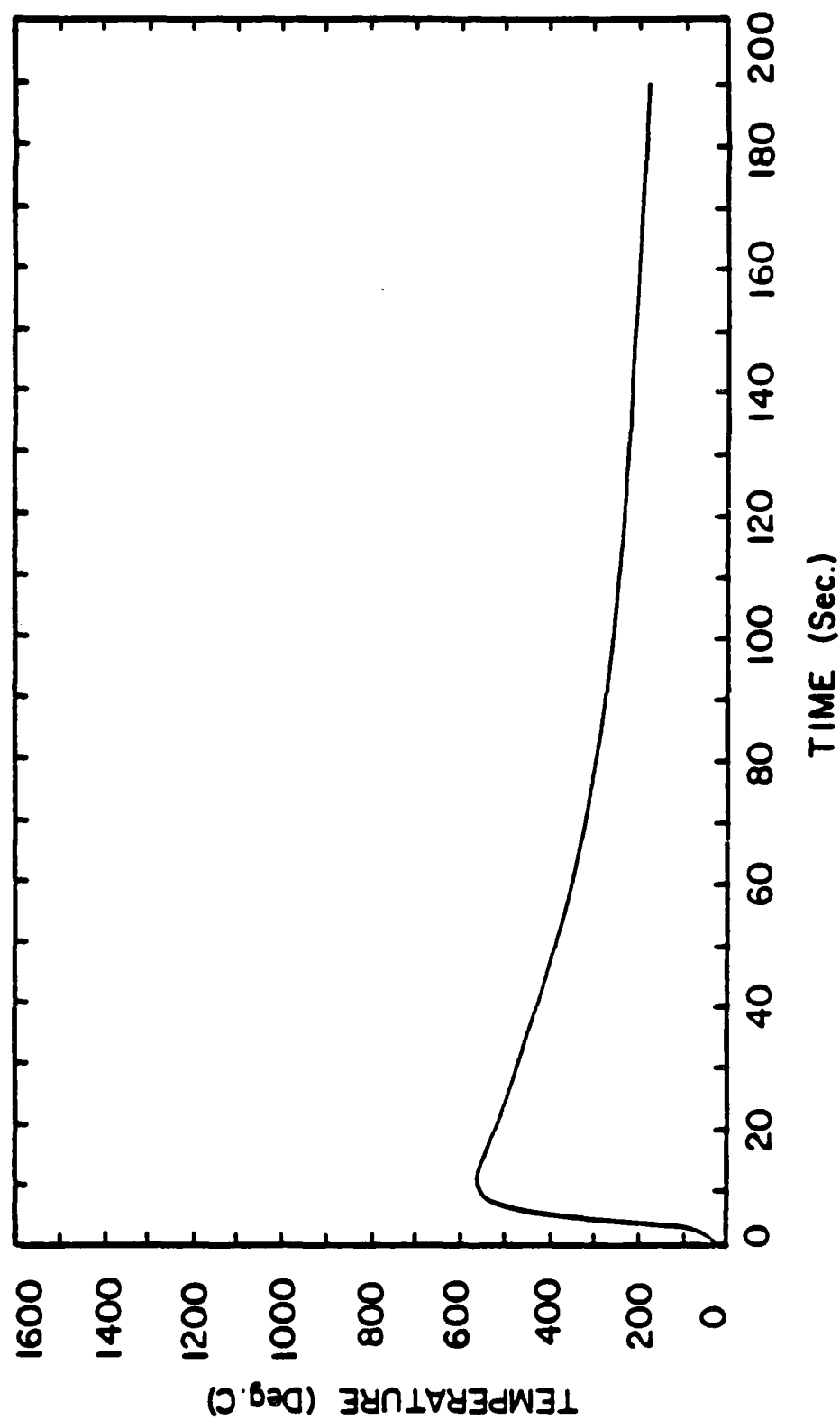
Figure 114. Experimental weld thermal cycle for Plate 5.TC2; nominal heat input=1.97 KJ/mm, Tp=803 deg.C, D_{FZL}=2.88mm.
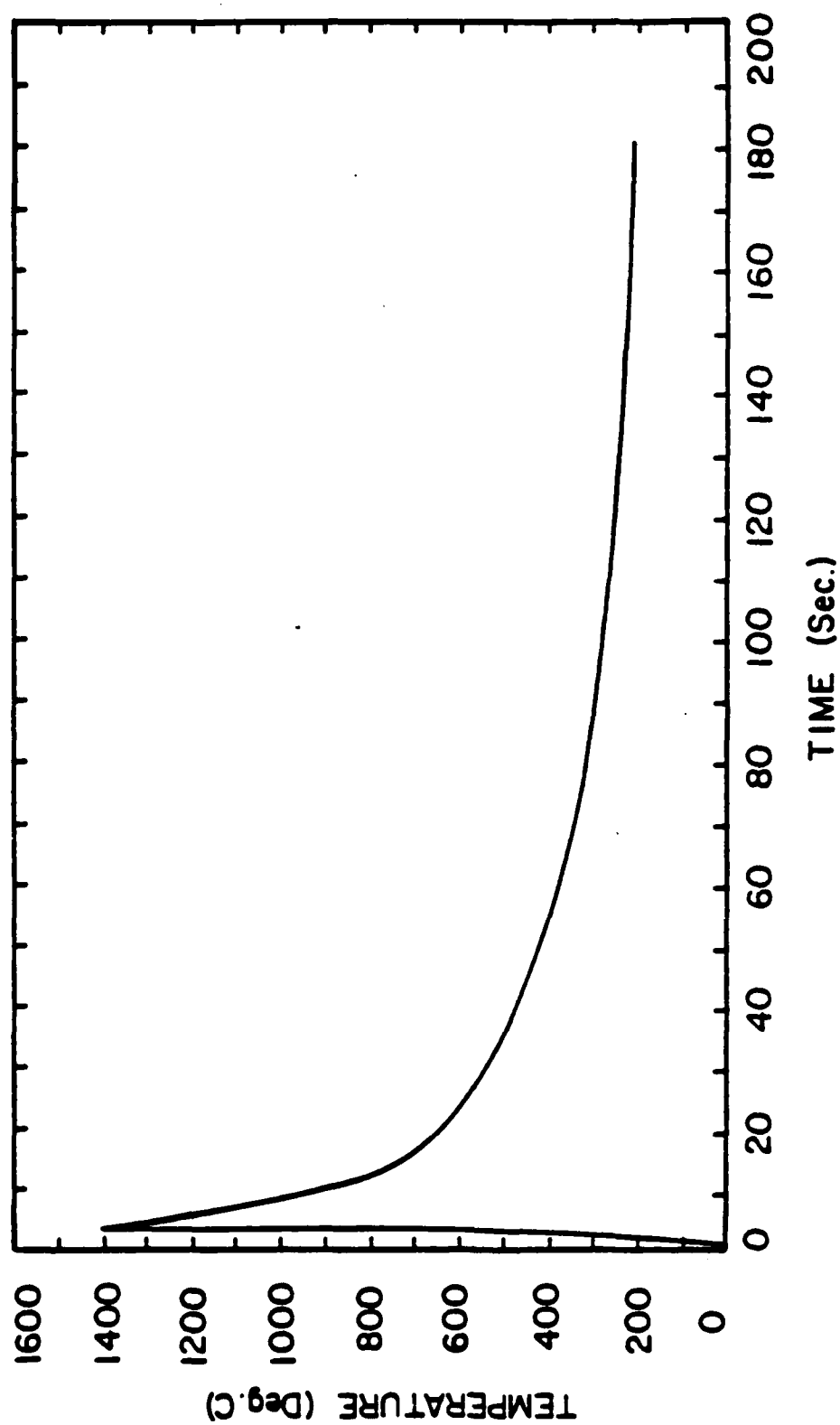
Figure 115.   Experimental weld thermal cycle for Plate 6.TC1;
               nominal heat input=1.97 KJ/mm, Tp=1398 deg.C,
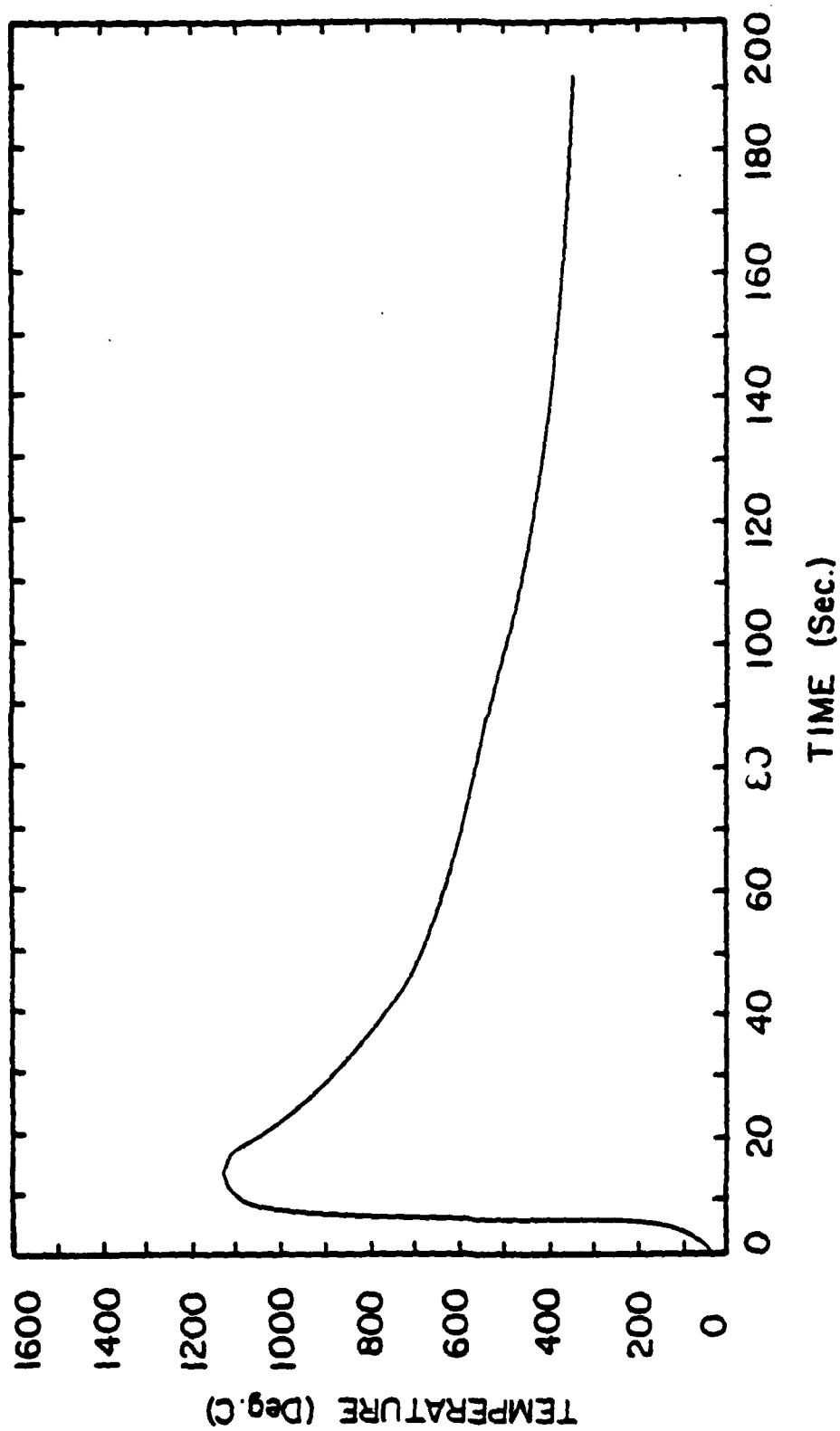 $D_{FZL}=0.09$mm.
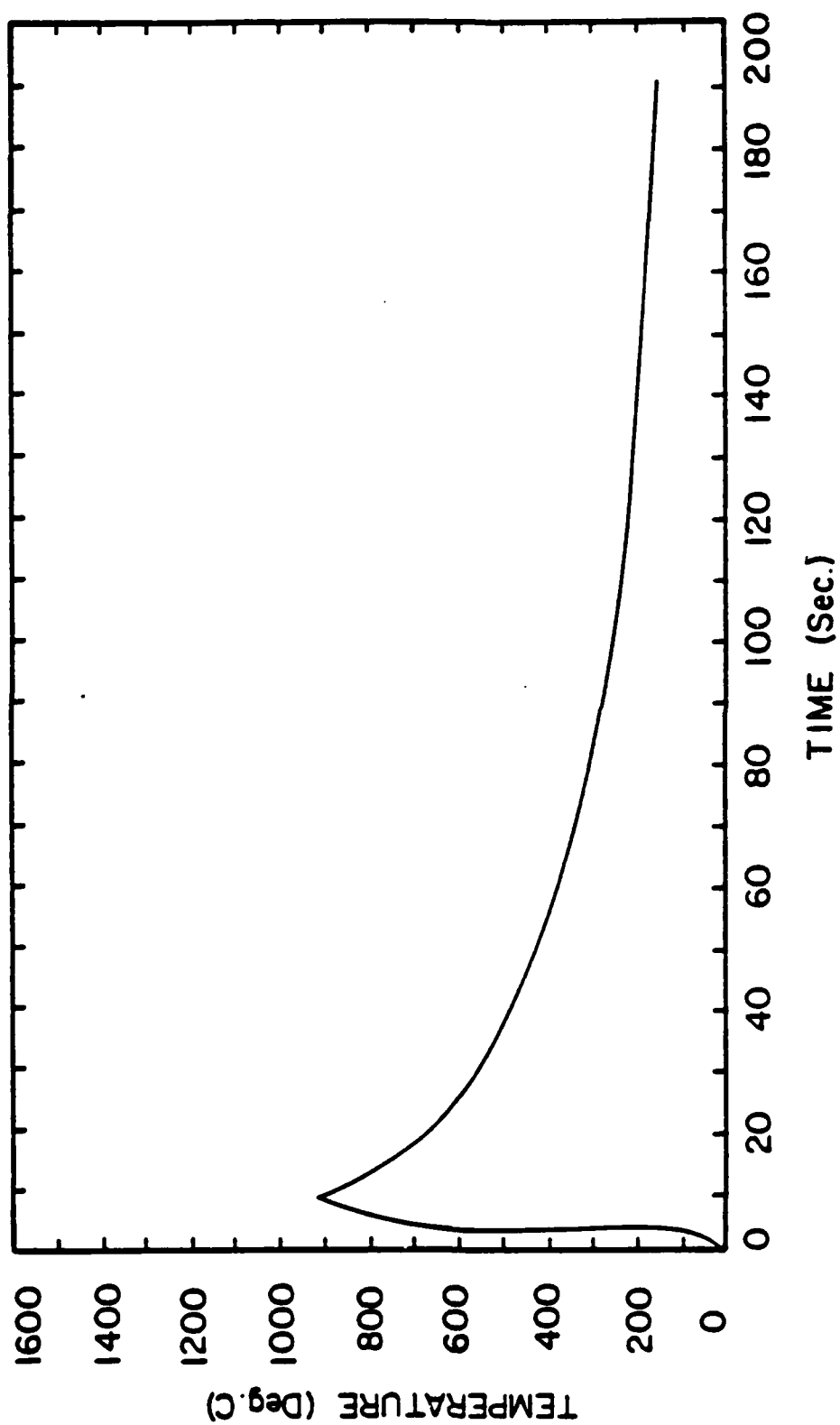
Figure 116. Experimental weld thermal cycle for Plate 6.TC2; nominal heat input=1.97 KJ/mm, Tp=916 deg.C, D_{FZL}=1.83mm.
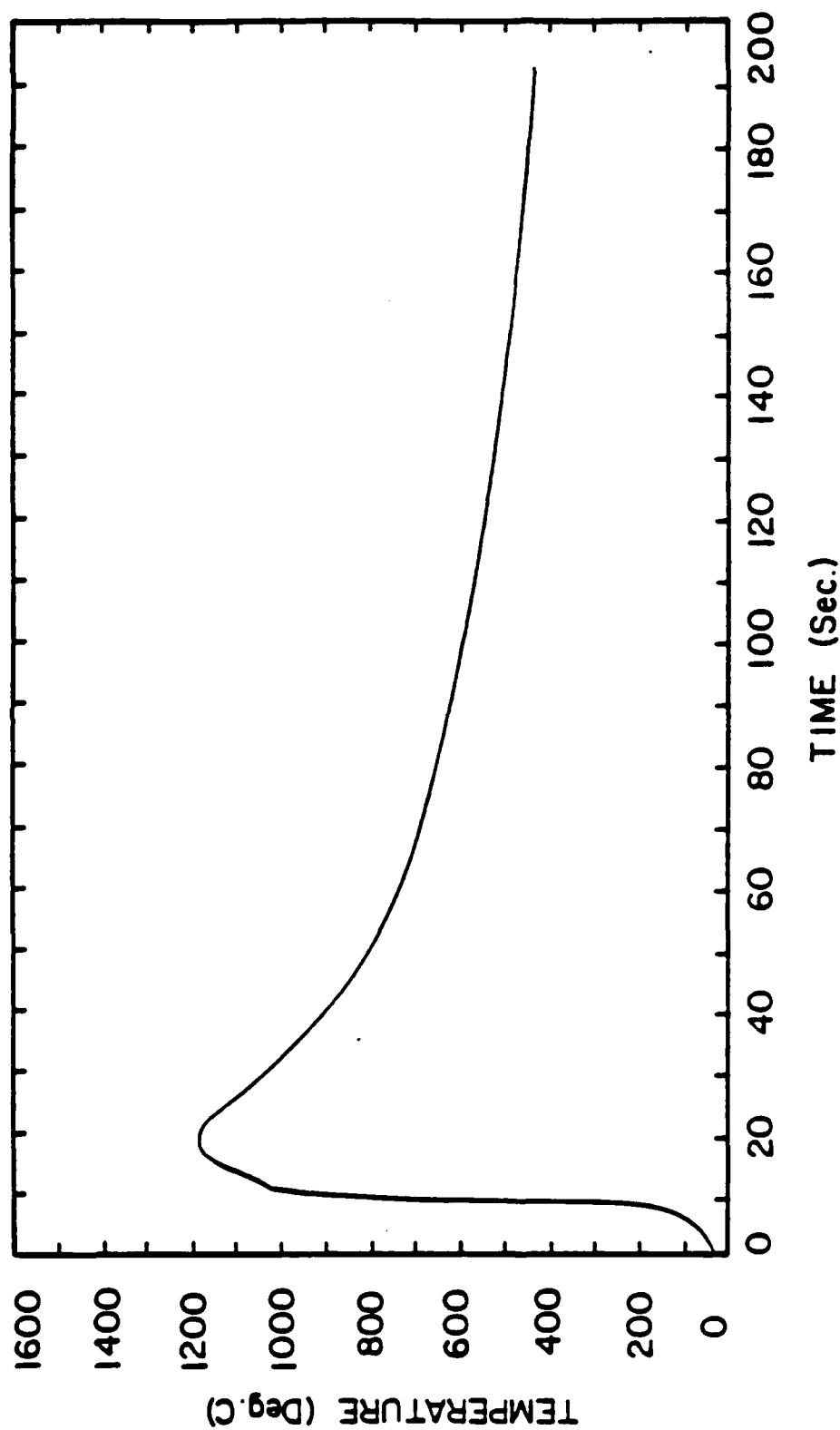
Figure 117. Experimental weld thermal cycle for Plate 7,TC1;
nominal heat input=4.92 KJ/mm. Tp=1180 deg.C.
D_{FZL}=1.64mm.
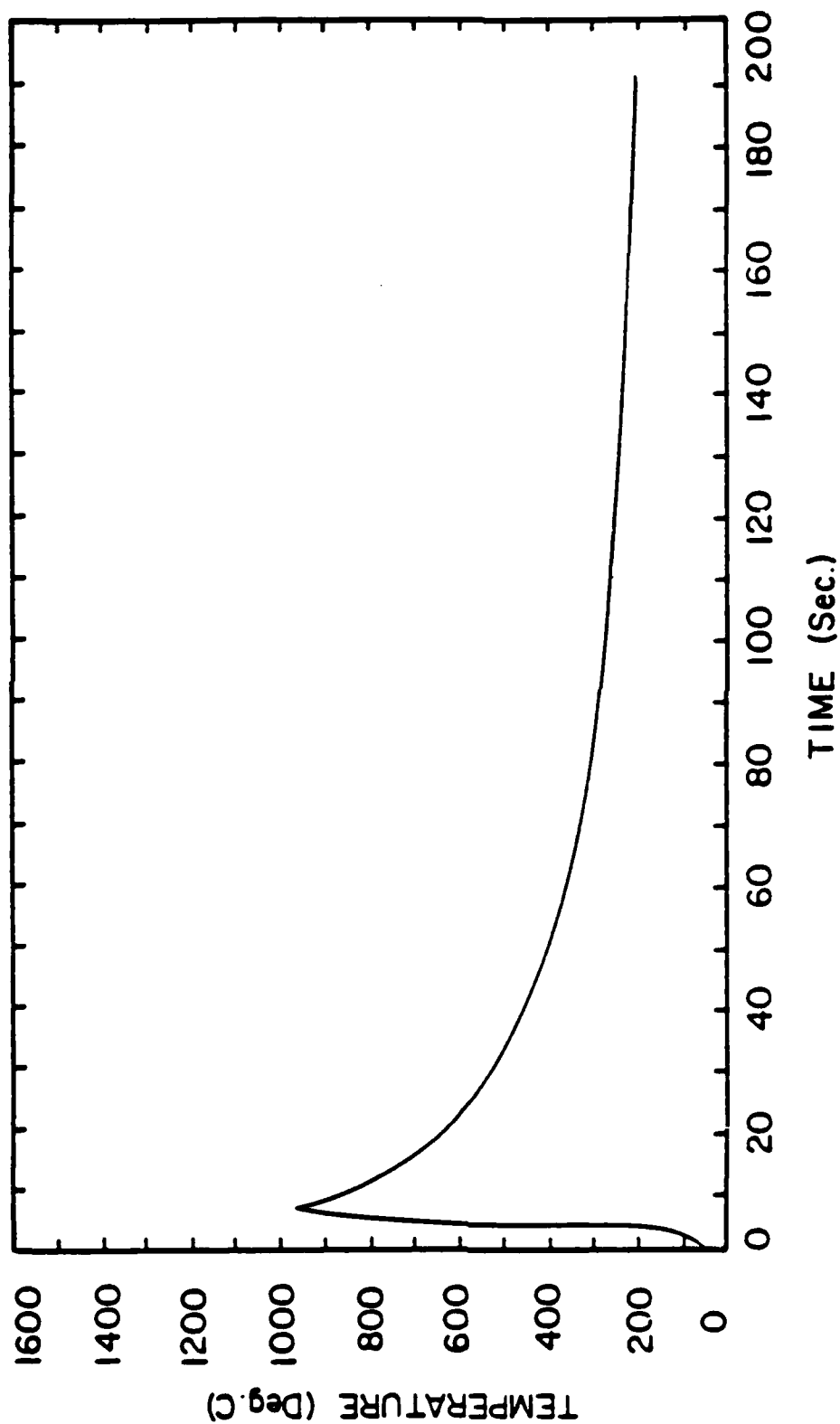
Figure 118. Experimental weld thermal cycle for Plate 8.TC1; nominal heat input=1.97 KJ/mm, Tp=954 deg.C, D_{FZL}=2.18mm.
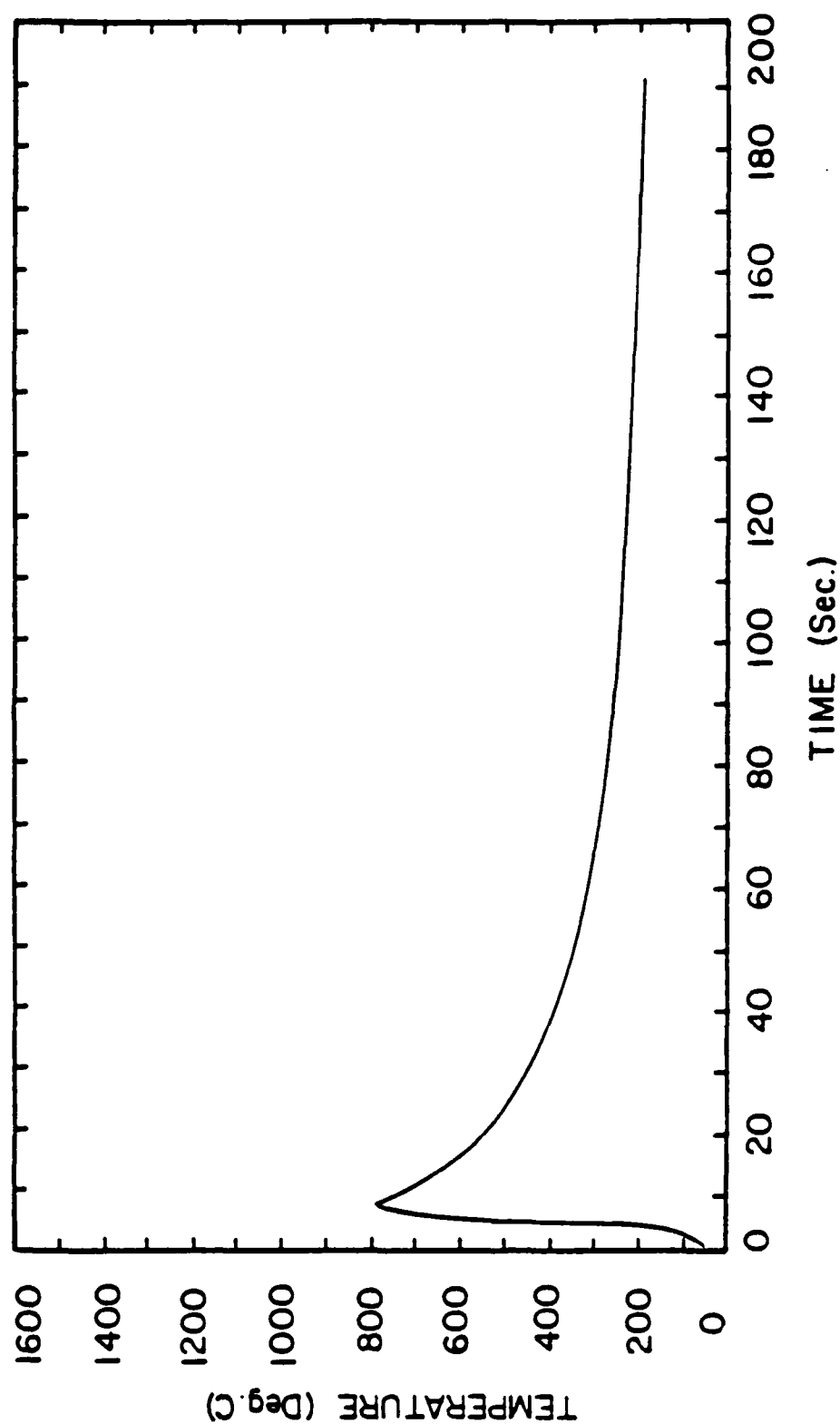
Figure 119.   Experimental weld thermal cycle for Plate 8.TC2;
nominal heat input=1.97 KJ/mm, Tp=785 deg.C,
D_{FZL}=2.04mm.
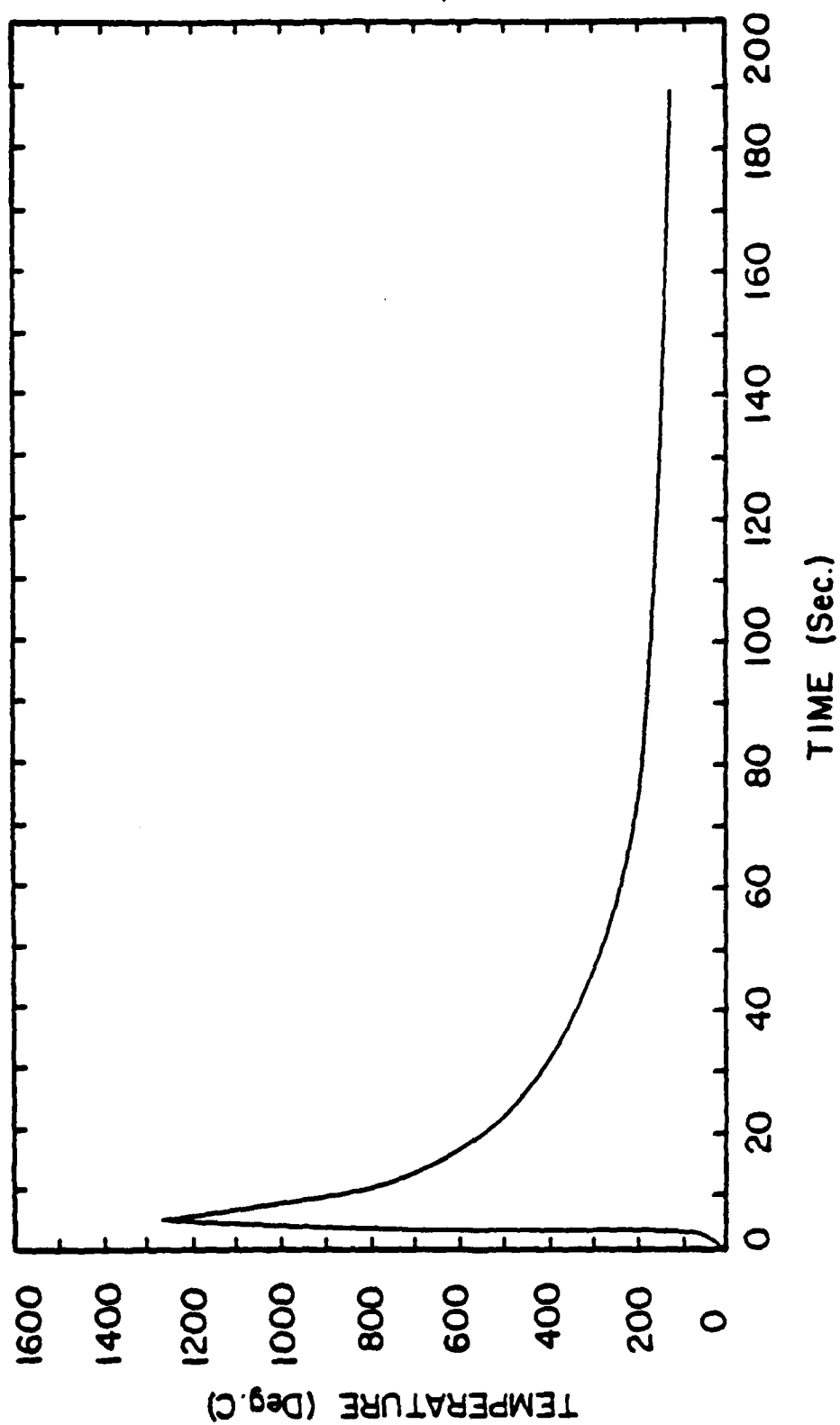
Figure 120. Experimental weld thermal cycle for Plate 9,TC1: nominal heat input=1.97 KJ/mm, T_p=1272 deg.C, D_{FZL}=0.19mm.
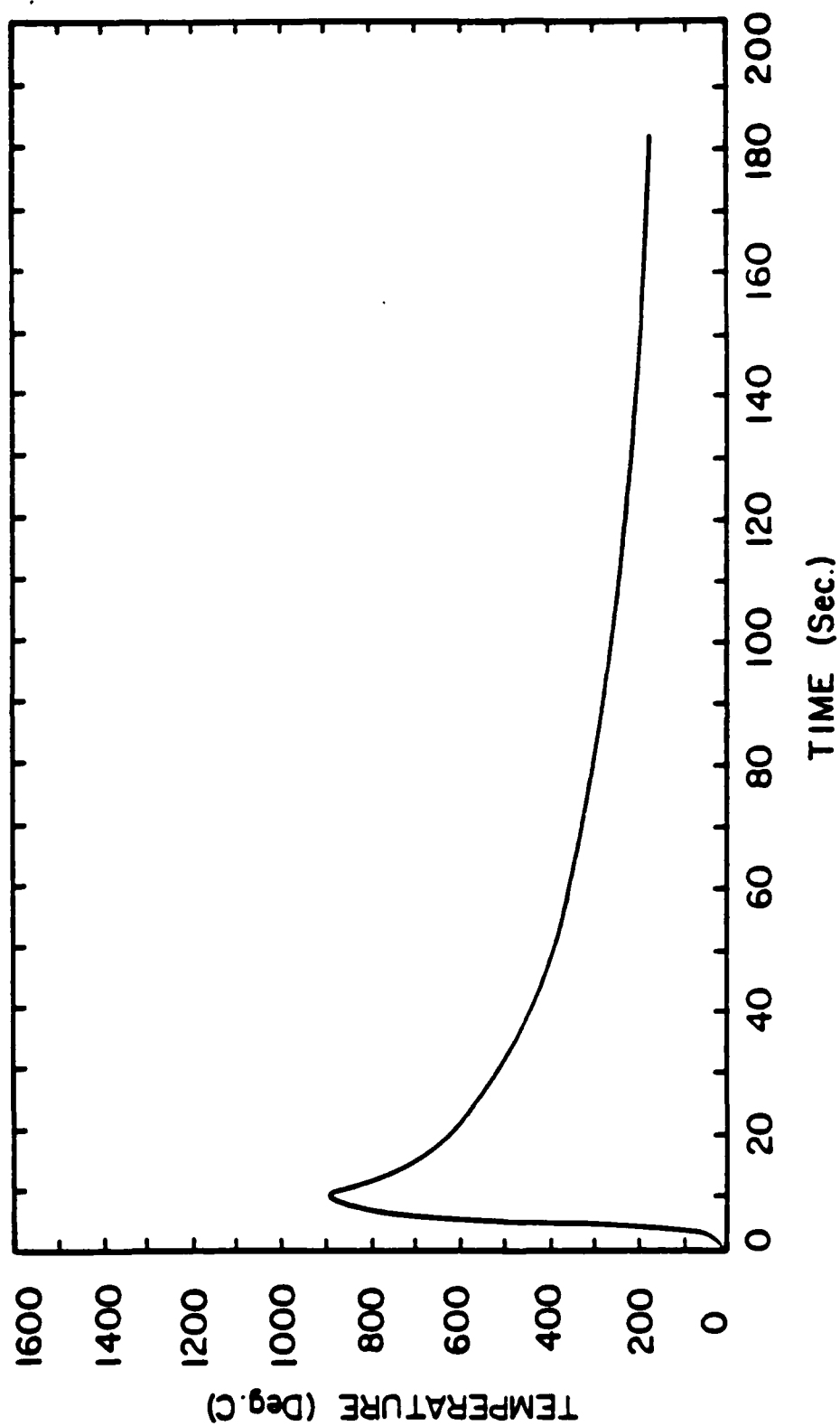
Figure 121.   Experimental weld thermal cycle for Plate 9.TC2;
               nominal heat input=1.97 KJ/mm, Tp=881 deg.C,
               D_{FZL}=0.88mm.
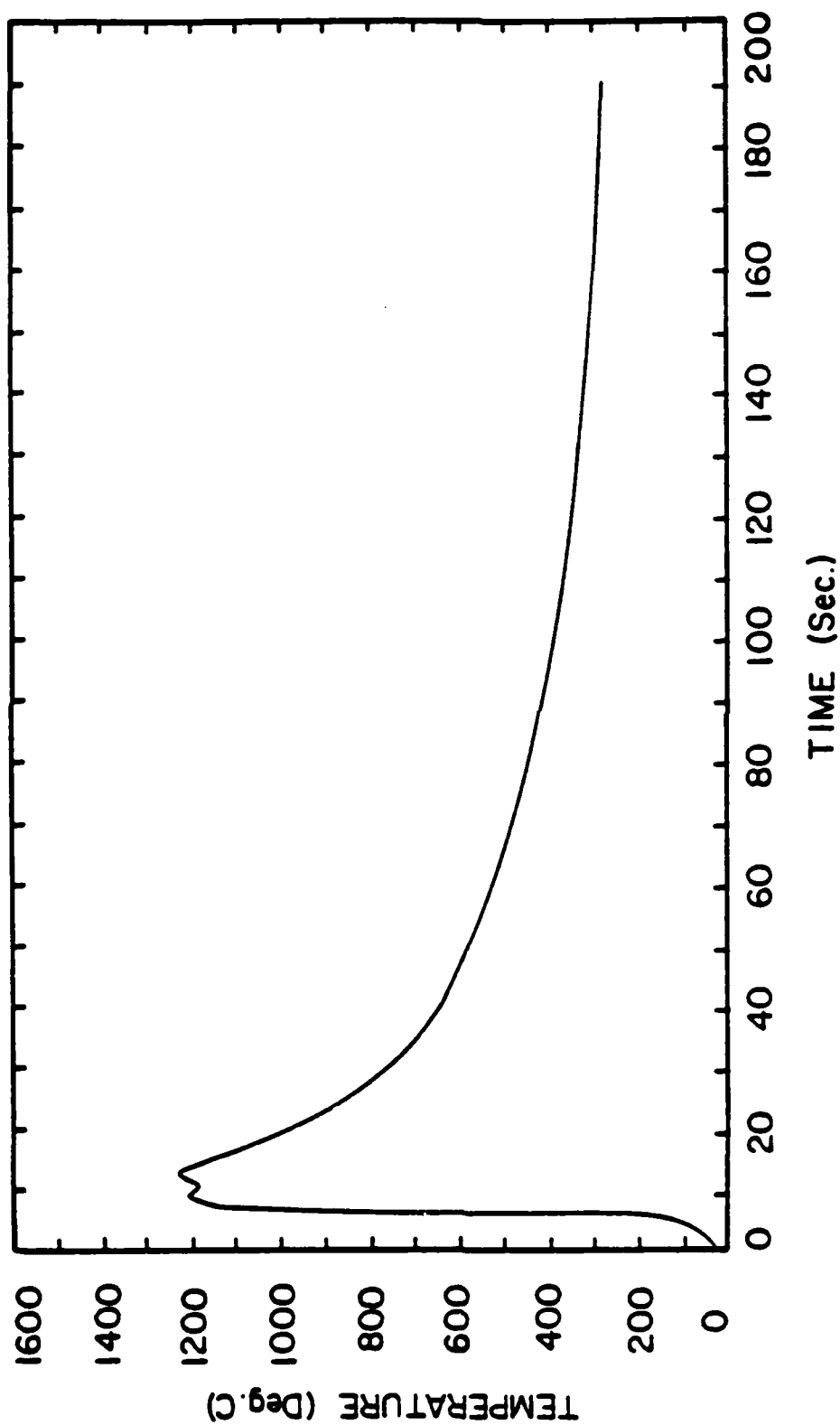
Figure 122. Experimental weld thermal cycle for Plate 10.TCI; nominal heat input=3.35 KJ/mm. Tp=1224 deg.C. $D_{FZL}=1.11mm.$
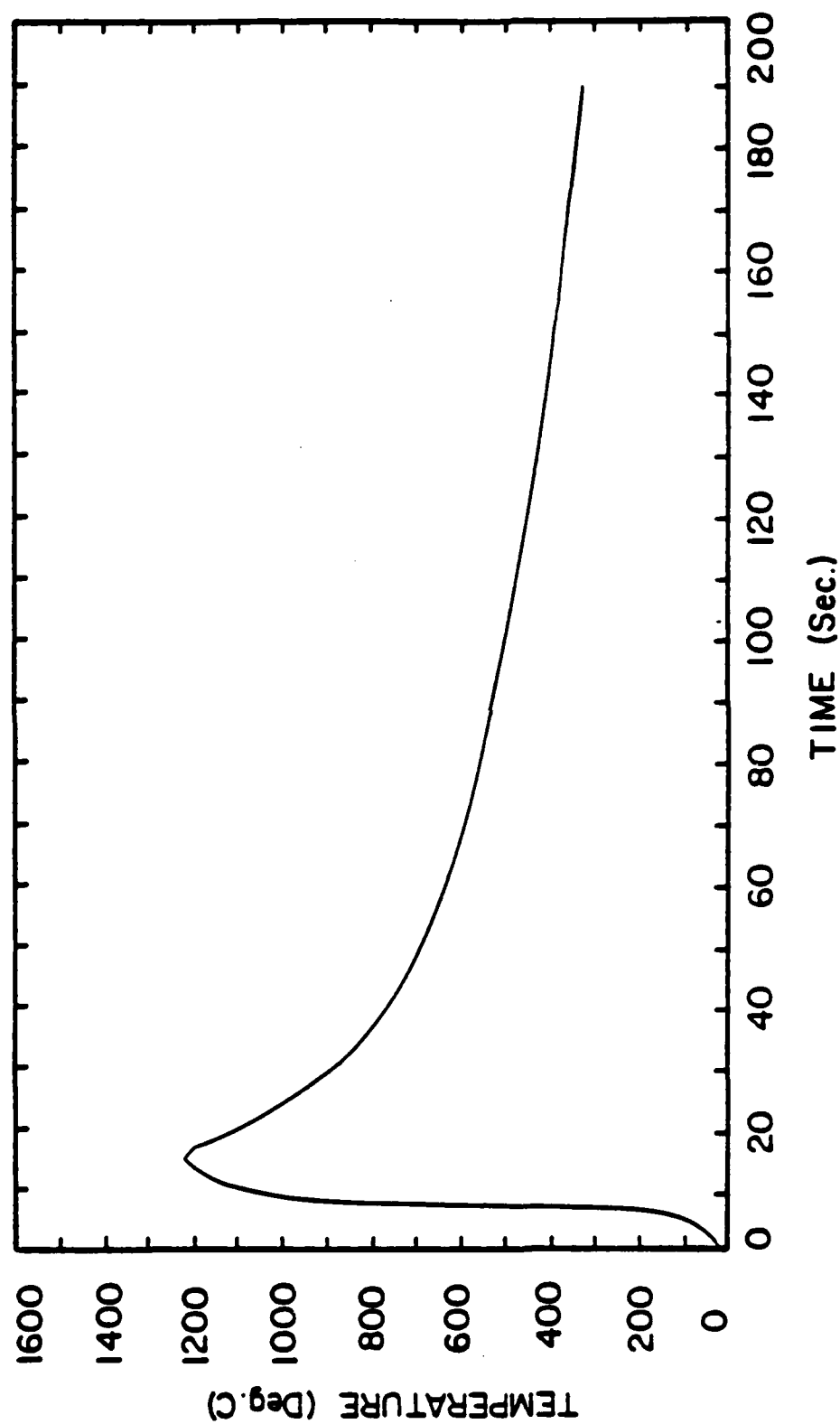
Figure 123.   Experimental weld thermal cycle for Plate 10,TC2;
               nominal heat input=3.35 KJ/mm, Tp=1245 deg.C,
               D_{FZL}=1.31mm.
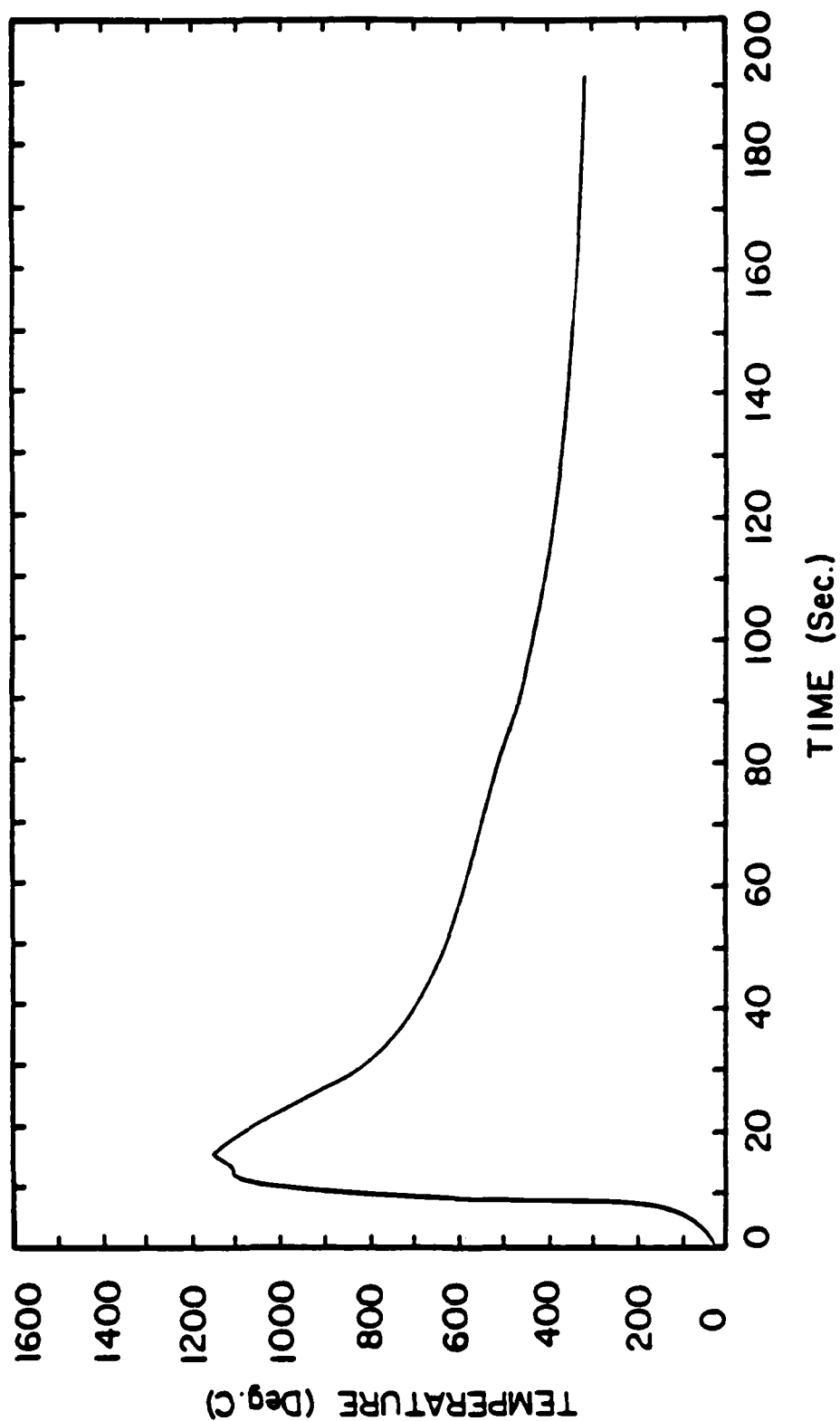
Figure 124. Experimental weld thermal cycle for Plate 11.TC1; nominal heat input=3.35 KJ/mm, Tp=1149 deg.C D_{FZL}=1.21mm.
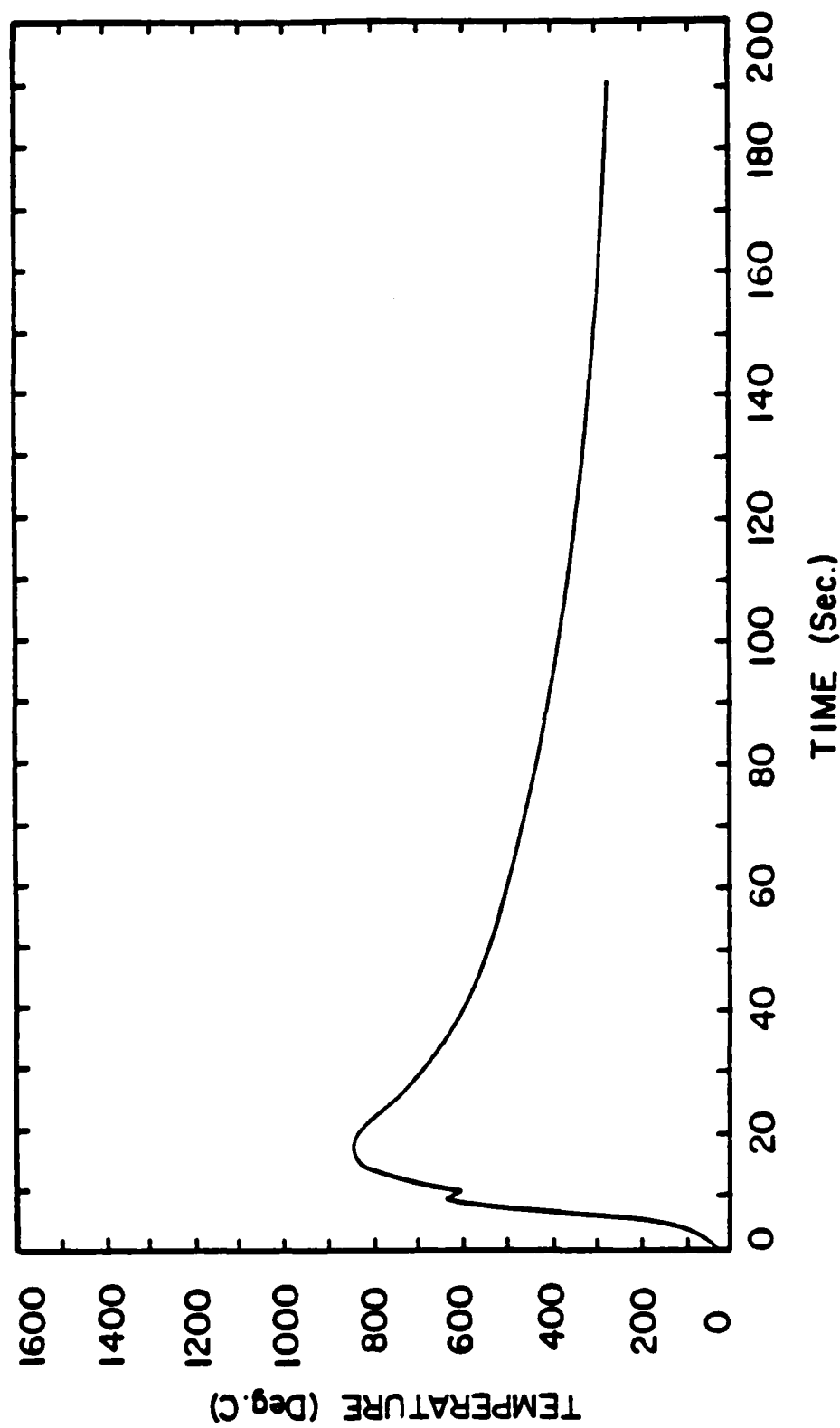
Figure 125. Experimentyal weld thermal cycle for Plate
             11.TC2; nominal heat input=3.35 KJ/mm, Tp=856
             deg.C, D_{FZL}=2.73mm.
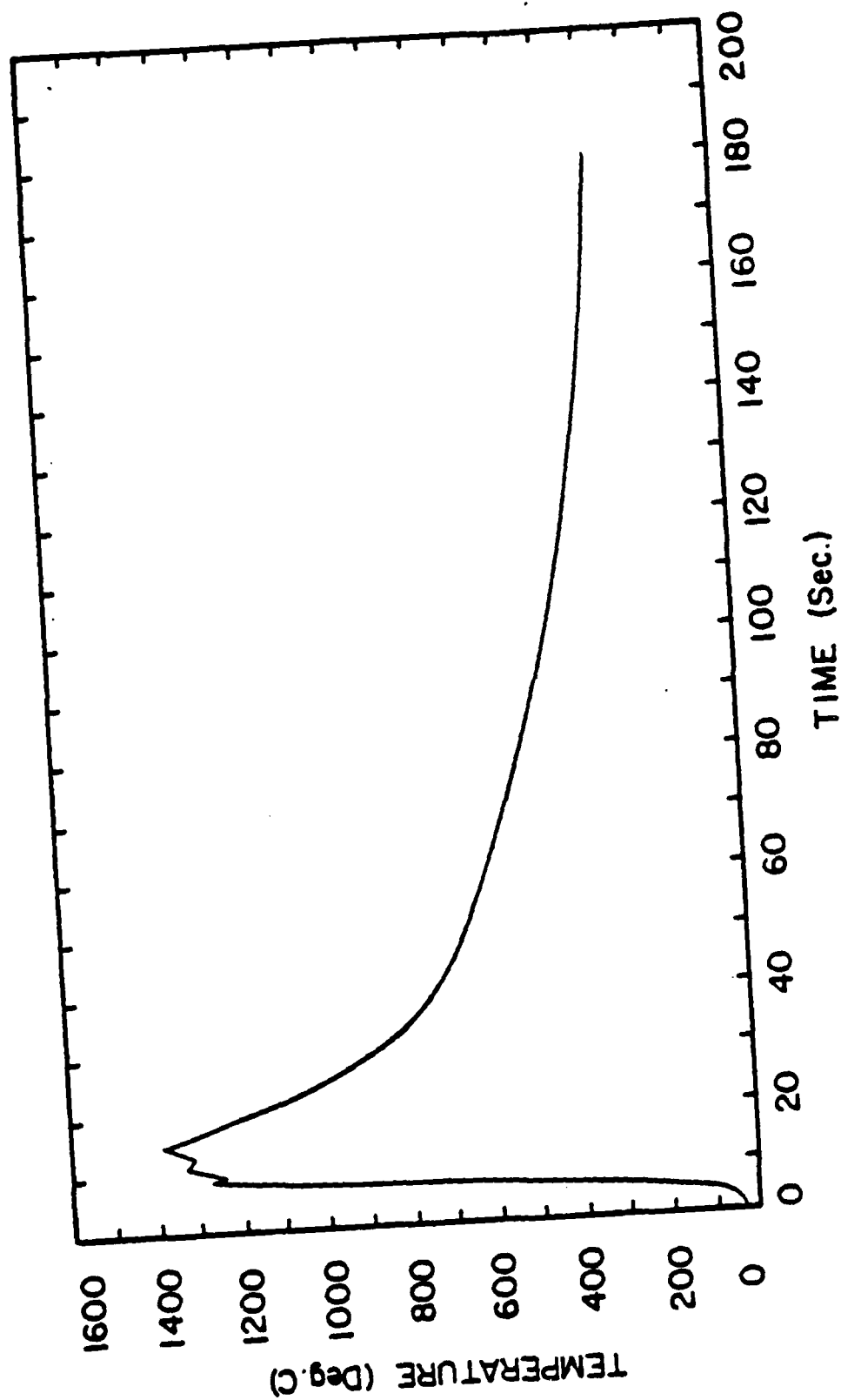
Figure 126.   Experimental weld thermal cycle for Plate 12.TC2;
nominal heat input=3.35 KJ/mm, Tp=1380 deg.C.
DFZL=0.39mm.
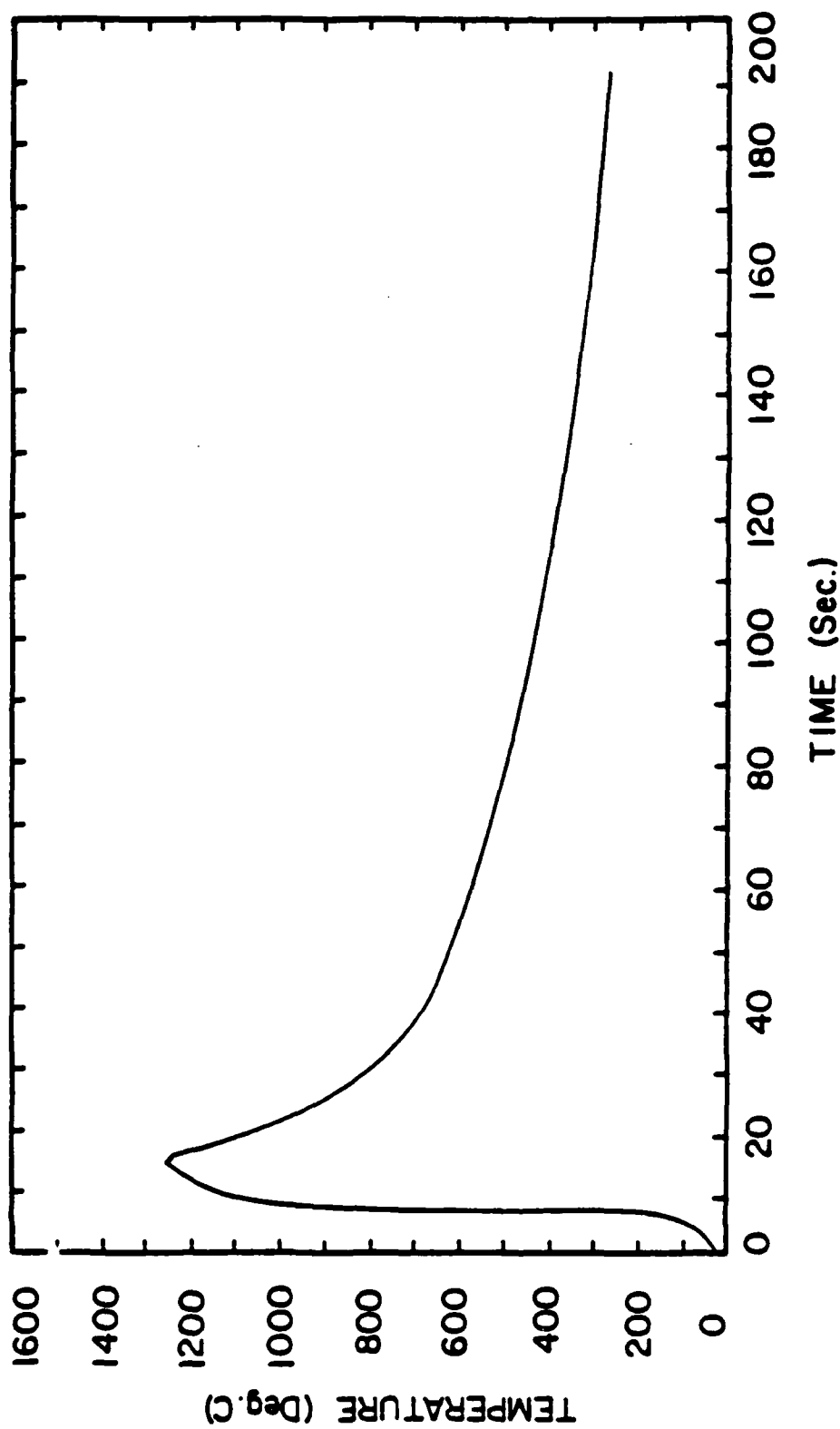
Figure 127.   Experimental weld thermal cycle for Plate 13.TCl;
nominal heat input=3.35 KJ/mm, Tp=1223 deg.C,
$D_{FZL}=1.44$mm.

Figure 128. Experimental weld thermal cycle for Plate 13.TC2; nominal heat input=3.35 KJ/mm, Tp=1058 deg.C, D_{FZL}=2.89mm.

Figure 129.   Experimental weld thermal cycle for Plate 14.TC1;
               nominal heat input=3.35 KJ/mm, Tp=1123 deg.C,
               $D_{FZL}=0.91$mm.

Figure 130.   Experimental weld thermal cycle for Plate 14, TC2;
nominal heat input=3.35 KJ/mm, Tp=1143 deg.C,
D_{FZL}=1.81mm.

APPENDIX 2

Simulation charpy impact transition temperature curves with corresponding thermal transient curves for the following weld plates:

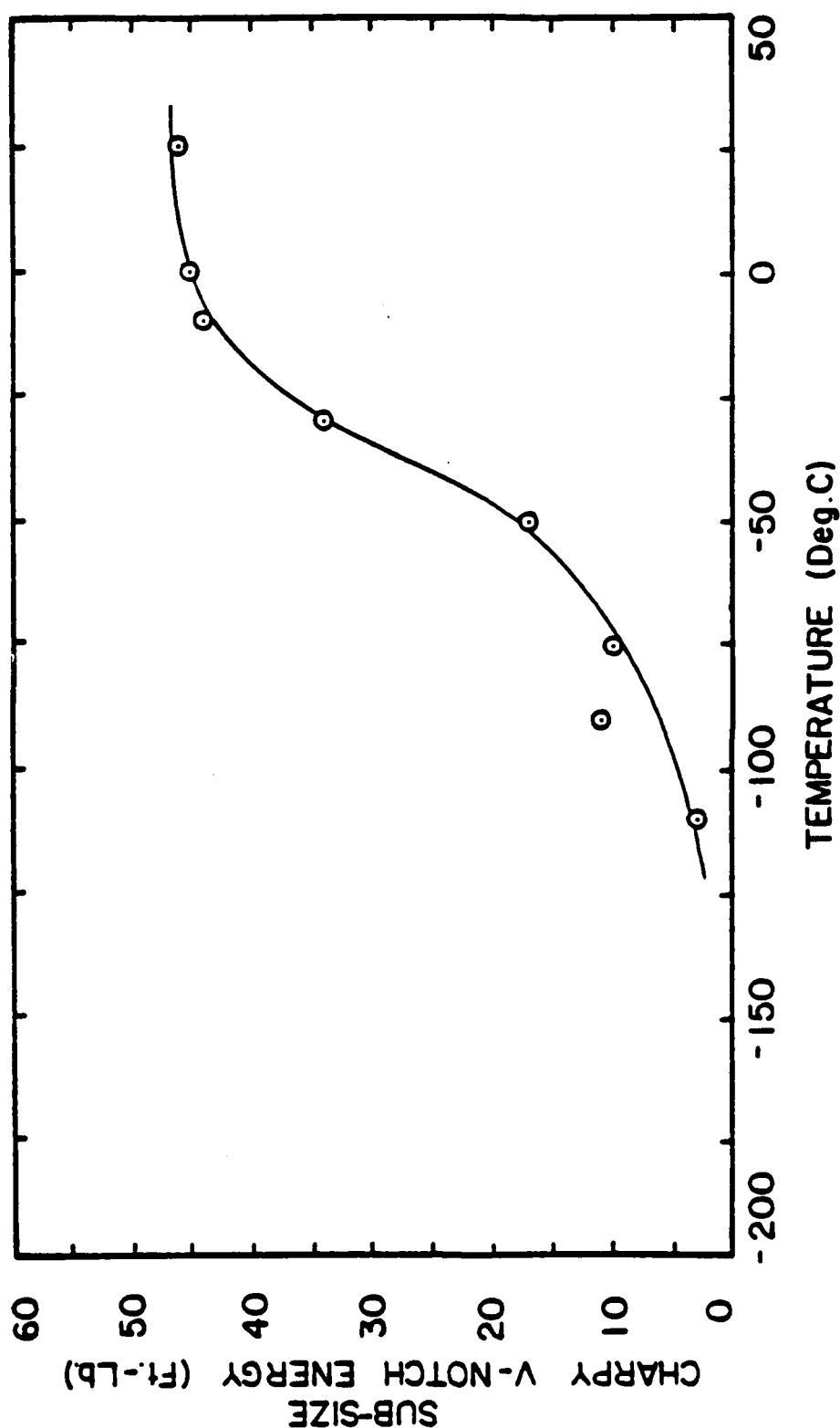Plate 12. TC2

Plate 6. TC1

Plate 4. TC1

Plate 5. TC1

Plate 9. TC2
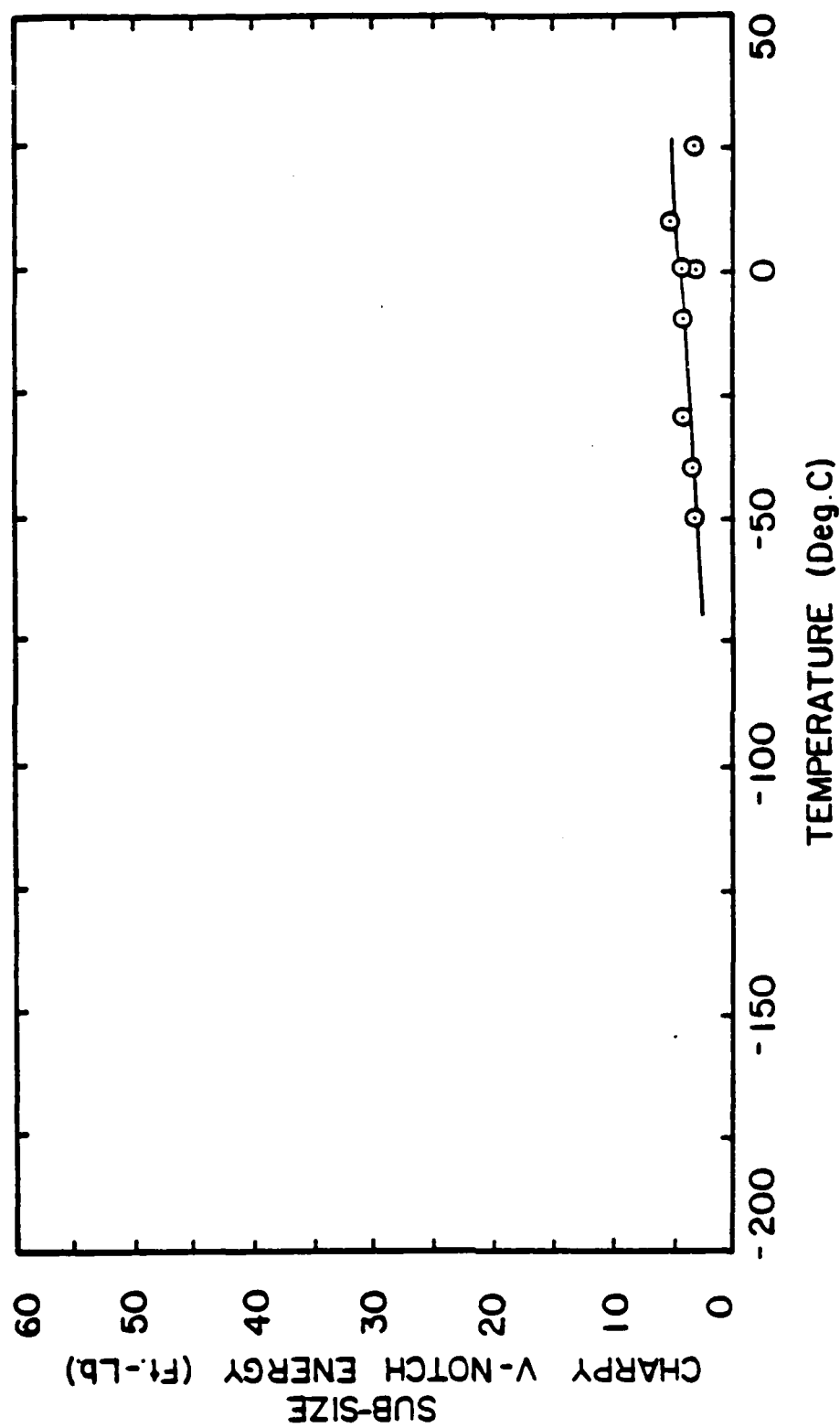
Figure 131. (a) Charpy impact energy as a function of temperature for simulated HAZ thermal cycle parameters; nominal heat input of 3.35 KJ/mm. T_p=1380 deg.C, D_{FZL}=0.40mm, DPH = 238.
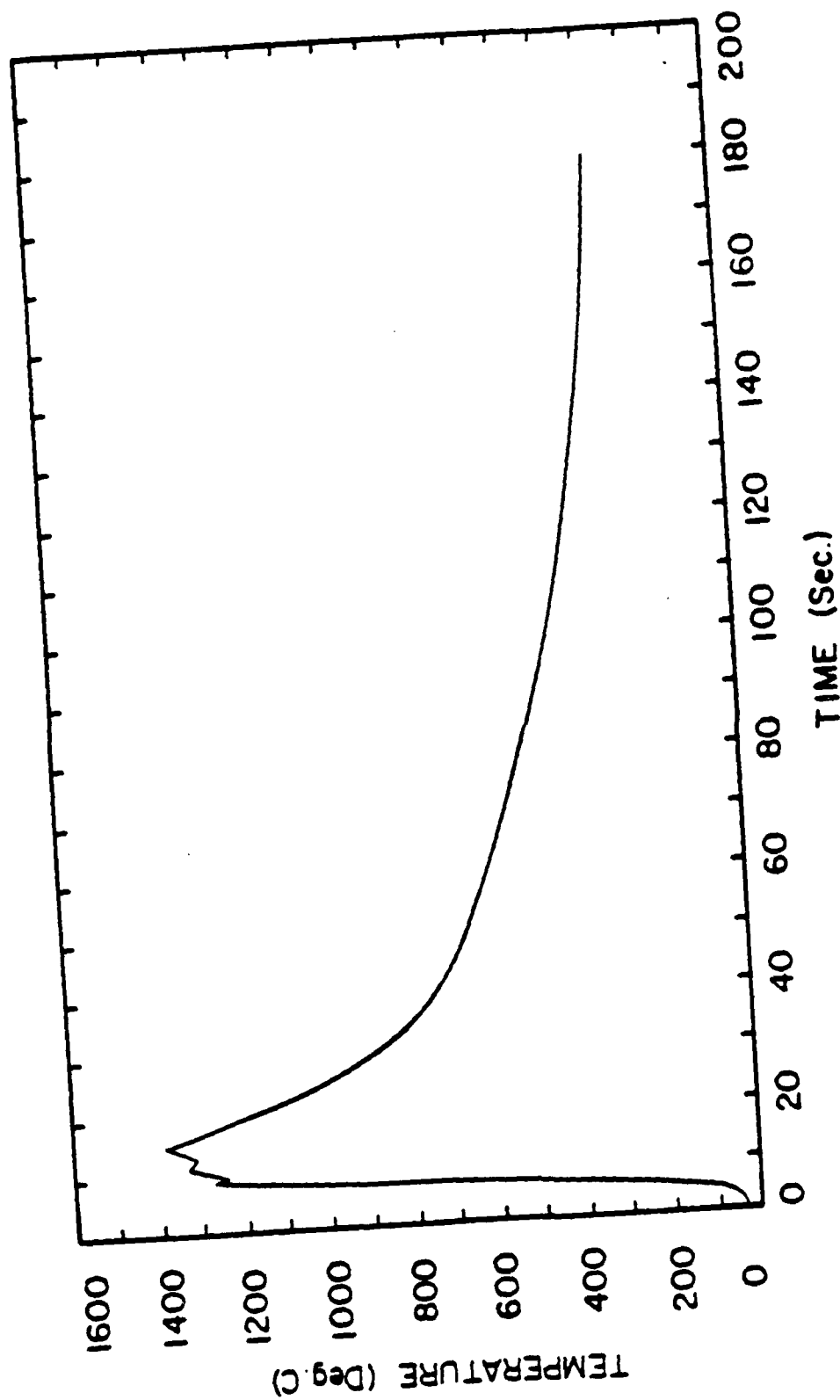
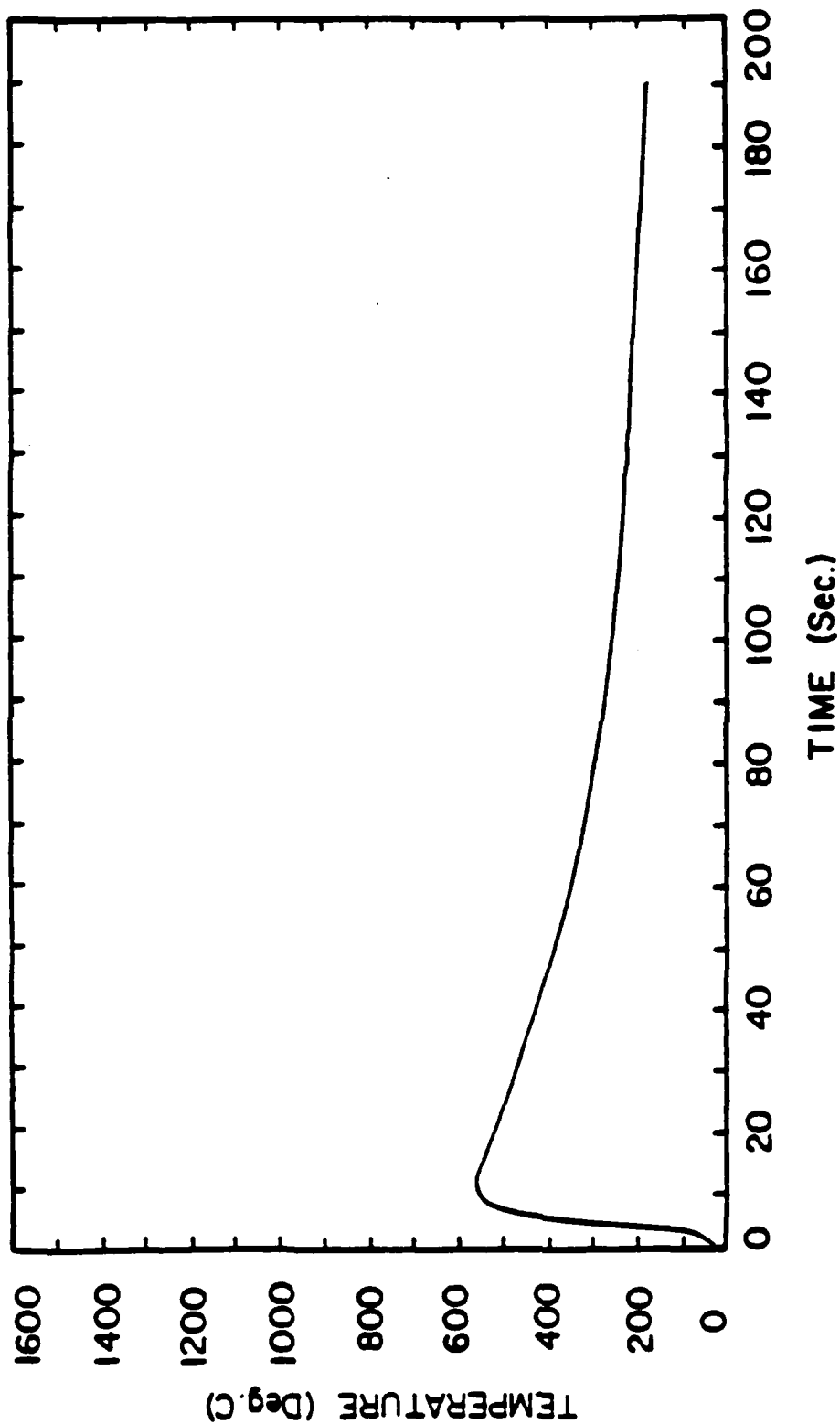Figure 131   (b) Experimental weld thermal cycle for Plate
12.TC2; nominal heat input=3.35 KJ/mm, Tp=1380
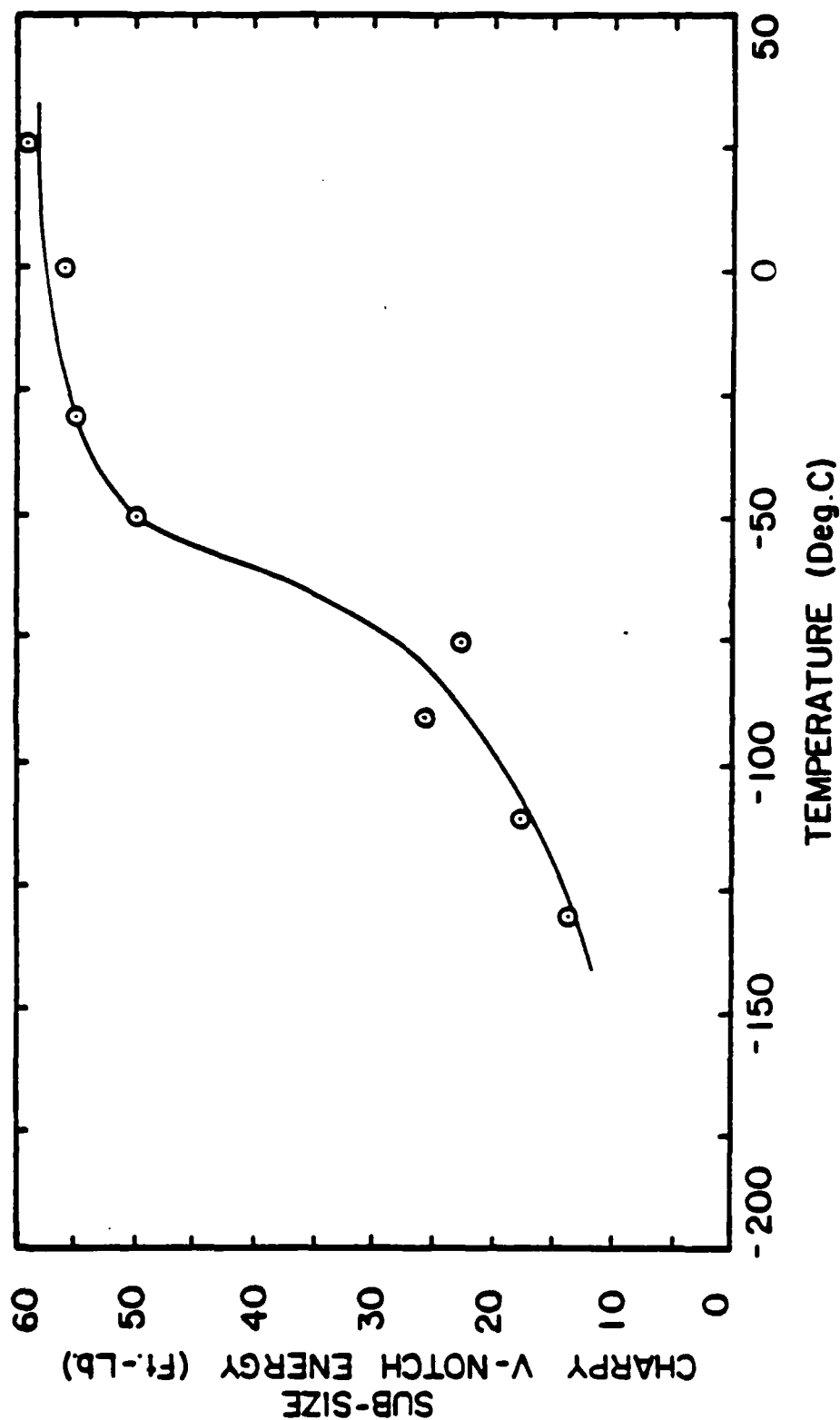deg.C, D_{FZL}=0.39mm.
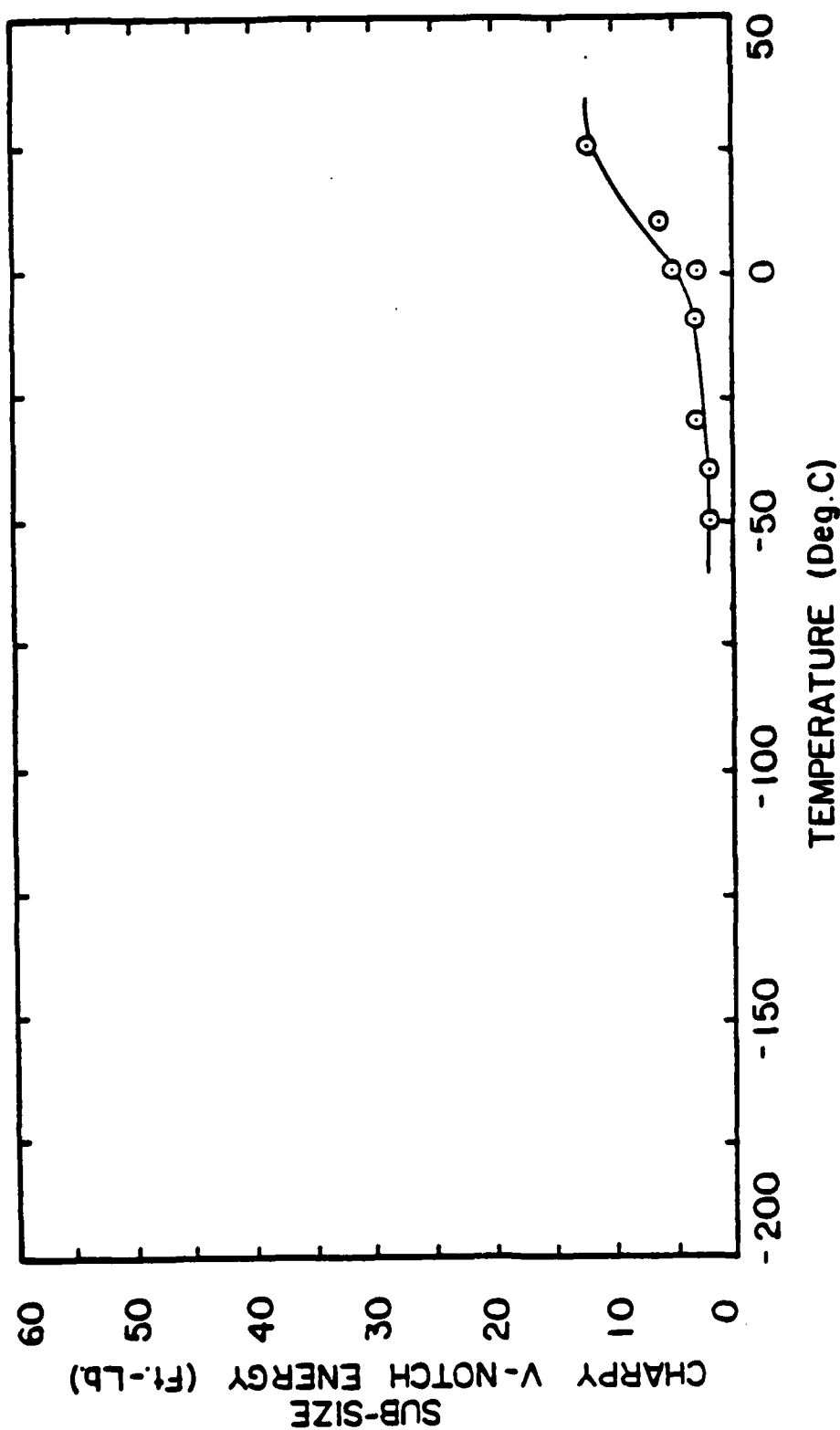
Figure 132.   (a) Charpy impact energy as a function of
Temperature for simulated HAZ thermal cycle
parameters; nominal heat input of 1.97 KJ/mm.
T_p=1398 deg.C, D_{FZL}=0.09mm, DPH = 285.
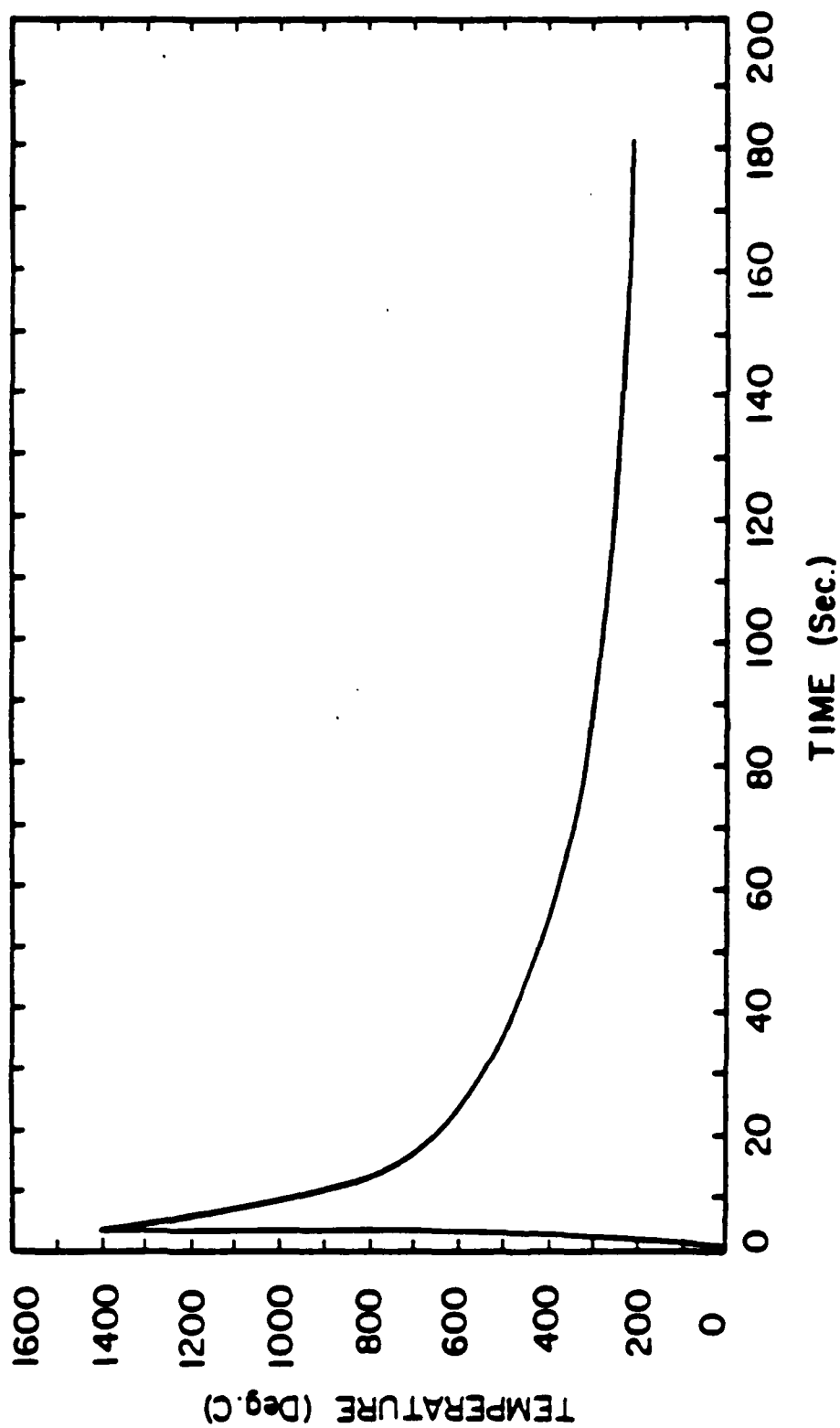
Figure 132. (b) Experimental weld thermal cycle for Plate 6.TCI; nominal heat input=1.97 KJ/mm, Tp=1398 deg.C. D_{FZL}=0.09mm.
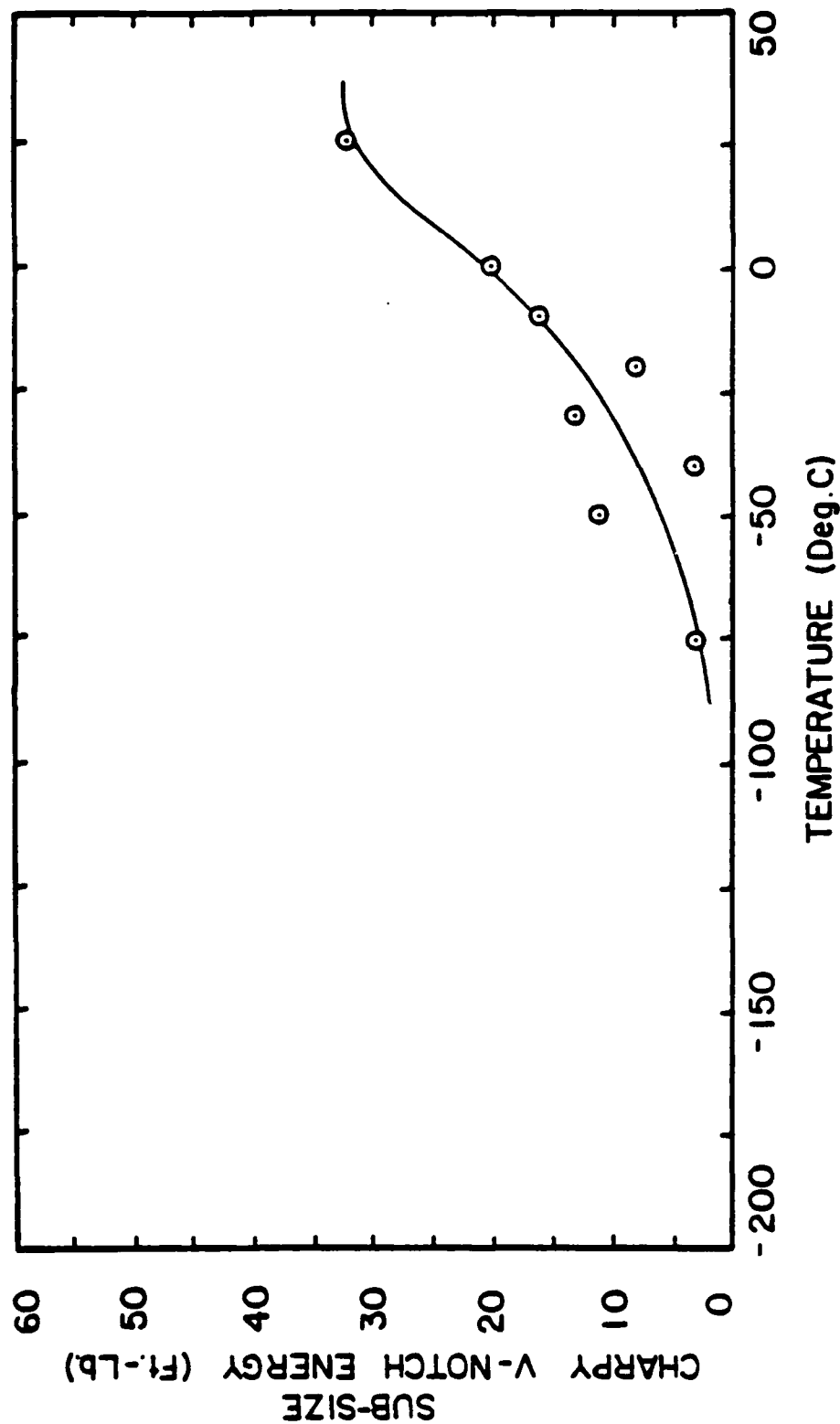
Figure 133.   (a) Charpy impact energy as a function of
              temperature for simulated HAZ thermal cycle
              parameters; nominal heat input 4.92 KJ/mm,
              T_p=1063 deg.C, D_{FZL}=3.53mm, DPH = 240.
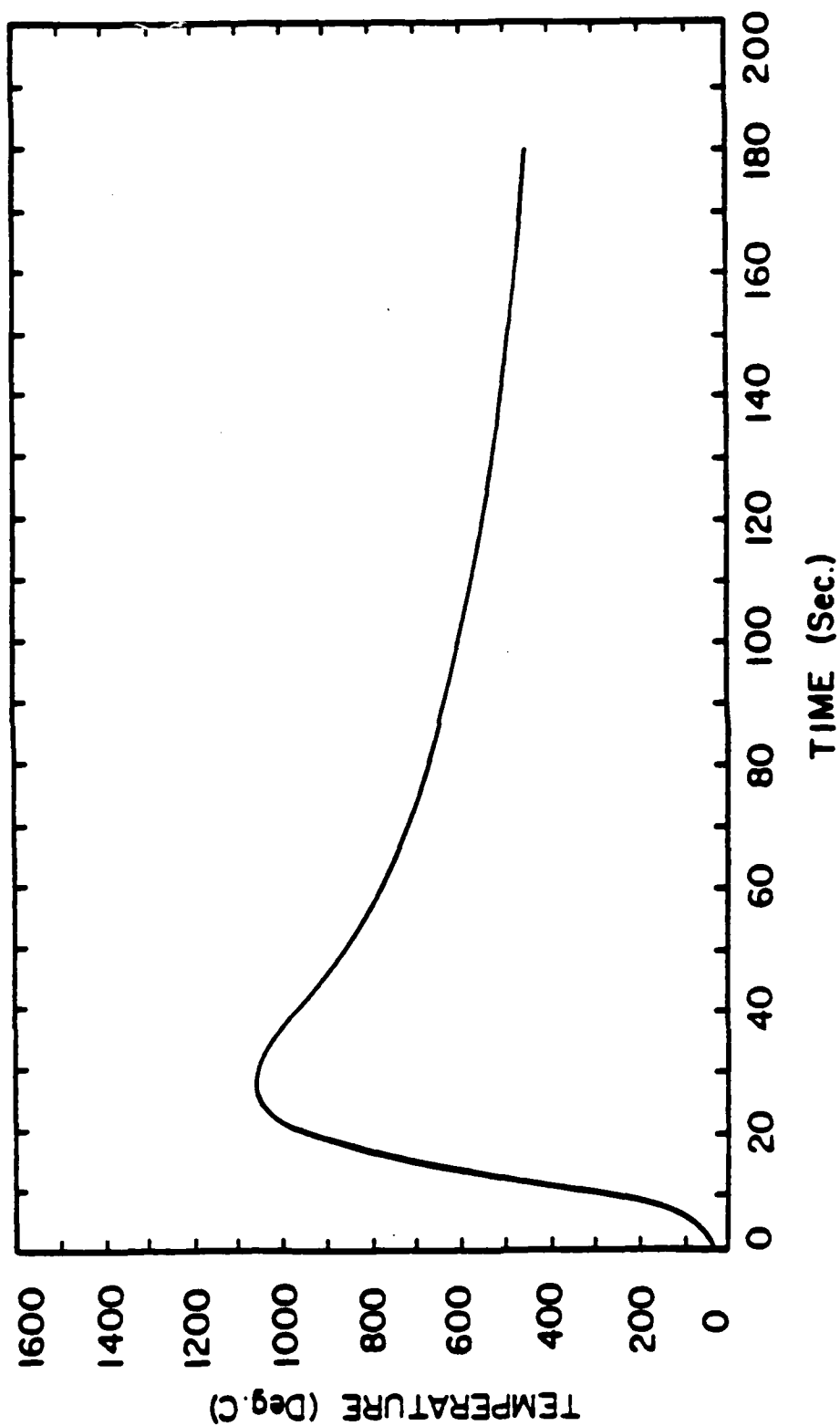
Figure 133.   (b) Experimental weld thermal cycle for Plate
               4.TC1; nominal heat input=4.92 KJ/mm, Tp=1063
               deg.C, DFZL=3.35mm.

Figure 134.   (a) Charpy impact energy as a function of temperature for simulated HAZ thermal cycle parameters; nominal heat input of 1.97 KJ/mm. T_p=558 deg.C, D_{FZL}=3.12mm, DPH = 215.

Figure 134.   (b) Experimental weld thermal cycle for Plate
5.TC1; nominal heat input=1.97 KJ/mm. Tp=558
deg.C D_{FZL}=3.12mm.

Figure 135.   (a) Charpy impact energy as a function of
temperature for simulated HAZ thermal cycle
parameters; nominal heat input of 1.97 KJ/mm.
T_p=881 deg.C, P_{FZL}=0.88mm, DPH = 250.
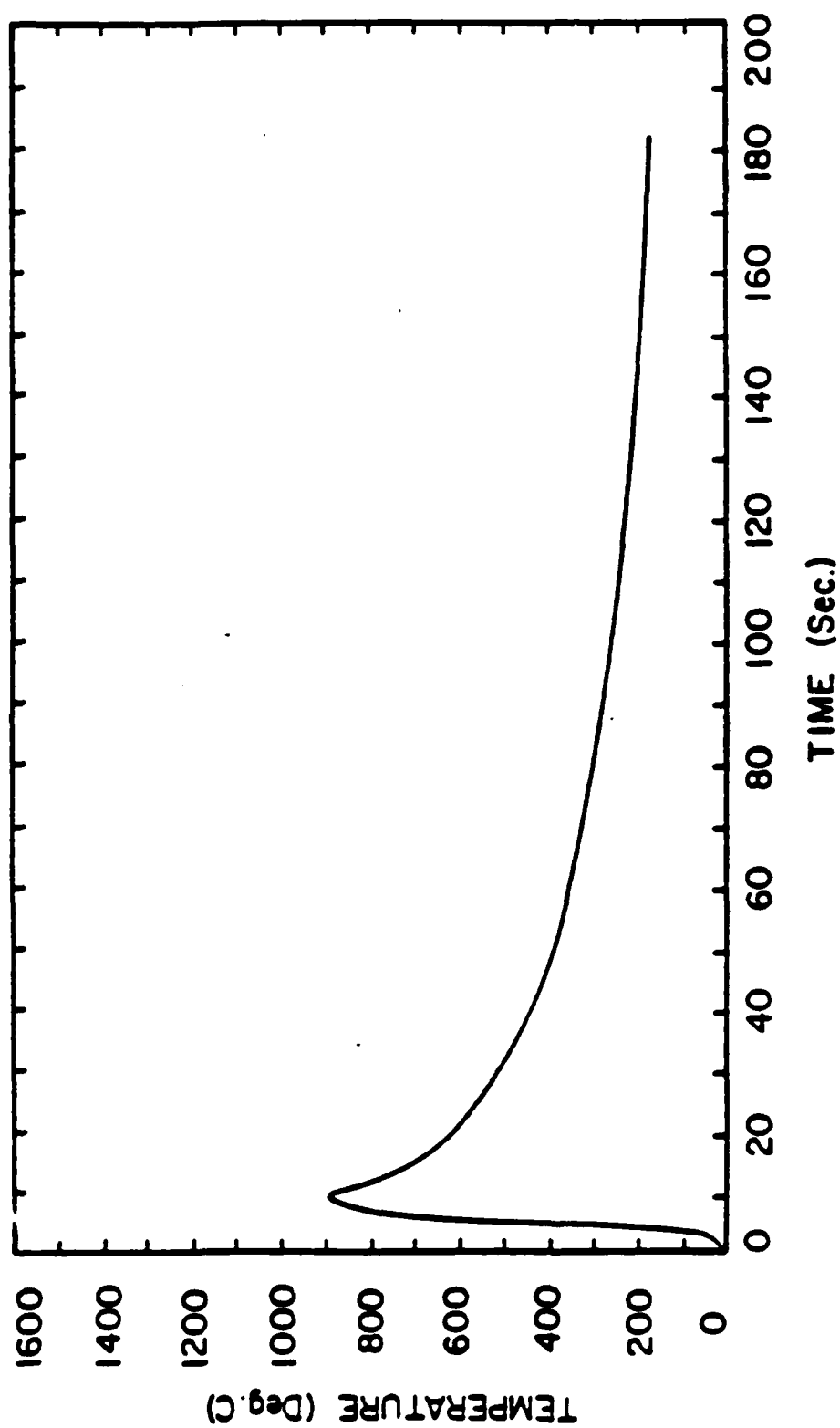
Figure 135.   (b) Experimental weld thermal cycle for Plate
9.TC2; nominal heat Input=1.97 KJ/mm. Tp=881
deg.C. DFZL=0.88mm.

APPENDIX 3

Comparison of actual HAZ and simulation HAZ charpy impact transition temperature curves.
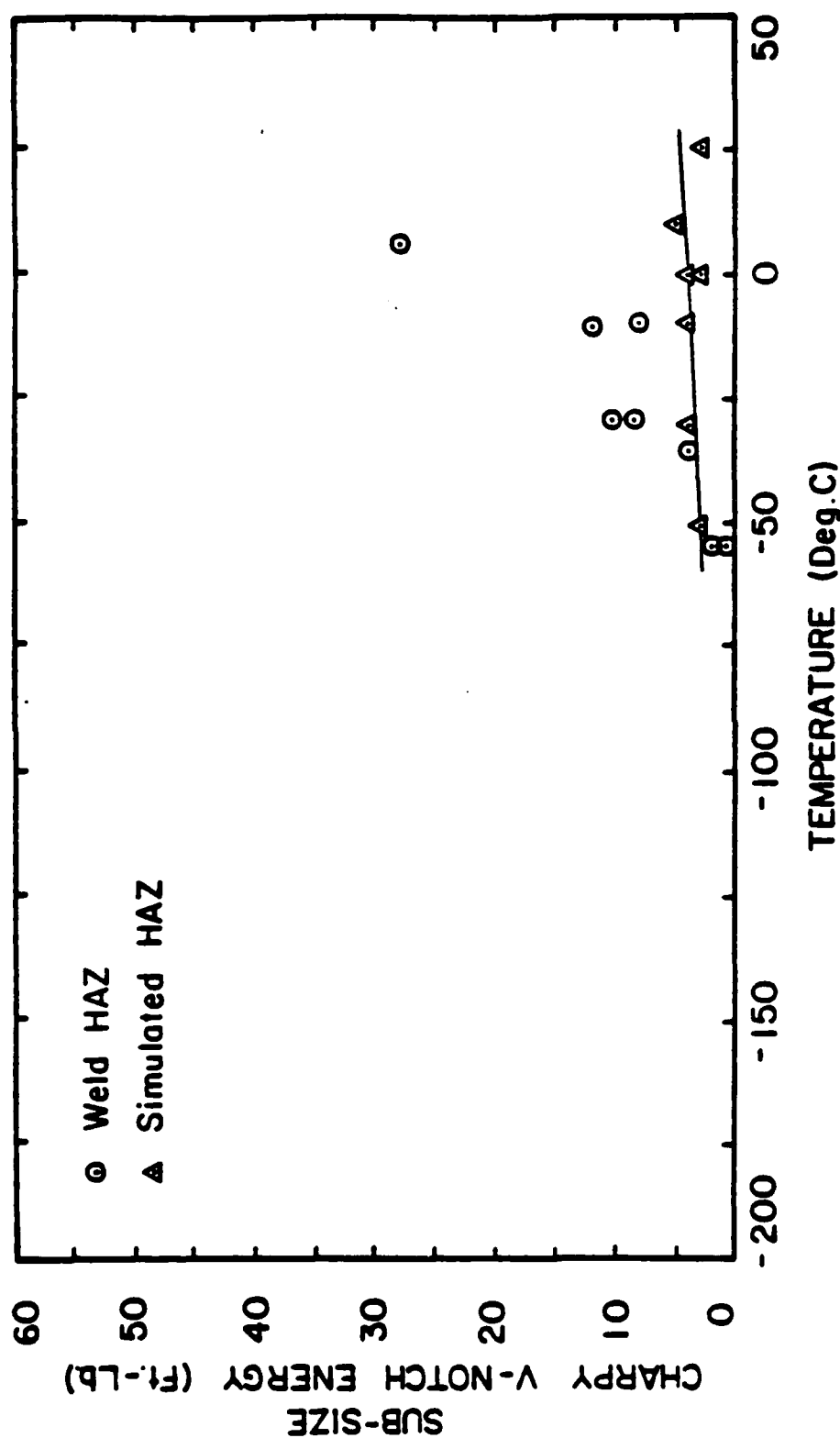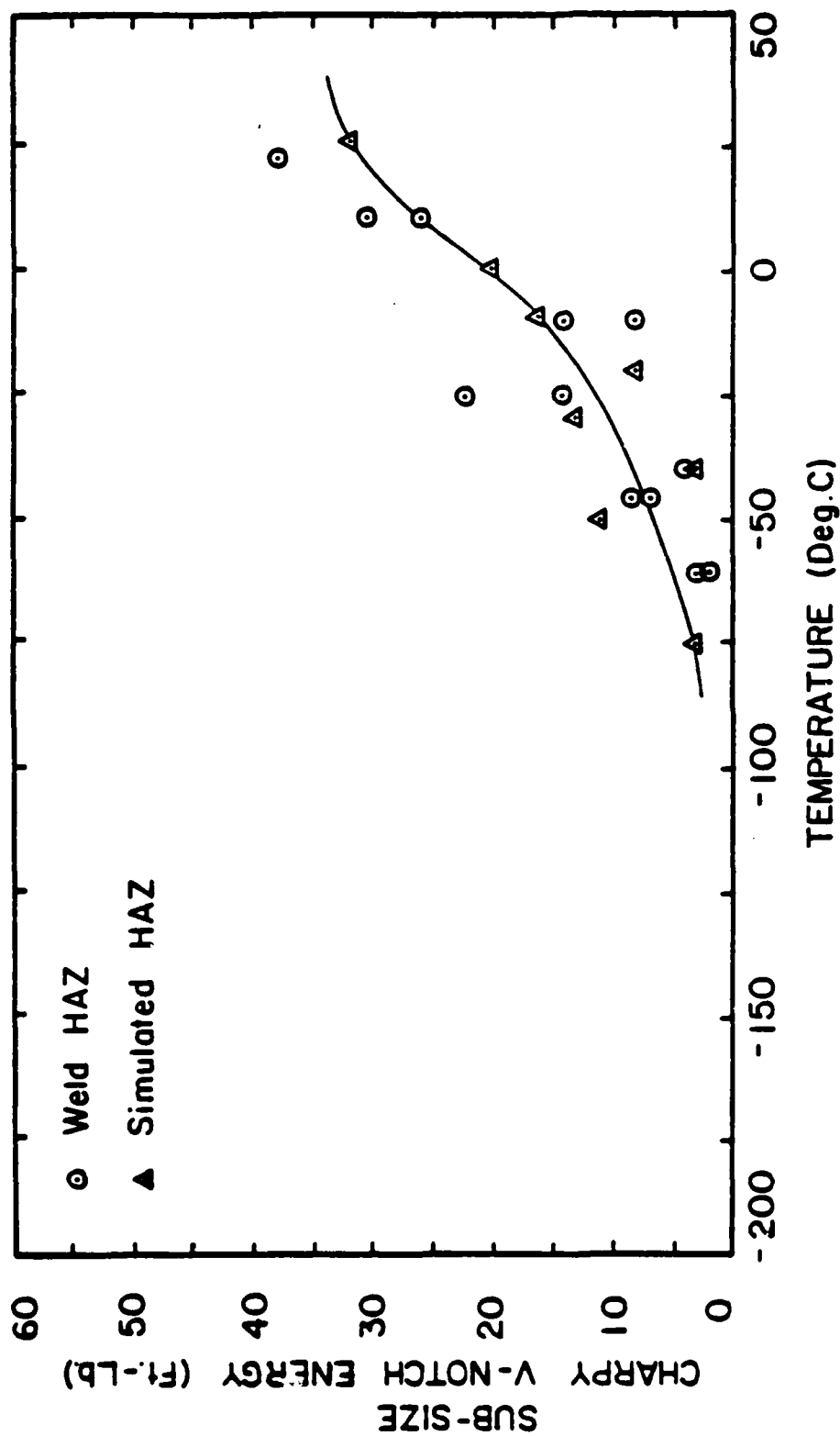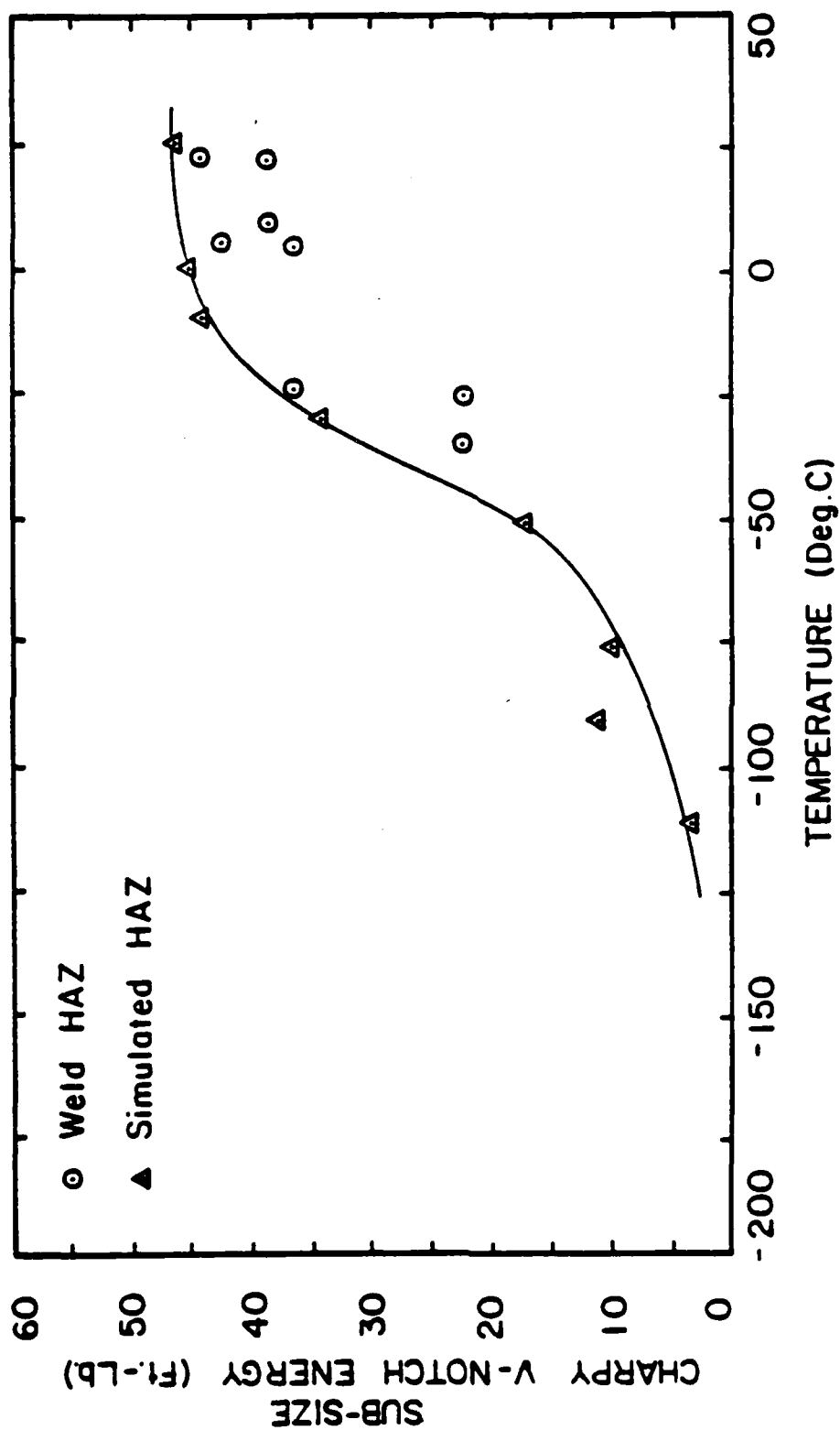
Figure 136.   Comparison of actual weld HAZ and
simulation HAZ subsize charpy impact
energy for a constant microstructure
as a function of temperature. Thermal cycle
parameters; nominal heat input = 3.35 KJ/mm.
Tp=1380 deg.C, D$_{FZL}$=0.40mm, DPH = 238.
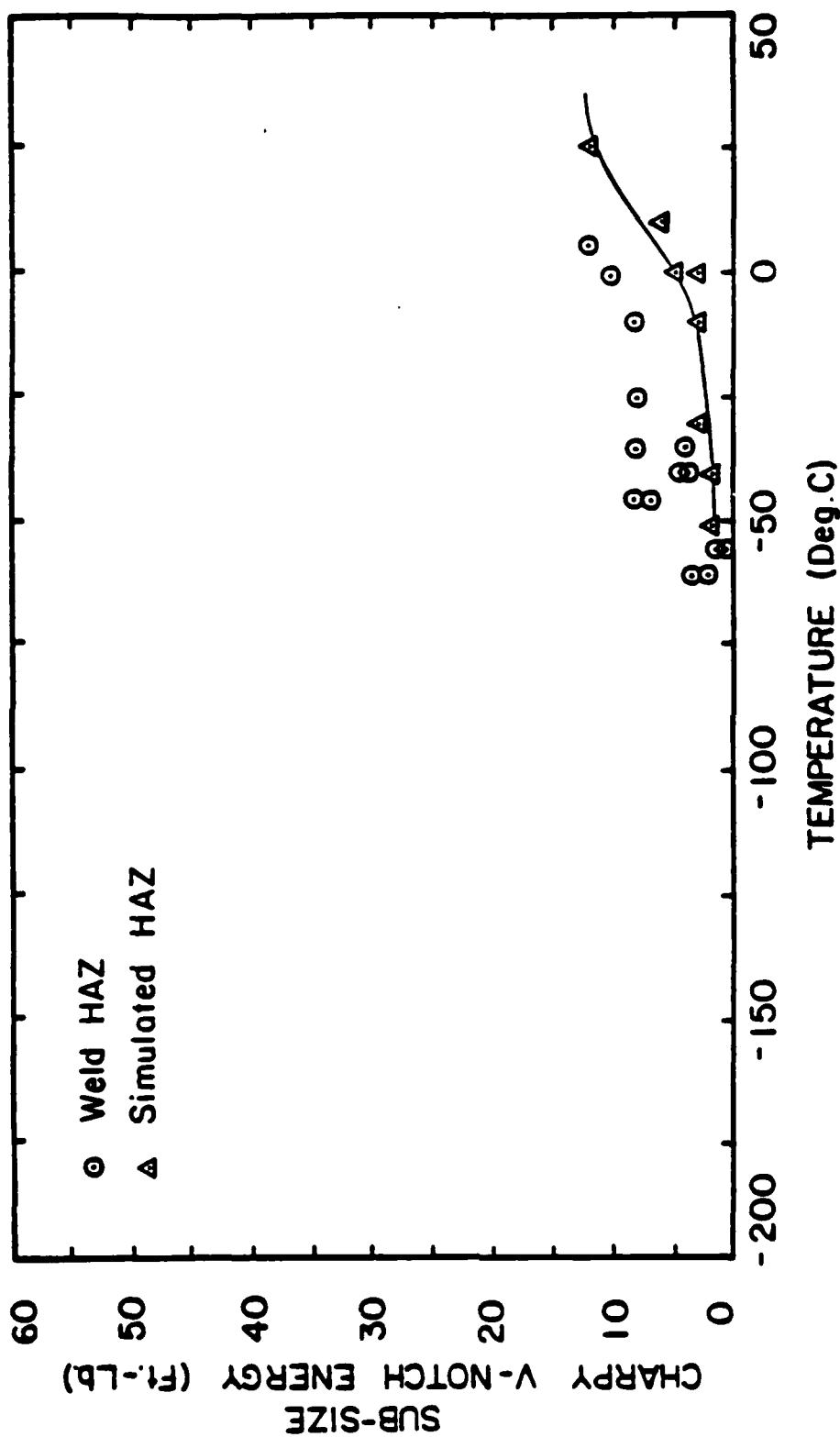
Figure 137.   Comparison of actual weld HAZ and
               simulation HAZ subsize charpy impact
               energy for a constant microstructure as a
               function of temperature.   Thermal cycle
               parameters; nominal heat input = 1.97 KJ/mm.
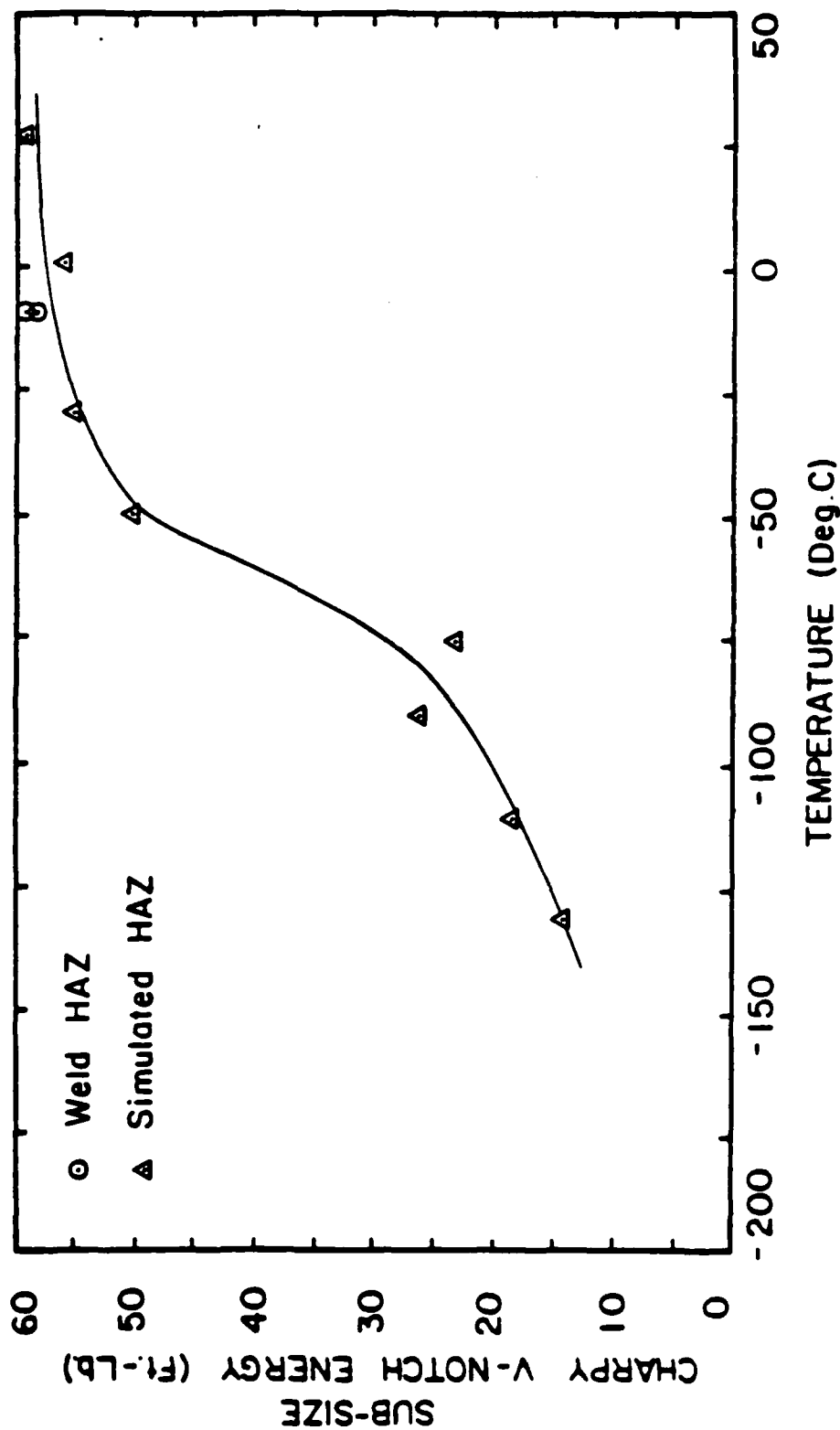   Tp=1398 deg.C, D_{FZL}=0.09mm, DPH = 285.

Figure 138. Comparison of actual weld HAZ and
simulation HAZ subsize charpy impact
energy for a constant microstructure as a
function of temperature. Thermal cycle
parameters; nominal heat input = 4.92 KJ/mm,
T_P=1063 deg.C, D_{FZL}=3.53mm, DPH = 240.

Figure 139.   Comparison of actual weld HAZ and
simulation HAZ subsize charpy impact
energy for a constant microstructure as a
function of temperature. Thermal cycle
parameters; nominal heat input = 1.97 KJ/mm.
Tp=558 deg.C, D_{FZL}=3.12mm, DPH = 215.

Figure 140.   Comparison of actual weld HAZ and
               simulation HAZ subsize charpy impact
               energy for a constant microstructure as a
               function of temperature.   Thermal cycle
               parameters; nominal heat input = 1.97 KJ/mm,
               T_P=881 deg.C, D_{FZL}=0.9mm, DPH = 250.

APPENDIX 4

Comparison between experimental thermal transient data
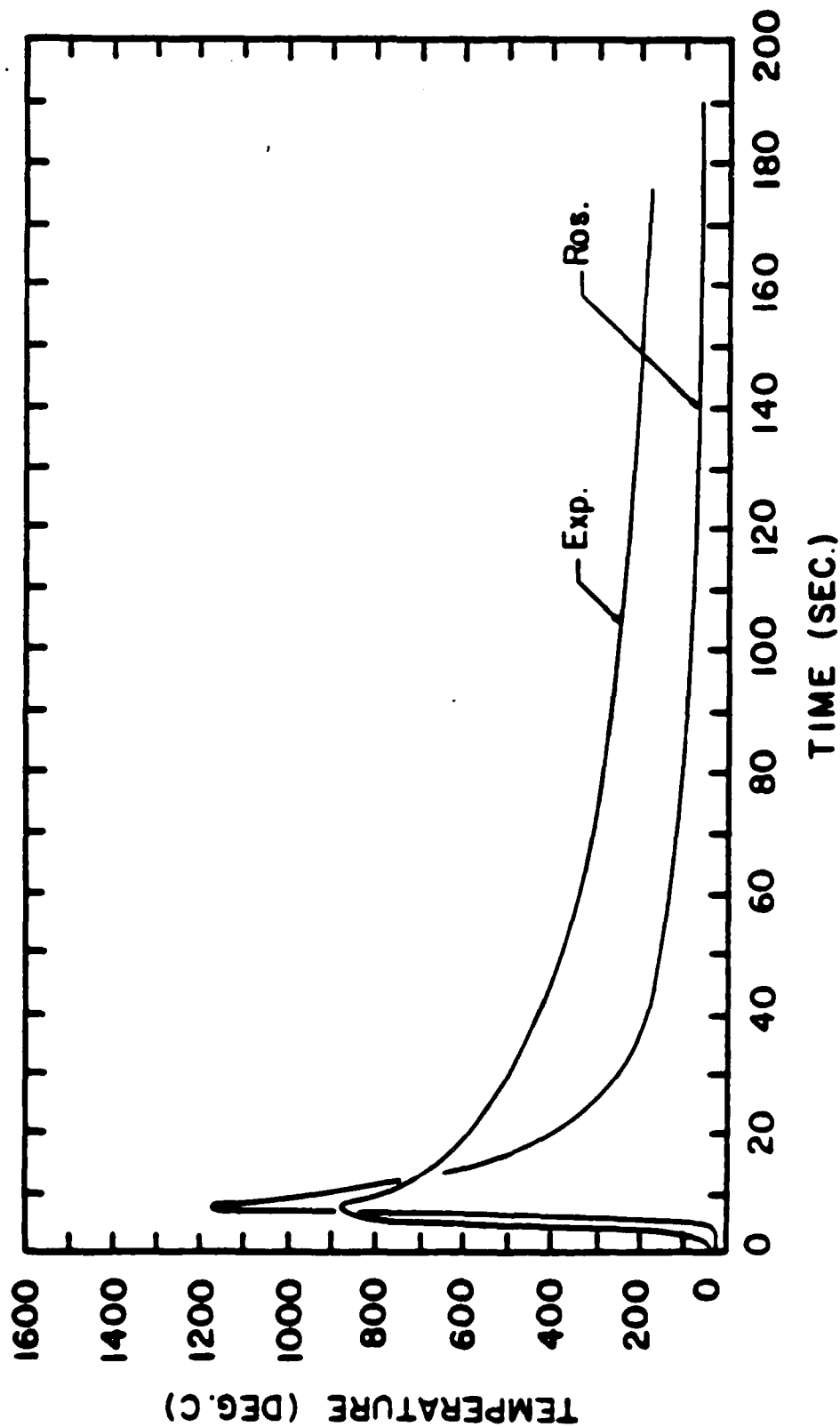
curves and theoretically determined thermal data curves.

Figure 141. Experimental and theoretical thermal cycles, nominal heat input=1.97 KJ/mm. D_{FZL}=0.88mm, T_p=881 deg.C. Theoretical thermal parameters: n=0.9, λ=0.10, a=0.08, T_p=1160-1163 deg.C.
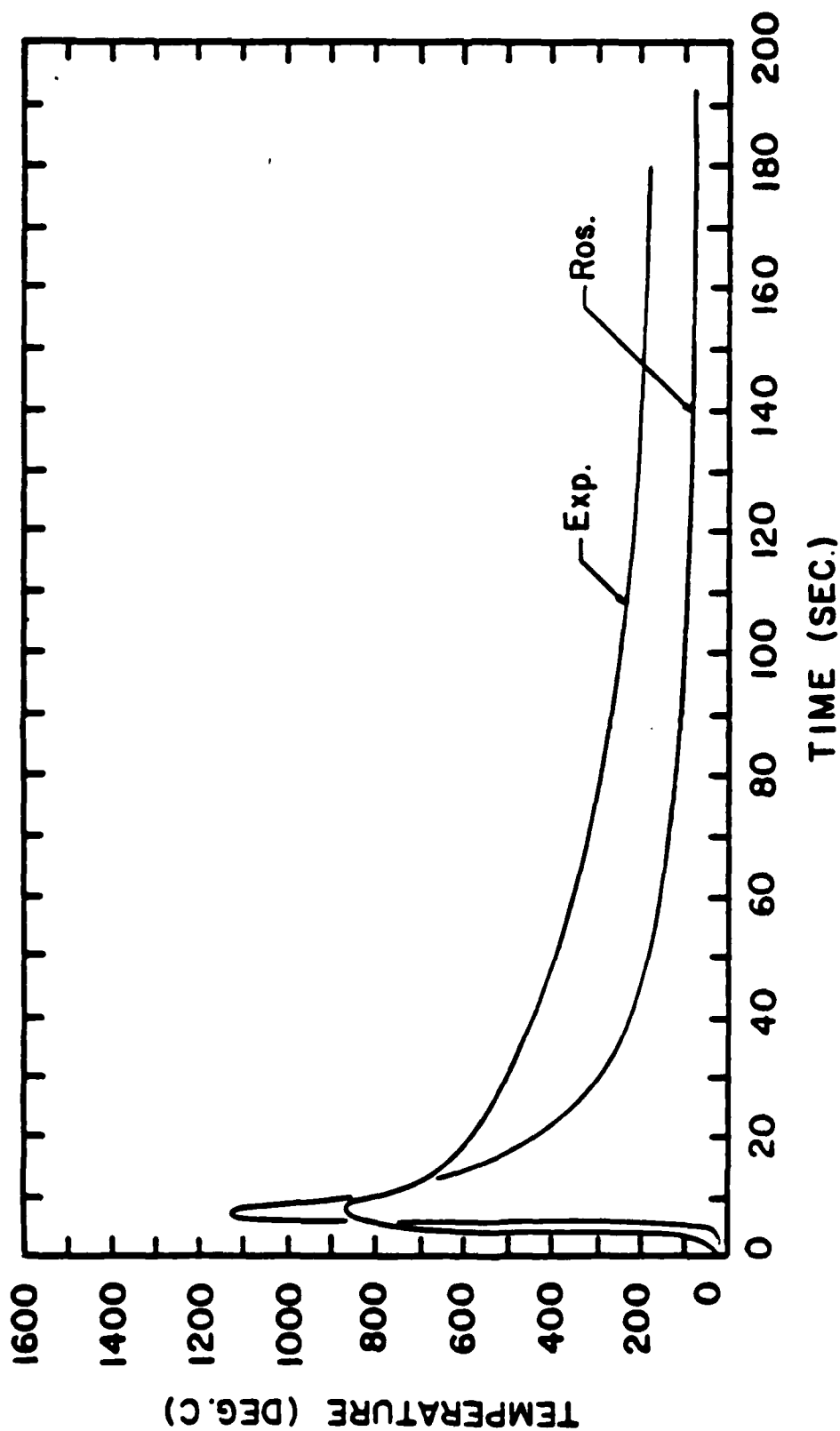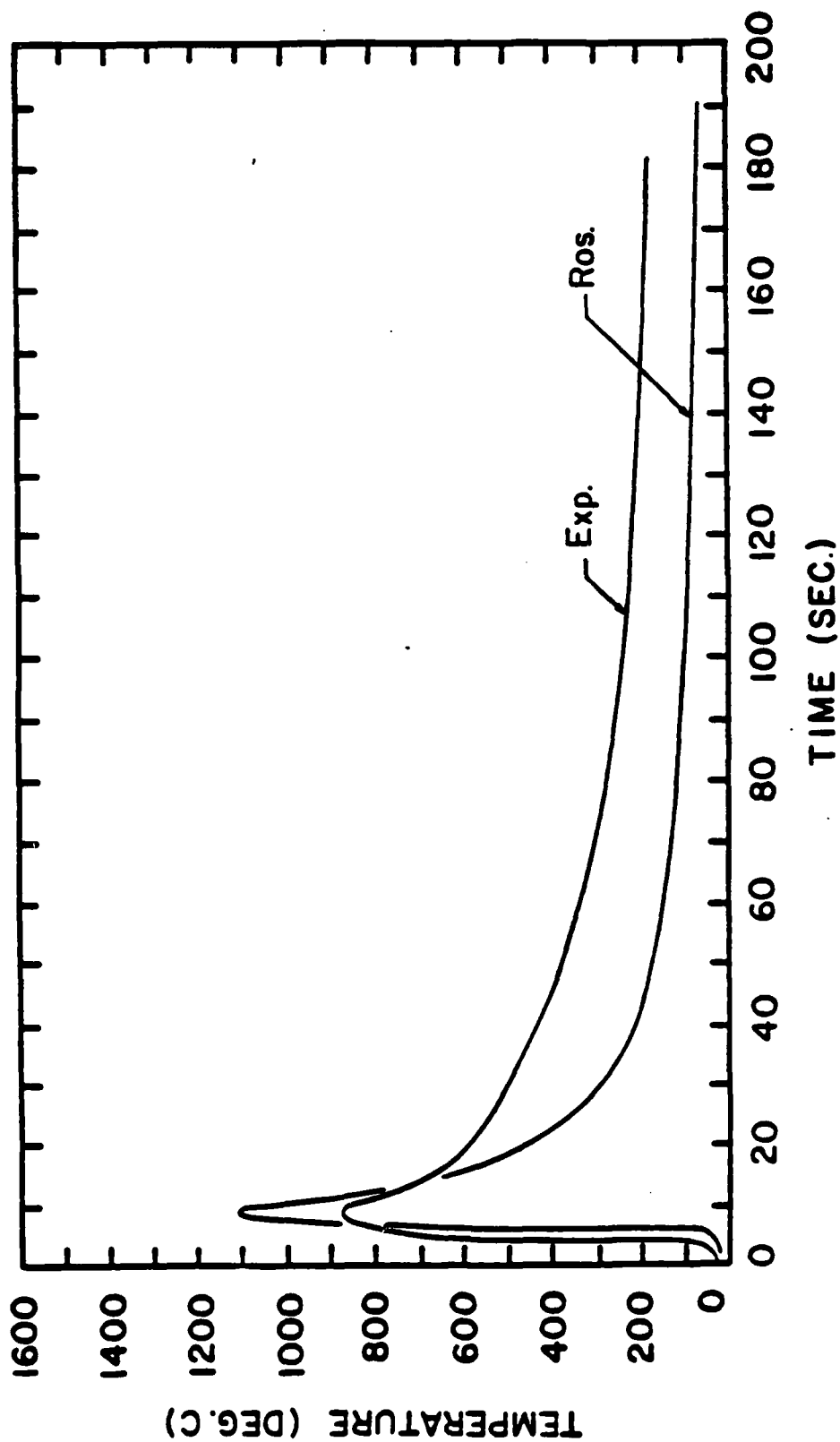
Figure 142. Experimental and theoretical thermal cycles, nominal heat input=1.97 KJ/mm. D_{FZL}=0.88mm. T_p=881 deg.C. Theoretical thermal parameters: n=0.9, λ=0.08, a=0.06, T_p=1140-1141 deg.C.

Figure 143. Experimental and theoretical thermal cycles nominal heat input=1.97 KJ/mm. D_{FZL}=.88mm, T_p=881 deg C. Theoretical thermal parameters: n=0.8, λ=0.06, a=0.06, T_p=1120-1123 deg.C .
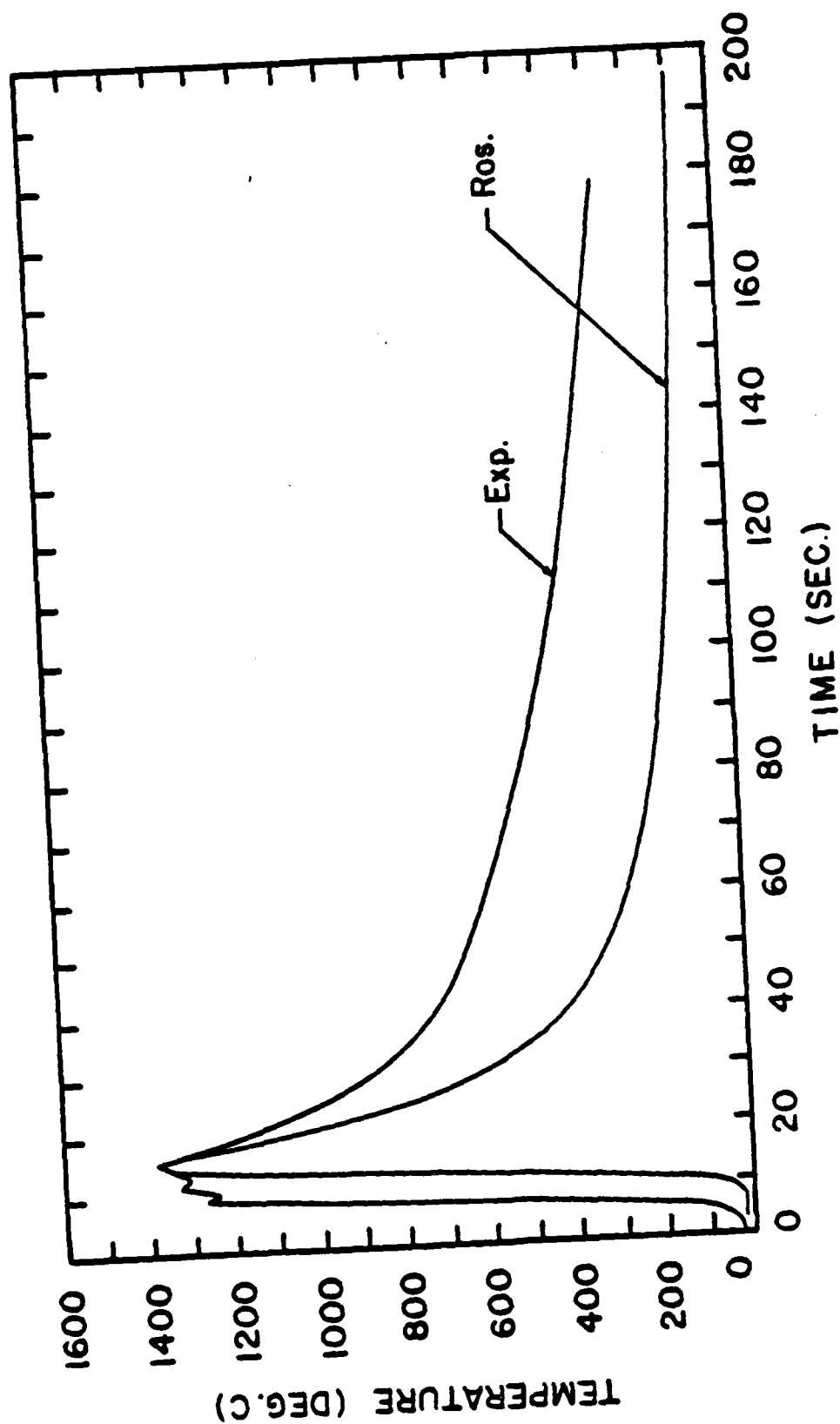
Figure 144. Experimental and theoretical thermal cycles, nominal heat input=3.35 KJ/mm. DFZL=.39mm, Tp=1380 deg.C. Theoretical thermal parameters: n=.9, λ=0.1, a=0.08, Tp=1355-1373 deg.C.

T-3136

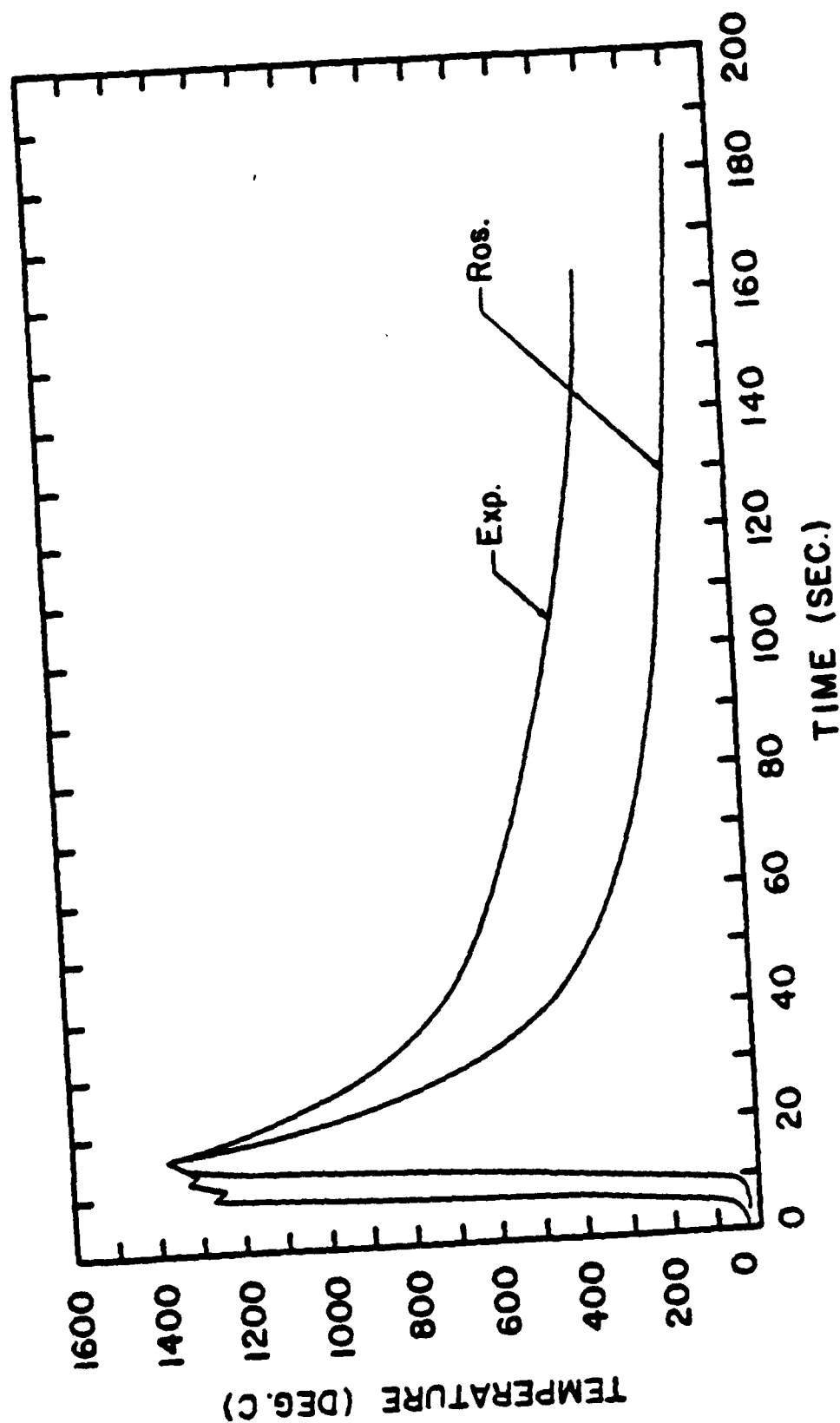Figure 145. Experimental and theoretical thermal cycles, nominal heat input=3.35 KJ/mm. D_{FZL}= 0.39mm, T_p=1380 deg.C. Theoretical thermal parameters; n=0.9, λ=0.08, a=0.06, T_p=1353-1362 deg.C.
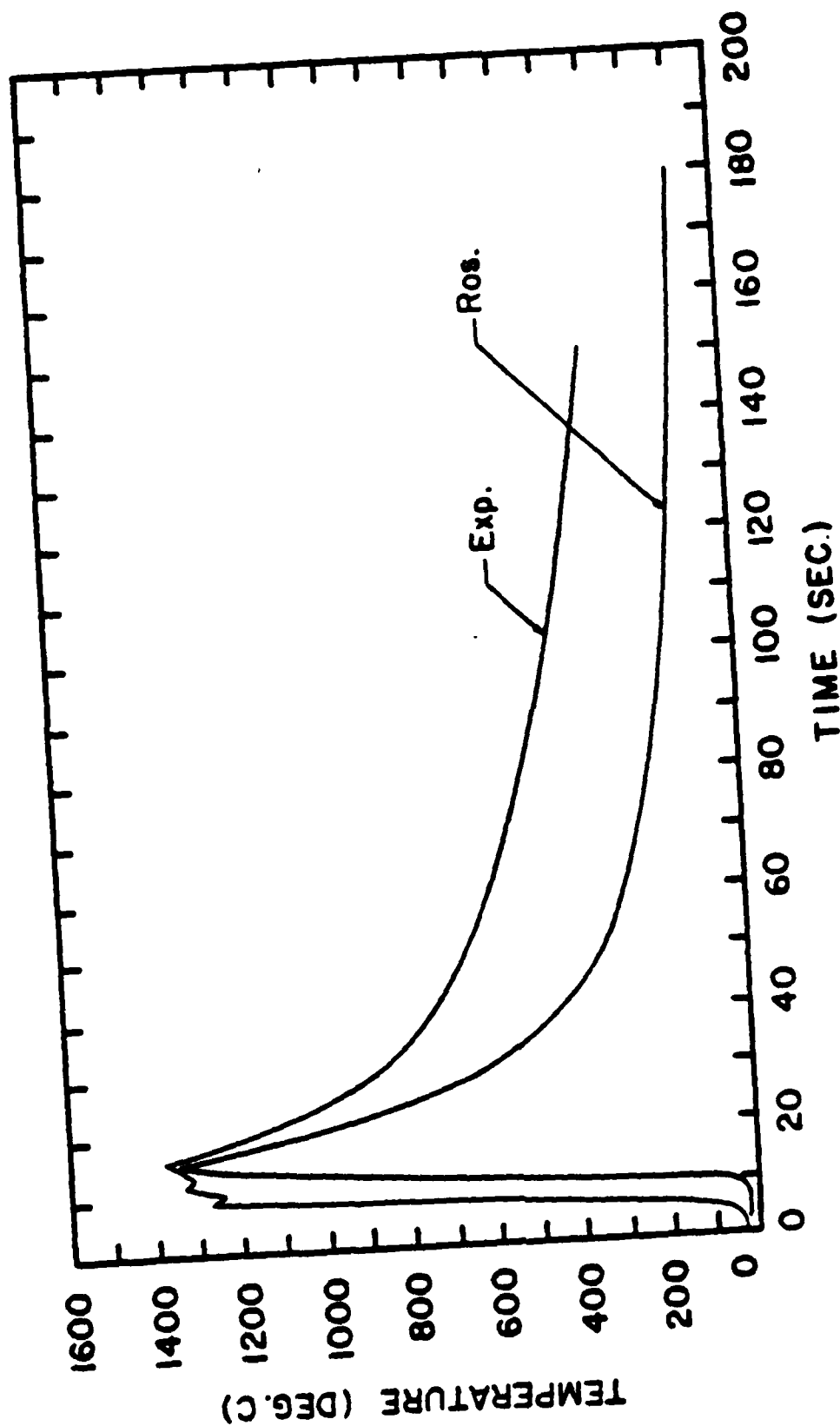
Figure 146. Experimental and theoretical thermal
cycles, nominal heat input=3.35 KJ/mm.
DFZL = 0.39mm, Tp=1380 deg.C.
Theoretical thermal parameters: n=0.8.
λ=0.08, a=0.06, Tp=1339-1353 deg.C.

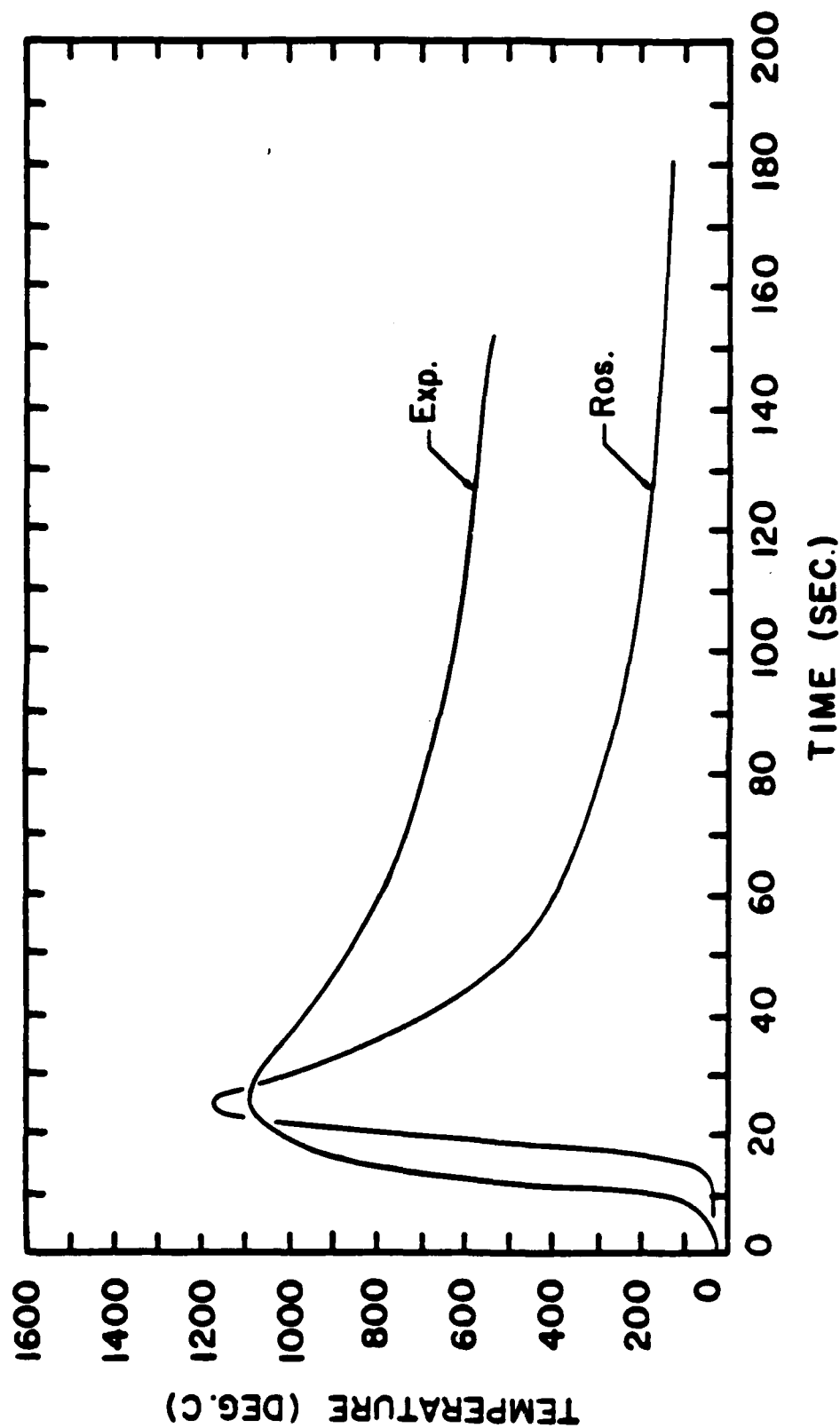Figure 147. Experimental and theoretical thermal
cycles, nominal heat input=4.92 KJ/mm.
D_{FZL}=1.52mm, Tp=1098 deg. C.
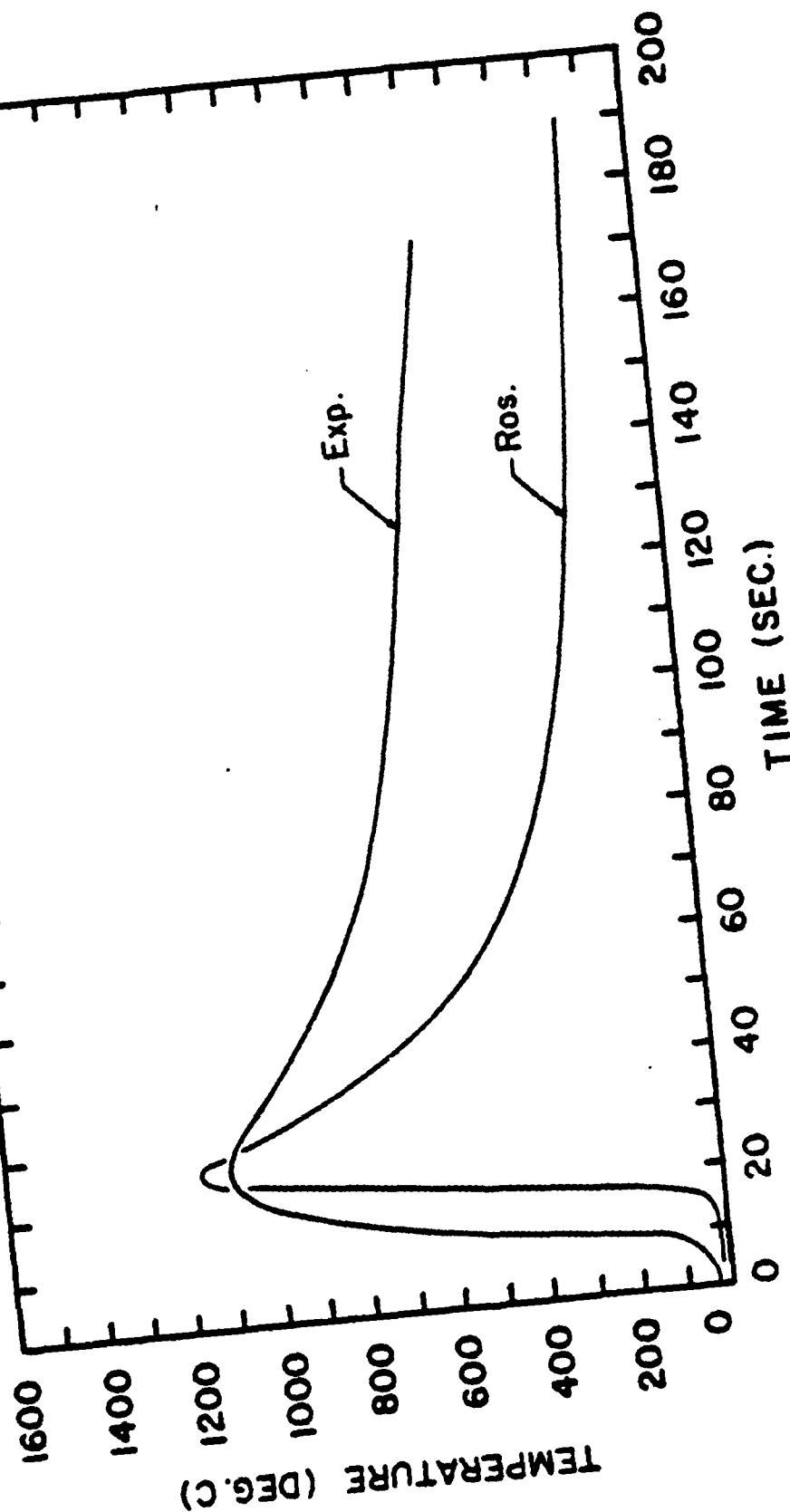Theoretical thermal parameters: n=0.9,
λ=0.1, a=0.08, Tp=1156-1177 deg. C.

T-3136

Figure 148. Experimental and theoretical thermal cycles, nominal heat input=4.92 KJ/mm. DFZL=1.52mm. Tp=1098 deg. C. Theoretical thermal parameters; n=0.9, λ=0.08, a=0.06, Tp=1146-1164 deg. C.

T-3136
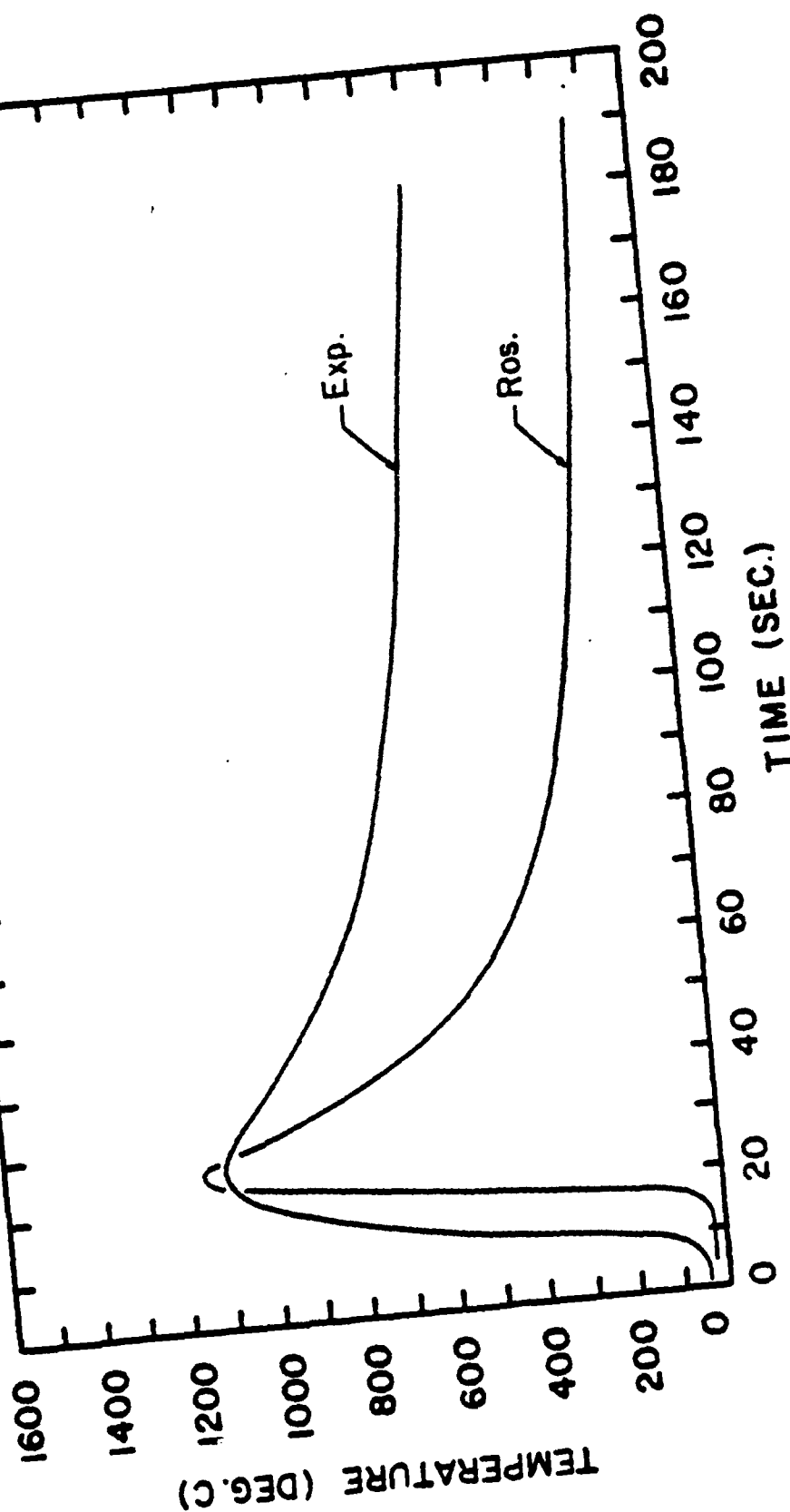
Figure 149. Experimental and theoretical thermal cycles, nominal heat input=4.92 KJ/mm. Tp=1098 deg. C. D_{FZL}=1.52mm. thermal parameters: n=0.8. Theoretical thermal parameters; n=0.8, Tp=1131-1146 deg. C. λ=0.08, a=0.06.

INITIAL DISTRIBUTION

Copies		CENTER DISTRIBUTION		
		Copies	Code
1	DDRE/Lib		
		1	012
1	CNO/OP 098T		
		1	012.5
2	OCNR		
	1 225	1	17
	1 Lib		
		1	28
1	NAVPGSCOL		
		1	2801
1	USNROTCU		
	NAVADMINU MIT	1	2803
2	NRL		
	1 Code 6380	1	281
	1 Code 6384		
		1	2812
7	NAVSEA		
	1 SEA 05M	1	2812 (Scoonover)
	1 SEA 05M2		
	1 SEA 05R	5	2814
	1 SEA 08S		
	1 SEA 55Y	2	2815
	1 SEA 55Y3		
	1 SEA 99612	1	2816
12	DTIC	1	522.1
		1	522.2
		1	5231

EMD

6 — 87

DTIC